Chiral Spin Textures and Dynamics in Multi-Sublattice Magnetic Materials

by

Lucas Marcelo Caretta

B.S. Materials Science and Engineering, University of Minnesota (2013)

Submitted to the Department of Materials Science and Engineering
in partial fulfilment of the requirements for the degree of

Doctor of Philosophy in Materials Science and Engineering

at the

MASSACHUSETTS INSTITUTE OF TECHNOLOGY

June 2019

Author . . . .
Department of Materials Science and Engineering
September 12, 2014

Certified by. . . . .
Geoffrey S. D. Beach
Professor, Co-director, Materials Research Laboratory (MRL)
Thesis Supervisor

Accepted by. . . . .
Donald R. Sadoway
Chairman, Department Committee on Graduate Students

To my father and mother who taught me how to engineer and endure

Chiral Spin Textures and Dynamics in Multi-Sublattice Magnetic Materials

by

Lucas Marcelo Caretta

Submitted to the Department of Materials Science and Engineering
on April 26th, 2019, in Partial Fulfillment of the
Requirements for the Degree of
Doctor of Philosophy in Materials Science and Engineering

ABSTRACT

Spintronics is a research field that aims to understand and control magnetic spins on the nanoscale and should enable next-generation data storage and logic. A promising approach is to encode bits of information using nanoscale spin textures, such as chiral domain walls or skyrmions that can be translated by currents across racetrack-like wire devices. One technological and scientific challenge is to stabilize small spin textures and to move them efficiently with high velocities, which is critical for dense, fast memory. For the past decade, work has focused on using ferromagnetic heterostructures to host chiral spin textures. However, ferromagnets have fundamental limitations that inhibit further progress: large stray fields limit bit sizes and precessional dynamics limit operating speeds. In this thesis, we examine a broader class of multi-sublattice materials: ferrimagnets. We show that by using ferrimagnets, the fundamental limits of ferromagnets can be overcome, realizing order-of-magnitude improvements in both size and speed. Using metallic, ferrimagnetic $Pt/Gd_{44}Co_{56}/TaO_x$ films with a sizeable Dzyaloshinskii–Moriya interaction (DMI), we realize a current-driven domain wall motion of $1.3\ \mathrm{km\ s^{-1}}$ near the angular momentum compensation temperature and room-temperature-stable skyrmions with diameters close to 10 nm near the magnetic compensation temperature. For the first time, we show that the DMI is present in ferrimagnetic insulator garnet films and that the DMI necessitates a rare-earth ion in the magnetic insulator. Thickness dependent studies and interface engineering show that the DMI manifests at the ferrimagnetic insulator – substrate oxide interface. We use a large spin-orbit torque from a Pt overlayer and the DMI to exploit ferrimagnetic dynamics, driving domain walls in low-damping and low-pinning GGG/TmIG/Pt heterostructures at velocities as high as $2.1\ \mathrm{km\ s^{-1}}$. Moreover, by utilizing the ultra-low damping nature of Bi-YIG and an in-plane field, we can drive domain walls in GSGG/Bi-YIG/Pt at near relativistic velocities exceeding $4.0\ \mathrm{km\ s^{-1}}$, where the domain wall velocity is no longer limited by a velocity plateau defined by the in-plane field, but the magnon group velocity in Bi-YIG. These results show that multi-sublattice ferrimagnetic films are a promising materials system for next-generation data storage, paving a path forward for the field of spintronics.

Thesis supervisor: Geoffrey S. D. Beach
Professor, Co-director, Materials Research Laboratory (MRL) at MIT

1. ACKNOWLEDGEMENTS

Coming to MIT to complete a PhD has been the most rewarding experience of my life. And it has been because of the people. Here, I would like to take the opportunity to thank those who have helped me grow as an engineer, a scientist, a thinker, a leader, and as a human.

First and foremost, I would like to show my extreme gratitude to my PhD advisor Professor Geoff Beach. Nearly six years ago, I was determined to join your research group not necessarily for the innovative research but because of you and the amazing people you have cultivated in your group. You kindness, contagious passion, and drive are what inspire me to get in early, leave late, and discover the unknown every day. Thank you for guidance, your patience, and above all, your enthusiasm for what we do. Thank you for pushing me to my limits intellectually and forcing me to be uncomfortable. You have made me a better trouble shooter, tinkerer, thinker, and presenter, and have helped me grow and develop my own passions. I could not have asked for a better thesis advisor and mentor.

Secondly, I would like to thank the other members of my thesis committee, Professor Caroline Ross and Professor Kim Kimerling. Thank you for your invaluable feedback, guidance, and direction throughout my PhD. Thank you for pushing me and asking the hard questions. In particular, I would like to thank Professor Ross for giving me the opportunity to collaborate with her group on many occasions and for teaching me all things magnetic oxide.

To David Bono, there's almost nothing in this PhD that doesn't have your fingerprints (or solder) on it. I cannot count the number of times you've helped me solve problems, helped me repair equipment, or made me laugh. Your ingenuity and creativity does not go unnoticed. Thank you for being patient with me with everything you taught me. Thank you for always going above and beyond to make help me design the best measurements systems imaginable. I will always remember what you told me a few years ago while we were designing an experiment in your lab, "Stop thinking like a PhD student and start thinking like an engineer!" Above all, thank you for your friendship. You have helped make this PhD enjoyable, and I can't wait to grab lunch again.

Thank you to Colin Marcus and Brian Neltner for helping me with everything high frequency and LED related along the way. In particular, I want to thank Colin for his friendship and for helping me to design several circuit not only for this thesis but for outreach efforts. Your creativity and willingness to always help does not go unnoticed. Thank you Brian for always being willing to help, always lending an ear, and for all the fun times at lunch.

One of the most valuable things I learned at MIT was how to build and fabricate. I relied heavily on the DMSE machine shops and other MIT shared facilities. I am extremely grateful for the guidance, expertise, and training from Mike Tarkanian. There usually isn't a thing you don't know how to build. I would also like to thank Chris Di Perna, not only for machine ship training but for being always willing to talk fitness in the hallway. Thank you, Tara Fadenrecht for always asking how I'm doing and making me laugh in the basement of Building 4. I would also like to thank Shaymus Hudson giving me the tips and trick of the machining world. I would like to sincerely thank Kurt Broderick in EML for sharing his expertise on fabrication, always answering his phone when I need help, and for the great company.

I've always loved teaching, and MIT cemented that belief. I would like to particularly thank James Hunter for being patient with me during the photocell lab and helping make that lab enjoyable. I

would like to thank Meri Treska and Geetha Berera for letting me learn from their valuable teaching experience. Finally, I would like to thank Professor Harry Tuller for giving me teaching freedom in 3.024 lab.

DMSE would not run without the administrative staff. And I wouldn't be where I am without them either. I would like to thank Rachel Kemper and Heather Upshaw for gracing me with invaluable opportunities throughout my PhD. In particular, I would like to thank Heather for her support in my entrepreneurial efforts, and Rachel for her guidance with the Lemelson-Vest fund and helping me with the cover artwork. Thank you to Ryan Kendal for the Photoshop help and for always exuberantly saying hi in the hallway! Adam Shervanian - Thanks for countless facilities issues you helped me fix and for your always fast responses. I would also like to thank Department Head, Professor Chris Schuh for always being willing to meet with me and mentor me on numerous occasions. Thank you to Tiffany Luongo for being a great friend and for always keeping the department candy jar protected.

I would like to especially thank DMSE staff Angelita Mireles and Elissa Haverty. Angelita – you have always been there to not only answer my crazy questions, but to be my ally and support system. From when I broke my nose to when I needed a signature, you've always been there. I will always appreciate your care. Elissa – Although you're not the reason I came to MIT, you are certainly one of the reasons I'm glad I came. Forget the ridiculous number of times you helped me with paperwork, I will always value the deep life-long friendship we created. Thank you for always being there when I needed it the most and for helping me survive the past six years.

My PhD has given me the opportunity to travel around the globe. I would like to thank the huge number of international collaborators I've had the pleasure of working with, include researchers at MBI-Berlin, TU-Berlin, DESY, BESSY, BNL, ALS, SLS, MPI-Stuttgart, and Mainz.

Being a member of the Beach is an unforgettable experience. Many names and faces have passed through the Beach group and each have had a unique impact on me. To Can Avci, Chi-Feng Pai, Daniel Suzuki, Felix Buettner, Ivan Lemesh, Jason Bartell, Kai Litzius, Kohei Ueda, Liz Rapoport, Mantao Huang, Minae Ouk, Parnika Agrawal, Pooja Reddy, Sara Sheffels, Sarah Schlotter, Sasha Churikova, Seonghoon Woo, Siying Huang, Uwe Bauer, Satoru Emori, and unofficial member Ethan Rosenberg - thank you for always being willing to help and for being my friends and family at MIT. I would like to particularly thank my "incoming class" into the group, AJ Tan and Max Mann. Thanks for all the laughs, memories, and brainstorming sessions. Not only have I learned more from you two than anyone else the past six years, I've laughed with you more than anyone. Thanks for the lifelong friendship we've created. And remember… "We just do things wrong enough times, we have to get it right eventually…"

This list would not be complete if not for my friends around MIT and around the globe. Thanks to the *nanographene conference*, comprised of Gregory Eckhian, Brad Nakanishi, Sam Wagstaff, and Cooper Rinzler. I wouldn't have made it through the first year and written exam without you guys. Thank for the countless late nights studying. See you in Idaho! I would also like to thank my friends outside of MIT – Cam Matheson, Caroline Brantley, Rachael McGillivray, Jamie Berman, Sruti Velamakani, and Kristy Helscel. Thank you for supporting me and believing in me. It has truly meant the world.

To Brooke – Thank you for being the unofficial creative director of my thesis and for helping me push through to the end. I wouldn’t have made it without you, and I will always be grateful for that.

Above all, I would like to thank my family. Thank you for your love and support. I owe everything to you. To Nick, Romina, and Marcia - Thanks for being the best older siblings one could ask for. You are my role models and my inspirations. You have taught me more than you know. Thank you for letting me brag about you and for always pretending I’m the smartest sibling.

To my mother, Diana – Thank you for your texts everyday asking if I’m eating well, if I’m sleeping well, and how I’m feeling. Your support and love is all I could ever ask for. You’ve taught me how to be a better human, endure through challenges, and always be the bigger person. Thank you for always pushing me to do my best, celebrating with me during the highs, and being there to help me during the lows. And thank you for tolerating not only one, but two mad scientists in the household.

To my father, Raul – You taught me how to engineer. Thank you for always believing in me and supporting me and my dreams. Thanks for teaching me how to think like engineer and scientist and for helping me forge my own path. From giving me extra math problems as a child to the many late night phone calls problem solving and discussing experiments, you’ve always been there with an open ear to help me grow and learn. Thanks for letting me following in your footsteps.

This work would not have been possible without the financial support of the National Science Foundation Graduate Research Fellowship Program and the National GEM Consortium Fellowship.

2. TABLE OF CONTENTS

Chiral Spin Textures and Dynamics in Multi-Sublattice Magnetic Materials

3. BACKGROUND

3.0 Introduction

Types of magnetic order

From engineered aluminum welds on automobile frames to color LED displays to corrosion coatings on airplanes, the achievements of materials science and engineering are ubiquitous in the world around us. Lesser known, but equally important, are the ever-present magnetic materials that the world relies on. Magnetic materials are the building blocks of a vast number of applications. Electric car motors, actuators, sensors, headphones, MRI's, and cybersecurity all rely on advanced magnetic materials. One notable application is high-density data storage. While today, many personal computers and electronic devices rely on electronic forms of memory, magnetic forms of data storage are still the premier choice for dense, inexpensive storage. In fact, "the cloud" relies on such dense forms of storage, including magnetic hard disk drives and even magnetic tape storage. Actually, the most dense forms of memory to-date are magnetic tape and disks, having a capacity of 31 Gbit/cm² (Sony 2017) and 201 Gbit/in² (Seagate 2017), respectively[1]. Moreover, new, immerging forms of magnetic memory, such as magnetic-RAM (MRAM) aim to outperform and replace current forms of non-volatile memory in personal electronics in the near future.

Our insatiable appetite for more data storage will undoubtedly be met with new materials innovations in magnetic storage, requiring fast, denser, lighter and more power-efficient designs. This thesis aims to make advances to magnetic memory and logic design by exploiting interface-driven chiral effects in multi-sublattice magnetic thin films. This chapter is intended to introduce the reader to the principles of magnetic materials in the context of thin films. Here, we will discuss what gives rise to magnetism, different forms of magnetism, and anisotropic magnetism. We will review domain wall and skyrmion energetics and how domain walls and skyrmions can be used in a device architecture.

3.1 Types of Magnetism

Magnetic moments or “spins” are the fundamental quantized units of magnetism. Magnetism arises when spins order themselves in the absence of a magnetic field. This can take various forms. For instance, when all the magnetic moments lie in the same, unique direction, this is called ferromagnetism[2]. Although ubiquitous, magnetic order in materials is a purely quantum mechanical phenomenon and cannot be explained by classical physics. Whenever possible, we will describe magnetic behavior using a semi-classical model. The quantum mechanical Hamiltonian for the Heisenberg exchange interaction takes the form of Eq. 3.1.

$$\hat{H} = -\sum_{ij} J_{ij} \boldsymbol{S_i} \cdot \boldsymbol{S_j} \tag{3.1}$$

where J_{ij} is the exchange constant, and $\boldsymbol{S_i}$ and $\boldsymbol{S_j}$ are adjacent spins. The dot product between the spins energetically prefers collinear alignment of spins. The exchange energy per unit volume can also be described by

$$E_{ex} = A\left(\frac{\delta\Theta}{\delta x}\right)^2 \tag{3.2}$$

where θ is the angle between neighboring spins and x is the separation between the spins. A is a stiffness, often called the exchange stiffness. It is worth noting that magnetic order governed by direct exchange (Eq. 3.1, 3.2) is only possible when the separation distance between neighboring electron spins (x) is very small, such that there is sufficient overlap of their wave function. In the case of a ferromagnet, J_{ij} is positive, ensuring parallel alignment of neighboring spins. When J_{ij}

is negative, neighboring spins prefer anti-parallel alignment, giving the system anti-ferromagnetic order. These are schematically shown in Fig. 3.1a,b. The sum of the total magnetic moments in a material per unit volume (or mass) is call the saturation magnetisation (M_s). In the case of an antiferromagnet, $M_s = 0$, meaning that although magnetic order exists, there is no net magnetisation in the film. Thus, an applied magnetic field has no effect of an antiferromagnet. Crystal structure often dictates if magnetic materials are ferro- or anti-ferromagnetic. For instance, FCC rocksalt structures and monoxides are commonly antiferromagnetic, where alternating 111 planes have oppositely oriented spins.

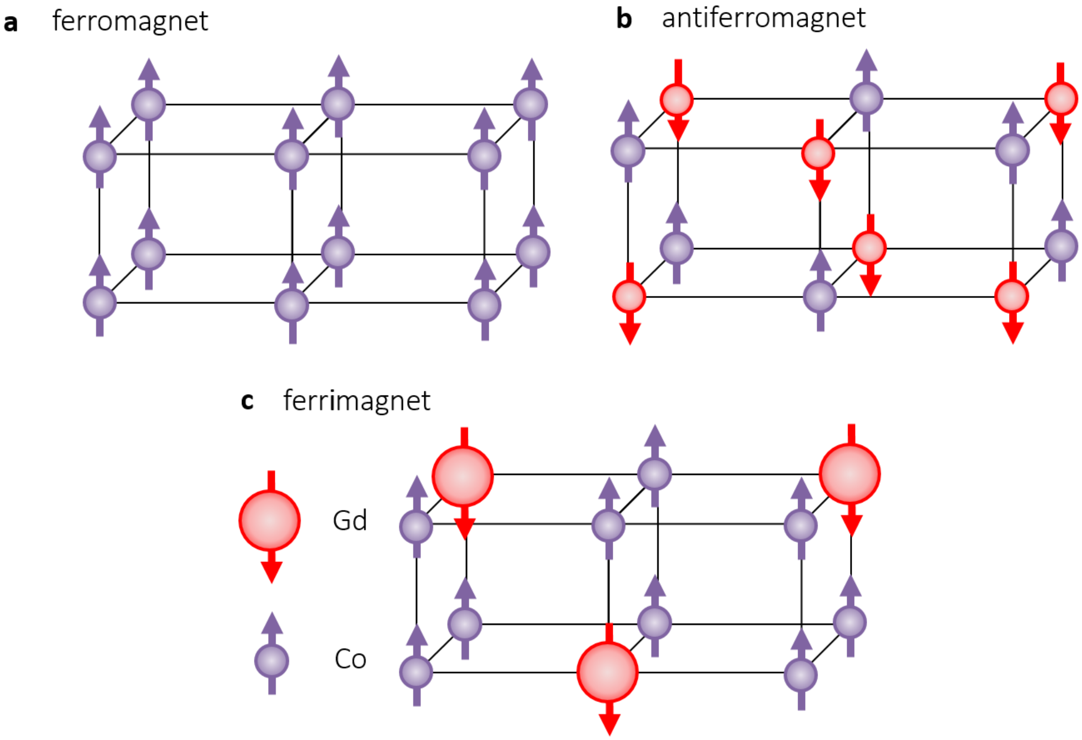

Figure 3.1 | Types of magnetic ordering. a) ferromagnetism occurs when spins are oriented along the same direction. Anti-ferromagnetic alignment occurs when spin are oriented anit-parallel. When the net moment is zero, this is an anti-ferromagnet (b), and when there is still a net moment, it is called a ferrimagnet (c).

A third case of magnetic ordering is called ferrimagnetism. In these systems, the magnetic order is anti-ferromagnetic; however, there is still a net moment (see Figure 3.1c). This is often the case in multi-sublattice systems, where different atoms are located on different crystal sites[3]. Spinel structures are often ferrimagnetic. Two classic ferrimagnet examples are iron oxide Fe_3O_4 (a spinel) and GdCo (an amorphous metal). In Fe_3O_4 iron atoms with different valences are found on different sites, giving rise to a net moment. In the case of GdCo, each element occupies a different site[2,3]. Rare earth- iron garnet materials are another type of ferrimagnet, which take the form: $RE_3Fe_5O_{12}$, where RE is a rare earth element. These materials have a cubic crystal structures with a very complicated multi-atom unit cell. Three iron ions are on tetrahedral sites, and two are on octahedral sites, while the Re ions are on sites of dodecahedral symmetry.

The different Curie temperatures of the multi-sublattices yields a non-zero moment that is very temperature-dependent, as each sublattice has its own unique temperature dependence. This can result in one sublattice being dominant at low temperatures and the other being dominant at high temperatures. When the sublattices effectively cancel each other out, the system behaves similarly to a natural anti-ferromagnet. This temperature is called the magnetic compensation temperature. Ferrimagnets have two compensation temperatures. The first is the magnetic compensation, T_M, where the net magnetisation of the film is zero. The second is the angular momentum compensation temperature, T_A, where the net angular moment (the net spin density) of the film is zero. These two compensation points are, in general, not the same temperature, as the lande g-factors, and hence the gyromagnetic ratio of each sublattice might be different (see Eq. 3.3)[3].

$$\mu = \gamma(\boldsymbol{L} + \boldsymbol{gS}) \qquad 3.3$$

where $\mu = e/2m$ is the magnetic moment, γ is the gyromagnetic ratio, e is the electron charge, m is the mass of the electron, g is the Lande g-factor, $\boldsymbol{S}$ is the spin angular momentum, and $\boldsymbol{L}$ is the orbital angular momentum. Eq. 3.3 shows that the total magnetic moment of an electron is the sum of its orbital and spin angular momentum components. The relative amounts of each are weighted by the Lande g-factor. The relationship between the moment and the angular momentum is a function of the gyromagnetic ratio and, hence, the g-factor of each sublattice element. Values for g are typically near 2, meaning that the spin angular momentum is about twice as effective in producing a magnetic moment.

Although $\boldsymbol{L}$ and $\boldsymbol{S}$ are separate quantum numbers, they can be coupled by an effect called spin-orbit coupling, whose Hamiltonian take the form:

$$\hat{H} = \xi \boldsymbol{L} \cdot \boldsymbol{S} \qquad 3.4$$

where $\xi \propto Z^4$, and Z is the atomic number. Spin-orbit couple simply means that the spin and orbital angular moments are related to each other. In other words, the bonding or crystal structure of the material will influence the preferred orientation of the moment. Fig. 3.2 illustrates this is a semi-classical way. In Fig 3.2a, a simplistic picture of an atom shows an electron with charge $-e$ is orbiting the nucleus of an atom of charge $+Ze$, with a velocity v. Figure 3.2b shows this same simplified picture, but in the rest frame of the electron. In the rest frame of the electron, the $+Ze$ charged nucleus is orbiting an electron with velocity $-v$. A moving charge current (the nucleus) generates a magnetic field, similar to a current-carrying wire. Effectively, the movement of the electron in its orbital (dictated by bonding and crystal structure) produces a magnetic field which influences the net moment of the electron. This is spin-orbit coupling. Also noticeable is that the larger the charge of the nucleus, the large the "current," and the larger the effective magnetic field, implying that heavier elements have larger spin-orbit coupling.

Magnetic order only occurs at sufficiently low temperatures. Above a critical temperature, spontaneous magnetic order no longer exists. This critical temperature is call Curie temperature in ferromagnets and the Néel temperature in anti-ferromagnets[2]. Ferromagnets are the most predominantly used in technological applications however, ferrimagnets are used in some high frequency applications. Many ferrimagnets are electrically insulting with very low magnetic damping. Their insulating properties imply that no eddy current are generated in large oscillating fields. Solids ferrite cores are used in a variety of high frequency applications such as aerials and transformers requiring high permeability. It has long been thought that anti-ferromagnets and ferrimagnets are not of great use in memory technology, but what we will find is that their near zero magnetisation and vanishing angular momentum make them prime candidate materials for information and data storage technologies.

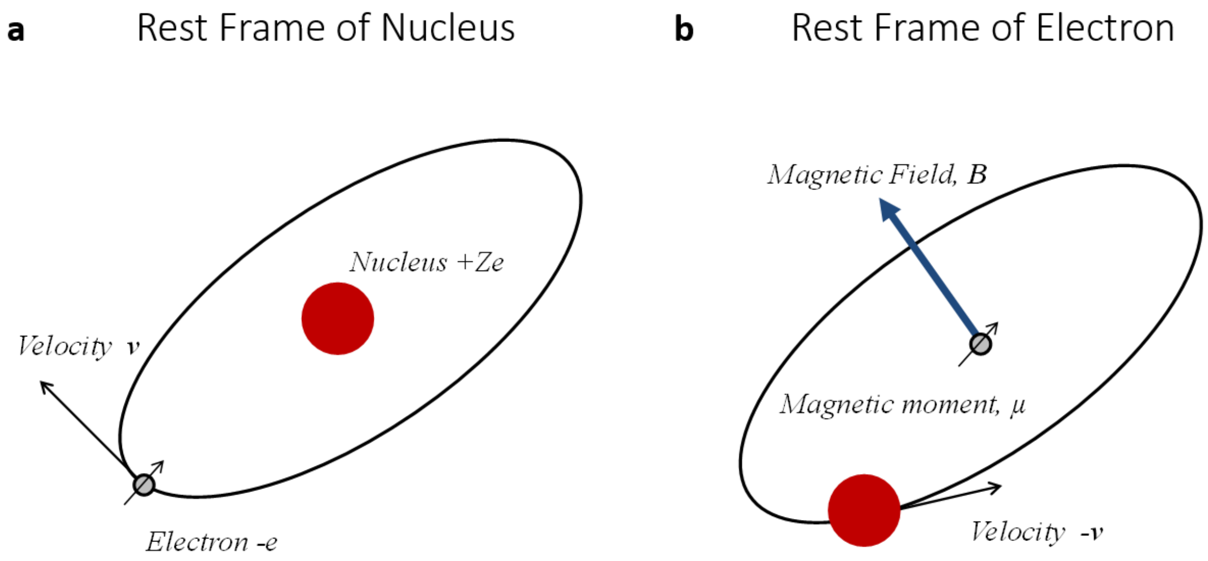

Figure 3.3 | a) Simplified schematic of an atom in the rest frame of the nucleus and b) in the rest frame of the electron. In the rest frame of the electron, the motion of the nucleus looks like a magnetic field acting on the electron's magnetic moment.

Indirect Exchange

Many of the ionic oxides in the previous section have antiferromagnetic ordering that does not occur through direct exchange. In particular, there is no direct overlap of neighboring electron orbitals in garnet oxides and fluorides. Instead, the exchange interaction is mediated through a third, non-magnetic ion in a long-range process called super-exchange. This type of order is the ground state, as there is a kinetic energy advantage for antiferromagnetic order in the material.

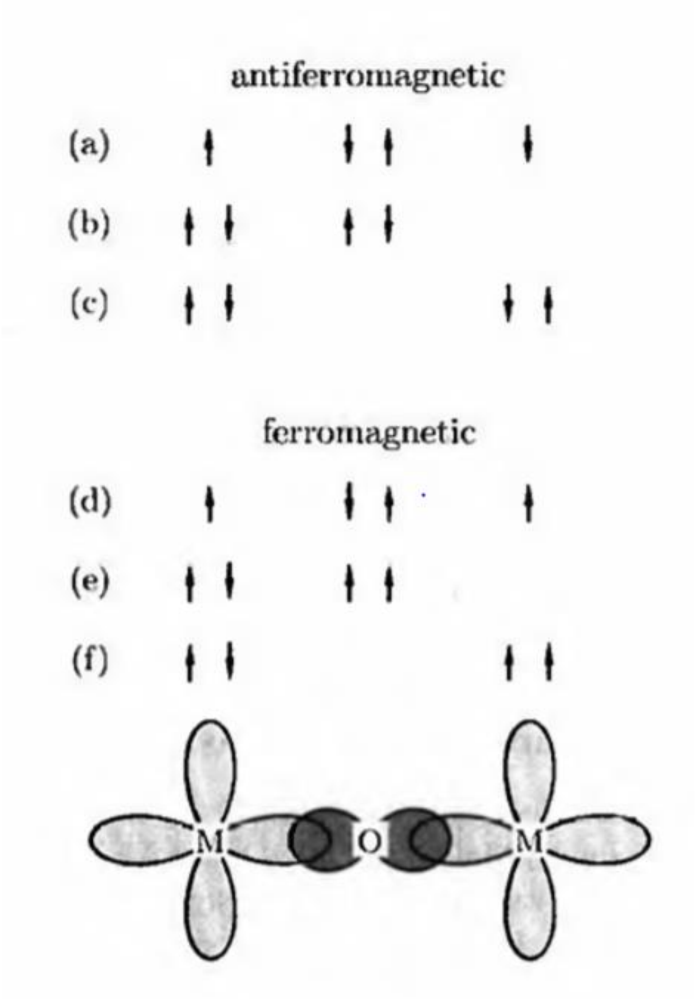

Figure 3.4 | Super exchange in an iron oxide. Antiferromagnetic coupling between the Fe, as in (a), (b), (c), the ground state (a) can mix with excited states (b), (b), delocalizing electrons. Ferromagnetic coupling of the two Fe ions, where (d) is the ground state and (e) and (f) are excited states cost energy, as these are prevents by the Pauli exclusion principle.

This can be understood by the schematic shown in Fig. 3.4, where Fe ion exchange is mediated by an oxygen ion. In this model, each Fe ion has one unpaired election in a d orbital and the oxygen ion has two unpaired electrons in a p orbital. Antiferromagnetic coupling between the Fe ions allows these outermost electrons to become more delocalized, thus lowering the energy of the system.

Magnetism in Metals

Magnetic ordering in metallically bonded materials does not follow same model as ionically bonded magnetic materials or oxides. In metallic materials, magnetism arises from band ferromagnetism, where magnetic order occurs from spontaneous splitting of electron bands. This can be readily described by examining the rigid band model for the density of states of electrons (see Fig. 3.5a), where spin-up and spin-down electrons are plotted independently[2]. In the rigid band model, the density of states of transition metal elements is assumed to remain unchanged across the transition metals and alloys of transition metals, the s and d bands are assumed to remain "rigid' with increasing atomic number. Here, s- (free electron) and d- (localized electron) bands are represented by the local- and free electron-like bands shown in Fig. 3.5a. This model allows us to explain ferromagnetism by simply moving the Fermi energy according to the number of electrons present in the transition metal. Spontaneous magnetism occurs because there is an energetic gain by having an uneven number of spin-up and spin-down electrons; however, this gain must be greater than the kinetic energy cost of moving spins from one sub-band to the other.

From Fig. 3.5a, we can estimate the kinetic energy cost as the energy is takes to move an infinitesimally small amount of minority spin electrons to the majority spin band. This kinetic energy cost is the area of the area of the infinitesimally small sliver multiplied by the Bohr magneton μ_B:

$$\Delta E_{KE} = \mu_B \frac{1}{2} g\left(E_f\right) \delta E \qquad 3.5$$

where $g\left(E_f\right)$ is the density of states and δE is the sliver of electrons. The total magnetic moment M is the imbalance of spin up and spin down elections:

$$\mathrm{M} = \mu_B (n_{up} - n_{down}) \qquad 3.6$$

where n_{up} and n_{down} are the number of up and down electrons. Combining Eq. 3.5 and 3.6, we get the following for the kinetic energy cost in terms of the magnetisation:

$$\Delta \mathrm{E}_{\mathrm{KE}} = \frac{1}{4} \frac{M}{\mu_B} \delta E \qquad 3.7$$

The exchange energy gain from having collinear alignment of spins, moving electrons from one spin subband to the other, is

$$\Delta \mathrm{E}_{\mathrm{Ex}} = U_{ex} n_{up} n_{down} - U_{ex} \left(\frac{n}{2}\right)\left(\frac{n}{2}\right) \qquad 3.8$$

where U_{ex} is the exchange energy and n is the total number of electrons. The first term describes the energy of unequal amounts of spin up and spin down electrons, and the second term describes the energy of equal numbers of spin up and spin down electrons. This can be rewritten in terms of the net magnetisation, Eq. 3.6,

$$\Delta \mathrm{E}_{\mathrm{Ex}} = \frac{-U_{ex}}{4\mu_B^2} M^2 \qquad 3.9$$

The total energy is then just the sum of the energy cost and gain,

$$\Delta \mathrm{E}_{\mathrm{total}} = \Delta \mathrm{E}_{\mathrm{Ex}} + \Delta \mathrm{E}_{\mathrm{KE}} = \frac{\delta E}{4\mu_B} M[1 - U_{ex}\, g(E_F)] \qquad 3.10$$

Eq. 3.10 is known as the Stoner criterion[3] for ferromagnetism in metal. When the total energy is negative, then spontaneous magnetism occurs. If U_{ex} is zero, then there is no net magnetisation. Eq. 3.10 also tells us that the larger the density of state at the fermi level, the larger the energy gain there is for having an imbalance of spins. Looking at the band structure in Fig. 3.5, this is most noticeable if the fermi energy lies in the local d-band of the metal. Using the rigid band model, we can fill electrons from lowest energy states to highest energy states, as we move down the transitions metals and the ones with the Fermi level in the d-band have a higher likelihood of ferrimagnetism. Figure 3.5b shows the Slater-Pauling curve[4–6], which illustrates the magnetic moment per atom of various magnetic allows. The peak in the curve occurs for transition metals with large density of states at the Fermi level (Co,Ni,Fe).

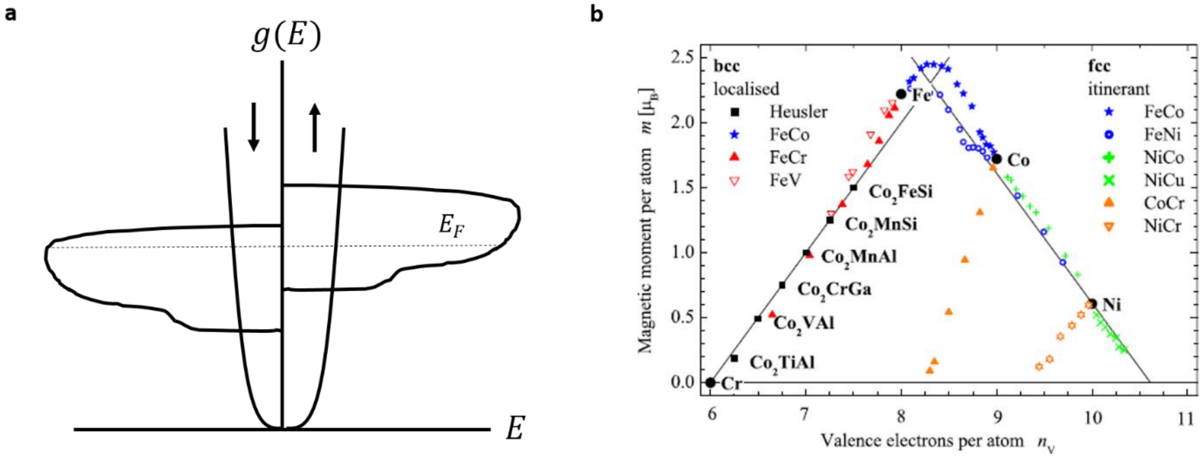

Figure 3.5 | a) Density of states for minority and majority spin bands. Band splitting occurs when there is a greater energetic gain from parallel alignment of spins. b) Slater-Pauling curve showing a larger magnetic moment for transition metals with large density of states at the Fermi level.

3.2 Magnetic Anisotropy

In the previous section, we discussed how magnetic order arises in a material; however, we have not said anything about the preferred direction the co-linear spins prefer to align. Magnetic anisotropy is the preference of the magnetic moment of a material to lie along a certain direction(s). As we will find out shortly, magnetic anisotropy is one of the most powerful properties of a magnetic material. It affects the stability of magnetic bits in memory application, the size of spin textures, how magnetic domain walls and skyrmions move, the shape of hysteresis loops, and much more. It is one of the most engineered parameters in magnetism. Large or small anisotropy and the types of anisotropy needed depend on the application. Here, we will consider where anisotropy arises in thin film magnetic systems, which can be dramatically different from bulk systems.

In thin film systems, magnetic anisotropy can come from a variety of sources. Perhaps, the easiest to understand in shape anisotropy, which, as its name eludes, comes from the shape of a magnetic material. Different amounts of free magnetic poles can form at the surfaces of materials, resulting in stray field or demagnetizing field it produces, as this raises the total energy of the system. Stray fields are a "long-range' magnetic interaction, so the magnetic material can essentially "sense" the edges of the material. A magnetic material will, in general, tend to minimize the stray field it produces. In other words, it follows Maxwell's equations and tries to minimize the divergence of the magnetisation $(\nabla \cdot \mathbf{M})$. This will cause the magnetisation to point along the long axis of a material, minimizing free poles. Magnetostatic energy is the term used to describe the energy resulting from stray fields or the shape of a material, and take the form:

$$\mathrm{E_d} = -\frac{1}{2} M \cdot H_d \tag{3.11}$$

where H_d is the demagnetizing field and is related to the magnetisation of the film, M, $H_d = -NM$, where N is a demagnetizing tensor that depends on the shape of the material. Calculating N is not trivial. In the case of a thin film, the film extends infinitely in two dimensions and is tightly constrained in the third dimension. The resulting demagnetizing energy for a thin film is:

$$E_d = -\frac{1}{8\pi V}\int MH_d dv = 2\pi M_s^2 \cos^2\theta \qquad 3.12$$

where V is the volume of the film, dv is a volume element, and θ is the angle between the magnetisation and the film normal. Eq. 3.11 agrees with intuition, and energy is minimized when the magnetisation of the film lies in the plane of the film. We will call this in-plane magnetization or IP for short.

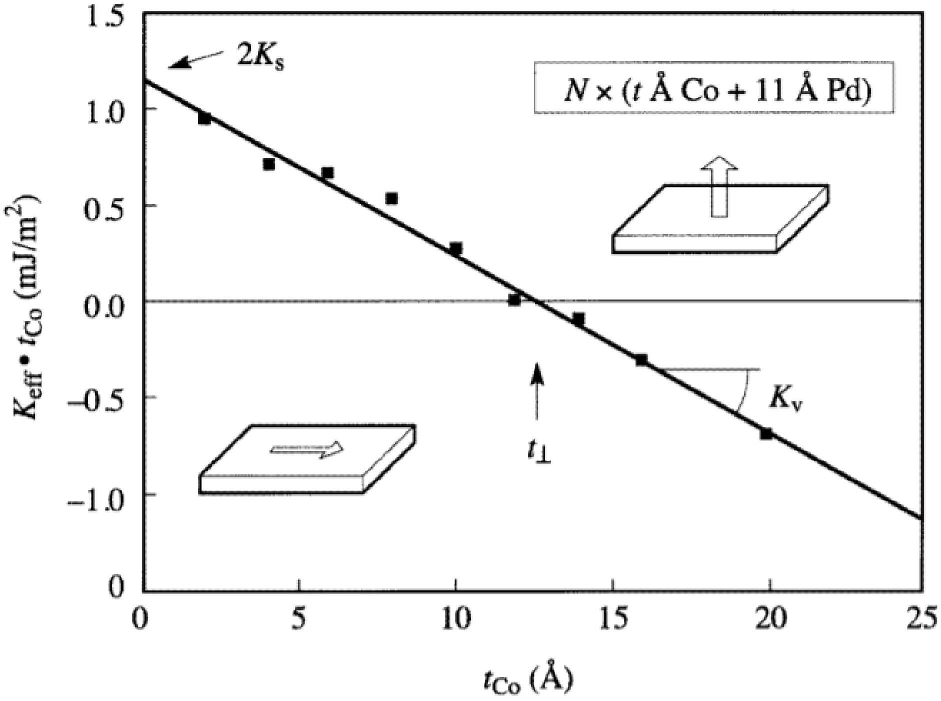

Figure 3.6 | Total anisotropy k_{eff} as a function of Co layer thickness. The fit to the data (line) is a linear fit described in Eq. 3.13, where the slope of the line describes the volume contribution to anisotropy k_v and the y-axis intercept describes the surface contribution k_s. Image taken from ref[7]

Dipolar or shape anisotropy is not the only factor that dictates a material's anisotropy in a thin film. Ultra-thin films have many properties that are dictated by the breaking of symmetry caused by interfaces[8]. Shape anisotropy tells us that a thin film would prefer to have its magnetisation lie in the plane of the film. However, in 1954 Néel predicted the existence of surface anisotropies that could change the preferred axis of orientation (or easy axis) of a film[9]. This was later confirmed in experiments, and notable it was discovered later that Pt/Co[10] and Pd/Co[10,11] magnetic multilayer thin films grow in a particular orientation (111) caused the easy axis of the material to be perpendicular to the plane of the film, so called perpendicular magnetic anisotropy (PMA). This can be seen in Fig. 3.6[7], which plot the total anisotropy of a film k_{eff} as a function of Co thickness d in Pd/Co multilayers. In this plot, when k_{eff} is positive the film has PMA and when it is negative it has in-plane magnetisation. Using Fig. 3.6, we can separate out the volume anisotropy effects from the surface (PMA) effects by fitting the line to the following expression[10,11]:

$$k_{eff} = k_v + \frac{k_s}{d} \tag{3.13}$$

where k_v is the volume anisotropy and k_s is the surface anisotropy. Below a certain thickness of Co (d_{srt}), the magnetisation will reorient itself to an out-of-plane orientation. This is the so-called spin-reorientation transition. Dipolar and strain are the main contributions to the volume anisotropy term, while spin-orbit coupling is mainly responsible for the surface term in Eq. 3.13. Since spin-orbit coupling describes the coupling between electron orbitals and their spin orientation, it is only natural that bonding or the crystal structure of a film plays a large role in its magnetic anisotropy.

Magnetic anisotropy is a vital parameter in the design of data storage. Anisotropy is the key metric which sets the standard for memory lifetimes. The energy barrier of magnetisation reversal is $E_{rev} = k_{eff}V$ where V is the volume of the magnetic bit. A large k_{eff} is necessary to keep the barrier large such that a bit remains stable for along time in the presence of thermal fluctuations. The industry standard for a 10-year lifetime is $E_{rev} > 60k_bT$, where k_b is the Boltzmann constant and T is temperature. As bits become increasingly smaller, more anisotropy is need to keep this figure above $60k_bT$; however, the energy barrier should be low enough to be able to switch the magnetisation with low energy when needed. The competition between the three industry requirements (small bits, low write energy, and stability) is often referred to as the magnetic recording trilemma.

As we will see in later chapters, perpendicular magnetic anisotropy can also be present in thicker ferrimagnetic allows, such as GdCo, TbCo, FeCo[12], and alloys of these materials. This is so-called "bulk perpendicular magnetic anisotropy," as it does not come from the interface, as in Pd/Co and Pt/Co thin films. The origin of bulk PMA in thin films is not clear. However, in these materials, one can increase their thickness (increase their volume), increasing E_{rev}, without having to increase k_{eff}, potentially solving one piece of the magnetic recording trilemma.

3.3 Magnetic Hysteresis Loops

Magnetic hysteresis loops are arguably the most powerful way to characterize a magnetic sample. A wealth of information can be gathered from hysteresis loops, including a number of magnetic and material properties. In a hysteresis loop, the magnetic field is swept in one direction, while the magnetisation of the film in that same direction is measured. A variety of techniques outlines in Chapter 5 can be used to measure the magnetisation of the sample during the field sweep. The amount of energy it takes to orient a magnetic moment in a particular direction is a strong function of the anisotropy of the film. We will see that the type of magnetic anisotropy will have an impact on the shape of the hysteresis loop. By this, we can also determine the strength of the anisotropy of magnetic material. For this thesis, we will only consider the case where there is one single easy axis of preferred magnetisation. This is called uniaxial anisotropy and can be used to describe all magnetic materials in this thesis.

We will use the Stoner Wohlfarth model to describe the magnetisation of a single domain as a function of field. This will allow us to correctly determine the qualitative shapes of hysteresis loops. In the Stoner Wohlfarth, the total energy of the system is described by the sum of the energy due to the applied magnetic field (Zeeman energy) and the anisotropy energy. The energy landscape of uniaxial anisotropy can be described by[2]

$$E_{uni} = Ksin^2(\theta) \tag{3.14}$$

where K is the uniaxial anisotropy constant, and θ is the deviation of the magnetisation from the easy axis. The Zeeman energy from a field acting on a magnetic moment is equal to[2]

$$E_{Zeeman} = -M_s Hcos(\theta') \tag{3.15}$$

where θ' is the angle between the magnetisation and the applied field. The total energy is equal to the sum of Eq. 3.14 and 3.15. The anisotropy energy landscape is plotted as a function of the angle θ in Fig. 3.7a. Here, we clearly see the degenerate easy axis along 0 and π radians, and a hard axis along $\frac{\pi}{2}$. Let's take a scenario where the magnetisation is current pointed along the $\theta = \pi$ direction. When a magnetic field is applied along the easy axis, say $\theta = 0$ radians, the energy landscape shifts, as the Zeeman energy begins to contribute, lowering the energy of the $\theta = 0$ states and raising the energy of the $\theta = \pi$ state. However, the horizontal position of the minimum does not change. As the field increases, the local minimum continue to shift vertically, but not horizontally on the plot, as indicated by the colored lines in Fig. 3.7a for various applied fields. When the $\theta = \pi$ state is within $k_b T$ of the maximum, then the magnetisation switches directly from $\theta = \pi$ to $\theta = 0$, the new preferred energy state. If we instead plot the magnetisation along the magnetic field direction M_x as a function of the field, this yields a square easy axis magnetic hysteresis loop (Fig. 3.7c[2]).

The story changes considerably if we now consider the case where we apply a magnetic field along the hard axis $\theta = \frac{\pi}{2}$. Here, the $\theta = \frac{\pi}{2}$ state lowers in energy, while the $\theta = 0, \pi$ states rise in energy (vertical shift), but there is also a horizontal shift of these minimum, which continues as we increase the hard axis applied field. This is show in Fi. 3.7b for various hard axis fields. Finally, when the magnetic field is strong enough the magnetisation is forces along its hard axis, $\theta = \frac{\pi}{2}$. If instead, we plot the magnetisation along the hard axis ($\theta = \frac{\pi}{2}$), we see a linear dependence of the magnetisation on field, until the moment is saturated along the hard axis (Fig 3.7d[2]).

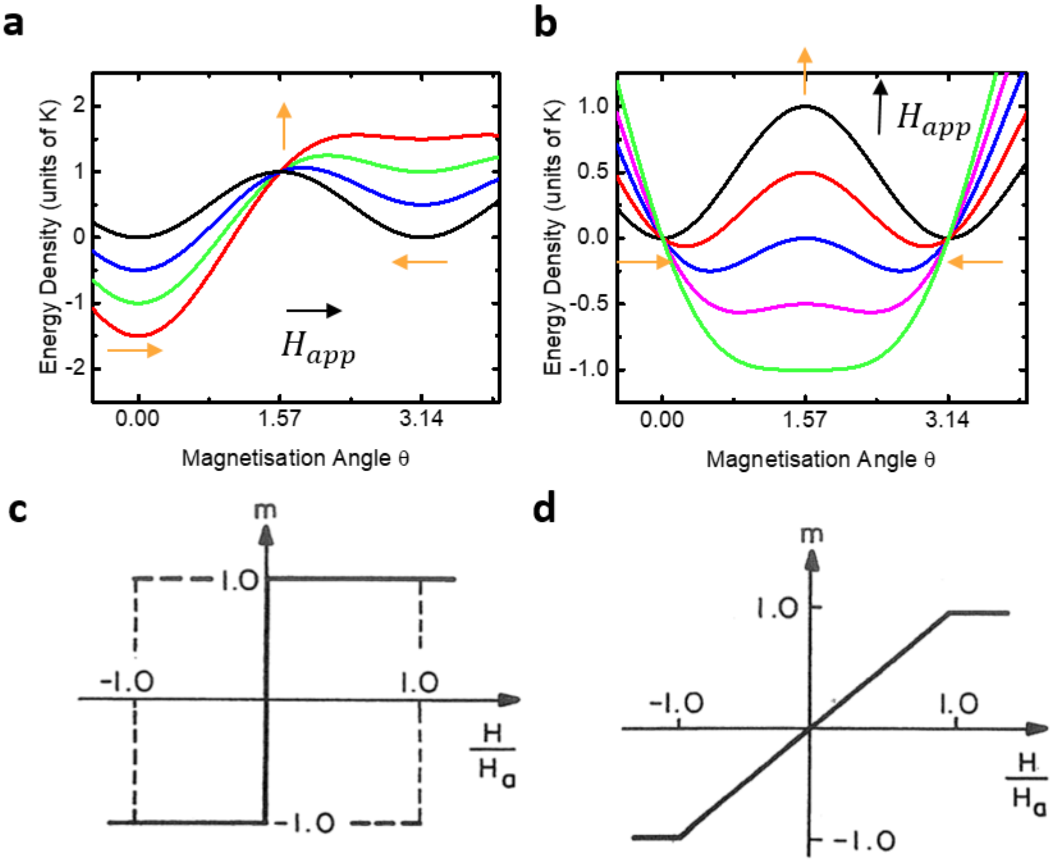

Figure 3.7 | Energetics a) easy axis and b) hard axis loops as a function of θ, the angle between the magnetisation and the easy axis. Resulting c) easy and d) hard axis hysteresis loops. c,d) adapted from ref[2].

From Fig 3.7c,d, we can define many magnetic material properties: the saturation magnetisation M_s, the remnant magnetisation M_r, the coercivity H_c, and the anisotropy field H_k. The coercive field H_c is given by the $M = 0$ crossing of the easy axis loop, ie- the field at which the magnetisation switches. The remnant magnetisation M_r is the $H = 0$ intercept of the loop, ie- the magnetisation that remains when the field is turned off. A common measure of the sqaureness of a hysteresis loop is M_r/M_s. An easy axis loop has an $\frac{M_r}{M_s}$ of 1, while for a hard axis loop, it is 0. Any loop in-between these two angles gives a value of $0 < \frac{M_r}{M_s} < 1$. For magnetic memory application, uniaxial anisotropy is useful. There are two distinct magnetisation levels depending on the prior magnetisation state of the sample. This is a binary system, and the up or down state can reflect a 1 or 0 bit of information.

Fig. 3.8 brings together both the concepts of interface anisotropy and magnetic hysteresis loops. Various out of plane magnetic hysteresis loops are plotted for a thin film system of Ta(4 nm)/Pt(3 nm)/Co(t_{Co})/Oxide(8 nm). We have varied the Co layer thickness t_{Co} between approximately 0.5 and 1.3 nm. The Ta layer serves as an adhesion layer between the Si/SiO$_2$ substrate and the Pt. The purpose of the oxide cap is to protect the Co layer from oxidation in the atmosphere. The hysteresis loops are obtained using a technique called the magneto-optical Kerr effect, which will be describe in detail in Chapter 5. The y-axis units represent the fraction of magnetisation out of the plane of the sample. As one can see, at $t_{Co} = 0.85\ nm$ the hysteresis loops is square, indicating the easy axis of the film is out of the plane (PMA). Here, surface anisotropy dominates. At very large $t_{co} = 1.33\ nm$, the sample hysteresis loop appear to resemble a hard axis loop that is not saturated, meaning that the hard axis is out of the plane and the easy axis is in the plane. Here, volume anisotropy dominates. Between these two thicknesses, $t_{Co} = 1.21\ nm$, the loops take a mixed shape, indicating that both surface and volume anisotropy contribute to the total anisotropy. At very thin $t_{Co} = 0.53\ nm$, the coercivity H_c drops slightly. This is an indication that the out of plane anisotropy has dropped slightly. This effects can be attributed to a lack of magnetic material. $0.5\ nm$ of Co is extremely thin, and there simply isn't enough magnetic material to retain full anisotropy.

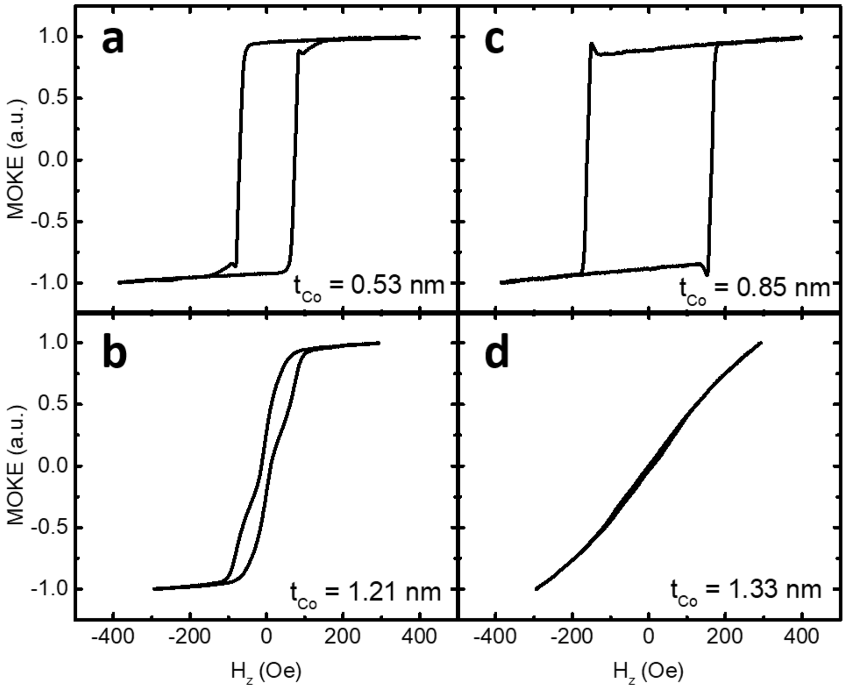

Figure 3.8 | MOKE magnetic hysteresis loops taken on Ta(4 nm)/Pt(3 nm)/Co (t_{Co})/Oxide(8 nm), where t_{Co}= a)$0.53\ nm$, b) $0.85nm$, c) $1.21\ nm$ and d) $1.21\ nm$.

In the Stoner Wohlfarth model $H_c = H_k$, but in reality this is almost never the case. H_c is almost always significantly smaller than H_k. The Stoner Wohlfarth model assume the all the spins in the magnetic material can be modeled by a single vector. This is called the single domain assumption. In reality, switching does not occur by coherent rotation of all moments in a ferromagnet. Instead, magnetic domains nucleated and expand across the sample until it has switched. Domain walls are the finite transition regions between oppositely oriented domains, and will be the focus of the next section 3.4.

3.4 Magnetic Domain Walls

So far, we assumed that all moments of a ferromagnetic material are aligned along the same direction; however this is not always the case. In fact, single domained magnets are quite rare. In the last section, we discussed how a magnetic material aligns along its long axis to minimize the divergence of $(\nabla \cdot \mathbf{M})$. A magnetic material can minimize its stray field (minimize its magnetostatic energy) even further by breaking up into differently oriented regions called magnetic domains (see Fig. 3.9a,b), such that the material is demagnetized, where the net magnetisation of a demagnetized material is zero[13]. There are finite regions between magnetic domains where the magnetisation smoothly rotates from one direction to another. These thin regions are called magnetic domain walls. There are two main types of magnetic domain walls in

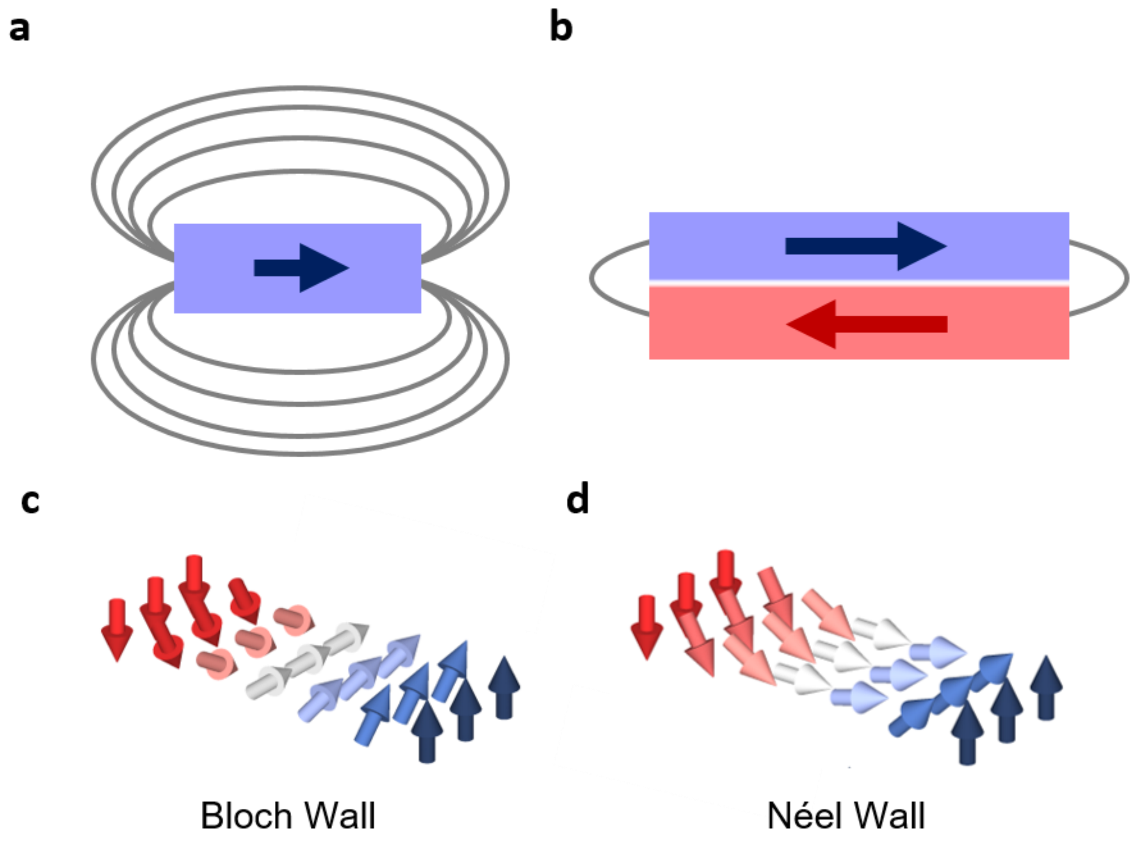

Figure 3.9 | a) uniformly magnetised and b) multidomain magnets. Breaking up into domains reduces magneto static energy. c) Bloch and d) Néel domain wall configurations.

thin films materials. In other words, there are two preferred ways that the magnetisation prefers to rotate from one domain to the next: Bloch domain walls and Néel domain walls. In a Bloch domain wall, the magnetic moment rotates perpendicular to the domain wall normal vector. In a Néel domain wall, it rotates parallel to the domain wall normal. These are schematically shown in Fig. 3.9c,d.

The formation of magnetic domain walls actually costs energy, as magnetic moments in the domain wall no longer lie along the easy axis of the material. The energy cost of forming a Bloch magnetic domain wall σ_B is a function of the anisotropy energy of the film K and the exchange constant A[3].

$$\sigma_{DW} = \pi\sqrt{AK} \qquad 3.15$$

Although domain walls cost energy, they spontaneously form in magnetic materials as they greatly reduces the demagnetizing field in the ferromagnet (see Fig. 3.9a,b). Domain walls also have a finite width Δ, which is also dependent on A and K[3].

$$\Delta = \sqrt{A/K} \qquad 3.16$$

In expression 3.16, the anisotropy competes with the exchange stiffness. The exchange stiffness prefers a wide, infinitely large, domain walls, as this keeps more moments in the domain wall to be closer to parallel aligned. The anisotropy prefers an infinitesimally small domain wall, as this keeps more moments along the easy axis of the film.

Néel walls are more common in materials whose domain wall width is larger than the thickness of the film and the lithographically patterned magnetic track. Bloch walls are more common in films where the domain wall width is larger than the thickness of the film, but smaller than the width of the magnetic track. This can be seen schematically in Fig. 3.10. The domain wall itself, represented by a white rectangle in Fig. 3.10, can be thought of as magnet itself. The Bloch wall in Fig. 3.10a would produce less demagnetizing field than the Néel domain wall in Fig. 3.10b, as the magnetisation of the Bloch wall lies along the long axis of the domain wall “rectangle” in the very wide track in Fig. 3.10a,b. The narrow track in Fig. 3.10c,d would favor a Néel domain wall, as the long axis of the domain wall “rectangle” lies along the domain wall normal. In a typical PMA, the width of a domain wall is typically tens of nanometers and the width of the magnetic trackis almost always several hundred nanometers or more. This geometry is best described by Fig. 3.10a. As a result, Bloch walls are more often observed in magnetic thin films with PMA[14].

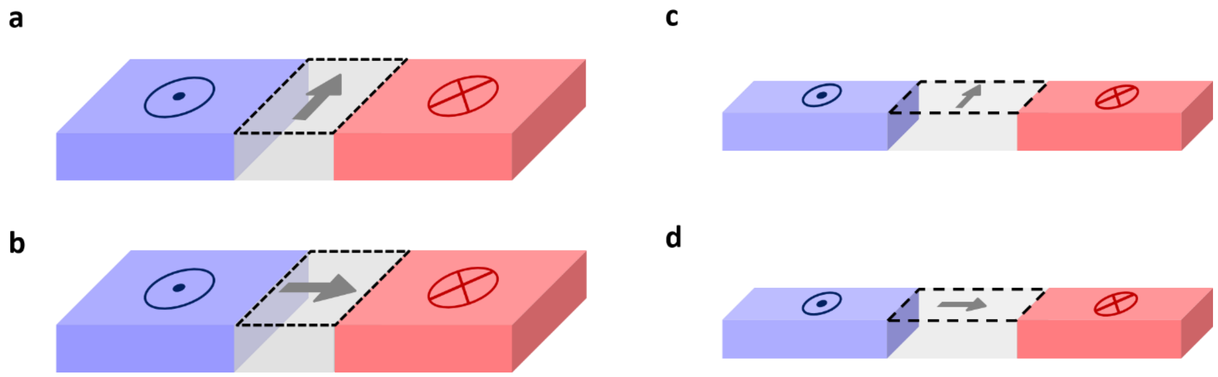

Figure 3.10 | a) Bloch and b) Néel domain walls in thin film patterned into a wide track. Bloch walls are energetically e preferred here. c) Bloch and d) Néel walls patterned in a thin film patterned into a narrow track. Here, Néel walls are energetically preferred.

The domain walls in a multidomain sample are mobile, ie- a multidomain sample can be made uniformly magnetized by driving domain walls into motion. This can be done by applying a magnetic field to the sample. When a magnetic field is applied to the sample, the domain oriented in the same direction of the applied field will grow, while the domains not oriented in the direction of the field will shrink (Fig. 3.11). The tendency of a magnet to orient in the direction of the applied field is called the Zeeman Effect, where the Zeeman energy is reduced when the magnetic moment is aligned with the field. The dynamics of the motion of the domain wall under an applied field will be discussed in the next chapter.

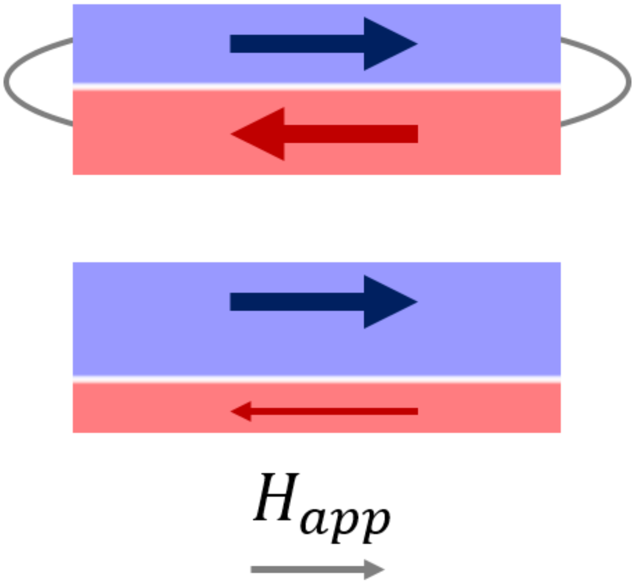

Figure 3.11 | Magnetic domain walls in a multidomain sample. When a magnetic field is applied, the domain oriented in the direction of the applied field will grow, while the domain oriented in the opposite direction will shrink.

The difference between a multidomain material and a multidomain material is also the reason why some materials are permanent magnets and other are not. For example, a nail would stick to your refrigerator, but nails don’t typically stick to each other. This is because the magnet in the refrigerator is a single domain magnet with large stray fields, while the nail is a multidomain material. If you bring a nail close to your refrigerator, the magnetic field produced by the single domain magnet in your refrigerator will cause the domain walls in the nail to move until the nail itself becomes single domain. Once the nail is single domain, the stray field produced by the nail and the refrigerator will cause them to attract to one another. Once the nail is pulled away from the refrigerator the domain walls will spontaneously reform. If you brought two nails together they would not be attracted to each other, since they are multidomain and have very small stray fields.

In some materials, domain walls can become pinned or "stuck" after the field is removed. This occurs when there is a local energy well for the domain wall to be pinned on. This can be a change in anisotropy K, magnetisation M_s, or even exchange stiffness A. Practically, this is a grain boundary, surface roughness, voids, or even a scratch of the surface of the material.

Note that when a domain wall or other spin textures such as skyrmions (to be discussed later) "move" in a material, no physical motion actually occurs. Magnetic domain walls are quasi-particles, meaning they aren't physical objects, but can be conveniently regarded as objects. Quasi-particles have properties that are characteristic of objects, like momentum, size, energy, and shape. They also can interact with one another like particles do. For instance, the carbon dioxide bubbles in sparkling water themselves are not particles, as they are just the displacement of water by CO_2. But the bubble itself (the absence of water) has properties similar to a particle. Bubbles can interact with each other, they float, etc. Another analogy, more similar to domain walls or skyrmions are the pixels on your cellphone screen. When watching a video of a moving car on your screen, the car itself isn't moving, but the pixels on the screen are changing colors giving the appearance of a moving car. This is similar to local electron spins in a material. The spins themselves aren't moving, however their rotation gives rise magnetic objects that can be treated as particles. For example, domain walls can be pinned and they interact with each other.

3.5 Dzyaloshinskii – Moriya Interaction and chiral spin textures

The Heisenberg exchange interaction introduced in this chapter energetically prefers collinear alignment of magnetic spins. This is explicitly written in terms of the Hamiltonian in Eq.

3.1. In some materials, a different type of exchange interaction, the asymmetric exchange interaction, is present. The asymmetric exchange interaction is also commonly referred to as the Dzyaloshinskii-Moriya interaction (DMI), named after the two physicists who predicted its existence. The DMI has a Hamiltonian of the form[15,16]:

$$\widehat{H_{DMI}} = -\sum_{ij} D_{ij}\boldsymbol{S_i} \times \boldsymbol{S_j} \tag{3.17}$$

where D_{ij} is the DMI tensor, and Si, j are adjacent magnetic spins in a material. The DMI manifests itself in materials whose structure lack inversion symmetry. The cross product prefers perpendicular alignment of these adjacent spins rather than collinear alignment. When both the Heisenberg exchange interaction and the DMI are significant in a material, magnetic twists and spiral can form. D_{ij} is also a chiral tensor, meaning it is not symmetric. Thus, spin textures that form have preferred handedness or chirality. We will find that this greatly impacts both the statics and dynamics of spin textures. There are two main ingredients to manifest DMI in a material: large spin-orbit coupling and broken inversion symmetry[15,16]. The DMI is actually an indirect exchange interaction that is mediated through an element of large spin-orbit coupling. The DMI was first

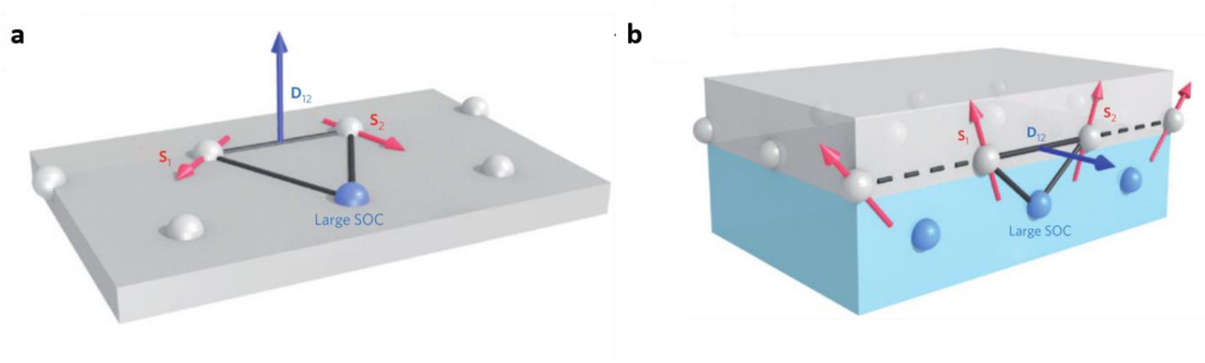

Figure 3.12 | a) Bulk and b) interfacial DMI manifesting in bulks and thin film systems, respectively. The DMI is mediated through an element of large spin-orbit coupling. Adapted from ref[17]

experimentally observed in bulk materials whose crystal structure lacks inversion symmetry, such as the B20 system. Fig. 3.12a[17] schematically illustrates the indirect DMI resulting in bulk materials, commonly referred to as "bulk DMI."

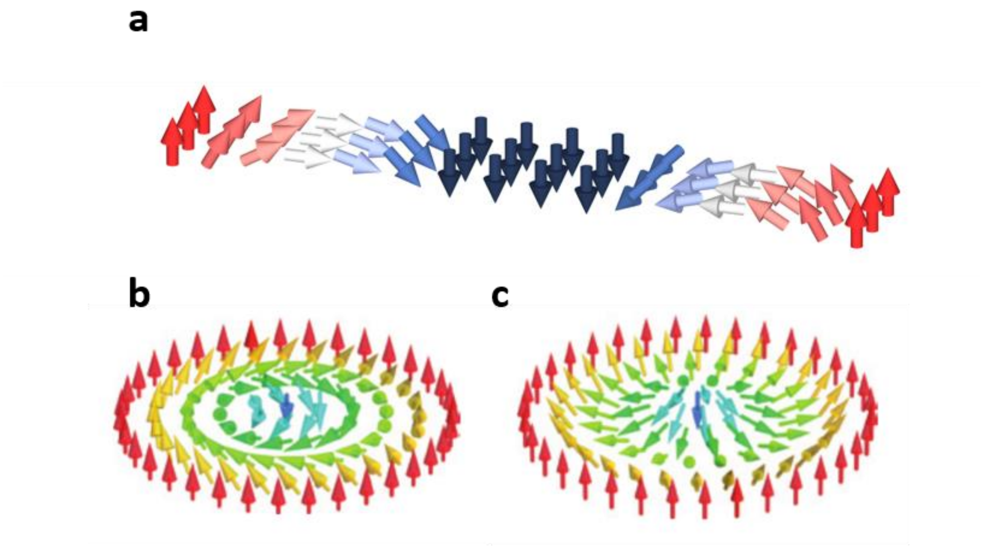

Figure 3.13 | a) A pair of right handed homochiral Néel domain walls. b) Bloch and c) Néel skyrmions. c,d) adapted from ref[17]sk

Chiral magnetic structures resulting from bulk DMI have been observed in MnW[18], FeMn[19], MnSi[20,21], FeGe[22], $Fe_{1-x}Co_xSi$[23], and $La_2Cu_{0.97}Li_{0.03}O_4$[24] systems. Until recently, chiral spin textures stabilized by the DMI had only been observed in single crystal B20 systems under cryogenic temperatures. However, it was discovered that interfaces between materials can also provide the necessary inversion asymmetry needed to manifest the DMI. Moreover, the same heavy metals that give rise to PMA in thin films systems also provide the large spin-orbit coupling for the DMI. Emori *et al*[25] and Ryu *et al*[26] separately discovered homochiral Néel domain walls at room temperature in Pt/Co(Fe)/Oxide films. This type of DMI is often called interfacial DMI, and is schematically described in Fig. 3.12b[17], where the asymmetric exchange between adjacent spins in mediated via the heavy metal in the adjacent underlayer. A pair homochiral Néel walls are shown in Fig. 3.13a. Notice that the magnetisation in the domain wall always rotates clockwise moving from wither an up to down domain or a down to up domain.

The discovery of interfacial DMI manifesting in room-temperature systems has sparked a remarkable amount of research in chiral magnetic systems and the different spin textures that evolve in these chiral systems. The most frequently studied are magnetic skyrmions. A skyrmion is a topologically wound circular spin textures that is defined by its winding number, which is the total number of times the spin textures' moments can be mapped onto a sphere. Two different types of skyrmions form from the DMI, a Bloch skyrmion and a Néel skyrmion. A Bloch skyrmion manifests from the symmetry of bulk DMI and a Néel skyrmion manifests from the symmetry of interfacial DMI. Néel and Bloch skyrmions are shown schematically in Fig. 3.13b,c[17], respectively. Similar to domain walls, a Bloch skyrmion's wall rotates perpendicular to the domain wall normal and a Néel skyrmion's wall rotates parallel to the wall normal. Another way to visualize skyrmions is simply domain walls wrapped around themselves. These topological "domains" are two-dimensional objects that can be stable down to a few nanometers in size[17]skyss. Moreover, from their topology, skyrmions exhibit a variety of topological and gyrotropic effects, such as the skyrmion Hall angle[27,28] and the topological Hall angle[29]. Since we only consider interfacial DMI in this thesis, a skyrmion will be assumed to be of Néel type, unless otherwise specified.

Bloch skyrmions have been extensively studied in B20 systems at cryogenic temperatures (Fig. 3.14a) using bulk imaging techniques, such as Lorentz TEM. And recently, room temperature Néel skyrmions have been observed in thin film systems exhibiting interfacial DMI (Fig. 3.14b)[30–32]. Like magnetic domain walls, skyrmions have been conceptualized as magnetic bits for information storage. Over the past few years, research efforts have focused on the nucleation, annihilation, and detection of skyrmions and chiral domain walls in thin films. Moreover, ultrafast motion of chiral spin textures has attracted a lot of attention and will be the primary focus of this thesis.

3.6 A brief appendix on magnetic units

Of all the branches of physics and materials science, magnetism has arguably the most confusing system(s) of units. Units are often equated when they should not be, and there is general misconception with the best way to represent these units. SI units are often advantageous because they are popular and adopted by the majority of scientists in the field; however, the Gaussian unit system has the advantage that it simplifies theoretical relations between electromagnetic phenomenon and SI units are often used incorrectly. Throughout this thesis, both SI and Gaussian units will he used. To aid the reader in relating these two, below is a table that summarizes the definitions of and relationships between the various magnetic units. The table below has been adapted from ref[33]

Quantity	**Symbol**	**Gaussian & cgs emu** [a]	**Conversion factor, C** [b]	**SI & rationalized mks** [c]
Magnetic flux density, magnetic induction	*B*	gauss (G) [d]	4-Oct	tesla (T), Wb/m^2
Magnetic flux	Φ	maxwell (Mx), Gϵcm^2	8-Oct	weber (Wb), volt second (Vs)
Magnetic potential difference,magnetomotive force	*U*, *F*	gilbert (Gb)	10/4π	ampere (A)
Magnetic field strength, magnetizing force	*H*	oersted (Oe),[e] Gb/cm	$10^3/4\pi$	A/m [f]
(Volume) magnetization [g]	*M*	emu/cm^3 [h]	103	A/m

(Volume) magnetization	$4\pi M$	G	$10^3/4\pi$	A/m
Magnetic polarization, intensity of magnetization	J, I	emu/cm^3	4π x 10^{-4}	T, Wb/m^2 [i]
(Mass) magnetization	σ, M	emu/g	1 4π x 10^{-7}	Am^2/kg Wbm/kg
Magnetic moment	m	emu, erg/G	3-Oct	Am^2, joule per tesla (J/T)
Magnetic dipole moment	j	emu, erg/G	4π x 10^{-10}	Wbm [i]
(Volume) susceptibility	χ, κ	dimensionless, emu/cm^3	4π $(4\pi)^2$ x 10^{-7}	dimensionless henry per meter (H/m), Wb/(Am)
(Mass) susceptibility	χ_ρ, κ_ρ	cm^3/g, emu/g	4π x 10^{-3} $(4\pi)^2$ x 10^{-10}	m^3/kg Hm^2/kg
(Molar) susceptibility	$\chi_{\mathrm{m}}, \kappa_{\mathrm{mol}}$	cm^3/mol, emu/mol	4π x 10^{-6} $(4\pi)^2$ x 10^{-13}	m^3/mol Hm^2/mol
Permeability	μ	dimensionless	4π x 10^{-7}	H/m, Wb/(Am)
Relative permeability [j]	μ_r	not defined	-	dimensionless
(Volume) energy density, energy product [k]	W	erg/cm^3	1-Oct	J/m^3
Demagnetization factor	D, N	dimensionless	$1/4\pi$	dimensionless

a. Gaussian units and cgs emu are the same for magnetic properties. The defining relation is $B = H + 4\pi M$.

b. Multiply a number in Gaussian units by C to convert it to SI (e.g., 1 G x 10^{-4} T/G = 10^{-4} T).

c. SI (*Système International d'Unitès*) has been adopted by the National Bureau of Standards.Where to conversion factors are given, the upper one is recognized under, or consistent with, SI and is based on the definition $B = \mu_o(H + M)$, where $\mu_o = 4\pi \times 10^{-7}$ H/m. The lower one is not recognized under SI and is based on the definition $B = \mu_o H + J$, where the symbol I is often used in place of J.

d. 1 gauss = 10^5 gamma (γ).

e. Both oersted and gauss are expressed as $\mathrm{cm}^{-1/2}\mathrm{g}^{1/2}\mathrm{s}^{-1}$ in terms of base units.

f. A/m was often expressed as "ampere-turn per meter" when used for magnetic field strength.

g. Magnetic moment per unit volume.

h. The designation "emu" is not a unit.

i. Recognized under SI, even though based on the defition $B = \mu_o H + J$. See footnote *c*.

j. $\mu_r = \mu/\mu_o = 1 + \chi$, all in SI. μ_r is equal to Gaussian μ.

k. BH and $\mu_o MH$ have SI units J/m^3; MH and $BH/4\pi$ have Gaussian units erg/cm^3.

3.7 References

1. Sony Storage Media Solutions Corporation. Sony Global - Sony Develops Magnetic Tape Storage Technology with the Industry's Highest*1 Recording Areal Density of 201 Gb/in2. (2017). Available at: https://www.sony.net/SonyInfo/News/Press/201708/17-070E/index.html. (Accessed: 6th March 2019)
2. O'Handley, R. C. *Modern magnetic materials : principles and applications*. (Wiley, 2000).
3. Blundell, S. *Magnetism in condensed matter*. (Oxford University Press, 2001).
4. Balke, B., Wurmehl, S., Fecher, G. H., Felser, C. & Kübler, J. Rational design of new materials for spintronics: Co_2FeZ (Z =Al, Ga, Si, Ge). *Sci. Technol. Adv. Mater.* **9,** 014102 (2008).
5. Slater, J. C. The Ferromagnetism of Nickel. II. Temperature Effects. *Phys. Rev.* **49,** 931–937 (1936).
6. Pauling, L. The Nature of the Interatomic Forces in Metals. *Phys. Rev.* **54,** 899–904 (1938).
7. Cullity, B. D. & Graham, C. D. *Introduction to Magnetic Materials*. (John Wiley & Sons, Inc., 2008). doi:10.1002/9780470386323
8. Johnson, M. T., Bloemen, P. J. H., Broeder, F. J. A. den & Vries, J. J. de. Magnetic anisotropy in metallic multilayers. *Reports Prog. Phys.* **59,** 1409–1458 (1996).
9. Néel, L. Anisotropie magnétique superficielle et surstructures d'orientation. *J. Phys. le Radium* **15,** 225–239 (1954).
10. Carcia, P. F. Perpendicular magnetic anisotropy in Pd/Co and Pt/Co thin-film layered structures. *J. Appl. Phys.* **63,** 5066–5073 (1988).
11. Carcia, P. F., Meinhaldt, A. D. & Suna, A. Perpendicular magnetic anisotropy in Pd/Co thin film layered structures. *Appl. Phys. Lett.* **47,** 178–180 (1985).
12. Hansen, P. & Heitmann, H. Media for erasable magnetooptic recording. *IEEE Trans. Magn.* **25,** 4390–4404 (1989).
13. Heinrich, B. & Cochran, J. F. Ultrathin metallic magnetic films: magnetic anisotropies and exchange interactions. *Adv. Phys.* **42,** 523–639 (1993).
14. Koyama, T. *et al.* Observation of the intrinsic pinning of a magnetic domain wall in a ferromagnetic nanowire. *Nat. Mater.* **10,** 194–197 (2011).
15. Dzyaloshinsky, I. & I. A thermodynamic theory of "weak" ferromagnetism of antiferromagnetics. *J. Phys. Chem. Solids* **4,** 241–255 (1958).
16. Moriya, T. Anisotropic Superexchange Interaction and Weak Ferromagnetism. *Phys. Rev.* **120,** 91–98 (1960).
17. Fert, A., Cros, V. & Sampaio, J. Skyrmions on the track. *Nat. Nanotechnol.* **8,** 152–156 (2013).
18. Bode, M. *et al.* Chiral magnetic order at surfaces driven by inversion asymmetry. *Nature* **447,** 190–193 (2007).
19. Meckler, S. *et al.* Real-Space Observation of a Right-Rotating Inhomogeneous Cycloidal Spin Spiral by Spin-Polarized Scanning Tunneling Microscopy in a Triple Axes Vector Magnet. *Phys. Rev. Lett.* **103,** 157201 (2009).
20. Mühlbauer, S. *et al.* Skyrmion lattice in a chiral magnet. *Science (80-.).* **323,** 915–919 (2009).
21. Neubauer, A. *et al.* Topological Hall Effect in the A Phase of MnSi. *Phys. Rev. Lett.* **102,**

186602 (2009).
22. Yu, X. Z. *et al.* Near room-temperature formation of a skyrmion crystal in thin-films of the helimagnet FeGe. *Nat. Mater.* **10,** 106–109 (2011).
23. Yu, X. Z. *et al.* Real-space observation of a two-dimensional skyrmion crystal. *Nature* **465,** 901–904 (2010).
24. Raičević, I. *et al.* Skyrmions in a Doped Antiferromagnet. *Phys. Rev. Lett.* **106,** 227206 (2011).
25. Emori, S., Bauer, U., Ahn, S.-M., Martinez, E. & Beach, G. S. D. Current-driven dynamics of chiral ferromagnetic domain walls. *Nat. Mater.* **12,** 611–616 (2013).
26. Ryu, K.-S., Thomas, L., Yang, S.-H. & Parkin, S. Chiral spin torque at magnetic domain walls. *Nat. Nanotechnol.* **8,** 527–533 (2013).
27. Litzius, K. *et al.* Skyrmion Hall effect revealed by direct time-resolved X-ray microscopy. *Nat. Phys.* **13,** 170–175 (2017).
28. Jiang, W. *et al.* Direct observation of the skyrmion Hall effect. *Nat. Phys.* **13,** 162–169 (2017).
29. Zeissler, K. *et al.* Discrete Hall resistivity contribution from Néel skyrmions in multilayer nanodiscs. *Nat. Nanotechnol.* **13,** 1161–1166 (2018).
30. Büttner, F. *et al.* Dynamics and inertia of skyrmionic spin structures. *Nat. Phys.* **11,** 225–228 (2015).
31. Woo, S. *et al.* Observation of room-temperature magnetic skyrmions and their current-driven dynamics in ultrathin metallic ferromagnets. *Nat. Mater.* **15,** 501–506 (2016).
32. Jiang, W. *et al.* Blowing magnetic skyrmion bubbles. *Science (80-.).* **349,** 283–6 (2015).
33. R. B. Goldfarb and F. R. Fickett. Magnetic Units. *NBS Special Publication 696, U.S. Department of Commerce, National Bureau of Standards* (1985). Available at: http://ieeemagnetics.org/index.php?option=com_content&view=article&id=118&Itemid=107. (Accessed: 12th March 2019)

4. DOMAIN WALL DYNAMICS AND DEVICES

4.0 Introduction

For millennia, humans have searched for new ways to store information and knowledge. The oldest known records of this are 35,000 year old[1] cave drawings of animals and handprints found in Spain. Since then, new forms of analog memory have sprouted. Religious texts written on papyrus and paper have surfaced, comprising written forms of memory as old as a few thousand years B.C[2]. Memory, as we know it today, began as analog magnetic audio memory, where music and sounds were recorded on magnetic wire, called a magnetic drum. This is considered the precursor to the magnetic hard disk drive, where instead of a flat platter, a large, cylindrical drum is used[3]. Magnetic tape and magnetic core memory soon followed and developed quickly. However, all of these forms of memory primarily used the stray field of a ferromagnetic for both writing and reading the bits of information. This fundamentally limits both the read time and the density of information that can be stored.

The discovery of magnetoresistive effects in multilayer magnetic thin film stacks has led to technological applications in magnetic read heads and computer memory. Memory applications make use of such magnetoresistive devices, termed magnetic tunnel junctions (MTJs), consisting of ferromagnetic electrodes separated by a dielectric. The resistance across the device is a function of the relative orientation of the ferromagnetic layers, an effect called tunneling Magnetoresistance (TMR). This chapter will begin with a review of magnetic tunnel junction and their operation. Then a discussion of using magnetic domain walls to store information will follow, along with the different ways magnetic textures can be manipulated in solid state

Magnetic Tunnel Junctions (MTJs)

Over the past decade, magnetic tunnel junctions (MTJs) have received a growing interest due to their possible applications in magnetic sensing and magnetic memory and logic technology[4].

As a consequence of Moore's law, a need for smaller, higher density information storage media at room temperatures has been a pressing issue. MTJs have offered a unique solution to sustain Moore's law for many years. In additional to practical applications, the fundamental physics governing MTJs and tunneling magnetoresistance (TMR) have been attractive, and have garnered considerable theoretical and experimental investigation[4–6]. The principles of operation of an MTJ arise from the concept of simple quantum mechanical tunneling.

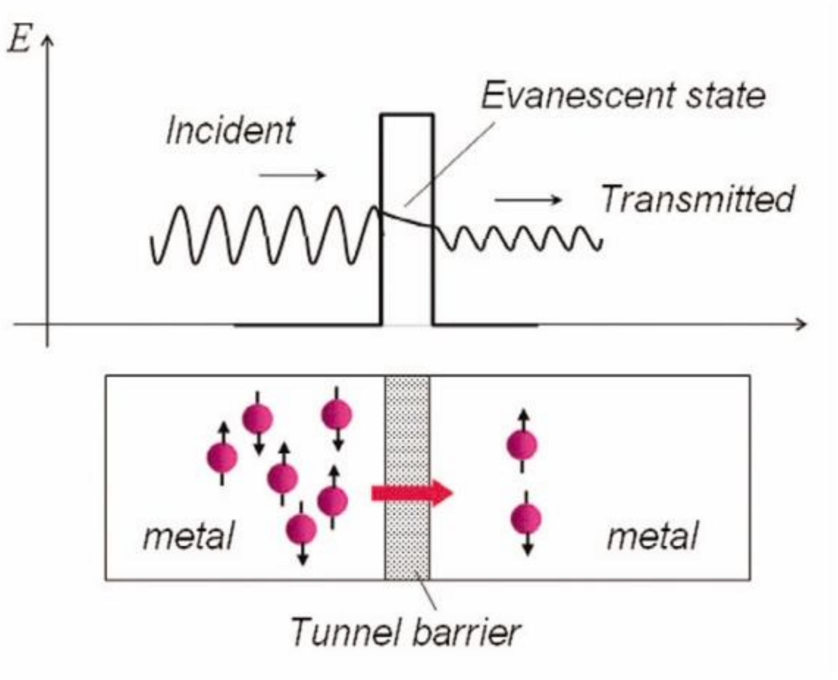

Figure 4.1 | Tunneling of electrons between two non-magnetic electrodes. The amplitude of the electron wave decreases exponentially through the tunnel barrier dielectric[4].

When conducting electrodes are separated by an extremely thin insulating (or dielectric) layer, electrons can "tunnel" through that barrier, resulting in electron conduction between the two electrodes[7]. This concept is a consequence of the wave nature of electrons. As depicted in Fig. 4.1, when an electron (wave) approaches a barrier height (dielectric), the electron wave passes through the barrier in an evanescent state[4]. The amplitude of the wave decreases exponentially with barrier thickness[8]. Thus the need for an extremely thin dielectric layer is crucial, such that the amplitude of the wave does not completely diminish through the dielectric layer. The ratio of the amplitude of the electron wave before and after passing through the dielectric layer is the probability of tunneling in the junction[9]. Replacing the two electrodes with ferromagnetic metals is the basis of an MTJ. Using ferromagnetic metals changes the physics of the device considerably.

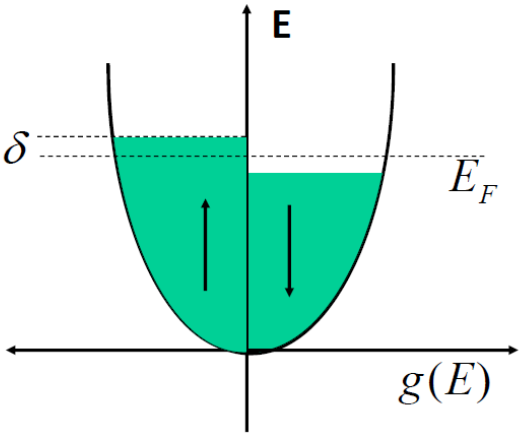

Figure 4.2 | Spontaneous spin splitting in metals. Kinetic energy and exchange energy compete, resulting in an imbalance on spin in the metal, leading to ferromagnetism. Adapted from ref[9].

Consider first, the concept of spontaneous spin splitting in ferromagnetic metals. In Fig. 4.2, a simplified rigid band model is shown for a typical metal, where the density of states is plotted for both majority- and minority-spin electrons. An energetic competition between the exchange interaction and kinetic energy gives rise to an imbalance of majority and minority spins in a metal. When two ferromagnetic metals are used as electrodes in a magnetic tunnel junction, the relative orientation of the magnetization of the ferromagnetic electrodes determines the probability of tunneling in the junction[9]. The origin of this is the differences in density of states (DOS) at the Fermi level for majority versus minority spins. Since an electron can only tunnel into a sub-band of the same spin orientation, the conductance is sensitive to the DOS at the Fermi-level. Thus, parallel versus anti-parallel ferromagnetic configurations will give rise to difference conductance, as shown in Fig. 4.3.

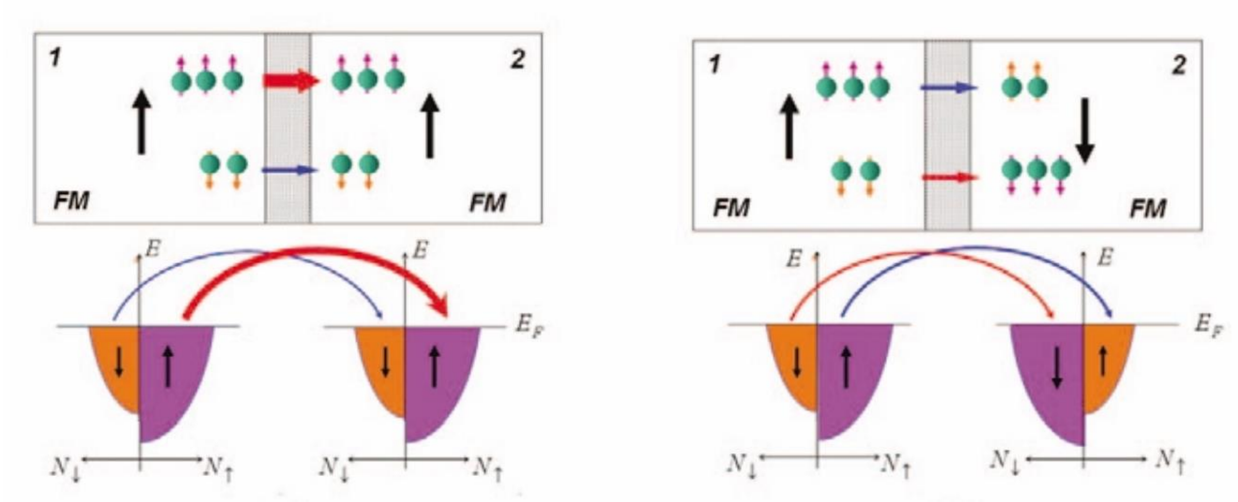

Figure 4.3 | Tunneling using ferromagnetic electrodes in which the ferromagnets are aligned a) parallel and b) anti-parallel. Adapted from ref[4]

In the MTJ device, tunneling is the rate-limiting step, so it dominates the effective resistance of the device[9]. If the density of available states (DOS at the Fermi level) in the electrode to which electrons are tunneling is low, the tunneling rate (and tunneling current) will be lower, and vice-versa. So the tunneling current will be proportional to the density of states. One can then control the number of available states by setting the adjacent electrodes' magnetization either parallel or antiparallel to each other. Parallels states result in a high tunneling probability and anti-parallel states result in a lower tunneling probability[9]. This leads to differences in device resistance for parallel versus antiparallel states.

Hard Disk Drive (HDD) read head- Principles of Operation

As previously mentioned, there is great interest in MTJs for memory technology. A classic example is the integration of MTJs into the read heads of hard disk drives (HDD).[4–8] Fig. 4.4 shows the basic structure of the read head in an MTJ[4]. The free layer is a ferromagnetic layer that senses the magnetization of the tiny magnetic dots on the spinning disk. The stray field of the magnetic dots causes the free layer to switch its magnetization. This is followed by a tunnel barrier and finally a "synthetic antiferromagnet" (SAF)[4]. The SAF forces the magnetization in the reference layer to be fixed due to an effective surface field called the exchange bias field. The free layer, tunnel barrier, and SAF form an MTJ, where relative orientations of the free and reference layers will result in a change of conductance of the MTJ.[4,7]

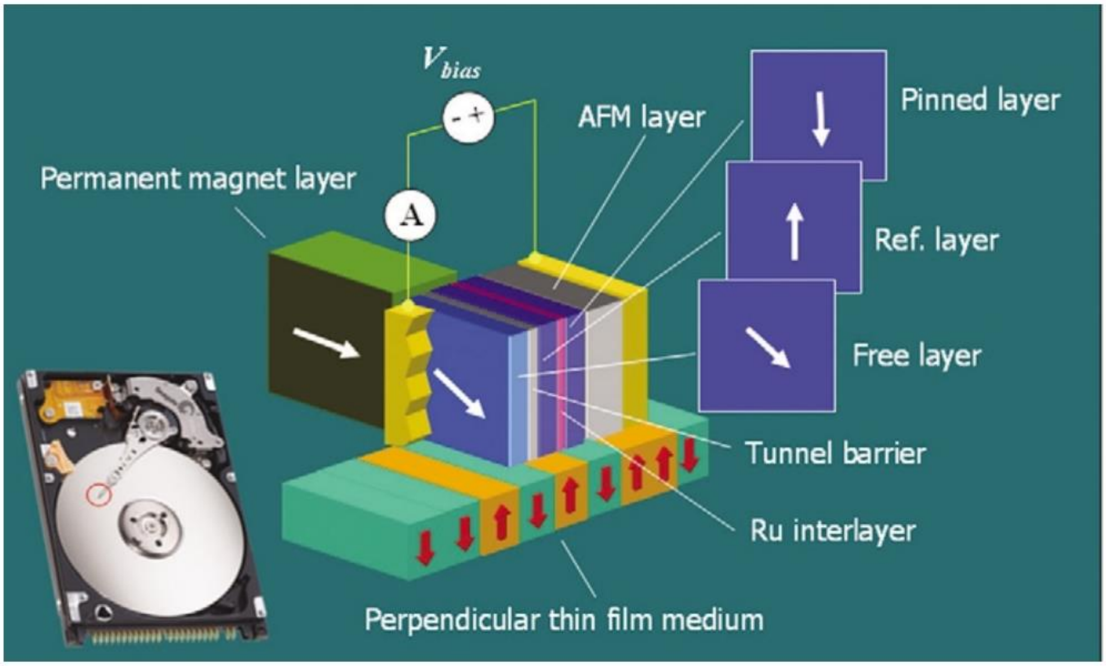

Figure 4.4 | MTJ read head in a HDD. A free layer senses the magnetization of the disk by rotation of magnetization and a reference layer remains at fixed magnetization, forming an MTJ. Adapted from ref[4]

While HDD read heads was the pioneering application for MTJs, its potential application in magnetic random access memory (MRAM) has been the larger emphasis of research and development in both academia and industry.

MTJ-MRAM

Conventional computer architecture relies on two distinct types of data storage: a volatile primary storage and a non-volatile secondary storage (eg. Hard disk drive). Primary storage comprises fast access memories such as SRAM and DRAM and is termed “primary” due to their close proximity to processors for fast data swapping. Secondary storage, on the other hand, are slow access devices but can hold larger magnitude of data, is non-volatile, and has higher density. However, with a steep trend in miniaturization, the current available memory technologies are facing a bottleneck in terms of power consumption and versatility which is fundamentally intrinsic. Static RAM (SRAM) has high speed and offers advantages over DRAM because it exhibits data remenance, but it has low storage density due to inherent limitations in design: it is constructed from a minimum of 4 transistors. It is also volatile where data is lost when memory is not powered. DRAM offers very high density due to its 1transistor-1MOS configuration but requires high refresh rate in order to retain data and hence consumes large power. Flash is based on NAND transistors like SRAM and exhibits good retention of data/nonvolatile based on concept of charge trapping by an insulation layer. Recent progress has also seen its storage capacity shoots up. However, due to the insulation layer, writing to flash requires a relatively high pump voltage in order for charge to tunnel through. This wears out the device and ultimately limits the number of read/write cycles.

MRAM is a type of storage that uses the spin degree of freedom to store data. MRAM offers relatively high read/write speed because data is read with voltage, not current (unlike Flash) and bits of data are written with small current pulse. It is nonvolatile due to high magnetocrystalline energy barrier to hopping. It also has potential to offer very high data density with the use of Spin-Transfer Torque (STT) configuration (discussed later) instead of the conventional 'toggling' configuration. With all these attributes, MRAM has the potential to replace SRAM, DRAM and Flash and is thought of as a "dream memory," as it can be used as a universal memory in which an entire computer can be fabricated on a single chip[4].

While MTJ-MRAM has many advantages, one of its main disadvantage is its scalability and durability. Each MTJ in MRAM require several transistors to provide the necessary currents and voltages for operation. This is often coined "single-bit per cell" architecture. This ultimately makes MRAM uncompetitive with current technologies like FLASH memory. However, utilizing domain walls (DW) or other spin textures for memory can circumvent these issues. The remaining sections of this chapter will focus on DW devices and how to manipulate DWs in magnetic materials.

4.1 Magnetic domain wall devices

As seen in Chapter 3, manipulating domain walls is an easy way to manipulate the magnetisation of a magnetic thin film. Applying a magnetic field to a magnetic material will drive domain wall into motion, where the preferred orientation is the orientation that is aligned with the magnetic field (Zeeman Effect). In 2006, Fikami *et al* used this concept to create a domain wall motion based memory device (DW-MRAM)[10]. In this scheme, a memory bit or cell is composed of a magnetic material that always contains a domain wall. In other words, there are two regions of oppositely pointing magnetisation in the film, as seen in Fig. 4.5a. The domain wall can be made a "permanent" feature of the device by interfacing it with very hard magnetic layers or by using a phenomenon called exchange coupling through an antiferromagnetic underlayer. This underlayer is represented by the orange rectangle in Fig. 4.5, where material on top of this layer is fixed in its current magnetisation state. The domain wall can this be moved across the portion of the device which is not fixed, in this case, the central region, between the two orange exchange biased layers.

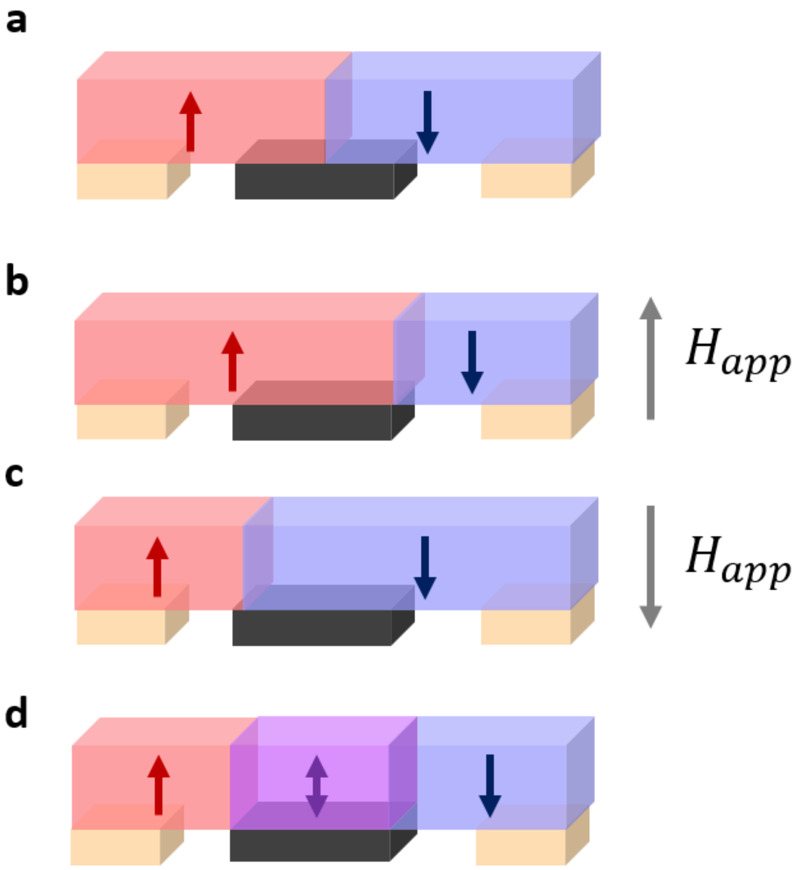

Figure 4.5 | DW-MRAM as conceptualized by NRC. A domain wall always present in a magnetic bit (a), where the orange layer is an antiferromagnet that provides exchange bias. The DW can be driven back and forth over a MTJ sensor (shown in black), creating “up” (b) and “down” (d) states. This central toggled region shown in purple (d) is coined the “free” layer.

Applying a magnetic field in either the up (Fig. 4.5b) or down (Fig. 4.5c) direction will cause the domain wall to propagate across the central (unfixed) portion of the device. By placing an MTJ or other magnetic sensing element in the center of this region (black rectangle in Fig. 4.5), one can measure the magnetisation state of this central region, which can be toggled back and forth from an “up” state to a “down” state, effectively a “1” or “0” bit of information. The central region of this device is often referred to as the “free” or “toggle” layer. This is indicated by the purple region in Fig. 4.5d.

A natural extension of the DW-MRAM concept is to use many magnetic bits in a long wire, such as those seen in Fig. 4.6a. However, using a magnetic field to translate a long array of bits will not work. Applying a magnetic field will cause two adjacent domain walls to move in opposite directions, seen in Fig 4.6. Unidirectional motion of domain walls is necessary to create a working logic or memory device. It has been proposed to use rotating magnetic fields for translate domain walls unidirectionally[11], but it is extremely difficult to localize magnetic fields to the nanoscale, such that one domain wall can be manipulated at a time.

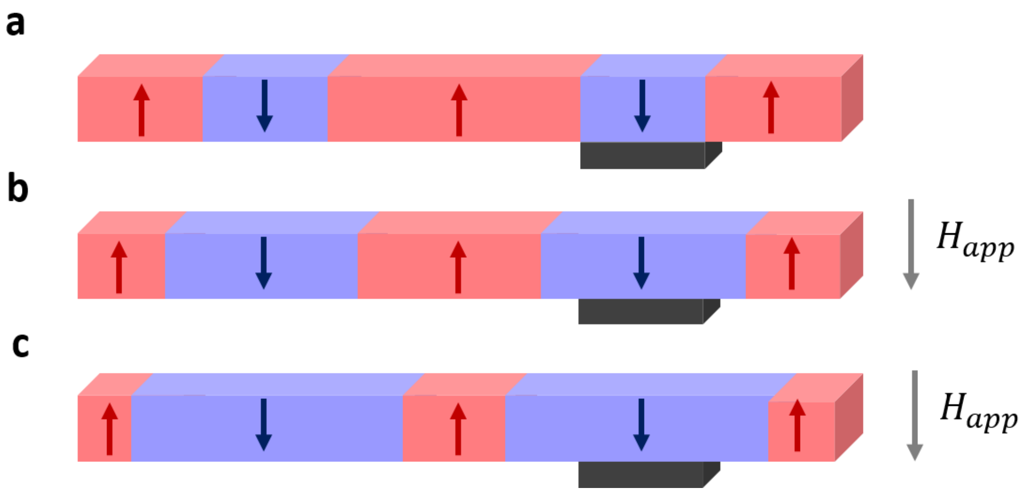

Figure 4.6 | a) A bit sequence in a long wire geometry. Applying magnetic field causes adjacent domain walls to move in opposite directions, making unidirectional motion difficult (b,c)

“Racetrack memory,” proposed by Stuart Parkin[12] aims to circumvent these issues. As the next section of this chapter will show, by using currents, instead of magnetic fields, one can exert a “spin-torque” onto the magnetic layer and thereby move the domain walls in a wire geometry unidirectionally (Fig. 4.7). This type of memory device holds promise to take advantage of the low cost and storage density of hard disk drives, while also achieving high speed, lower power, solid state performance of memory products today. The next section will take a deeper dive into the mechanisms by which a field and a current can exert a spin torque on a domain wall.

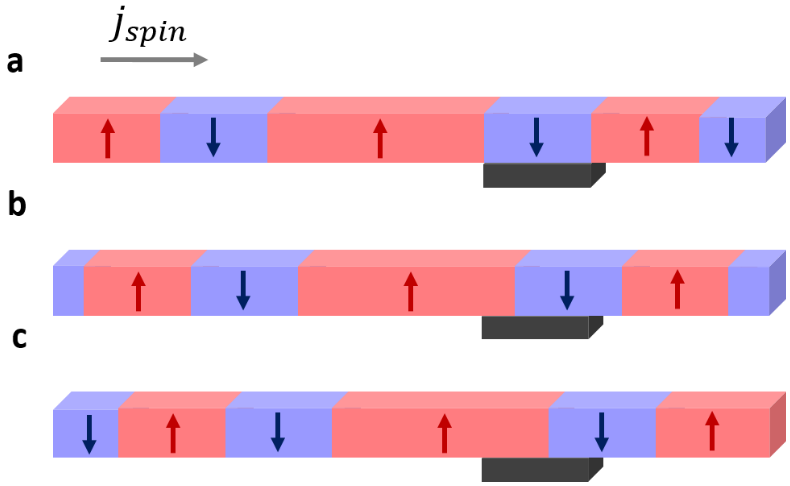

Figure 4.7 | Racetrack memory, as envisioned by Stuart Parkin[12]. A current is used to expert a spin torque on domain walls, providing unidirectional motion of magnetic bits in a wire (a-c).

4.2 Domain Wall Dynamics

Field Driven Domain Wall Motion

First, we explore the dynamics of field-driven domain wall motion. Although field-driven domain wall motion is not very useful for device applications, field-driven domain wall motion is very well understood. Because of this, different mechanisms of current driven domain wall motion are often mathematically manipulated to appear as “effective magnetic fields.” In Chapter 2, we showed how domain walls grow in the direction of the applied field, but we will find that the dynamics of this process are much more complicated than a simple rotation of magnetic moments.

The dynamics of magnetisation are typically modeled using the Landau-Lifshitz-Gilbert Equations (LLGE). The LLGE describes the time rate of change of the normalized magnetisation moment $\boldsymbol{m} = \frac{\boldsymbol{M}}{M_s}$ driven by a force:

$$\frac{\delta \boldsymbol{m}}{\delta t} = -|\gamma| \boldsymbol{m} \times \boldsymbol{H}_{eff} + \alpha \boldsymbol{m} \times \frac{\delta \boldsymbol{m}}{\delta t} \qquad 4.1$$

where γ is the gyromagnetic ratio and α is the gilbert damping parameter. $\boldsymbol{H}_{eff}$ is the "effective magnetic field" acting on the domain wall. This includes the anisotropy field, the ferromagnetic exchange field, magnetostatic fields, and any externally applied magnetic fields. The first term on the right-hand side of expression 4.1 is a precessional term. This term causes the moment to precess or oscillate around the direction of the applied magnetic field $\boldsymbol{H}_{eff}$, as shown in Fig. 4.8 by the grey circle rotating the magnetisation in a circle out of the plane. The second term in Eq. 4.1, is the damping term, which aligns the magnetic moment towards the direction of the applied force, $\boldsymbol{H}_{eff}$, This is illustrated in Fig. 4.8 by the purple arrow directing the moment towards $\boldsymbol{H}_{eff}$. The combination of these two terms is the oscillating decay trajectory of the magnetic moment towards $\boldsymbol{H}_{eff}$. Thus, the magnetic moment does not simply directly align towards the applied force, such as in Newtonian mechanics, but rather it takes a loss-y, viscous like motion.

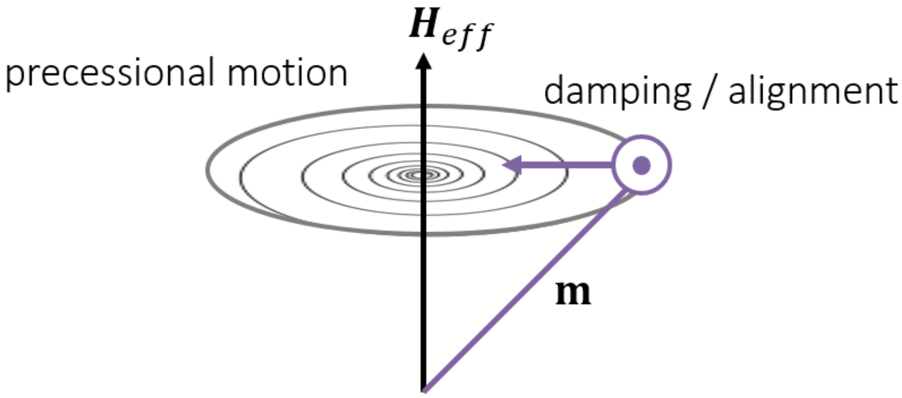

Figure 4.8 | Magnetisation dynamics of a moment with an applied magnetic field. The magnetic moment takes precesses around the applied field $\boldsymbol{H}_{eff}$ and dampens towards it.

This can easily be applied to a domain wall moment, as well. Here we will examine the case of out-of-plane magnetised thin films. When a vertical (up) magnetic field is applied to a domain wall $\boldsymbol{H}_{app}$, the precessional moment in the domain wall cants in the plane of the film in the direction of the "up" domain, towards a Néel configuration $-|\gamma|\boldsymbol{m}\times\boldsymbol{H}_{app}$ (Fig. 4.8a). Néel domain walls in thin films have additional stray field, so this canting causes an extra demagnetizing field to form, which opposes the canting. This is analogous to the demagnetizing field that opposes stray fields. If the angle of the domain wall moment does not cant beyond $\frac{\pi}{4}$, the precessional terms also acts on the demagnetizing field that develops $-|\gamma|\boldsymbol{m}\times\boldsymbol{H}_d$, and this cants the magnetisation out of the plan in the direction of the applied field $\boldsymbol{H}_{app}$ (up) (Fig. 4.8a). This drives the domain wall, expanding the "up" domain. This is a very efficient process of domain wall motion. However, if the magnetic field is large enough such that the domain wall cants beyond $\frac{\pi}{4}$ (the so-called Walker field[13] H_W), then the domain wall can no longer hold is statics canting angle and it begins to precess in the plane of the film (Fig. 4.9c), alternating between Bloch and Néel configurations. The damping term in Eq. 1 $\alpha\boldsymbol{m}\times\frac{\delta\boldsymbol{m}}{\delta t}$ drives the domain wall into motion.

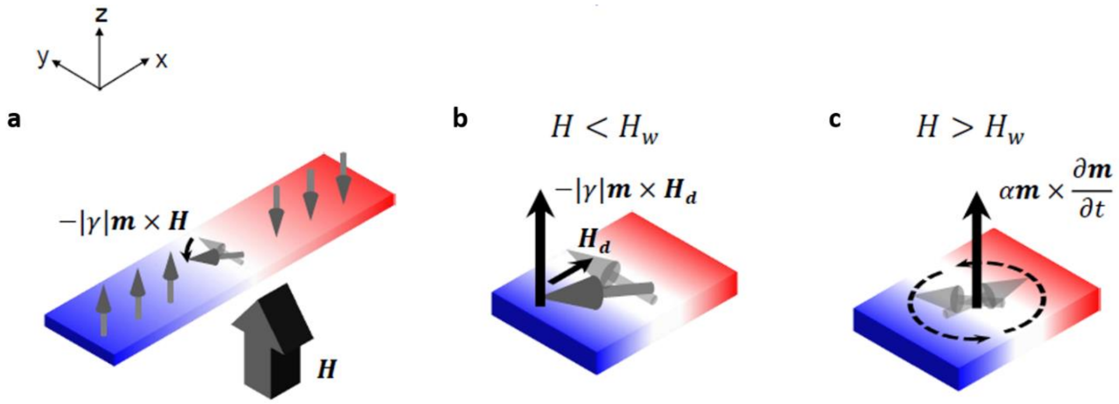

Figure 4.9 | Field driven domain wall dynamics in an out-of plane magnetised film. adapted from ref[14]

The velocity of the moving domain wall as a function of the driving force is often described by its mobility:[15,16]

$$\mu = \frac{|\gamma|\Delta}{\alpha} \tag{4.2}$$

where Δ is the domain wall width. This linear relationship occurs below the Walker field H_W. Above the Walker field, the velocity takes the form[13]:

$$v \propto \alpha^2 \mu H \tag{4.3}$$

In most magnetic material, $\alpha < 1$ and thus $\alpha^2 \ll 1$. Therefore, above the Walker field, the velocity of a domain wall decreases drastically in a process called "Walker breakdown." This qualitatively makes sense, as above Walker breakdown, loss-y, precessional motion of the domain wall moment occurs. This non-linear motion was predicted theoretically and in magnetic simulations before it was experimentally observed in in-plane permalloy wires by G.S.D.Beach *et al*[17]. Walker breakdown is shown in Fig. 4.10. The Walker field for an out-of-plane magnetised film is significantly lower than for an in-plane magnetised film, as the energetic cost of processing a

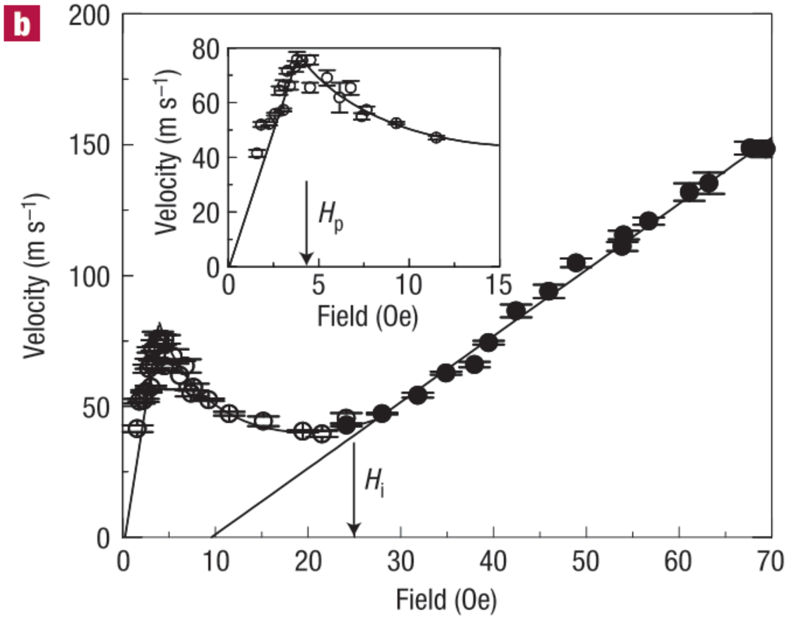

Figure 4.10 | Walker breakdown as observed by G.S.D. Beach *et al*[17] in in-plane magnetised permalloy films.

domain wall between Bloch and Néel character is significantly less than it is for precessing the domain wall moment from in-plane to out-of-plane, which is the case for IP-magnetised Walker breakdown. We will find that spin torque induced by currents can also be represented by effective magnetic fields, and the LLGE can be adapted very easily for these effects.

Spin Transfer Torque Motion of Domain Walls

Electrical currents can also be used to manipulate the magnetic texture of a thin film. Traditionally currents have been used to create Oersted fields generated from wires. This is called Amperes law. This type of method of manipulating spin textures is extremely power inefficient (relative to what is needed for computer memory) and very hard to localize down to the nanoscale. And as mentioned before, an Oersted magnetic field does not have the proper symmetry to drive domain walls in a unidirectional manner needed for memory and logic applications. Electrons can instead be utilized in a different manner that allows for unidirectional motion of domain walls.

When electrons flow through a normal nonmagnetic material, the electrons have random spin orientations, where the net spin orientation of the moving electrons is zero. The case is different when electrons are flowed through a magnetic material, such as Co, Ni, or Fe. Here, the electron spins become polarized, where a majority of the spins are oriented in one direction. The preferred orientation direction is that which the magnetic moment of the material is pointed. This is because electrons of different type spins have different resistivity in when flowed through a magnetic material. The resistivity of an electron is proportional to the density of states at the fermi level $g(E_F)$. From Fig. 4.3, we can see that $g(E_F)$ is different for "up" spins and "down" spins, and thus have different resistivity. The resistivity of "up" and "down" spins are related to the spin-polarization ratio of the magnetic material. In other words, how good the spin filter is.

$$P = \frac{\rho_{-} - \rho_{+}}{\rho_{-} + \rho_{-}} \qquad 4.3$$

where P is the polarization and ρ_{+} and ρ_{-} are the resistivity of up and down spins, respectively. Spin-polarization ratios for 3D transition metals are typically between $0.4 - 0.7$[18].

Spin-polarization can be used to drive domain walls in magnetic materials, as well. A torque can be exerted on the magnetisation of the domain wall through a process called “spin-transfer torque” (STT). The mechanism of STT is rooted in the conservation of angular momentum of both the conduction electrons and the local electrons in the magnetic material. As electrons pass through the material, they become spin polarized, tracking the local magnetisation of the material. Thus, as a mobile electron passes across a domain wall, its orientation flips. The flipping of the electron spin causes the spin angular momentum to change. In order to conserve angular momentum, there must also be a change in the angular momentum of the local electrons. In other words, magnetic moments of the local electrons in the domain wall must also flip. This results in the net motion of the domain wall. This type of local tracking STT is termed “adiabatic.” There is an intrinsic energy barrier for domain wall motion via adiabatic STT. This barrier exists even in defect free materials. Adiabatic STT does not directly translate the domain wall into motion via ridged translation, but via precessional motion. We can add the adiabatic STT to the LLGE in the following way:

$$\frac{\delta \boldsymbol{m}}{\delta t} = -|\gamma| \boldsymbol{m} \times \boldsymbol{H}_{eff} + \alpha \boldsymbol{m} \times \frac{\delta \boldsymbol{m}}{\delta t} - (\boldsymbol{u} \cdot \nabla)\mathbf{m} \qquad 4.4$$

where the third term on the right-hand sides is the adiabatic STT. $\boldsymbol{u}$ is the spin drift velocity, which is defined as

$$\boldsymbol{u} = \frac{g \mu_B P \boldsymbol{J_e}}{2|e| M_s} \qquad 4.5$$

where g is the g-factor and $\boldsymbol{J_e}$ is the current density in the direction of the electron flow. Eq. 4.4 is often simplified to the 1D case, where $\nabla = \frac{\delta}{\delta x}$. From Eq. 4.5, it may appear as though the adiabatic STT directly translate the domain wall along the direction of the electron flow. However, the damping term in Eq. 4.4 $\alpha\boldsymbol{m} \times \frac{\delta \boldsymbol{m}}{\delta t}$ points in the plan of the film, which, along with the adiabatic STT, generates a demagnetizing field $\boldsymbol{H_D}$ similar to field induced domain wall motion. The adiabatic STT needs to overcome the strength of the demagnetizing field, otherwise the domain wall moment will stay motionless. If the adiabatic STT is sufficiently large, the domain wall will move via precession in a corkscrew-like manner. This is shown schematically in Fig. 4.11.

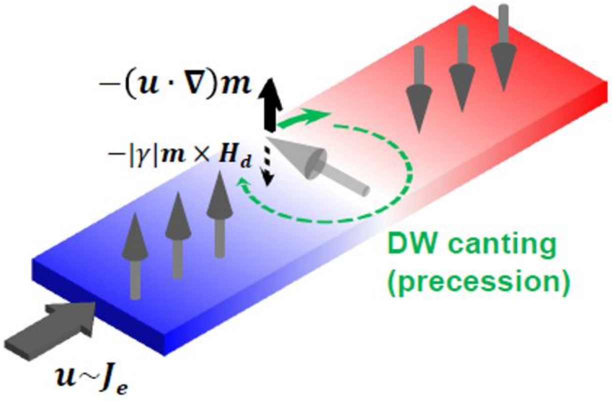

Figure 4.11 | Dynamics of domain wall motion driven by spin-transfer torque in an out-of-plane magnetised film. adapted from ref[14]

An additional term in the LLGE, the nonadiabatic STT can be added, as well. The nonadiabatic STT has a symmetry exactly like that of a field acting on a domain wall and any barrier for domain wall motion is extrinsic. Therefore, in defect free materials, a domain wall can be driven at very low current densities. This additional term is added in Eq. 4.6.

$$\frac{\delta \boldsymbol{m}}{\delta t} = -|\gamma|\boldsymbol{m} \times \boldsymbol{H}_{eff} + \alpha\boldsymbol{m} \times \frac{\delta \boldsymbol{m}}{\delta t} - (\boldsymbol{u} \cdot \nabla)\mathbf{m} - \beta\mathbf{m} \times [-(u \cdot \nabla)\mathrm{m}] \tag{4.6}$$

where β is the nonadiabatic STT parameter. Here, domain walls can move via rigid translation rather than loss-y precession. This mechanism has been proposed to explain why experimentally domain wall motion via STT has been seen well below intrinsic theoretical limits[18,19] and has been found to very with the strength of the pinning landscape of a film[12].

Spin Orbit Torque Motion of Domain Walls

Adiabatic and non-adiabatic STT accounted for much of the current-induced domain wall motion observed in magnetic nanowires. However, there were still numerous observations of current-induced domain wall motion that could not be explain by STT. In fact, there were observation of domain wall motion that exceeded the theoretical limit of STT in asymmetric multilayer films. In particular, domain wall velocities exceeding $100\frac{m}{s}$ were observed in asymmetric Pt/Co/AlOx[20], Pt/Co/MgO[21], and Pt/Co/Ni[22] multilayers. Moreover, it was observed that the domain walls are driven *against* current flow in these systems, unlike STT.

To explain these observations, Moore and Miron *et al*[23] report a very large Rashba field in these systems that aids in the switching of Pt/Co/AlOx. The Rashba effect is the spin-polarization of electrons due to the splitting of the electron bands. Specifically, it is has be proposed to arise at the interfaces of thin film materials with structural inversion asymmetry. For instance, in Pt/Co/AlOx, the asymmetry of the structure creates an electric potential along the out-of-plane direction of the film. Consequently, conduction electrons passing through the ferromagnetic layer feel an electric field from the Rashba effect. In the rest frame of the moving electrons, the electric field looks actually like a magnetic field, causing the conduction electron spins to become tiled, and hence polarized. For this reason, a torque is exerted on the magnetisation of the thin film. This type of torque is often referred to as a “spin-orbit torque[24],” as the spin orientation is influenced by the electron orbitals. The Rashba field can be mathematically described by Eq. 4.7[23].

$$\boldsymbol{H}_R = -2\frac{\alpha_R m_e}{\hbar|e|M_s}P|J_e|(\hat{\boldsymbol{z}} \times \boldsymbol{J}_e) \tag{4.7}$$

where α_R is the Rashba parameter, m_e is the electron’s mass, $\hbar$ is Planck’s constant, and J_e is the direction of the electron flow. The Rashba field alone isn’t enough to cause DW motion. Consequently, Miron *et al* have attributed the domain wall motion to a large negative nonadiabatic STT[25]. The torque arising from the Rashba effect can be interpreted as a “field-like” torque (Eq. 4.8) or a “Slonczewski-like” torque (Eq. 4.9). A schematic of the symmetry of the Rashba torque is in shown in Fig. 4.12a.

$$\tau_{\mathrm{R,FL}} = -|\gamma|\boldsymbol{m} \times \boldsymbol{H}_R \tag{4.8}$$

$$\tau_{\mathrm{R,SL}} = -|\gamma|\boldsymbol{m} \times (\boldsymbol{m} \times \beta\boldsymbol{H}_R) \tag{4.9}$$

An alternative spin-orbit explanation for the fast domain wall motion in asymmetric structures was proposed by Liu *et al*. Liu *et al*[26] propose a mechanism based on the spin-Hall effect. The spin-Hall effect is the creation of a spin-current from a charge current flowing through a heavy metal (Pt, Ta[26], or W[27]). Spin-dependent scattering of conduction electrons causes electrons of one spin type to deflect in the opposite direction of the other. The deflected spins then can accumulate on the top and bottom side of the heavy metal, which then exert a torque on the magnetisation. The spin-Hall effective field H_{SH} can be described by

$$\boldsymbol{H}_{SH} = \frac{\hbar\theta_{\mathrm{SH}}|J_e|}{2|e|M_s t_F} \tag{4.10}$$

where t_F is the thickness of the ferromagnet and $\theta_{SH} = I_e/I_e$ is the spin-Hall angle of the heavy metal material, which is the ratio of spin-current produced to charge current flowed through the material. This is effectively the efficiency of the spin-Hall metal. The resulting spin-Hall torque is

$$\tau_{\mathrm{SH}} = -|\gamma| \boldsymbol{m} \times (\boldsymbol{m} \times \boldsymbol{H}_{SH}(\hat{\boldsymbol{z}} \times \widehat{\boldsymbol{J}_e})) \qquad 4.11$$

This torque is schematically shown in Fig. 4.12b. Both the Rashba Slonzcewski-like torque and the spin-Hall torque act as effective fields in very similar ways, causing the same quantitative effects on domain wall motion. Consequently, this has caused great controversy in the field over which the dominant effect in both current induced magnetic switching and domain wall motion. The spin-Hall torque (or Rashba Slonzcewski-like torque) symmetry is such that it only acts on domain walls of Néel configuration, or having some Néel component[28]. The torque is zero on a completely Bloch domain walls. Moving domain walls via the spin-hall effect has historically been done by applying an in-plane field to a domain wall to force a Néel configuration. Even so, the symmetry of the Slonzcewski-like torque is such that up-down versus down-up domain walls move in opposite directions, making this torque appear quite useless for a racetrack memory despite its large effects.

However, as explained in Chapter 3, Emori *et al* discovered that the Dzyaloshinskii-Moriya interaction (DMI) is present in the same asymmetrically stacked films that gives rise to the spin-Hall effect, where the DMI can stabilize homochiral Néel domain walls. The Pt or Ta heavy metal underlayer provides perpendicular magnetic anisotropy (PMA), interfacial DMI, and the spin-Hall torque. Thus, in films with interfacial DMI, up-down and down-up domain walls move in the same direction (against electron flow) with very high speeds.

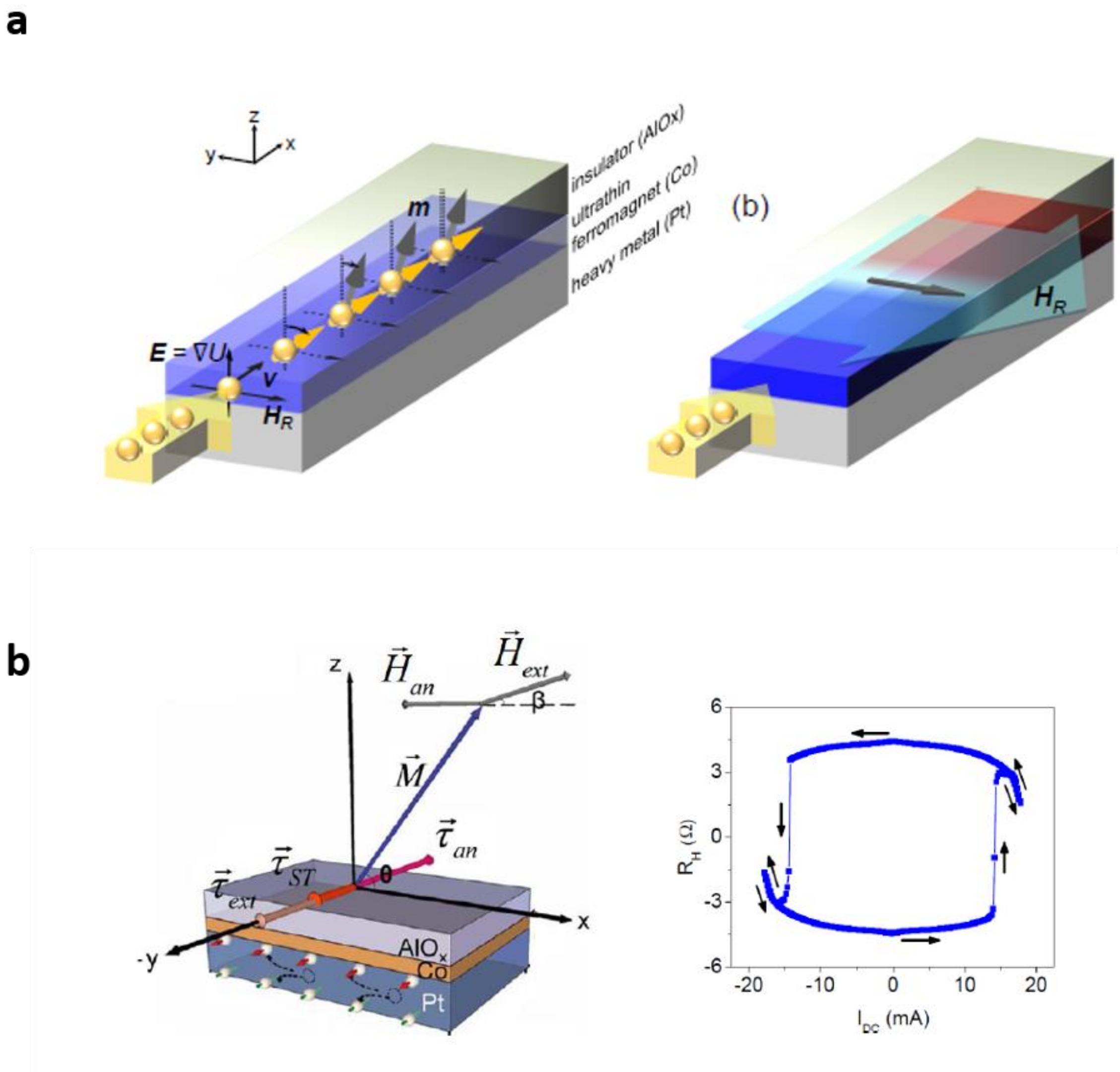

Figure 4.12 | a) Schematic of Rashba effect in an asymmetric PMA film. An electric field gradient is formed from a built-in potential due to the asymmetric interfaces. The electrons see this as a magnetic field and thus feel a torque from the electric field, resulting in magnetic moment tilting. Adapted from ref[14] b) The Slonczewski-like torque arising from the accumulation of spins due to the spin Hall effect. The right image shows current induced magnetisation switching from the spin Hall effect. Adapted from ref[26]

Summary

Using magnetic materials to store information and data is not a novel concept; however, more efficient, dense, and fast means of magnetic storage have been recently proposed. Among these is racetrack memory, based on solid state motion of magnetic spin textures, such as skyrmions and domain walls. In recent year, novel ways of current induced domain wall motion have been discovered, including the most efficient and most promising: spin orbit torque (SOT) motion of domain walls. In combination with interfacial DMI, SOT motion of homochiral domain walls allows for solid state, efficient, unidirectional motion of spin textures needed for memory applications. In this thesis, we will examine an often overlooked class of magnetic materials, ferrimagnets. These multi-sublattice systems enable both ultrafast motion of domain walls as well as ultrasmall, non-interacting (dense) spin-textures. Next, we will turn towards utilizing low-damping magnetic insulators for ultrafast motion of domain walls. Finally, we will investigate using light as a means of domain wall motion and the advantages this has of current-induced domain wall motion.

4.3 References

1. 7 Oldest Cave Paintings in The World | Oldest.org. (2019). Available at: http://www.oldest.org/artliterature/cave-paintings/. (Accessed: 18th March 2019)
2. 10 Oldest Religious Texts in The World | Oldest.org. (2019). Available at: http://www.oldest.org/religion/religious-texts/. (Accessed: 18th March 2019)
3. Magnetic drum. Available at: http://cs-exhibitions.uni-klu.ac.at/index.php?id=222. (Accessed: 18th March 2019)
4. Zhu, J.-G. (Jimmy) & Park, C. Magnetic tunnel junctions. *Mater. Today* **9,** 36–45 (2006).
5. Wills Smullen, C. I. Designing Giga-scale Memory Systems with STT-RAM. (University of Virgina, 2011).
6. Huai, Y. Spin-Transfer Torque MRAM (STT-MRAM) : Challenges and Prospects. (2009).
7. Blundell, S. *Magnetism in condensed matter*. (Oxford University Press, 2001).
8. Tsymbal, E. Y. (Evgeny Y. . & Zutic, I. *Handbook of spin transport and magnetism*. (CRC Press, 2012).
9. O'Handley, R. C. *Modern magnetic materials : principles and applications*. (Wiley, 2000).
10. Fukami, S. *et al.* Low-current perpendicular domain wall motion cell for scalable high-speed MRAM. *Symp. VLSI Technol.* (2006).
11. Allwood, D. A. *et al.* Magnetic domain-wall logic. *Science (80-.).* **309,** 1688–1692 (2005).
12. Parkin, S. S. P., Hayashi, M. & Thomas, L. Magnetic domain-wall racetrack memory. *Science* **320,** 190–4 (2008).
13. Schryer, N. L. & Walker, L. R. The motion of 180° domain walls in uniform dc magnetic fields. *J. Appl. Phys.* **45,** 5406–5421 (1974).
14. Emori, S. Magnetic domain walls driven by interfacial phenomena. (2013).
15. Jung, S.-W., Kim, W., Lee, T.-D., Lee, K.-J. & Lee, H.-W. Current-induced domain wall motion in a nanowire with perpendicular magnetic anisotropy. *Appl. Phys. Lett.* **92,** 202508 (2008).
16. Martinez, E. The stochastic nature of the domain wall motion along high perpendicular anisotropy strips with surface roughness. *J. Phys. Condens. Matter* **24,** 024206 (2012).
17. Beach, G. S. D., Nistor, C., Knutson, C., Tsoi, M. & Erskine, J. L. Dynamics of field-driven domain-wall propagation in ferromagnetic nanowires. *Nat. Mater.* **4,** 741–744 (2005).
18. Ueda, K. *et al.* Temperature dependence of carrier spin polarization determined from current-induced domain wall motion in a Co/Ni nanowire. *Appl. Phys. Lett.* **100,** 202407 (2012).
19. Thiaville, A., Nakatani, Y., Miltat, J. & Suzuki, Y. Micromagnetic understanding of current-driven domain wall motion in patterned nanowires. *Europhys. Lett.* **69,** 990–996 (2005).
20. Moore, T. A. *et al.* High domain wall velocities induced by current in ultrathin Pt/Co/AlOx wires with perpendicular magnetic anisotropy. *Appl. Phys. Lett.* **93,** 262504

(2008).

21. Koyama, T. *et al.* Current-Induced Magnetic Domain Wall Motion in a Co/Ni Nanowire with Structural Inversion Asymmetry. *Appl. Phys. Express* **6,** 033001 (2013).
22. Ryu, K.-S., Thomas, L., Yang, S.-H. & Parkin, S. S. P. Current Induced Tilting of Domain Walls in High Velocity Motion along Perpendicularly Magnetized Micron-Sized Co/Ni/Co Racetracks. *Appl. Phys. Express* **5,** 093006 (2012).
23. Mihai Miron, I. *et al.* Current-driven spin torque induced by the Rashba effect in a ferromagnetic metal layer. *Nat. Mater.* **9,** 230–234 (2010).
24. Gambardella, P. & Miron, I. M. Current-induced spin-orbit torques. *Philos. Trans. R. Soc. A Math. Phys. Eng. Sci.* **369,** 3175–3197 (2011).
25. Miron, I. M. *et al.* Perpendicular switching of a single ferromagnetic layer induced by in-plane current injection. *Nature* **476,** 189–193 (2011).
26. Liu, L. *et al.* Spin-torque switching with the giant spin Hall effect of tantalum. *Science* **336,** 555–8 (2012).
27. Pai, C.-F. *et al.* Spin transfer torque devices utilizing the giant spin Hall effect of tungsten. *Appl. Phys. Lett.* **101,** 122404 (2012).
28. Khvalkovskiy, A. V. *et al.* Matching domain-wall configuration and spin-orbit torques for efficient domain-wall motion. *Phys. Rev. B* **87,** 020402 (2013).

5. EXPERIMENTAL METHODS

5.0 Introduction

This chapter will cover a variety of experimental methods used throughout this thesis. In particular, two deposition techniques will be discussed: sputtering and pulsed-laser deposition, and the advantages and disadvantages of each technique will be described in detail. The chapter will then discuss patterning of micrometer-scale using both optical light and electron beams, and compare and contrast "lift-off" lithography versus ion milling. Finally, the chapter will end with a variety of basic magnetic materials characterization techniques and examples of how they can be used to probe magnetic properties and image magnetic materials. In the imaging section, I will focus on using polarized light (visible, UV, and x-ray) as probes for imaging.

5.1 Material Deposition

Sputter Deposition

Sputter deposition (often referred to as sputtering) is a very commonly used thin film deposition technique, both in industry and academia. Its popularity arises because of its versatility, vacuum and microscale lithographic patterning compatibility[1]. Sputtering is a physical vapor deposition process (PVD), as opposed to a chemical vapor deposition process (CVD). In CVD, a chemical precursor is used in a reaction chamber, where the reaction is controlled by the flow of this precursor gas. CVD is a higher temperature (300^{o}C-900^{o}C) process, where a reaction occurs on the surface of the substrate material. PVD Sputtering does not require the use of precursor materials, as the target material is the exact material that is deposited making the process applicable to a wide range of materials. The exception to this is the case of reactive sputter, which will be discussed later. In fact, nearly all classes of solid materials can be deposited via sputter deposition, including metals, oxides, and semiconductors. CVD has the advantage that there is typically very little waste material involved and higher base pressures are used, unlike sputtering; however, CVD precursors can be dangerous and toxic if handled inappropriately.

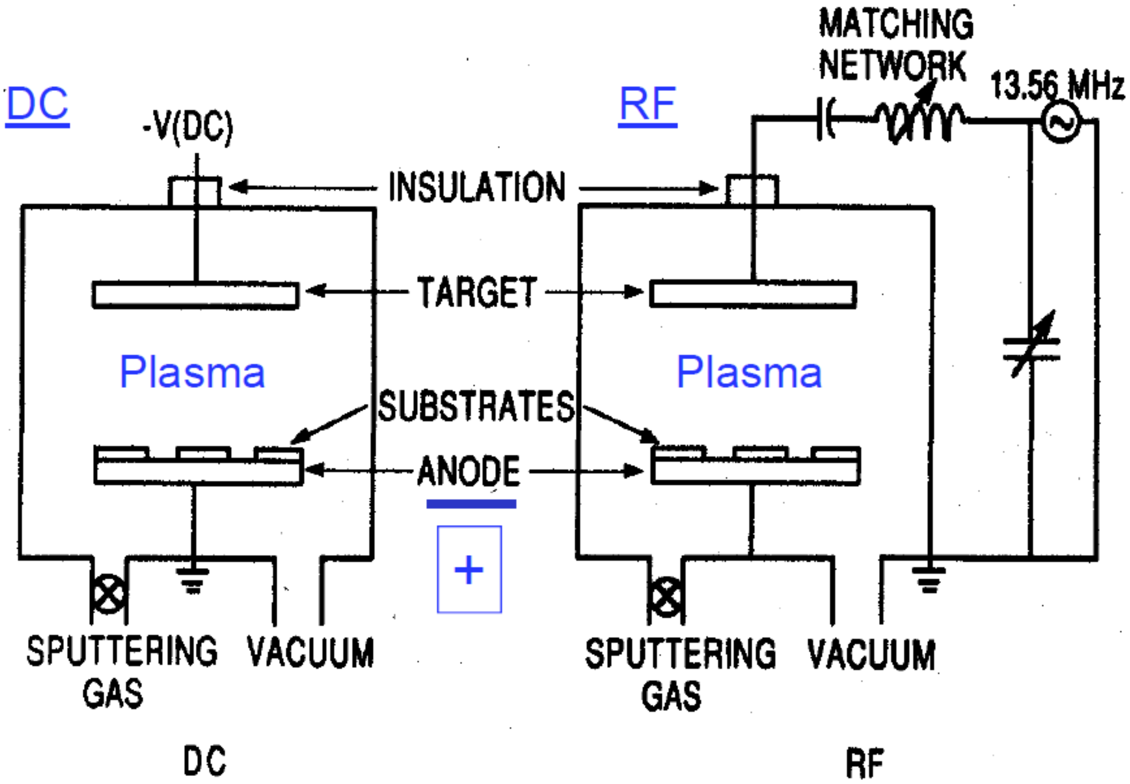

Figure 5.1 adapted from ref[1] **|** a) Direct current (DC, left) and b) radio frequency (RF, right) sputter deposition system schematics

The vast majority of the films in this thesis are deposited via high vacuum magnetron sputter deposition. The basic principle of sputter deposition is described in Fig. 5.1[1]. In sputter deposition, both the solid substrate material and source material are inserted into a vacuum chamber. Base pressures for sputter deposition generally occur between 10^{-5} and 10^{-9} torr[2]. A heavy, inert metal (typically Ar) is inserted into the chamber. This is the sputtering gas. A strong bias is place on the source (cathode, -) and the substrate (anode, +). Typically the substrate anode is also the chamber ground. This large bias causes the Ar to ionize via an avalanche process, forming Ar^+ and e^-, a plasma. The heavy, positively charged, Ar^+ ions are attracted to the negatively charged

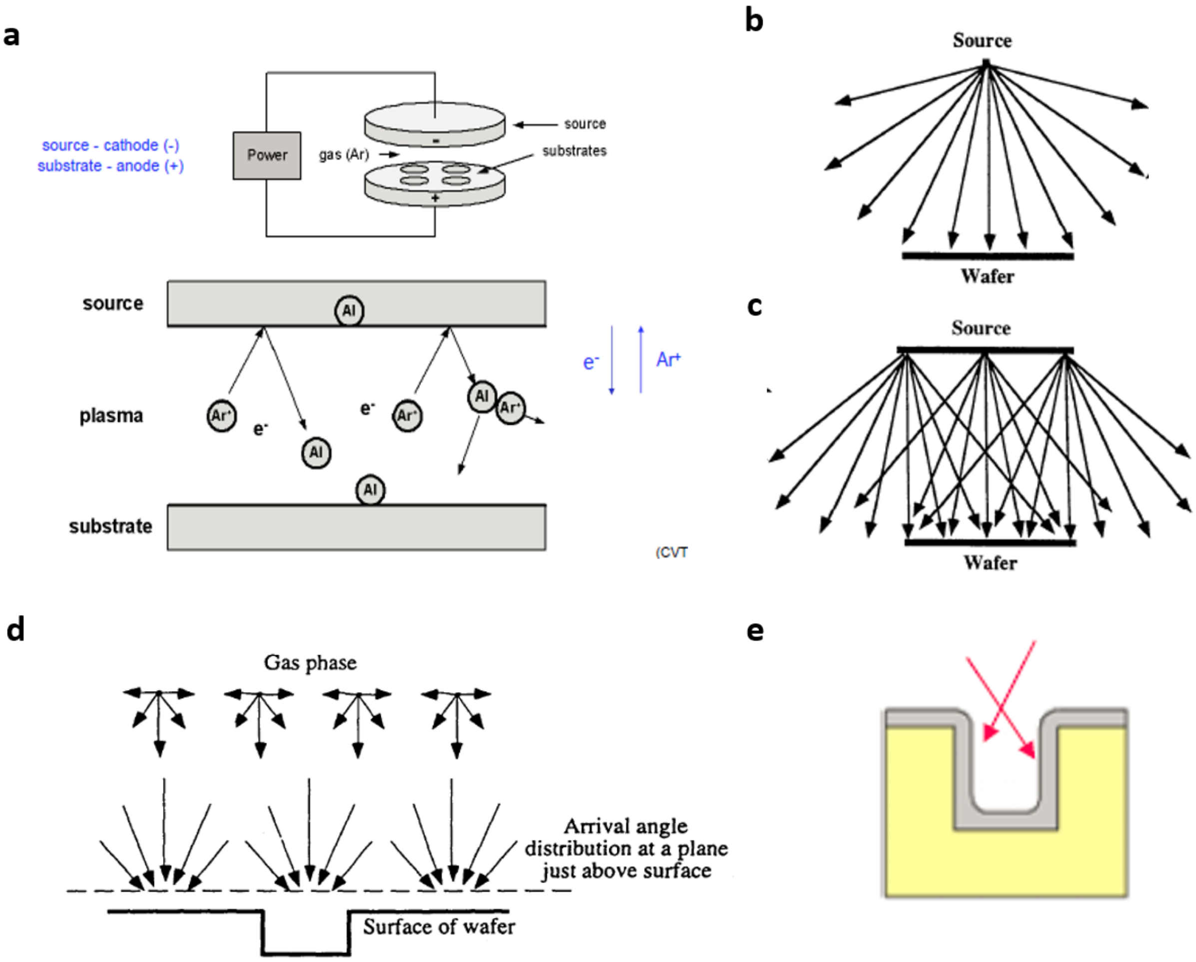

Figure 5.2 | a) Schematic[2] of typical sputter deposition system, where Al is the source material. Material flux lines from a point source[3] (b) and from a extended source[3] (c). Sputtering follows the extended source model where the sputtered material arrives at the sample at many angles[3] (d), creating conformal growth over steps[3] (e)

sputter source and bombard the sources material with high energy (see Fig. 5.2a). This bombardment forces clusters of atoms to be ejected from the source material and deposit of the substrate in an energetic process. Process parameters include the amount of bias (gun current), substrate temperature, sputtering gas pressure and flow rate, plasma confinement (magnetron sputtering), and any reactive gas pressure and flow rate. These process parameters effect the control parameters: deposition rate, microstructure, stress, impurity content, and stoichiometry[2]. We now explore how these parameters affect the final film quality.

Sputter deposition is considered an extended source deposition technique (Fig 5.2c), as opposed to a point source deposition technique (Fig 5.2b). In an extended source, the material flux lines extend from the source from a very wide angle distribution compared to the point source[3]. This results in conformal growth of material on the substrate, as opposed to line-of-sight deposition from point sources, such as evaporation or molecular beam epitaxy (Fig 5.2d, e). Conformal growth provides very good step coverage, but we will find in the *lithography* section of this thesis that this can cause difficulties in lift-off processes. Another potential disadvantage of sputtering is the quality of film produced. Later in this section we will see that sputter deposition produces polycrystalline or even amorphous films. Epitaxial films are very difficult to produce by standard deposition processes.

Sputtering rates generally scale inversely with the mass of the source materials, ie- the heavier the material, the slower it will sputter; however, sputtering maintains stoichiometric control of the source material, even it is an allow. The initial sputtering rate for some elements in an alloy target is initially faster than others (light elements versus heavy elements, for instance). Since solid state diffusion is slow, the surface of the target becomes quickly enriched with the slower sputtering species, allowing for a steady-state sputtering composition that is equal to bulk composition of the source material[2]. This gives sputtering a large advantage over evaporation techniques. Different vapor pressures of different alloying elements make maintaining composition difficult in alloy systems. The sputtering gas pressure is also critical for producing fast growth rates. As depicted in Fig 5.3[1], there is an optimum pressure for producing a fast sputter

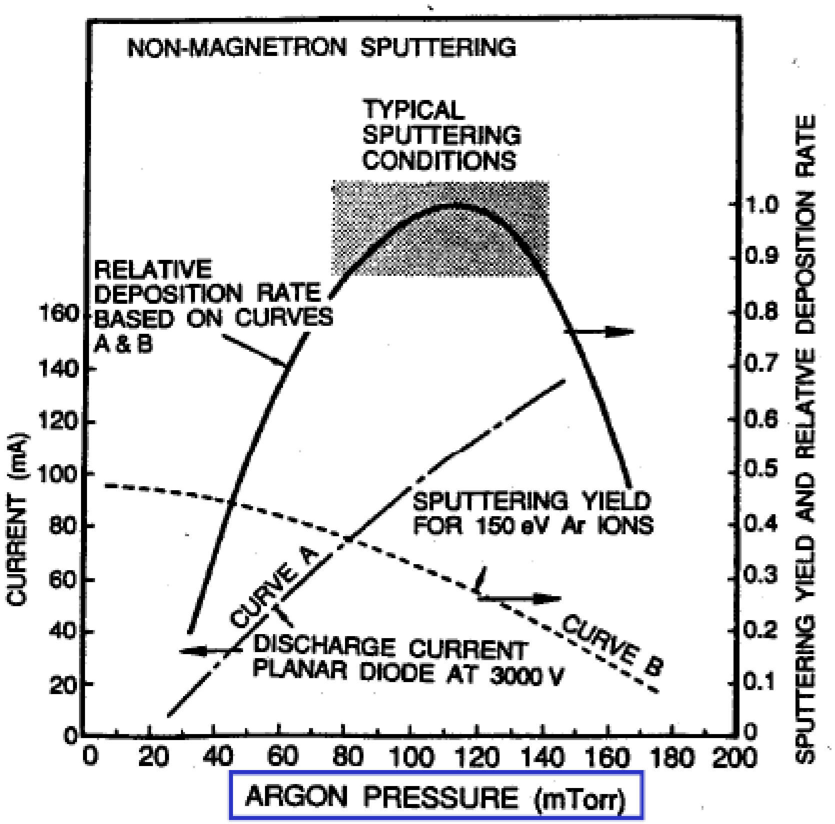

Figure 5.3 Adapted from ref[1]**|** Sputtering rate as a function of sputtering gas (Ar) pressure growth rate. Increasing the Ar pressure in the system lowers the means free path of any electrons ejected during the ionization process. This increases the ionization efficiency, as this leads to more collisions, creating more ionization (avalanche process). More ionized gas typically means a higher deposition rate. However, if the argon pressure is too high, then there are too many collisions, namely between the sputtered clusters of atoms and sputtering gas/ions. Therefore, it is important to optimize the Ar pressure in the system for an ideal growth rate. Most sputtering systems take advantage of magnets to ignite and sustain a plasma near the target material, allowing for faster deposition rates. In this configuration, a magnet is placed in the source material gun. The magnetic fields from this ferromagnetic confine and localize the plasma electrons to close to the gun (source material) via the Lorenz force.

The sputter deposition system used in this thesis is described in Fig. 5.4[4–6]. The system is equipped with four sputter sources (guns), capable of depositing four different materials in a single pump down. The system is pumped down using a combination of a rough pump and a turbomolecular pump, allowing pressures as low as $3x10^{-7}$ torr. Two liquid nitrogen old traps can be used to condense vacuum impurities and lower the pressure further to $< 1x10^{-7}$ torr. The system base pressure can be reduced even further by using spare guns as “getters.” Highly reactive metals, such as Ta, Ti, Gd, can be ignited (see below) and reactively sputter with native oxygen impurities in the chamber. This is estimated to drop the pressure to $\sim 7x10^{-8}$ torr.

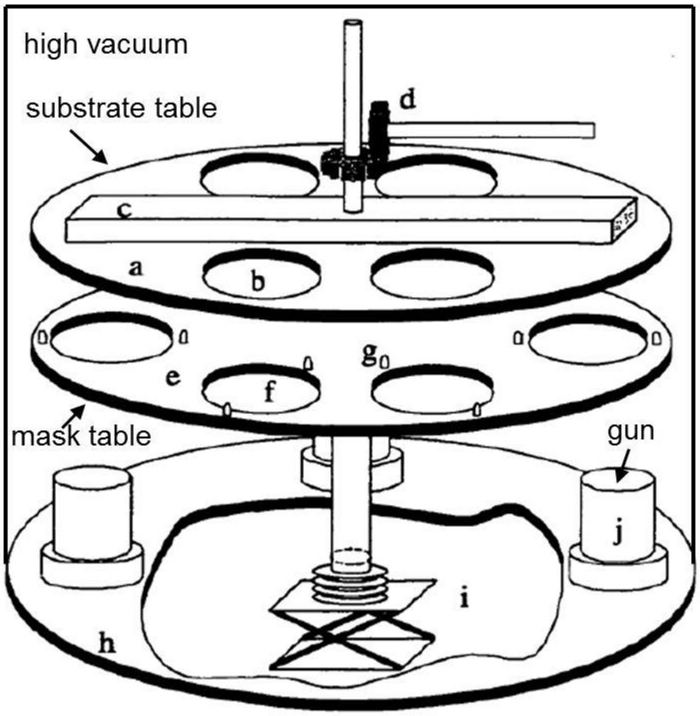

Figure 5.4 adapted from ref[5] **|** Modified sputter system designed by Sputtered Films Inc. a) substrate holder table, b) window for mounting substrates, c) liquid nitrogen reservoir, d) sample table rotation gears and motor assembly, e) mask changer table, f) window for mounting masks, g) alignment features for connecting mask and sample tables, h) sputter chamber floor, i) cutaway showing scissor jack and bellows for training and lowering the mask assembly, j) sputter chimney

Ar (99.999% purity) is used as the sputtering gas. Ar is flowed into the chamber at a constant rate of 30 scc/m, and the pressure of Ar in the chamber varies between 3.0-3.5 mTorr depending on the material being deposited. All sputtered metals in this thesis are DC sputtered with pure Ar and metal oxides are DC sputtered with a background partial pressure of O_2 (99.993% pure). In this case, the O_2 flow rate is typically 3.0 scc/m, producing 0.05 mTorr of O_2 pressure. the oxygen reacts at the substrate with the metal to form a metal-oxide[7]. Two guns in the sputter system are planar guns and two guns are "SFI" guns. Nobel metals and most non-magnetic materials are deposited using the planar guns. Magnetic materials are typically deposited with SFI shaped guns, as the magnetic flux in the gun allows for better magnetic properties. One planar gun can be connected to a RF supply in order to sputter insulating or semiconducting targets (see Fig. 5.1).

On each gun is a cylindrical chimney (see Fig. 5.4j). The chimney localizes the sputtered material flux directly above each gun. At the top of each chimney is a pneumatically actuated shutter, which can be opened or closed to control the substrates exposure to the gun and sputtered material. Substrates are mounted on magnetic samples holders, which aids in growing magnetic materials. The sample holders are placed face-down on the substrate table (Fig 5.4a). As many as four different material systems can be grown at once. The temperature of the substrates can be controlled using a liquid nitrogen reservoir located on the substrate table (Fig. 5.4c). Below the substrate table is the mask changer table. Windows in the mask changer table (Fig. 5.4f) can be closed or opened by inserting custom metal masks into the windows. By rotating the mask changer table relative to the substrate holder table, one can cover or expose individual substrates.

Samples are be deposited in two methods: rotational mode and stationary mode. In rotational mode, the substrate table (and mask changer table) are rotated at ~0.58 Hz over each gun using a motor and gear assembly (Fig. 5.4d). In stationary mode, the each individual substrate is placed over the desired gun. This produces a sputter rate ~7 times faster than rotation mode. However, sputtering in rotation mode provides much better thickness uniformity across the film and allows for sub-nm control of thickness. All materials in this thesis are sputtered in rotation mode except for Au contact pads, where precise control of thickness is not necessary.

Sputter deposition are calculated from pre-grown calibration samples. Calibration samples are grown in stationary sputter mode for fixed amount of time. Using x-ray reflectivity, the thickness is precisely determined and a rate (nm/min) is calculated by dividing the total thickness by the total deposition time. Sputtered samples are grown on p-type Si (100) substrates with 50nm of thermally grown oxide. Ta, Co, Gd, Au, Pt, and Tb are grown in rotation mode under 3.0 mTorr or Ar pressure and have calibrated sputter rates between 1-3 nm/min. GdO_x films are grown with 3.0 mTorr of Ar pressure and under .05 mTorr of O_2, producing a slightly higher sputter rate.

All sputtered metallic films in this thesis use Ta and a buffer or adhesion layer between the SiO_2 and the metal layer to avoid flaking off of material. An appropriate buffer layer material can be selected by examining an Ellingham diagram (see Fig 5.5[8]). An Ellingham diagram plots the free energy of a reaction (ΔG) as a function of temperature. In this case, we are interested in the free energy of formation of an oxide, since we are depositing metals on an oxide (SiO_2). Typically the free energy of formation of an oxide is negative, so $\Delta G = 0$ is usually plotted at the top of the diagram and all number are negative. Standard Ellingham diagrams assume atmospheric pressure. As you can see, most curves slope upwards ($\Delta S < 0$), because a solid phase (metal) is reaction with a gas phase (O_2) to produce a solid phase, reducing the entropy[2]. Reactions at the top of the Ellingham diagram are more noble (Pt, Au, etc). Reactions at the bottom of the diagram are much more difficult to reduce. Therefore a given metal can reduce any oxide that is above it on the Ellingham diagram. When selecting a buffer or adhesion layer, it is important to pick one that oxidizes more easily than Si. For this reason, we use Ta. Ta deposited on SiO_2 will become oxidized, creating an oxide-oxide interface with $Si0_2$ and a metal-metal interface with any noble metal deposited above it. This is ideal for buffer layers.

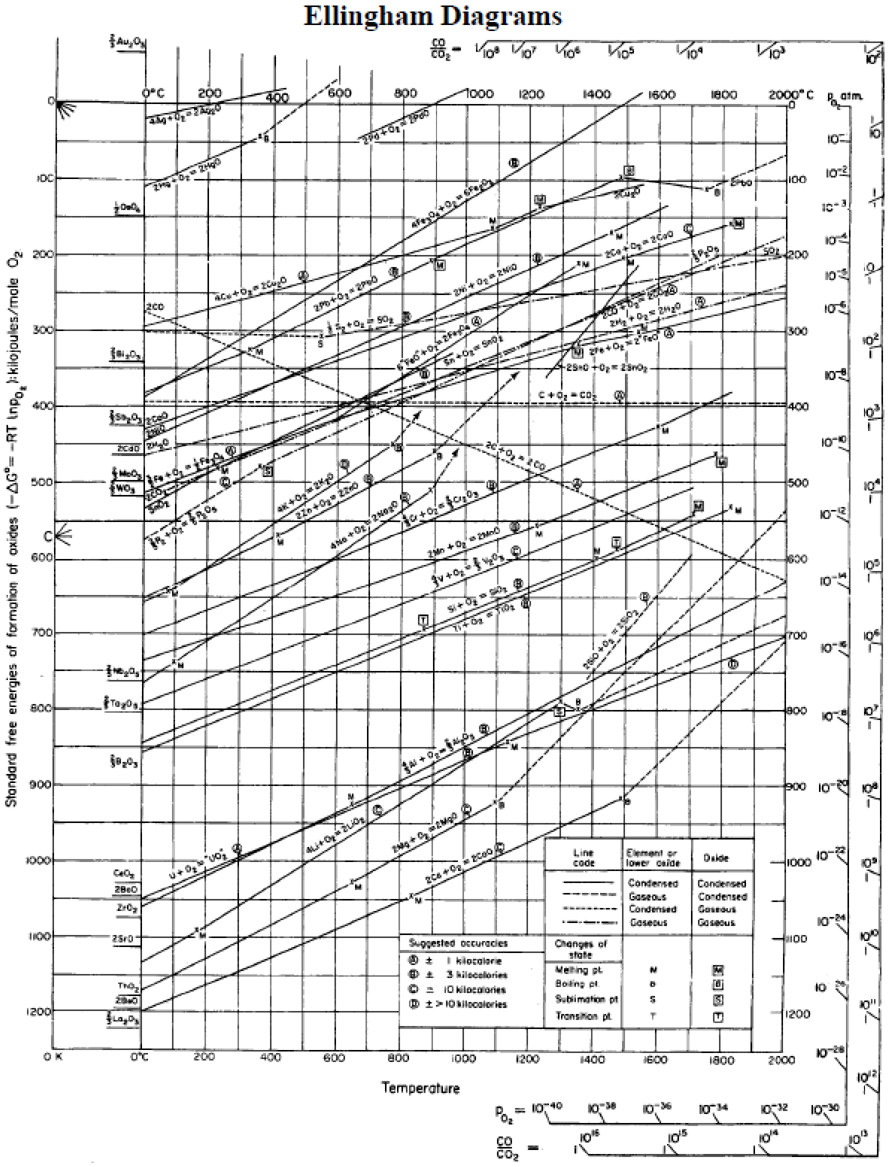

Figure 5.5 | Ellingham diagram[8] showing free energy of oxidation.

Pulsed Laser Deposition

Garnet magnetic materials in this thesis were grown using an epitaxial technique called pulsed laser deposition (PLD) by Caroline Ross' group at MIT. PLD is a physical vapor technique that combines several advantages (and disadvantages) of molecular beam epitaxy and sputtering[9]. In PLD, a focused laser is pulsed onto a target material. For sufficiently high laser fluence, the laser will vaporize or ablate the target material. A plasma plume is ablated material is then directed towards a substrate, where it is deposited[9,10]. PLD offers several advantages over sputter deposition. It allows for epitaxial growth and stoichiometric control from target to substrate during deposition. During deposition, laser conditions are chosen such that the ablated species are primarily atomic or diatomic species (not clusters of atoms). This is achieved by using UV light and by using nanosecond length pulses.

Stoichiometric transfer of atoms is possible because the ablation process is not an evaporation process[10,11]. In other words, the laser fluence is chosen such that the target material receives significantly more energy than that required for evaporation. The ablated species absorbs the material and becomes a plasma. Since the vaporization is not an evaporation process, is does not depend on the vapor pressure of the constituent atoms.

There are a few disadvantages to PLD. 1) Because the plume of ions created is very direction, film uniformity can be an issue[9]; however, this can be helped by ablating the target material in an array, rather than in one stop[9]. 2) This is a very high energy process, and high energy cations depositing on the surface of the substrate could damage or strain the substrate itself through defect formation, which can be problematic for epitaxially grown films.

Polycrystalline thin film growth

Sputter deposition typically results in a polycrystalline or amorphous film. Grains in the material form from nucleation, growth and coalescence of clusters of atoms arriving at the substrate surface. The types of grains formed can be described by basic structural zones and are a function of many deposition and materials parameters, such as bombardment energy, substrate temperature, and material grain boundary mobility[12,13]. The most commons zones are described in Fig. 5.6 for various Ar gas pressures and substrate temperatures T_S (relative to melting temperature T_M). Zone 1 occurs when the substrate temperature is low, $\frac{T_S}{T_M} < 0.1$. Here, the substrate temperature is low enough where surface diffusion of adatoms is negligible[2,12,13]. Columnar growth of grains occurs in combination with showing, resulting in cone like formations and voids and defects in the film. Cone formations typically occur in thicker films (>20nm in metallic systems). This is indicative of dome like structures on the surface of the film. Zone T[2,12,13] (a transition zone) is similar to Z1. It occurs when $0.1 < \frac{T_S}{T_M} < 0.4$. Here, columnar growth still occurs, but no domes or voids are present. At higher substrate temperatures, $0.4 < \frac{T_S}{T_M} < 0.7$, Zone 2 growth occurs. Here, surface diffusion is significant, and the film forms with tight grain boundaries. The size of the grains increases with increasing temperature. Facets form on the surface of the film. When $\frac{T_S}{T_M}$ is between 0.6 and 1, Zone 2 growth occurs[2,12,13]. Here, equiaxed grains form. In thin films, such as those in this thesis, the grain size is on the order of the film thickness, where bulk, surface and grain boundary diffusion are high[2,12,13].

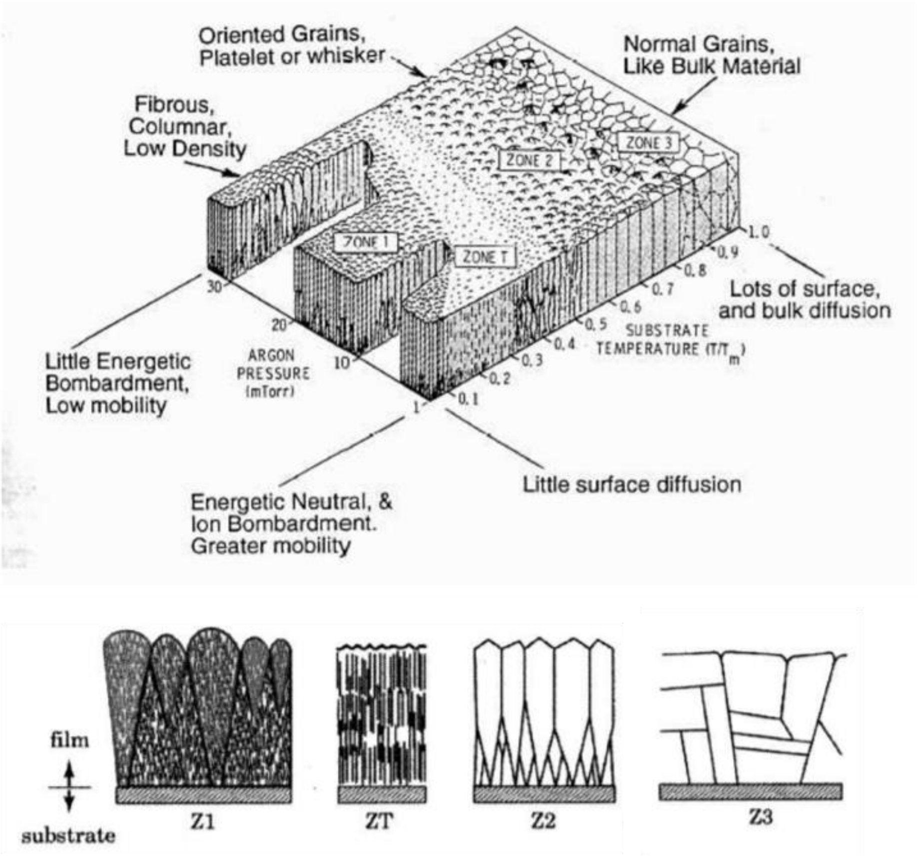

Figure 5.6 adapted from[12,13] **|** Thin film growth zones as a function of samples temperature and a sputtering gas pressure

In summary, grain size in films in determined by the mobility of atoms on the surface. And the mobility is a function of the substrate temperature, the bulk and surface diffusivities, and the bombardment energy (Ar pressure). Z1 films typically have very high porosity, leading to high resistance and poor optical properties. But these films are advantageous for sensor applications and catalytic applications. In the deposition system used in this thesis, the substrates are not heated, however heat does accumulate in the vacuum system from the energetic process itself. In general, we expected polycrystalline films with ZT or Z2 type microstructure. Post-processing can also change the grain structure of the film. Annealing the film will cause grain coarsening, enlarging the grains, and effectively rendering Z3 type microstructure.

Microstructure has a large impact on the magnetic properties of the sample[14]. Spin textures, such as domain walls and skyrmions get pinned at material (and hence magnetic) non-uniformities and defects[14].

5.2 Lithography

Following deposition, patterning the resulting materials into devices is often necessary to characterize on the sample or stimulate the sample (for example with a current or voltage). There are a variety of tools in the researchers toolbox that can be used to achieve this depending on the size of the structures needed and materials requirements. Among these are photolithography (laser writing and mask) and electron-beam lithography. Each of these lithographic steps can be done via a process known as “lift-off,” or via ion milling.

Photolithography

Photolithography is a very analogous process to film photography. The word *photograph* comes from the Greek photo, meaning light and *graphos* meaning writing. Photography literally means “writing with light.” The film in photography coated with an emulsion that is sensitive to light[3]. This emulsion contains microcrystals of silver salts (halides). When the emulsion is exposed to light, the salt breaks down, allowing metallic silver to form. More exposed light results in more metallic silver. The film is then put into a developer to speed up the reaction causing metallic precipitate to form, and then is neutralized by placing in an acidic bath.

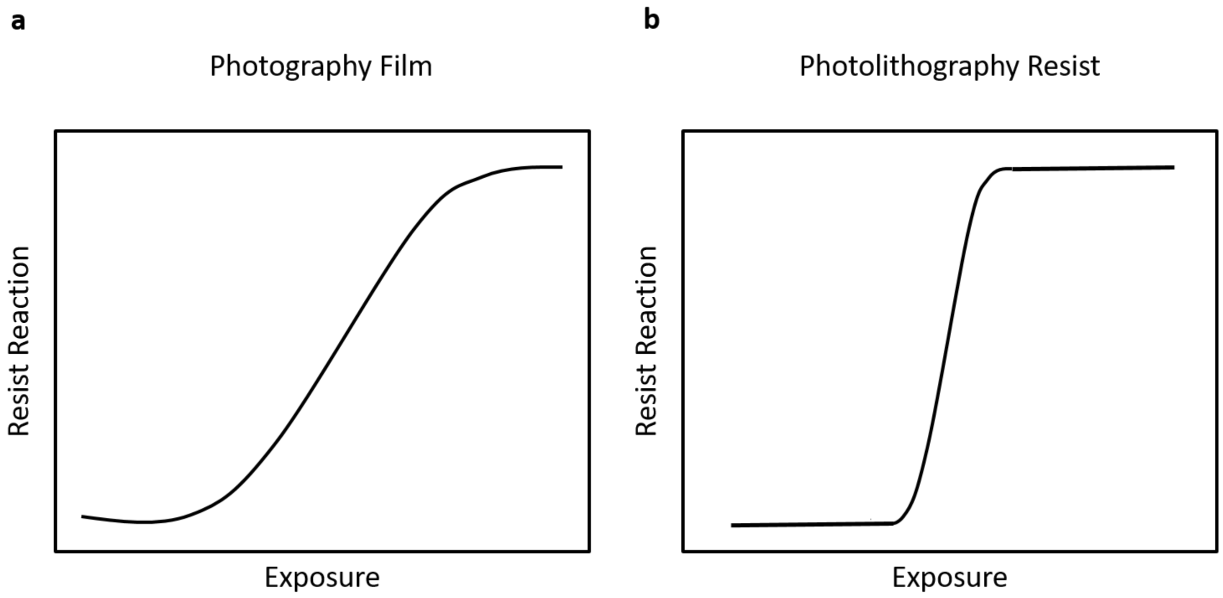

Figure 5.7 | Light exposure to photographic film (a) is proportional to the amplitude of exposure, providing grey-scale in the image, whereas photolithography resist (b) has a sharp transition to full exposure, giving features sharp edges.

In photolithography a photoactive polymer called a resist is coated on a wafer. Exposure to UV light causes exposed areas of the resist to become more soluble (positive resist) or become less soluble (negative resist)[3]. Patterns can be made on the wafer by either using a pre-made mask which contains desired features printed with chrome or by using a US laser writer which rasters over designed areas of the film. The written pattern is revealed by developing the film, where the soluble part of the film is washed away. Due to its ease of use and very high throughput, photolithography is widely used both in academia and in industrial applications. Lithography is also used in screen printing of apparel and signage, where different types of "resist" materials are used. Because this process uses UC light, the smallest features sizes achievable are on the order of

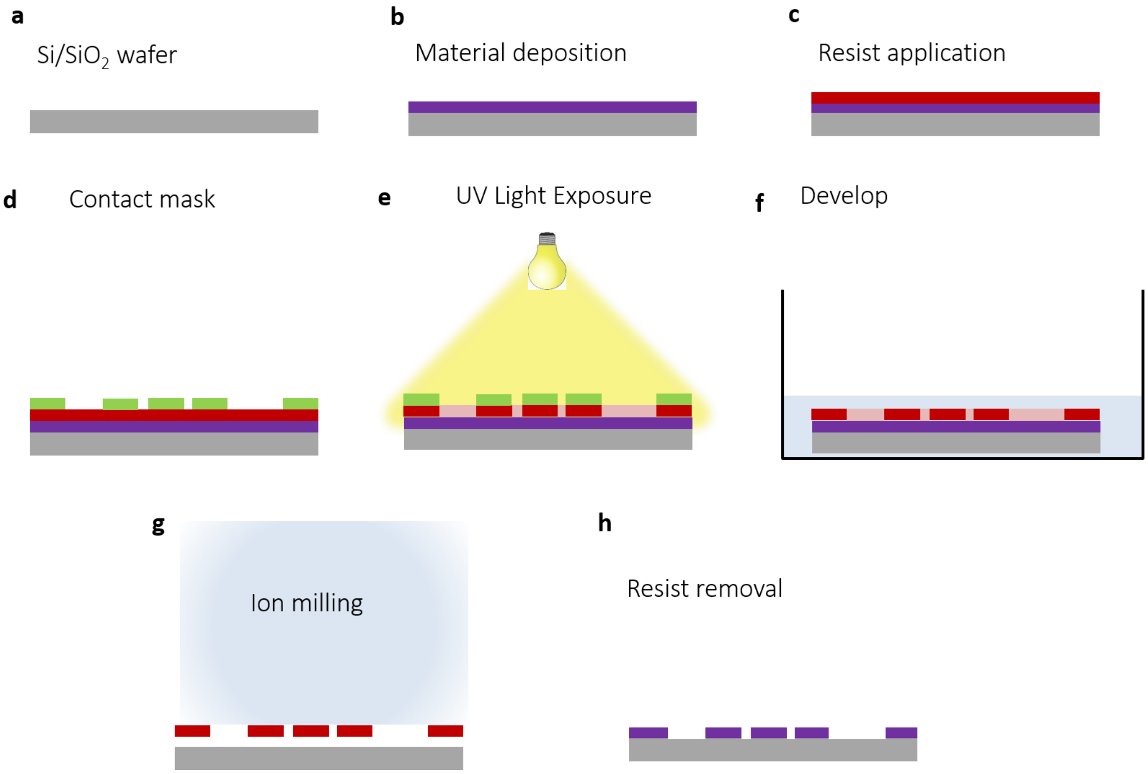

Figure 5.8 | Patterning devices via ion milling. Material is already deposited on a Si/SiO$_2$ wafer (a,b). c) Photoresist is coated on the sample. The sample is then exposed to UV light through a contact mask (d,e). After developing (f), undesired areas of the film are exposed to Ar plasma (g), which mills away mater. Excess resist is then removed (h), revealing the desired structure.

$\sim 1 \mu m$. As shown in Fig. 5.7a, the emulsion in photographic film is designed such that the more light that hits the film, the further the reaction progress. This results in a gradient of exposure, giving the photographic image grey-scale. This is an undesired effect in photolithography of microscale devices, where very sharp edges are required. The chemical reaction that causes polymer hardening (or softening) for photolithographic resist depends primarily on the energy of light, not the amplitude of the light the resist is exposed to. This creates the very sharp edges needed for patterned devices, see Fig 5.7b. The majority of samples made in this thesis used mask photolithography. Electron beam (e-beam) lithography is used when features smaller than $1 um$ are needed. A focused electron beam is used to write patterns on an electron-sensitive film. Here, the electrons modify the resist similar to how UV light modifies the photoactive resist. Electron beam lithography can define features with much higher resolution ($< 10nm$); however it is a costly process that has significantly lower throughput. Samples patterned using e-beam lithography are noted throughout the thesis.

Samples can be patterned before or after material deposition. Most samples require two patterning steps: the first for patterning the magnetic devices and the second for patterning contacts pads. In the first step, the samples are patterned after materials deposition, and the second step (contact pads), the sample is patterned prior to materials deposition. This requires two different procedures to remove the unnecessary material from the samples. Fig. 5.8 shows the fabrication steps for the first of these procedures, ion milling. In ion milling the resist is coated on a sample

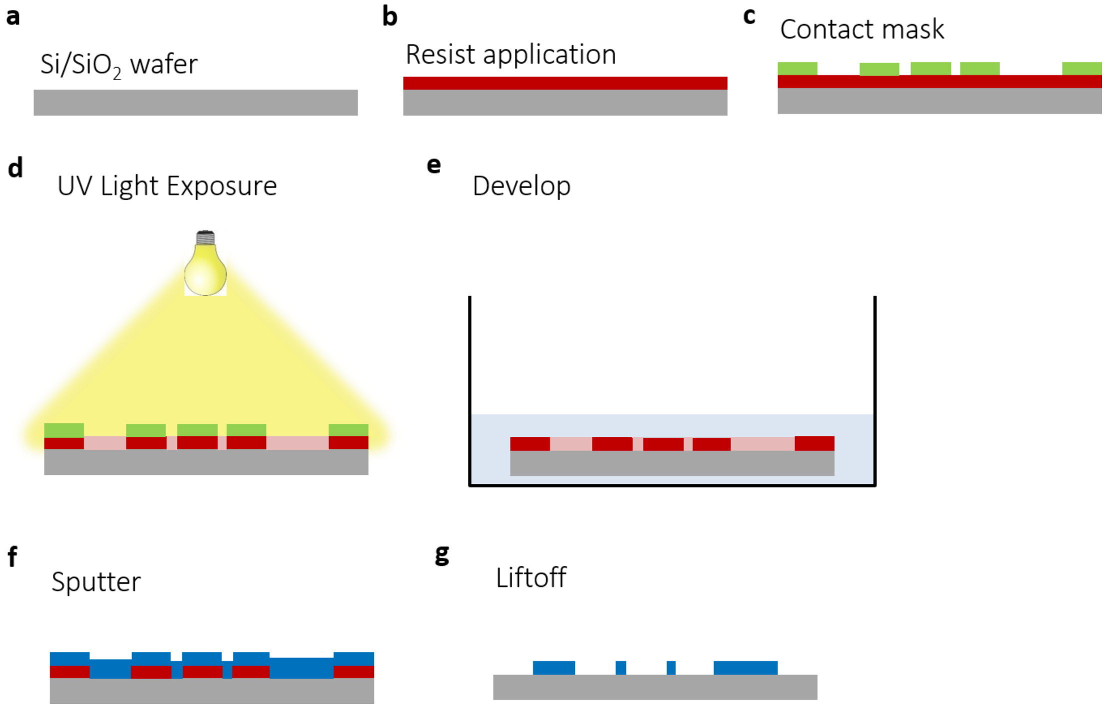

Figure 5.9 | Patterning devices via liftoff. Resist of coated on a Si/SiO$_2$ wafer (a,b). c) The sample is then exposed to UV light through a contact mask (d,e). After developing (f), material is sputtering onto the film (f). Areas with resist gaps are filled with desired materials. Excess resist is then removed (g) via liftoff, revealing the desired structure.

with the desired material already deposited. In this process, the resist that remains after exposure and development will protect desired areas of the film. The patterned film is then placed in an ion miller, where a plasma (typically Ar) mills away at the film, leaving behind only protected regions.

Alternatively, a process called liftoff can be used (Fig 5.9). During liftoff, material is deposited after the resist is coated on the sample. Deposited material fills in the gaps of the developed resist. The resist is then washed away using a process called "liftoff." It can be very difficult to achieve very small feature sizes using liftoff when sputtering. As sputtering is a conformal deposition technique, the sidewalls of the resist will be coated[2] (See Fig. 5.9a), meaning that the lift-off chemical must penetrate through this sidewall to reach and dissolve the polymeric resist. This usually limits the thickness of a sputtered materials to $< 200\ nm$[3], otherwise list-off can be very difficult. Lift-off has the advantage of taking less process steps to complete. Moreover, ion milling can lead to significant heating of the sample, potentially causing unwanted annealing.

In this work we use ion milling to pattern magnetic features and lift off to pattern contact pads. Opposite polarities of photomask is used so that the same kind of resist can be used for both layers. First, the wafer is heated for $1\ min$ at $100^{o}C$ to remove any excess water on the sample. The sample is then washed with acetone and IPA for $\sim 15\ sec$ each. Following these cleaning steps, the sample is spin-coated with $700 - 800\ nm$ of SPR-700 photoresist. A rotation speed of $\sim 4.5\ krpms$ is needed to achieve this thin thickness of resist. The coated wafer is then heated on a hotplate at $100^{o}C$ for $90\ sec$. This causes the resist to spread more uniformly on the wafer, and also hardens the resist. The low temperature chosen here is to prevent undesired annealing of the underlying metallic/oxide layers. After hardening, the sample is exposed to UV light for $10\ sec$ using Kar; Suss model MA-4 mask aligned. Following exposure, the sample is developed in CD-26 for $\sim 1\ min$. After liftoff (or ion milling), excess resist not removed chemically can be removed via a de-scumming process called "ashing," where an oxygen plasma at ~50W burns away any residual polymer.

5.3 Magneto-optical Kerr effect

Principles of Operation

Probing the magnetization state of a thin film very locally and very quickly is a powerful tool in spintronics research. The magneto-optical Kerr effect (MOKE) allows for such measurements. Moreover, MOKE is a very versatile technique that can probe monolayers of magnetic material, making it a popular technique for measuring ultra-thin magnetic films. This is in contrast to vibrating sample magnetometry (VSM), which is a non-local, volume averaged technique and requires a relatively large total volume of magnetic material to produce a signal. The disadvantage of MOKE is that it does not provide a quantitative measure of the sample magnetisation.

During MOKE, linearly polarized light is incident on the magnetic sample. Reflected light from the magnetic sample will have a rotation of polarization (Kerr rotation) and slight ellipticity (Kerr ellipticity)[15]. The extent of the Kerr rotation is proportional to the magnetisation of the sample in the direction of the incident light[16]. The reflected light passes through a second polarizer (the analyzer), which is set nearly cross polarized to the first polarizer. The light is then sent into a photodetector, where the voltage on the diode is proportional to the light intensity. This results in an optical setup that is very sensitive to the Kerr rotation angle, where the light intensity is proportional to the thin films magnetisation component in the direction of the light. Mathematically, the Kerr intensity takes the form[17]:

$$I = I_0(\delta^2 + 2\delta\Phi') \qquad 5.1$$

where I is the Kerr intensity. δ is a small angle the analyzer is set off cross polarized with the incident polarizer. Φ' is the Kerr rotation. Instead of an analyzer, a quarter wave plate can be used. In Eq. 5.1, Φ' is replaced by Φ”, the Kerr ellipticity[16],

$$I = I_0\left(\delta^2 + 2\delta\Phi''\right) \qquad 5.1$$

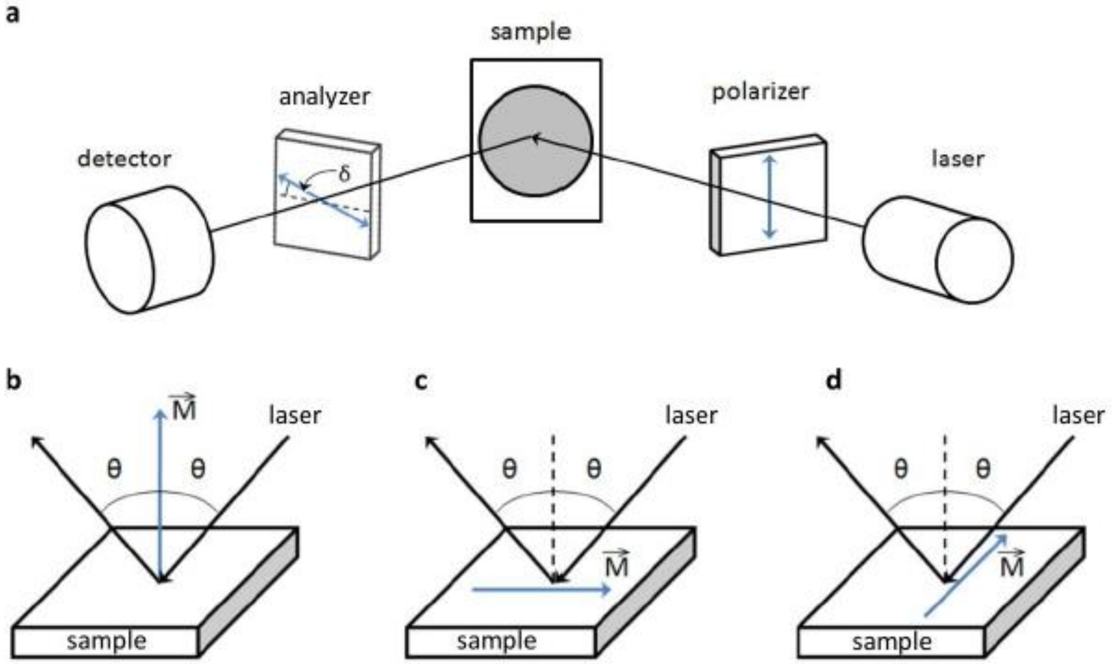

Figure 5.10 adapted from ref | a) Typical MOKE setup. Linear light is incident of the sample surface. Reflected light has a Kerr rotation (ellipticity) proportional to the magnetization of the sample. A crossed polarizer (quarter wave-plate) acts as an analyzer to detect the Kerr rotation (ellipticity).

A hysteresis loop can be measured by sweeping the field and measuring the resultant Kerr intensity. The Kerr intensity can also be dependent on the material and the wavelength of light used, in addition to the polarization and ellpticity of the sample. MOKE is considered a surface technique (commonly referred to as surface-MOKE, SMOKE) and is only sensitive the skin depth of the light used, $\sim 10\ nm$. A typical laser MOKE setup is depicted in Fig. 5.10a[18]. If instead of a laser and diode, a wide-field light source and a CCD camera is used, one can probe the 2D surface magnetisation of the sample.

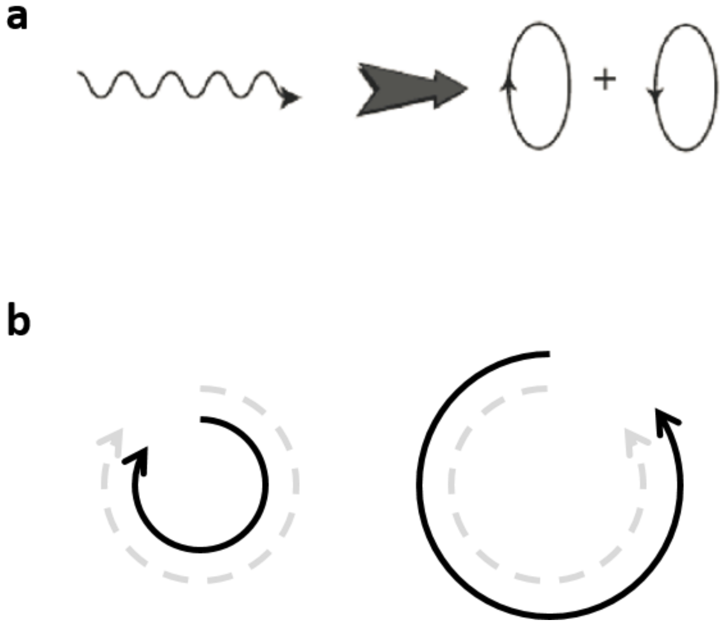

Figure 5.11 | a) Linearly polarized light shown as a superposition of equal amounts of right- and left- handed circularly polarized light, adapted from ref[19]. b) Magnetic materials have spin dependent absorption of light, leaving reflected light have unequal amount of right- and left-handed circularly polarized light, superimposed, results in a rotation of the linearly polarized light.

Physically, MOKE can be conceptualized as spin-dependent absorption of light, driven by spin-orbit coupling[20]. Linearly polarized light is a superposition of left- and right-handed circularly polarized light (see Fig 5.11a), where each photon has angular momentum of either $L = +1$ or $L = -1$. These photons can excite electrons in individual subbands ($S = +\frac{1}{2}$ majority band or $S = -\frac{1}{2}$ minority subband[6]. In a magnetic material (or a material with a magnetic field applied), the minority and majority subbands are not degenerate. There are more of one type of spin in the ground state. This leads to preferential absorption of one type of circularly polarized photon relative to the other. Essentially, right- and left- handed circularly polarized light effectively have different indices of refraction. Thus, the reflected light has an imbalance of left-left and right-handed circularly polarized light, a makeup different than the incident light[19,21] (Fig. 5.11b). The superposition of these photons is linearly polarized light that is rotated relative to the incident light.

MOKE is performed one of three modes: 1) polar (Fig. 5.10b), 2) longitudinal (Fig. 5.10b) and 3) transverse (Fig. 5.10b)[18]. longitudinal MOKE and transverse MOKE are used when the magnetisation orientation in in the plane of the film. Here, the incident light is typically at 45^{o} in order to probe the in-plane component of the magnetisation. In polar MOKE, the light in parallel to the fil, normal, so that magnetisation perpendicular to the plane can be probed. MOKE is proportional to the square of the refractive index of the film, so polar MOKE typically produces signal that is an order-of-magnitude higher than in the in-plane modes. All samples in this thesis have perpendicular magnetisation, so polar MOKE will be the primary optical probing technique used.

In-situ, time-resolved focused MOKE/ MOKE microscope

Probing the dynamics of domain walls and chiral spin-textures requires high temporal and spatial resolution MOKE. To accomplish this, we have built a time-resolved focused scanning MOKE with MOKE microscope capabilities[22]. The basic setup is shown in Fig. 5.12. In addition to the standard polar MOKE setup, a scanning focused MOKE includes an objective lens to focus the laser to a spot size of $\sim 5\ \mu m$. The laser power can be varied from 25 to $< 1 mW$. In addition, the sample is mounted on a 3-axis motorized stage with stepper motors providing <1 μm resolution. This allows for probing the magnetisation very locally on the samples and on small lithographically defined magnetic features. A custom built pre-amp and high bandwidth photo diode detector is used to achieve sub-ms time resolution and high signal-to-noise ratio, critical for measuring domain wall dynamics. The setup also includes a wide-field light source, with three light colors/combination (red, blue, and white), and a CCD camera with in-line polarizers and a wave-plate, providing MOKE microscopy capabilities.

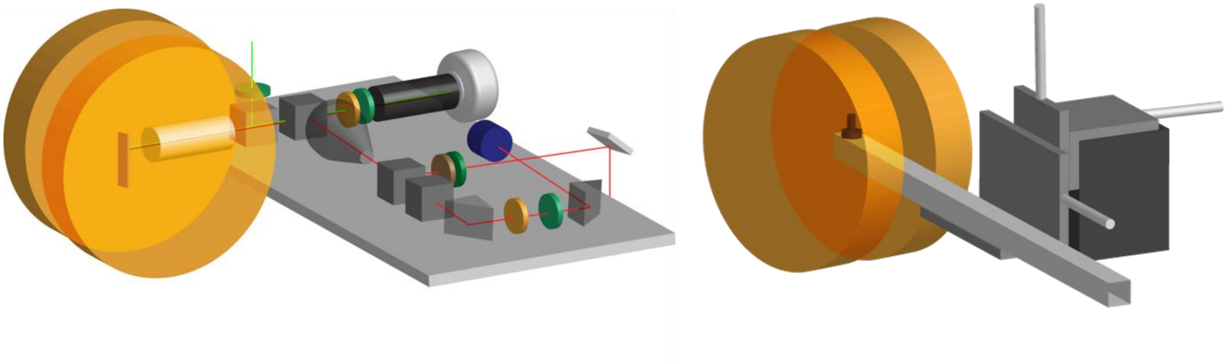

Figure 5.12 | Custom-built Kerr microscope with independent out-of-plane and in-plane field control and an integrated flow cryostat for temperature control

The setup has independent in-plane and out-of-plane magnetic field control. Out-of-plane fields can reach up to $2000\ Oe$ with ms rise times, while in-plane fields can reach up to $10{,}000\ Oe$ with sub $1\ s$ rise times. The out-of-plane electromagnet is an air coil with no core, so that magnetic field is proportional to current. The in-plane electromagnet has an iron core and is controlled via a magnetic field-feedback system to precisely control the field within $1\ Oe$. The temperature can be controlled via a custom built flow-cryostat with an optical via port to allow for MOKE access. Dry nitrogen gas is cooled with liquid nitrogen and is then passed through a small gas oven before entering the sample chamber. The temperature can be feedback controlled between $-120°C$ and $120°C$ with $\pm 0.1°C$ precision with a thermocouple placed adjacent to the oven output. The sample temperature is monitored with a second K-type thermocouple places adjacent to the sample.

Electrical contact is made to the sample via a custom printed circuit board (PCB) waveguide that was designed to provide high-bandwidth electrical stimulation to the sample. The sample is wire bonded to a chip carrier which is connected to the PCB. DC currents and voltages were applied via a Keithy 2400 source-meter. A custom-built, $45V$ $600ps$ risetime pulse generator was designed for high bandwidth, high voltage experiments. Custom designed LabView programs were used for data acquisition and signal generation.

Differential Kerr microscope images are taken using a custom algorithm developed in LabVIEW. A reference/background image is taken using the CCD camera. This can be averaged over an arbitrary number of frames, but most images in this thesis are averaged to 8 frames. The references frame average is then subtracted from all incoming frames and amplified with a gain. Exposure times as low as 0.5 ms can be acquired. All MOKE images in this work are differential MOKE images.

Measuring domain wall dynamics

To measure DW dynamics in magnetic thin films, the films are patterned into a domain wall racetrack geometry, shown in Fig. 5.13a. The grey features are the magnetic device. Patterned over the devise are contact pads. A metallic strip line is overlaid perpendicular to the magnetic devise, where a large current pulse can nucleate a DW via Oe field generation. A driving force can then be used to drive the DW down the racetrack devices. The driving force can be an in-plane current or an out-of-plane magnetic field. Magnetisation reversal is detected by a ~ 5 μm focused laser positioned at a fixed distance away from the nucleated DW with a 3-axis scanning stage. Exemplary MOKE transients are shown in Fig. 5.13b for a Ta4/Pt3/Co0.9/GdOx6 (thickness in nm) sample with perpendicular magnetisation. Each transient is an average of ~100 transients. The reversal time $\left(t_{\frac{1}{2}}\right)$ is the when the probability of magnetisation reversal is 50%. $t_{\frac{1}{2}}$ is measured at various distances away from the DW nucleation line. The sharp transition is indicative of a repetitive process. The DW velocity is measured by measuring DW propagation transients at a series of positions away from the DW nucleation site and plotting the transient time as a function of distance. Fig. 5.12c shows an example of the velocity extracted from the transients in Fig. 5.12b.

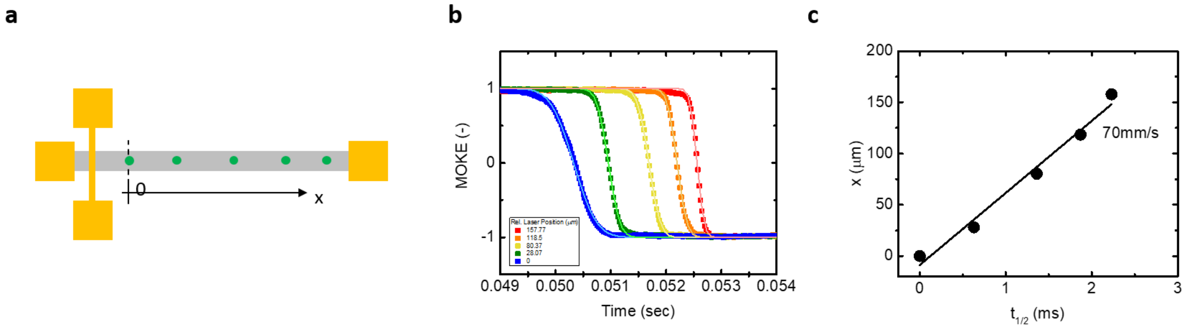

Figure 5.13 | a) schematic of magnetic device used to nucleate and drive DWs. Overlaid metallic stripline acts as an Oe field generator to nucleate a DW. b) DW transients corresponding to laser positions indicated in (a) in green. c) $t_{\frac{1}{2}}$ measured at various distances away from the DW nucleation line. The slope of the curve is the DW velocity, $\sim 70\,\frac{mm}{s}$

5.4 Vibrating Sample Magnetometry

Vibrating Sample Magnetometry (VSM) is a very common technique to measure the magnetisation of a sample[23]. VSM relies of Faraday's law of magnetic induction $\left(V \sim \frac{d\Phi}{dt}\right)$, where a changing magnetic field induces a voltage in a nearby coil. A magnetic sample is placed on a Pyrex or quart sample holder and vibrated at a fixed frequency typically between $60-100\ Hz$. The vibrating sample is placed between a pair of pickup coils that can sense the magnetisation of the vibrating sample. The induced voltage in the pickup coils is directly proportional to the component of the magnetisation in the sample parallel to the normal vector of the coil. The linear scale factor can be calibrated with a reference samples of known magnetisation. A standard VSM is equip with a large electromagnet. By ramping the field and measuring the magnetisation, a hysteresis loop can be obtained.

Thin films can be particularly hard to measure via VSM, as the total volume of magnetic material is small. For thin magnetic films of $< 1\ nm$, stacking individual pieces of film can be used to increase the total signal. For reference, the VSM used in this thesis has a sensitivity of $\sim 5\ \mu emu$[23]. The temperature can also be varied using a similar flow cryostat as the MOKE system. The VSM has a temperature range of $-190^{o}C\ to\ 200^{o}C$. As opposed to MOKE, VSM is one of the few techniques that directly measures the magnetisation of the sample.

5.5 X-ray imaging

Imaging with x-rays, rather than visible light offers a number of advantages. In particular, image spatial resolution can be significantly better, approaching $5 - 10\ nm$. Moreover, x-ray imaging is element specific, allowing the user to probe individual elements or sublattices. As explain in Section 3, and illustrated in Fig. 5.14, magnetic materials contain an imbalance of majority and minority spins. This leads to a different density of states at the Fermi level for spin up and spin down electrons. When x-rays are incident on the sample core electrons (typically from the p orbitals) are excited into empty states at the Fermi level. Since right- and left- handed circularly polarized light will be absorbed by different subbands, and since the density of states at the Fermi level is different for minority and majority spins, there will differential absorption of the left- and right- handed circularly polarized light (Fig. 5.14). This technique is element specific because the energy of the x-rays used can be tuned to different band edges for different materials. This method of imaging is called x-ray magnetic circular dichroism. Soft x-rays are used in this technique, with energies below $1-5\ keV$, and therefore synchrotron radiation sources are needed for this type of imaging.

Scanning x-ray transmission microscopy and X-ray holography

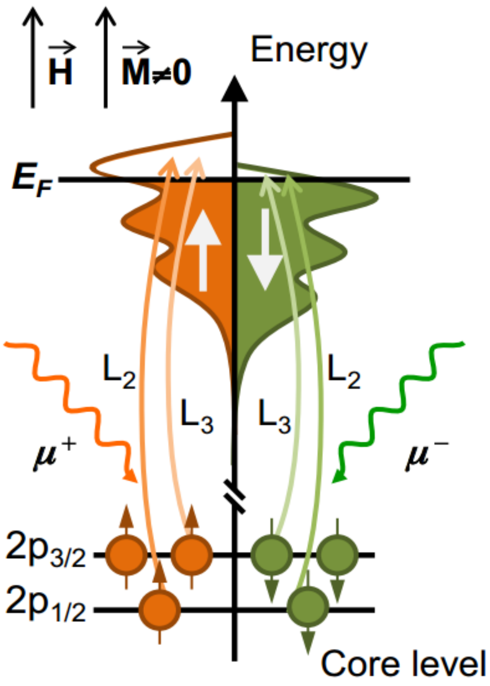

Figure 5.14 | Principles of XMCD. Spin dependent absorption of light in magnetic materials with uneven density of states at the Fermi level for spin-up an spin-down electrons.

In scanning x-ray transmission microscopy (STXM), x-rays of a specified energy are focused onto a magnetic samples using a zone plate (an x-ray lens) from a synchrotron x-ray source. State of the art zone plates can focus x-rays down to $\sim 20\ nm$.[24] The small x-ray spot is then rastered across the sample. In most systems, the x-ray beam location remains fixed, and the sample moves relative to the x-ray beam. Samples can be manipulated and stimulated with magnetic fields and voltages. X-ray transmitted through the sample are detected by a soft-x-ray sensitive CCD camera. Unlike MOKE, this is a transmission experiment. Since there are no true "x-ray transparent" materials, the magnetic material must be grown on membrane windows no thicker than $100nm$. In this thesis, materials are grown on SiN membranes that vary between $100-150\ nm$ thick, unless noted elsewhere. An x-ray setup schematic is shown in Fig. 5.15a. Notably, STXM suffers from drift during image acquisition, and many applications, including some in this thesis, require sub 10 nm resolution, making this technique not useful.

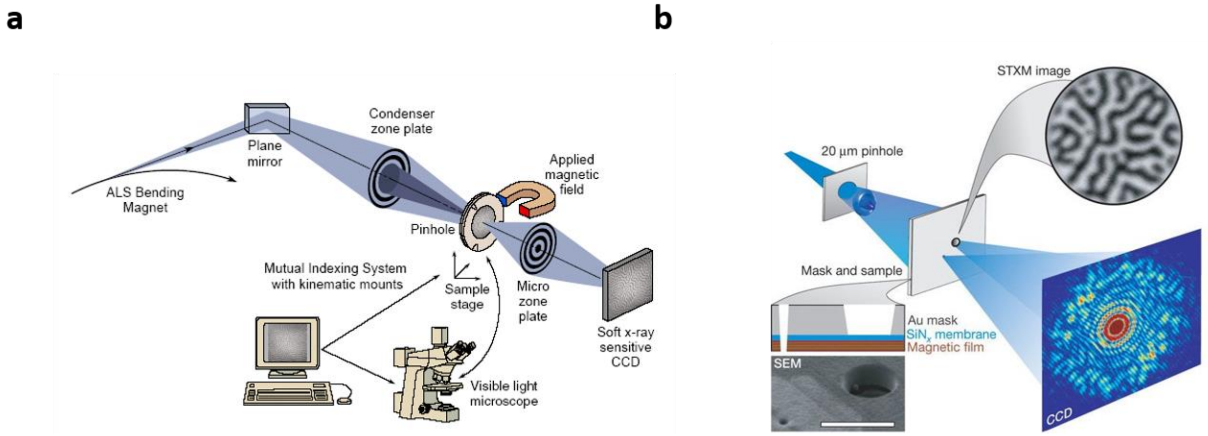

Figure 5.14 | | a) Schematic of a scanning transmission x-ray microscope. Coherent, soft, circularly polarized x-rays are focused and rastered onto a sample via a zone plate. Transmitted x-rays are detected by a CCD camera. Adapted from ref[24] b) X-ray holography schematic. Coherent, circularly polarized x-rays are incident on the sample. Object apertures and reference holes are defined by a mask and a hologram is recorded by a detector. A Fourier transformation reveals the real space image of magnetic texture. Adapted from ref[27]

Another technique that uses x-rays to image magnetic textures is x-ray Fourier-transform holography. X-ray holography is a coherent imaging technique that uses no lenses[25–27]. The sample is placed behind a lithographically defined mask with a small, $< 1\ \mu m$ sized aperture and a separate hole that defines a reference beam. The interference pattern created by x-rays passing through the reference hole and the aperture can be reconstructed to reform the aperture image by using a Fourier inversion. Used in combination with XMCD, this technique is particularly powerful to image magnetic textures because it does not need a zone-plate that is conventionally used in x-ray imaging, and it is a single shot technique. Thus, there is no drift. However, this requires significant sample preparation, as all the optics need to patterned directly on the sample, requiring hours of labor at a focused ion beam tool. Moreover, the field of view is limited to $\sim 1\ \mu m$ in size, limiting the types of experiments that can be performed. A schematic of the setup is shown in Fig. 5.15b, adapted from Eibebitt *et al*[27].

5.6 Summary

Sputter deposition was used to grow metallic thin films in this thesis. Sputtering yields conformal growth of polycrystalline films. Pulsed laser deposition was used to epitaxially grow single crystal magnetic insulating garnet films. Films are lithographically patterned by either liftoff or ion milling. The patterns were written by using a UV light via a laser or wide-field sources, such as a lightbulb. Electron beam lithography was used to write patterns with features sizes smaller than 1 μm. All magnetic layers were patterned with ion milling, and all contact pads were patterned with liftoff. Magnetic samples were characterized using the magneto optical Kerr effect. A focused scanning laser with a high bandwidth detector was used for very local probing of magnetisation dynamics, whereas a wide-field course and CCD camera was used to probe the 2D surface of the magnetic film. Vibrating sample magnetometry was used to characterize continuous thin films, where an absolute value of the magnetisation is quantified. For imaging sub 1 μm length scales, soft x-ray sources are needed. XMCD was applied to scanning transmission x-ray microscopy, as well as x-ray holography to produce images where image contrast corresponds to magnetisation direction.

5.7 References

1. Ohring, M. *Materials science of thin films : deposition and structure*. (Academic Press, 2002).
2. Thompson, C. V. Sputter Deposition. (2015).
3. Plummer, J. D., Deal, M. D. & Griffin, P. B. *Silicon VLSI technology : fundamentals, practice, and modeling*. (Prentice Hall, 2000).
4. Beach, G. S. D. The cobalt-iron metal/native oxide multilayer. *University of California, San Diego* (2003).
5. Price, E. P. Characterization of transport processes in magnetic tunnel junctions. (2001).
6. Emori, S. Magnetic domain walls driven by interfacial phenomena. (2013).
7. Hollands, E. & Campbell, D. S. The mechanism of reactive sputtering. *J. Mater. Sci.* **3,** 544–552 (1968).
8. Pierret, R. F. *Semiconductor device fundamentals*. (Addison-Wesley, 1996).
9. Norton, D. P. Pulsed Laser Deposition of Complex Materials: Progress Toward Applications. in *Pulsed Laser Deposition of Thin Films* 1–31 (John Wiley & Sons, Inc., 2006). doi:10.1002/9780470052129.ch1
10. Eason, R. *Pulsed laser deposition of thin films : applications-led growth of functional materials*. (Wiley-Interscience, 2007).
11. Lowndes, D. H., Geohegan, D. B., Puretzky, A. A., Norton, D. P. & Rouleau, C. M. Synthesis of Novel Thin-Film Materials by Pulsed Laser Deposition. *Science* **273,** 898–903 (1996).
12. Thornton, J. A. Influence of apparatus geometry and deposition conditions on the structure and topography of thick sputtered coatings. *J. Vac. Sci. Technol.* **11,** 666–670 (1974).
13. Thornton, J. A. High Rate Thick Film Growth. *Annu. Rev. Mater. Sci.* **7,** 239–260 (1977).
14. Woo, S. *et al.* Observation of room-temperature magnetic skyrmions and their current-driven dynamics in ultrathin metallic ferromagnets. *Nat. Mater.* **15,** 501–506 (2016).
15. Qiu, Z. Q. & Bader, S. D. Surface magneto-optic Kerr effect. *Rev. Sci. Instrum.* **71,** 1243–1255 (2000).
16. Blundell, S. *Magnetism in condensed matter*. (Oxford University Press, 2001).
17. Bauer, U., Choi, J., Wu, J., Chen, H. & Qiu, Z. Q. Effect of step decoration on the spin reorientation of Ni films grown on vicinal Cu(001). *Phys. Rev. B* **76,** 184415 (2007).
18. Bauer, U. Magnetic anisotropy of Fe films grown on Ag(017). (University of Würzburg, 2009).
19. Spaldin, N. A. (Nicola A. *Magnetic materials : fundamentals and applications*. (Cambridge University Press, 2011).
20. Bland, A. (Anthony) & Heinrich, B. (Bretislav). *Ultrathin magnetic structures. I, An introduction to the electronic, magnetic and structural properties*. (Springer, 1994).
21. Zak, J., Moog, E. R., Liu, C. & Bader, S. D. Universal approach to magneto-optics. *J. Magn. Magn. Mater.* **89,** 107–123 (1990).
22. Nistor, C., Beach, G. S. D. & Erskine, J. L. Versatile magneto-optic Kerr effect polarimeter for studies of domain-wall dynamics in magnetic nanostructures. *Rev. Sci. Instrum.* **77,** 103901 (2006).
23. Foner, S. Versatile and Sensitive Vibrating-Sample Magnetometer. *Rev. Sci. Instrum.* **30,** 548–557 (1959).
24. Fischer, P. The Center for X-Ray Optics - Beamline 6.1.2 - XM-1. (2019). Available at:

http://www.cxro.lbl.gov/BL612/. (Accessed: 5th March 2019)
25. Marchesini, S. *et al.* Massively parallel X-ray holography. *Nat. Photonics* **2,** 560–563 (2008).
26. Gorniak, T. *et al.* X-ray holographic microscopy with zone plates applied to biological samples in the water window using 3rd harmonic radiation from the free-electron laser FLASH. *Opt. Express* **19,** 11059 (2011).
27. Eisebitt, S. *et al.* Lensless imaging of magnetic nanostructures by X-ray spectro-holography. *Nature* **432,** 885–888 (2004).

6. MEASURING AND QUANTIFYING THE DZYALOSHINSKII-MORIYA INTERACTION

6.0 Introduction and Motivation

Current-induced domain wall and skyrmion motion has attracted significant attention in the spintronics community as a potential technological path towards ultra-fast and ultra-dense memory and logic devices[1–4]. In particular, one approach has focused on encoding domain walls and skyrmions as magnetic nano-bits in racetrack like geometries[1]. Recently, fast soliton motion $(> 100\ m/s)$ has been seen in ultra-thin magnetic films with perpendicular magnetic anisotropy (PMA)[3,5–7]. An interesting observation is that these spin textures move in an opposite direction to the conventional, well-understood spin-transfer torque[8,9]. Such observation has sparked debate in the community over the origins of the fast, unidirectional current-driven motion of domain walls. It has been proposed that the peculiar, high-speed motion can be well explain by the spin-Hall effect or Rashba effect acting on chiral Néel domain walls stabilized by the Dzyaloshinskii-Moriya interaction (DMI)[9,10].

As the DMI is a chiral interaction, it only manifests in material systems which lack inversion symmetry, such as systems whose crystal structures lack symmetry. A prime example of this is the B20 crystal structure[11–15], which gives rise to what has been termed “bulk DMI,” meaning that the DMI manifests from the bulk structure of the material. However, interfaces between materials inherently lack inversion symmetry and could act as a source of the DMI[16]. The type of DMI is often coined “interfacial DMI,” and arises in thin-film magnetic systems. This has led to the discovery of chiral spin textures in thin film magnetic systems lacking inversion symmetry[8,9,17,18].

In addition to symmetry breaking, the second, necessary ingredient to manifest the DMI is strong spin-orbit coupling. Thus, the thin film magnetic material should be adjacent to a heavy-metal or other material that has large spin-orbit coupling (SOC). Figure 6.1 shows an example of such a structure, where Pt is used as a large SOC material. Conveniently, Pt is also a source of the large spin-Hall angle required for exerting a torque on the DW, and it also provides the magnetic material with PMA. The discovery of DMI in room-temperature thin films systems has ignited much research in to measuring and quantifying the strength of this interaction in asymmetric thin-film systems, as this is key to optimizing micromagnetic parameters for racetrack devices[9,10,19–22].

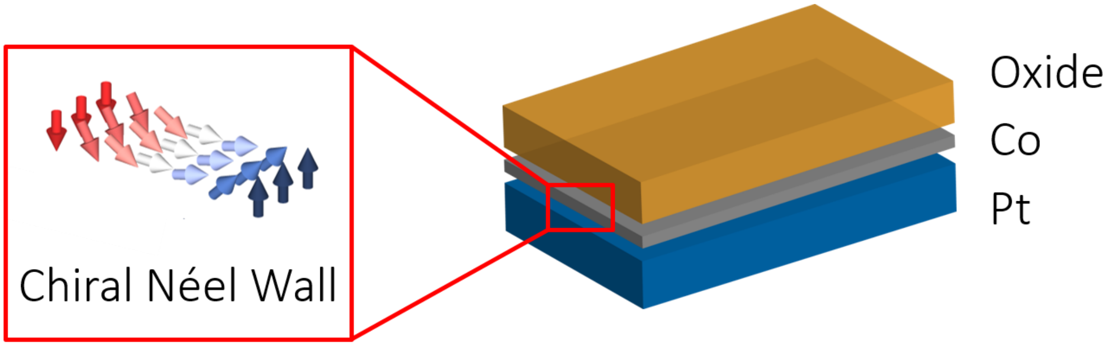

Figure 6.1 | Chiral Néel domain walls forming in a thin films system, where the DMI manifests from the Pt (heavy metal)/Co (magnetic material) interface

This chapter will outline various techniques used to measure the strength of the DMI interaction in a thin film. In particular, the following three methods and their limitations will be discussed:

1. Asymmetric field-driven expansion of domain walls in the in the creep regime
2. SOT Dynamics of DW Motion
3. Brillouin light scattering (BLS)

In the first section, we will derive the creep law for DW motion, which can also extend to other creep systems found in nature. In the second section, we will discuss how DW transport measurement can indirectly quantify the DMI. Of these three techniques, only the last technique discussed here (3. BLS) is a direct measurement of the DMI. Techniques 1 and 2 are indirect measurements and rely on how the DMI acts on the domain wall itself.

6.1 Asymmetric field-driven expansion of domain walls

Deriving the DW creep law

Creep law of magnetic domain walls describes the motion of a wall through a pinning potential, where the pinning potential height is higher than the driving force (in this case, a magnetic field); however, there is still a net motion of the domain wall due to fluctuations in energy (typically thermal or quantum). This is generally described by an Arrhenius law, where a fluctuation of temperature costs elastic energy, but yields energy in the driving force term. As these energy costs and gains scale differently, there is an ideal or optimum fluctuation for motion of a domain wall. Following Hartmann *et al*[23], the goal of creep derivation is to calculate the elastic energy cost and the driving energy gain as a function of a deformation length, L. The net energy is then calculated and optimized for L. Guided by the work of Hartmann *et al*[23] and Je *et al*[19], we will perform these for two cases: dispersive and non-dispersive energy density.

Dispersive Energy Derivation of Creep Model

In this case, we consider a straight domain wall with a deformation segment length, L. An external field is applied such that driven the wall to the right (positive) is energetically favorable due to lowering of the Zeeman energy. However, this causes the domain wall to stretch, and is elastically unfavorable. Let's say that the pinning potential has a length scale, u. We can approximate the increase in domain wall length using a right angle triangle made from L and u as show in Figure 6.2 (adapted from Hartman *et al*[23]) , and described mathematically below:

$$d = 2\left(u^2 + \left(\frac{L}{2}\right)^2\right)^{1/2} - L = 2u^2/L \qquad 6.1$$

Here, we have not included any effects of the DMI or any in-plane fields. This also assumes that u is small, and the elastic energy ϵ_{el} is proportional to $2u^2/L$. One can now calculate the change in energy from the deformed domain wall.

$$\Delta E = \epsilon_{\mathrm{el}}\frac{2u^2}{L} - (\Delta\xi^2 L)^{\frac{1}{2}} - M_s H_z t\frac{Lu}{2} \qquad 6.2$$

where ϵ_{el} is the elastic energy density, t is the film thickness, Δ is the pinning potential, ξ is the characteristic length of the pinning potential, M_s is the saturation magnetisation, and H_z is the out-of-plane magnetic field. Equation 6.2 describes the change in energy in terms of the stretching F_s, pinning potential F_p, and Zeeman energy F_z. The elasticity can be determined looking at the difference between a stretched DW and an un-stretched DW. In the case of a non-dispersive energy

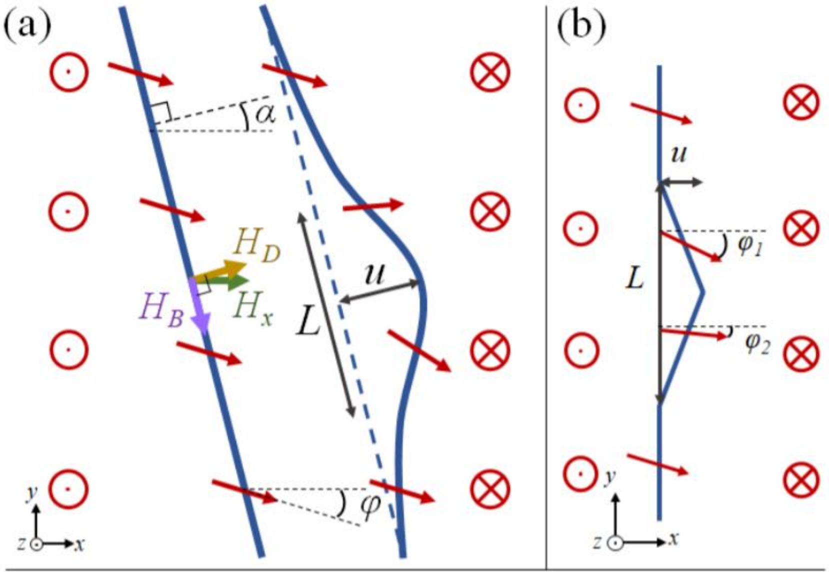

Figure 6.2 adapted from ref[23] | a) DW (blue) stretched a distance u over a length segment L of the DW. The DW is at some angle α, whose internal magnetization is described by the red arrows at some angle ϕ. H_B is the Bloch field, H_D is the DMI field, and H_x is the applied in-plane field. **b)** is model describing the deformation of the DW, where the displacement is approximated by two straight lines, comprising a triangle.

model, which is our case here, this equal to the energy density times the change in domain wall length.

Let's define L_c as the optimum length that the domain wall stretches elastically with respect to the pinning potential under no applied field, also known as the Larkin length. Therefore, to calculate L_c, we set the pinning potential energy equal to the elasticity for a deformation of $u = \xi$. This is, when $F_s = F_p$. This is a metastable state that the DW has "hopped" into. Solving this, we find

$$L_c = 2\left(\frac{2\epsilon_{el}^2\xi^2}{\Delta}\right)^{\frac{1}{3}} \tag{6.3}$$

We now define H_c as the magnetic field necessary to move the DW of length L_c and $u = \xi$ with no thermal fluctuations. This is when $F_p = F_z\ @\ L = L_c$ and $u = \xi$.

$$H_c = \frac{e\epsilon_{el}\xi}{L_c^2 M_s t} \tag{6.4}$$

Using the appropriate thermally and spatially averaged correlation function, one finds

$$u(L) = u_c\left(\frac{L}{L_c}\right)^{\zeta} \tag{6.5}$$

where u_c is the transverse scaling parameter. $\zeta = \frac{3}{2}$ for a one-dimensional domain wall. To determine the optimum length L_{opt} we can insert this expression in Eq. 6.2, to yield the flowing expression for the change in energy from the deformed DW:

$$\Delta E(L) = \frac{2\epsilon_{el}u_c^2}{L_c}\left(\frac{L}{L_c}\right)^{2\zeta-1} - \frac{1}{2}M_s H_z t u_c\left(\frac{L}{L_c}\right)^{\zeta+1} \tag{6.6}$$

Maximizing this expression and solving for L,

$$L_{opt} = L_c \left(\frac{\zeta + 1}{2\zeta - 1} \, M_s \frac{H_z t L_c^2}{4 u_c \epsilon_{el}} \right)^{\frac{1}{\zeta - 2}} \qquad 6.7$$

Inserting $\zeta = \frac{2}{3}$ we find that the energy barrier for domain wall motion in the creep regime is

$$F_{barrier} = C \frac{u_c^{\frac{9}{4}} \Delta^{\frac{1}{2}}}{\xi} \left(\frac{\epsilon_{el}}{H_z M_s t} \right)^{\frac{1}{4}} \qquad 6.8$$

Using the Arrhenius equation for hopping, the domain wall velocity is proportional to the hopping rate. That is, the exponential of the Arrhenius Boltzman energy barrier is proportional to the DW velocity[23]:

$$\ln(v) \propto - \left(\frac{\epsilon_{el}}{H_z} \right)^{\frac{1}{4}} \qquad 6.9$$

In the non-dispersive model, we have assumed $\epsilon_{el} \propto \frac{2u^2}{L}$. Using this model and Eq. 6.9 as a starting point, there have been several approaches to adding both the DMI and in-plane fields to the creep law. We will outline one useful technique below, coined the “chiral energy” model of asymmetric DW expansion.

Chiral Energy Model of DW Motion

In this model, Je *et al*[19] and Hrabec *et al*[20] and others[24,25] assume that the DMI and in-plane field only effect the energy of the DW σ_{DW}, and all other terms are left unchanged. In this section, we will how this assumption affects the creep model derived above, and thus how the DMI can be extracted by using very simple field driven motion of domain walls. This section will also outline the limitations and disadvantages of this technique, motivating other means of extracting the DMI rom thin film systems.

As shown earlier, in conventional field-driven DW motion, the DW follows a creep scaling law,

$$v = v_0 exp\left(-\alpha^* H_z^{-\mu}\right) \tag{6.10}$$

where v is the velocity of the domain wall, v_0 is the characteristic speed, H_z is the out-of-plane field, α is the scaling constant, and $\mu = \frac{1}{4}$ is the creep exponent. Here, α is related to the domain wall energy σ_{DW} through the following relation:

$$\alpha(H_x) = \alpha_0 \left[\frac{\sigma_{DW}(H_x)}{\sigma_{DW}(0)}\right]^{\frac{1}{4}} \tag{6.11}$$

In films with significant DMI, the DMI can be represented as a local, effective magnetic field stabilizing Néel domain walls, H_{DMI}, as shown in Figure 6.3a. Je *et al*[19] and Hrabec *et al*[20] have taken the non-dispersive creep model and shown that the strength of the DMI can be quantified by examining the dynamics of domain walls in a field-driven, expanding bubble. In this very simple technique, out-of-plane field-driven DW motion is examined under the influence of a DC in-plane field bias H_x.

In this model, the domain wall energy, σ_{DW}, is a strong function of the DMI energy, D and any in-plane fields, H_x,

$$\sigma_{DW}(H_x, \psi) = \sigma_0 + 2K_D\lambda \cos^2(\psi) - \pi\lambda M_s(H_x + H_{DMI}) \cos(\psi) \tag{6.12}$$

Where σ_0 is the Bloch type DW energy density, K_D is the DW anisotropy energy density, ψ is the azimuthal angle, and λ is the DW width. An equilibrium angle, ψ_{eq} can be calculated by minimizing the derivative of the domain wall energy with respect to ψ, $\frac{\delta\sigma_{DW}}{\delta\psi} = 0$. This gives a $\psi_{eq} = \frac{\pi M_s(H_x+H_{DMI})}{4K_D}$. For small applied field, $H_x + H_{DMI} < \frac{4K_D}{\pi\, M_s}$,

$$\sigma_{DW} = \sigma_0 - \frac{\pi^2 \lambda M_s^2}{8K_D}(H_x + H_{DMI})^2 \qquad 6.13$$

From Eq. 6.13, one can see that the domain wall energy becomes zero when the DMI effective field H_{DMI} is equal and opposite the applied magnetic field H_x. This leads to a minimum in the DW velocity as a function of in-plane field H_x. Under the influence of an external in-plane magnetic field (H_x), up-down and down-up domain walls see a different effective in-plane field ($H_{DMI} \pm H_x$), leading to a difference in the domain wall energy σ_{DW}. Therefore, up-down and down-up DWs travel with different velocities. This results in asymmetric expansion of a bubble driven by an external out-of-plane and in-plane field (Fig 6.3b). The asymmetric expansion is reported to be caused by a change in the domain wall energy arising due to symmetry breaking from the external in-plane field. The domain wall velocity has a minimum at an in-plane field equal to the effective magnetic field in the domain wall, when $H_x = H_{DMI}$. Thus, the strength of the DMI can be directly extracted from a measurement of the domain wall velocity under external in-plane fields.

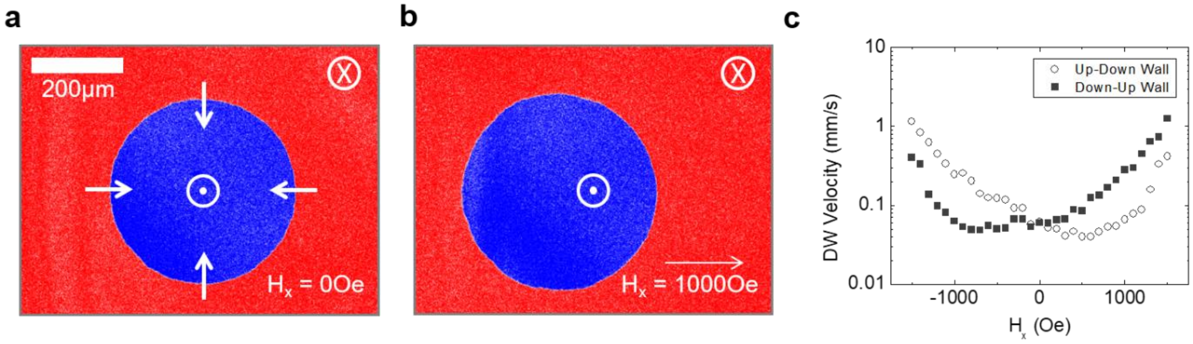

Figure 6.3 | a) Kerr microscopy image of a magnetic bubble domain in Ta(4)/Pt(3)/Co(0.9)/Gd(1)/GdO$_x$(8) (thickness in nm). The arrows on the domain wall indicate the DMI effective field H_{DMI} stabilizing a homochiral Néel wall. b) Asymmetric domain wall expansion under the influence on an in-plane field H_x. c) The velocity of the domain wall as a function of H_x. Minimum in energy corresponds to the strength of H_{DMI} in the chiral energy DW creep model.

Example asymmetric domain expansion, as imaged by Kerr microscopy, is seen in Fig.6.3a,b, with a corresponding DW velocity v_{dw} versus H_x curve shown in Fig. 6.3c. The film measured here is Ta(4)/Pt(3)/Co(0.9)/Gd(1)/GdO$_x$(8) (thickness denoted in nm). In this film, the Pt acts as the source of DMI, while the Gd/GdO$_x$ capping layer provides the necessary inversion asymmetry to manifest the DMI. Here, the Ta acts as an adhesion layer. The minimum of this curve can be interpreted as the effective DMI field, H_{DMI}. This can be converted in to a DMI energy following simple magnetic characterization and the following expression: $H_{DMI} = \frac{D}{\mu_0 M_s \Delta}$, where Δ refers to the DW width. Not only does this technique quantify the magnitude of the DMI, but also implies the sign of the DMI. A positive (negative) in-plane magnetic field which hinders an up(down)-down(up) domain wall defines a left(right)-handed chiral wall.

While this model is relatively simple and allows for easy extraction of the DMI effective field, H_{DMI}, there have been numerous reports showing anomalous behavior that deviates significantly from this simplistic model[25–27]. Here, we investigate the strength of the DMI in perpendicularly magnetized Pt(3nm)/Co(0.9nm)/Pt(x)/GdOx(8nm) (x = 0 to 3nm) films using asymmetric domain expansion. Inserting small amounts of Pt at the interface between the ferromagnet and oxide was used investigate the sensitivity of the DMI at this interface. This has two effects: 1) countering the DMI produced at the bottom interface and 2) changing the oxygen stoichiometry at the top interface between Co and Pt. Films were sputtered using DC magnetron sputtering onto thermally oxidized Si. The samples were grown at room temperature under 3mTorr Ar at a background pressure of ~2x10^7 Torr for metallic layers. A thin adhesion layer of Ta(4nm) was deposited prior to growing the layered stack. GdOx layers were grown using reactive sputtering with an oxygen partial pressure of 5x10^5 Torr. Domain wall motion was observed at room temperature using a custom differential wide-field magneto-optical Kerr microscopy system with independent in-plane and out-of-plane field control. To observe domain expansion, films are saturated and a domain is nucleated using a short (~10ms) out-of-plane (H_z) pulse. Subsequent pulses (~5-200ms) are used to drive domain expansion under an in-plane bias. The in-plane magnet is tilt correct to within 0.02^{o} to minimize out-of-plane field component due to misalignment of the in-plane magnet.

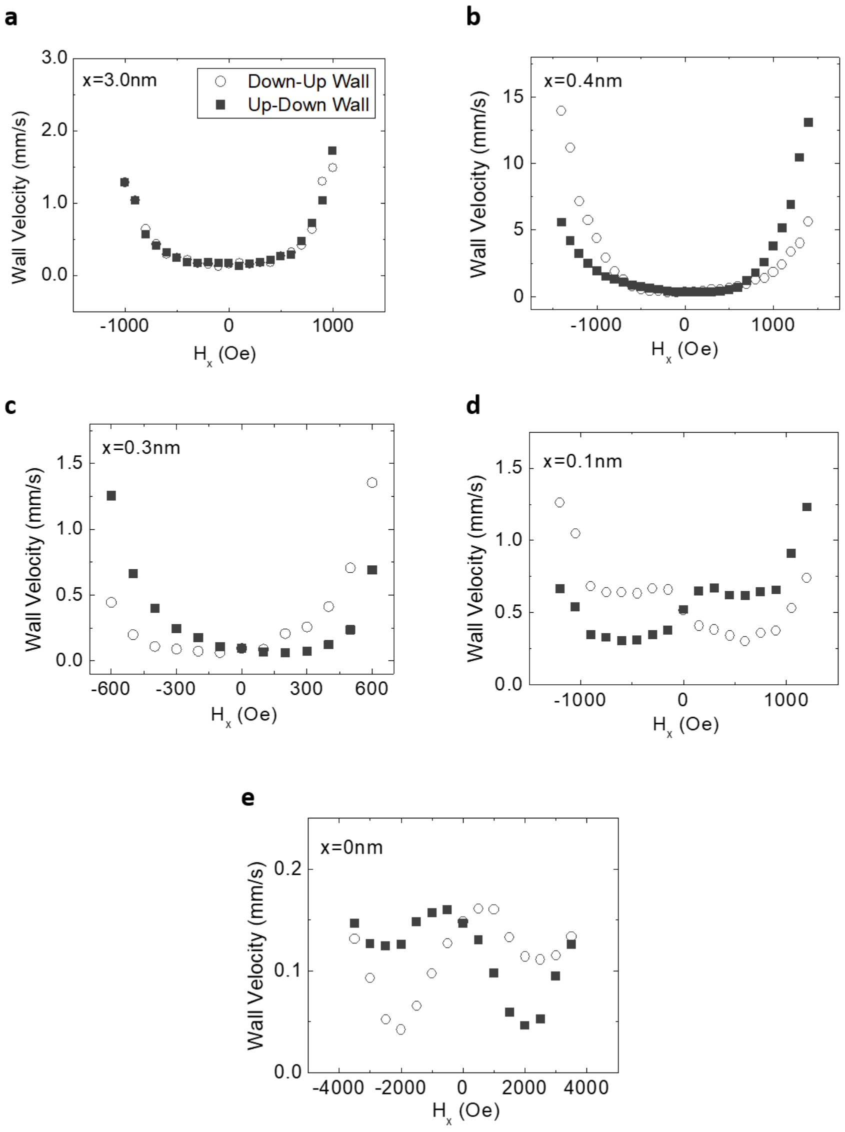

Figure 6.4 | Domain wall velocity as a function of in-plane field in Pt(3nm)/Co(0.9nm)/Pt(x)/GdOx(3nm), where x ranges from a) $x = 3\,nm$ to e) $x = 0\,nm$. Anomalous behavior occurs as the Pt layer thins.

Domain wall velocity versus in-plane field curves for the left and right domain walls of the expanding domain are shown in Fig. 6.4 for various spacer layer thicknesses of Pt at the top interface. When the Pt spacer layer thickness is large enough ($x = 3\ nm$), the DMI at the bottom interface is effectively negated from the Pt at the top interface, leading to symmetric domain expansion and a DMI value near zero. However, as the Pt spacer layer thickness decreases ($x < 0.4\ nm$), asymmetry arises in the domain wall dynamics indicating a non-zero DMI. Moreover, an oscillatory nature to the DMI is observed, as the direction of domain wall expansion alternates as the thickness of the Pt spacer layer decreases. This is indicated by a change in asymmetry in the velocity curves. We speculate that the oscillatory nature could be attributed to the change in the oxidation coordination of Co at this interface as the Pt spacer layer thickness changes. Oscillatory DMI has been demonstrated by first-principles calculations on Fe/Ir(001), where the oscillatory nature is credited to the presence of oxygen at the interface.

Also observed is a qualitative transition in the domain wall dynamics in the expanding bubble domains as the Pt spacer layer thickness decreases. This transition to anomalous behavior occurs over a very narrow Pt spacer layer thickness (0.3nm), and is characterized by the emergence of a peak in velocity, in addition to the characteristic minimum, when the external in-plane field is aligned with the DMI effective field in the domain wall. The transition in domain wall dynamics is accompanied by a large change in the strength of the DMI. The DMI effective field increases by nearly an order of magnitude, from ~25mT to ~250mT (Fig. 6.4c-e) over a change in 0.3nm of Pt spacer thickness. While samples with low DMI exhibit domain wall dynamics that is well described by the chiral energy expansion models, the anomalous behavior seen in samples with high DMI cannot be accounted for by the dimple chiral energy model of domain wall expansion.

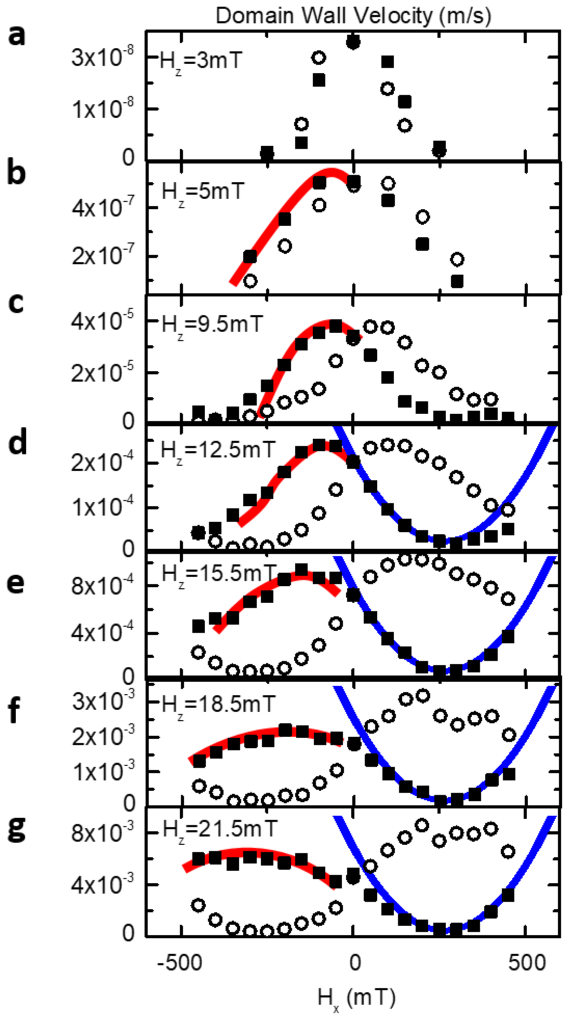

Figure 6.5 | Domain wall velocity in Pt(3)/Co(0.9)/GdOx(8) as a function of in-plane field for various out-of-plane drive fields (a-g). The blue overlay is a guide-to-the-eye of the characteristic quadratic minimum in the chiral energy model. The red overlay highlights the anomalous maximum seen as the drive field is lowered.

To investigate its cause, the drive-field (H_z) sensitivity of the anomalous behavior was measured on a second, nominally identical sample to that shown in Fig 6.4e. Fig 6.5 shows an overlay of the domain wall velocities vs in-plane field at various drive fields for both down-up and up-down domain walls. Notably, at all drive-field values, the location of the domain wall velocity minimum is constant (~250mT). However, the dynamics of the DW velocity significantly change as a function of drive field. At high drive fields, we find that the DW follows a behavior that can be well-described by the chiral energy model. The DW velocity curves show a clear minimum, which can be interpreted as the DMI effective field H_x. As the drive field is lowered, the nature of the curves qualitatively change. Lowering the drive-field deeper into the creep regime brings the appearance of the anomalous maximum seen in Fig 6.4e. In fact, if the drive field is significantly lowered, the characteristic velocity minimum disappears, leaving only a pronounced maximum in velocity. Moreover, at extremely low drive fields, we find that the asymmetry of the expanding bubble inverts, a phenomenon not reported elsewhere. This is more clear depicted in Fig. 6.6a,b, where two expanded bubbles are shown using Kerr microcopy. Both domains were expanded under the same in-plane bias field on the same sample. However, one bubble domain was expanded under a high drive field similar to that shown in Fig 6.5g, while the other was expanded under a very low drive field similar to Fig 6.5a. Clearly seen is that the bubble expanded at low drive field expands asymmetrically in the opposite direction then the bubble expanded at high drive field. Notably, under low drive fields, the domain wall depicted in Fig 6.5a appears rough, indicative of creep motion "hopping." The domain wall in Fig 6.5b (expanded under high drive fields) appears smooth.

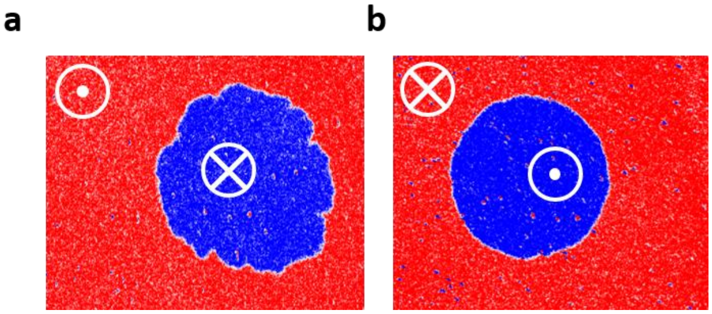

Figure 6.5 | Kerr microscopy images of bubbles expanded under a) low H_z drive field and b) high H_z drive field under an in-plane bias field $H_x = 1000\ Oe$. Asymmetry inverts at low H_z

The anomalous behavior of the DW dynamics (anomalous maximum/peak in velocity) and the inversion asymmetry in bubble expansion are clear indications that the chiral energy model does not accurately model the field-driven bubble expansion in chiral systems under an in-plane field bias in all cases, making this technique not always suitable to quantify the DMI. The anomalies seen here also open a new window into understanding creep dynamics in magnetic systems.

Dispersive Energy Derivation of Creep Model

In this section, we will derive and show how to numerically solve the creep model for a dispersive energy system, which hopes to more accurately model DW creep dynamics in chiral systems under an in-plane field bias, providing a means of quantifying the DMI in thin films using the simple experiment of bubble domain expansion.

The Arrhenius law of thermally activated DW motion states that the rate at which a DW deformation or "hop" survives is determined by the activation energy. This is the well understood exponential expression in Eq. 6.9, where $\ln(v) \propto -F/k_bT$, where F is the free energy of the segment of DW that has "hopped." As shown earlier, F depends on the segment length L but also the displacement of the DW u, how far the DW "hops" through the elastic energy cost and the Zeeman energy gain. Eq 6.5 Shows us how to express u as a function of L, $u(L) = u_c\left(\frac{L}{L_c}\right)^{\frac{2}{3}}$. In the non-dispersive model, our goal was to calculate the elastic energy, and thereby computer F in terms of L. In the case of a non-dispersive energy model, we assume that the elastic energy was equal to the energy density times the change in domain wall length. However, when an in-plane field is applied, the DW energy depends on the orientation of the DW moment with respect to the applied in-plane field H_x and the exchange interaction, which add an energy cost to bending the DW. Moreover, the orientation of the domain wall plays a large role in its elasticity. An in-plane field applied to a Bloch versus Néel wall will cause the wall to become more or less flexible. Thus in this more thorough model, Hartmann *et al*[23] take into account these three effects of stretching, bending, and orientation.

Blatter *et al*[28] originally models the deformation of the domain wall by including the angular dependence of the shape of the deformation. Here, we follow Hartmann *et al*[23], where the cost of energy due to bending is approximated as a nearest neighbor exchange energy cost. The energy of the system can then be minimized, in this case, numerically. Here, we skip some detailed steps, and from Hartmann *et al*, the computed elasticity of the domain wall, when accounting for Zeeman energy, as well as the bending (which is not accounted for in the non-dispersive creep model) is:

$$\begin{aligned}\frac{E_{el}(u,L)}{t} = \min_{\phi_1\phi_2}\Bigg[&\frac{L}{2}sqrt\left(1+\left(\frac{2u}{L}\right)^2\right)\left(\epsilon\left(\alpha_0+\arctan\left(\frac{2u}{L}\right),\phi_1\right)\right.\\&\left.+\,\epsilon\left(\alpha_0-\arctan\left(\frac{2u}{L}\right),\phi_2\right)\right)\\&+\frac{J\lambda}{\alpha(3-\cos(\phi_0-\phi_1)-\cos(\phi_0-\phi_2)-\cos(\phi_1-\phi_2))}\Bigg]-L\epsilon(\alpha_0,\phi_0),\end{aligned} \tag{6.14}$$

The first term in 6.14 is the energy associated with each of the two segments of the stretched DW. The second term accounts for bending of the domain wall (exchange cost), and the third term accounts for the energy of the domain wall in its unperturbed state. Then to calculate the domain wall velocity, optimizing a number of parameters is necessary $(\alpha_0,\phi_0,\phi_1,\phi_2,L_c,F_b)$, and therefore, this cannot be solved analytically, but only numerically. Using this more advanced model, one can extract the DMI from the asymmetric bubble expansion measurements.

Asymmetric bubble expansion has the advantage that no patterning is need to extract the DMI. Moreover, one only needs to applied out-of-plane and in-plane fields. However, as we have seen, the resulting analysis can become cumbersome and often time the data is not straight forward to interpret. A more difficult technique relying on DW transport will be described below, but the results are much simpler and easier to interpret.

6.2 SOT Dynamics of Domain Wall Motion

Current driven DW dynamics under an in-plane bias field

An alternative approach to probe the energetics and structure of the DMI in a domain wall is to examine the angular dependence of spin-Hall torque acting on DW[9,10,22]. As shown in Section 4 of this thesis, it has been shown that the spin-Hall torque (H_{SL}) only acts on a DW is the domain wall has a component of its moment parallel to the domain wall normal vector. This is described by Eq. 6.15,

$$H_{SL} = \frac{\pi}{2} H_{DL} \, cos(\psi) \qquad 6.15$$

where here, ψ is the "DW-type angle", or the angle between the DW normal vector and the moment of the DW ($\psi = 0$ for Néel DWs, $\psi = 0$ for Bloch DWs). Thus, a spin-orbit torque acts as an effective easy axis field driving the domain wall only when the wall has some Néel character. Fig 6.6 illustrates these two types of DWs, emphasizing that spin-orbit torque (SOT) motion of DWs only occurs for Néel-type DW, where the Slonczewski-like effective field is non-zero.

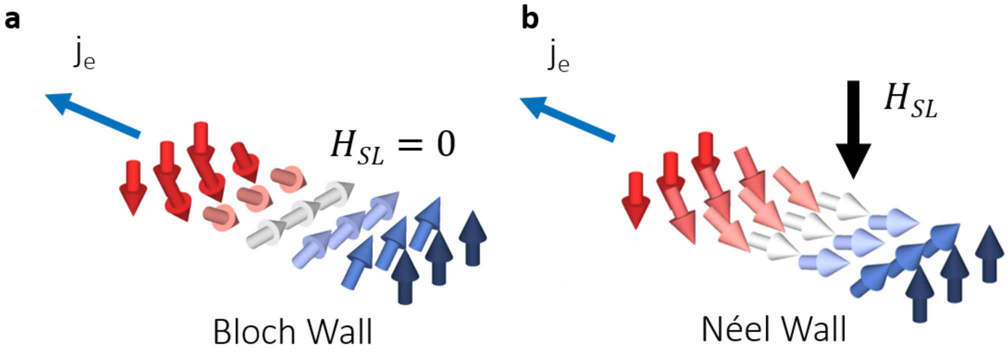

Figure 6.6 | a) Bloch and b) Néel domain walls. In the case of a Néel domain wall, the Slonczewski like torque manifests as an effective easy-axis field driving the domain wall in motion.

The DW chirality and DMI effective field H_{DMI} can be obtained from measuring the dependence of SOT-driven domain wall velocity v_{DW} on longitudinal field H_x [8,9]. The SOT-driven motion of a DW increases (decreases) when H_x is parallel (antiparallel) to H_{DMI}, which sets the orientation of the Néel DWs. If the magnitude of the applied longitudinal field H_x is exactly equal and opposite to the DMI effective field H_{DMI}, then the domain wall is effectively Boch, the SOT no longer acts on the domain wall, and the measured DW velocity $v_{DW}$is zero. Extrapolation of v_{DW} to $v_{DW} = 0$ yields H_{DMI}, which is related to D through $H_{\mathrm{DMI}} = \frac{D}{\mu_0 M_s \Delta}$ with Δ the DW width, and $M_s$the saturation magnetisation[29]. An example of this type of measurement can be seen in Section 7, Figure 7.8d.

Spin Hall torque magnetometry of chiral DWs

In spintronics, it is very common to try relate new magnetic phenomenon to well-understood phenomenon. For example, it is well understood how easy-axis magnetic fields drive DWs in motion. Thus new phenomenon that also drive DWs in motion are often thought of as “effective field.” This has already been seen in this thesis on numerous occasions, namely with the DMI effective field H_{DMI}, and the SOT effective field H_{SL}. Here, we say that the DMI acts like an effective magnetic field in the DW in its Néel orientation. And the SOT effective field acts like an easy axis magnetic field that drives the DW in motion.

In this section we will show how measuring the affective SOT field H_{SL} as a function of in-plane field can help to extract the DMI in a thin film system, in particular one with very low DMI. Moreover, this technique will allow us to extract a number of other parameters about the domain wall, such as the DW anisotropy field and the domain wall width. In this technique developed by Emori *et al*[30], a domain wall is first nucleated, and then it is propagated with an easy axis magnetic field and a small DC in-plane drive current j_{assist} . Here, we measure the propagation field of the domain wall as a function of the in-plane drive current. The current-to-field ratio can be extracted and used as a measure of the efficiency χ (effective field per unit current density). The experimental procedure is as follows: The magnetic material is patterned into a wire geometry with an overlaid current shunt line, which acts as a DW nucleation line. A DW is nucleated be passing a current J_{Nuc} across the shunt wire, generating an Oe field. A triangle magnetic field wave is swept at a fixed rate and a focused laser measures the local magnetization of the sample at a fixed distance away from the DW nucleation line via MOKE. When a DW is pre-nucleated, the measured coercivity is the propagation field of the DW H_{prop}. If the DW is not pre-nucleated, then the coercivity is the nucleation field of the DW H_{Nuc}. This technique assumes the $H_{Nuc} > H_{prop}$, which is generally true in most magnetic systems. Figure 6.7 shows a typical device structure and waveform for measure the propagation field. A typical MOKE hysteresis loop

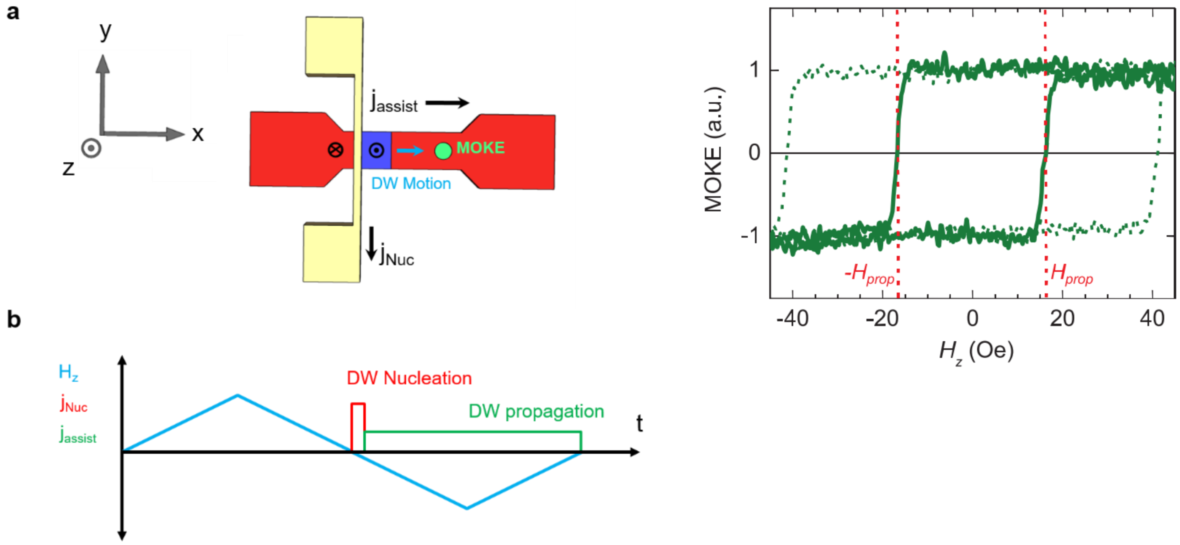

Figure 6.7 | a) Device structure for measurement of DW propagation field. A DW is pre-nucleated from an overlaid shunt line (yellow) via Oe field. The DW is driven with a magnetic field and a DC current that either assist or hinders the DW motion. b) Typical waveforms for measure H_{prop}. c) An example MOKE hysteresis loop adapted from Emori *et al* with (solid green line) and without (dashed green line) prenucleated DWs

adapted from Emori *et al*[22] with (solid green line) and without (dashed green line) prenucleated DWs in Ta/CoFeB/MgO.

As stated in the previous section, an in-plane longitudinal bias field can force a Néel DW to have Bloch character (and vice versa). This would cause the efficiency χ to drop (increase). Figure 6.8 plots the in-plane field dependence of χ, as adapted from Emori *et al*[22] in Ta/CoFeB/MgO. Remarkably, from this plot, we can directly extract a number of parameters from this plot. Figure 6.8 is effectively a hard axis hysteresis loop of the domain wall, where instead of plotting the DW moment m_{DW} on the y-axis, here we plot $\chi \propto m_{DW}$. The horizontal breadth of the curve gives the shape anisotropy field of the DW H_k. And the zero-crossing yields the effective DMI field H_{DMI}. Any vertical shift in the curve can be attributed to spin-transfer torque acting on the DW. The curve can be fit to a very similar expression to Eq. 6.15

$$\chi = \frac{\pi}{2}\chi_0\, cos(\psi) \qquad 6.16$$

where $\frac{\pi}{2}\chi_0$ is the efficiency of a fully Néel wall.

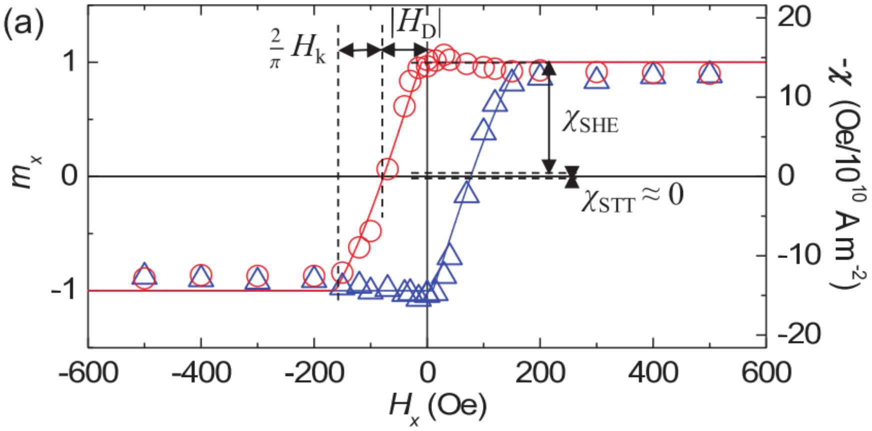

Figure 6.8 | spin Hall torque magnetometry of DWs. The SOT efficiency χ plotted as a function of longitudinal field in Ta/CoFeB/MgO. Effective fields can read directly from the plot. H_k is the DW anisotropy field, χ_{SHE} is the spin Hall (SOT) efficiency, χ_{STT} is the spin

transfer torque efficiency, and H_D is the DMI effective field. Open circle and a open triangles correspond to down-up and up-down DWs respectively.

We will find that this method of extracting the DMI is quite useful for measuring samples with extremely small values of H_{DMI}. In fact, it may be the only known way to measure very small values of DMI. This technique does, however, rely on DW transport in thin films and time-consuming lithography steps. Below we will outline an approach that is one of the only ways to directly measure the DMI (not its effects on DWs) and requires no lithographic patterning steps.

6.3 Brillouin light scattering (BLS)

Direct measurements of the DMI have been limited to very specialized samples and systems, such as synchrotron-based x-ray scattering interferometry of $FeBO_3$[31], spin polarized EELS of Fe on W(110)[32], and spin polarized scanning tunneling microscopy of Mn on W(110)[18]. However, several theoretical works have showed asymmetric dispersion relations of thermal spin waves due to the DMI. Inspired by these studies, Nembach, *et al*[21] and others have directly measured the DMI via Brillouin light scattering (BLS). This GHz bandwidth technique allows one to directly measure the predicated asymmetric dispersion shift, allowing direct calculation of the DMI. In BLS, light is incident on the sample and is in-elastically scattered. Incident light energy is used in GHz (long-range) processes is inelastically backscattered by magnons. The reflected light shows a shift in frequency (energy), altering the dispersion relation.

Ferromagnetic materials containing spin waves (or magnons) have a spatial chirality that depends on the spin wave propagation direction relative to the magnetization. In a symmetric material containing no DMI, clockwise (+z spin waves propagating in the +x direction) and counterclockwise (+z spin waves propagating in the -x direction) occur in equal amounts. When the DMI is present, this symmetry is broken and the preferred chirality is set by the sign on the DMI vector, D_{ij}. Following Nembach, *et al*, in an in-plane magnetized film with spin waves propagating perpendicular to the magnetization direction, the DMI alters the spin wave frequency according to:

$$f_M = f_0 + \Delta f_{DMI} \qquad 6.16$$

where f_0 is the spin-wave frequency in the absence of the DMI and

$$\Delta f_{DMI} = \frac{g\mu_B}{h} sgn(M_z) \frac{2D}{M_s} k_x \qquad 6.17$$

where $D \propto D_{ij}$ is the volumetric DMI constant, g is the in-plane spectroscopic splitting factor, M_s is the saturation magnetization, k is the wavevector of the spin waves, μ_B is the Bohr magneton, and h is the Bohr magneton.

Magnons that are propagating towards the incident laser are annihilated (anti-Stokes), and magnons propagating away from the laser are created (Stokes) as momentum in conserved. Thus, energy conservation identifies the inelastic frequency shift of the backscattered light with the propagation direction of the magnons. Therefore, the photon energy shift can be used as a probe of magnon propagation direction and thus the DMI. Figure 6.9 shows a cartoon sketch of a BLS spectrum from Nembach, *et al*[21] of the frequency shift associated with the inelastic scattering for Stokes and anti-Stokes processes. The center figure shows the spin wave dispersion relation in the absence (dashed) and presence (solid) of the DMI.

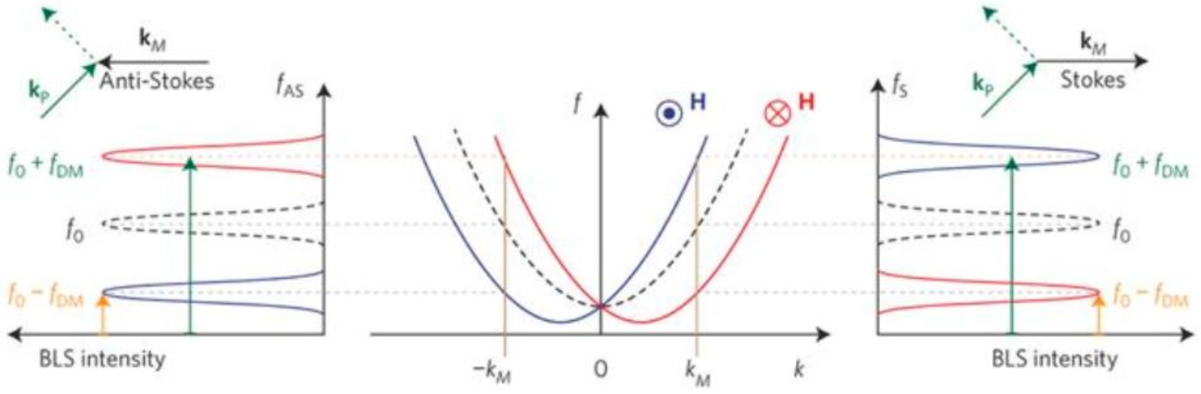

Figure 6.9 adapted from ref[21] **|** Sketched BLS spectrum showing Stokes (magnon generation) and anti-Stokes (magnon annihilation) processes. The center sketch shows a schematic dispersion relation in the absence (dashed) and presence (solid) of the DMI.

Using BLS, we have measured the DMI in Pt(3nm)/Co(0.9nm)/Pt(x)/GdOx(3nm) thin films. The results are shown in Fig. 6.10 (solid red squares). For comparison, these are nominally the same films that we performed asymmetric domain wall expansion measurements on in Fig. 6.4, the results of which are overlaid in Fig 6.10 (solid blue circles). There is a notable difference between the results obtained by bubble expansion and BLS, which highlights the challenges associated with DMI measurements, particularly those of bubble expansion measurements. BLS measurements show a (more-or-less) linear dependence of the DMI on Pt overlayer thickness, whereas the DMI measurements show oscillatory behavior, where the DMI changes sign. Moreover, the absolute value of the DMI at a given Pt overlayer thickness is approximately a factor of 2 different for the different types of measurements.

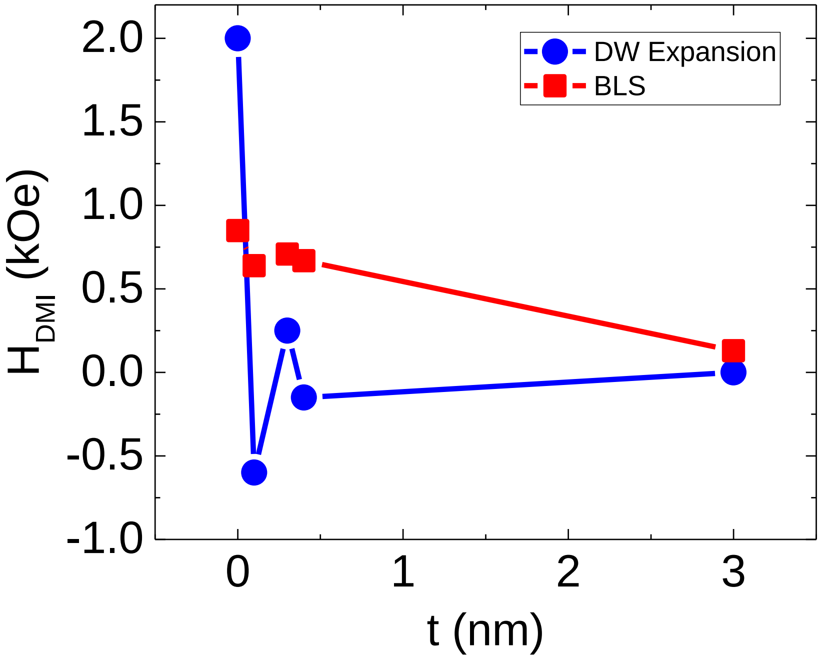

Figure 6.10 | Measurement of H_{DMI} via BLS (solid red squares), and via asymmetric DW expansion (solid blue circles).

From Fig. 6.10, it is clear that BLS offers a method of measuring DMI that is much simpler to interpret than bubble expansion and requires no lithography, unlike current driven DW motion. However, measuring DMI in samples with very small DMI is difficult with BLS. In BLS, we look for a frequency shift of the in-elastically backscattered light. The data in BLS typically has signal to noise ratio that is unable to resolve such small frequency shifts, making it hard to resolve small DMI values. We will see in later sections of this thesis that this becomes important when measuring samples with very small M_s, where small DMI values can have significant effects on the DW type.

6.4 Summary of methods to measure DMI

The table below highlight the key advantages and disadvantages of the three methods of measure DMI in this chapter.

Method	***Advantages***	***Disadvantages***
Asymmetric DW Expansion	• No lithography required • Relatively simple measurement	• Indirect measurement of DMI • Difficult to interpret creep dynamics results
SOT Driven DW Motion	• Resolves both small and large values of DMI	• Indirect measurement of DMI • Complex measurement scheme • Requires lithographic patterning
Brillouin Light Scattering	• Direct measurement of DMI • No patterning involved • Easy interpretation of data	• Difficult to measure very small values of DMI

6.5 References

1. Parkin, S. S. P., Hayashi, M. & Thomas, L. Magnetic domain-wall racetrack memory. *Science* **320,** 190–4 (2008).
2. Fert, A., Cros, V. & Sampaio, J. Skyrmions on the track. *Nat. Nanotechnol.* **8,** 152–156 (2013).
3. Caretta, L. *et al.* Fast current-driven domain walls and small skyrmions in a compensated ferrimagnet. *Nat. Nanotechnol.* **13,** 1154–1160 (2018).
4. Torrejon, J. *et al.* Neuromorphic computing with nanoscale spintronic oscillators. *Nature* **547,** 428–431 (2017).
5. Woo, S. *et al.* Observation of room-temperature magnetic skyrmions and their current-driven dynamics in ultrathin metallic ferromagnets. *Nat. Mater.* **15,** 501–506 (2016).
6. Yang, S., Ryu, K. & Parkin, S. Domain-wall velocities of up to 750 m s − 1 driven by exchange-coupling torque in synthetic antiferromagnets. *Nat. Nanotech.* **10,** 221–226 (2015).
7. Kim, K.-J. *et al.* Fast domain wall motion in the vicinity of the angular momentum compensation temperature of ferrimagnets. *Nat. Mater.* **16,** 1187–1192 (2017).
8. Emori, S., Bauer, U., Ahn, S.-M., Martinez, E. & Beach, G. S. D. Current-driven dynamics of chiral ferromagnetic domain walls. *Nat. Mater.* **12,** 611–6 (2013).
9. Ryu, K.-S., Thomas, L., Yang, S.-H. & Parkin, S. Chiral spin torque at magnetic domain walls. *Nat. Nanotechnol.* **8,** 527–533 (2013).
10. Emori, S., Bauer, U., Ahn, S.-M., Martinez, E. & Beach, G. S. D. Current-driven dynamics of chiral ferromagnetic domain walls. *Nat. Mater.* **12,** 611–616 (2013).
11. Mühlbauer, S. *et al.* Skyrmion lattice in a chiral magnet. *Science (80-.).* **323,** 915–919 (2009).
12. Rößler, U. K., Bogdanov, A. N. & Pfleiderer, C. Spontaneous skyrmion ground states in magnetic metals. *Nature* **442,** 797–801 (2006).
13. Münzer, W. *et al.* Skyrmion lattice in the doped semiconductor Fe 1 − x Co x Si. *Phys. Rev. B* **81,** 41203 (2010).
14. Yu, X. Z. *et al.* Real-space observation of a two-dimensional skyrmion crystal. *Nature* **465,** 901–904 (2010).
15. Yu, X. Z. *et al.* Near room-temperature formation of a skyrmion crystal in thin-films of the helimagnet FeGe. *Nat. Mater.* **10,** 106–109 (2011).
16. Fert, A. & Levy, P. M. Role of Anisotropic Exchange Interactions in Determining the Propertiesof Spin-Glasses. *Phys. Rev. Lett.* **44,** (1980).
17. Heinze, S. *et al.* Spontaneous atomic-scale magnetic skyrmion lattice in two dimensions. *Nat. Phys.* **7,** 713–718 (2011).
18. Bode, M. *et al.* Chiral magnetic order at surfaces driven by inversion asymmetry. *Nature* **447,** 190–193 (2007).
19. Je, S.-G. *et al.* Asymmetric magnetic domain-wall motion by the Dzyaloshinskii-Moriya interaction. *Phys. Rev. B* **88,** 214401 (2013).
20. Shahbazi, K. *et al. Domain Wall Motion and Interfacial Dzyaloshinskii-Moriya Interactions in Pt/Co/Ir(t Ir)/Ta Multilayers*.

21. Nembach, H. T., Shaw, J. M., Weiler, M., Jué, E. & Silva, T. J. Linear relation between Heisenberg exchange and interfacial Dzyaloshinskii–Moriya interaction in metal films. *Nat. Phys.* **11,** 825–829 (2015).
22. Emori, S. *et al.* Spin Hall torque magnetometry of Dzyaloshinskii domain walls. *Phys. Rev. B* **90,** 4427 (2014).
23. Hartmann, D. M. F., Duine, R. A., Meijer, M. J., Swagten, H. J. M. & Lavrijsen, R. *Creep of Chiral Domain Walls*.
24. Petit, D., Seem, P. R., Tillette, M., Mansell, R. & Cowburn, R. P. Two-dimensional control of field-driven magnetic bubble movement using Dzyaloshinskii–Moriya interactions. *Appl. Phys. Lett.* **106,** 22402 (2015).
25. Lavrijsen, R. *et al.* Asymmetric magnetic bubble expansion under in-plane field in Pt/Co/Pt: Effect of interface engineering. *Phys. Rev. B* **91,** 104414 (2015).
26. Kim, D.-Y., Kim, D.-H. & Choe, S.-B. Intrinsic asymmetry in chiral domain walls due to the Dzyaloshinskii–Moriya interaction. *Appl. Phys. Express* **9,** 53001 (2016).
27. Jué, E. *et al.* Chiral damping of magnetic domain walls. *Nat. Mater.* **15,** 272–277 (2016).
28. Blatter, G., Feigel’man, M. V., Geshkenbein, V. B., Larkin, A. I. & Vinokur, V. M. Vortices in high-temperature superconductors. *Rev. Mod. Phys.* **66,** 1125–1388 (1994).
29. Martinez, E., Emori, S., Perez, N., Torres, L. & Beach, G. S. D. Current-driven dynamics of Dzyaloshinskii domain walls in the presence of in-plane fields: Full micromagnetic and one-dimensional analysis. *J. Appl. Phys.* **115,** 213909 (2014).
30. Emori, S., Bono, D. C. & Beach, G. S. D. Interfacial current-induced torques in Pt/Co/GdOx. *Appl. Phys. Lett.* **101,** 42405 (2012).
31. Dmitrienko, V. E. *et al.* Measuring the Dzyaloshinskii–Moriya interaction in a weak ferromagnet. *Nat. Phys.* **10,** 202–206 (2014).
32. Zakeri, K. *et al.* Asymmetric Spin-Wave Dispersion on Fe(110): Direct Evidence of the Dzyaloshinskii-Moriya Interaction. *Phys. Rev. Lett.* **104,** 137203 (2010).

7. FAST CURRENT-DRIVEN DOMAIN WALLS AND SMALL SKYRMIONS IN A COMPENSATED FERRIMAGNET[1]

---

[1] This chapter contains work previously published in L. Caretta, M. Mann, F. Büttner, K. Ueda, B. Pfau, C. M. Günther, P. Hessing, A. Churikova, C. Klose, M. Schneider, D. Engel, C. Marcus, D. Bono, K. Bagschik, S. Eisebitt, and G. S. D. Beach, "Fast current-driven domain walls and small skyrmions in a compensated ferrimagnet," *Nat. Nanotechnol.* 3 (2018)

7.0 Introduction and Motivation

Spin-based devices are being widely pursued for high-performance solid-state data storage and logic applications[1–4]. A promising approach is to encode bits by nanoscale domain walls (DWs) or skyrmions that can be shifted by current in racetrack-based devices[2,3]. The key challenges are achieving small bits and translating them at high speed. Tremendous progress has already been made utilising new materials and physical phenomena. The early focus on in-plane magnetised ferromagnets with wide DWs (~100 nm) driven by conventional spin transfer torque[2] has given way to perpendicularly-magnetised ferromagnetic heterostructures in which interfacial spin-orbit coupling stabilises nanoscale chiral spin textures (~1-10 nm)[2,5–8] that are efficiently driven by spin-orbit torques (SOTs)[5,6]. However, ferromagnets suffer from fundamental limitations impeding further progress: stray field interactions limit bit size[9–12] and precessional dynamics limit operating speeds[10,11].

By contrast, antiferromagnets lack stray fields, allowing for atomically-thin domain walls with high packing density[9] and sub 10 nm skyrmions with room-temperature stability[12]. Antiferromagnets also exhibit much faster dynamics than ferromagnets, with THz switching speeds[4,10,11,13], and relativistic spin texture dynamics[14]. Although some methods have been proposed[15–19], manipulating and detecting antiferromagnetic spin textures is, unfortunately, challenging. However, in ferrimagnets the opposing sublattices can fully compensate one another to achieve behaviours similar to antiferromagnets[20], while remaining individually detectible and addressable if the electronic or optical properties of the constituent elements are different.

Here, we show that by using ferrimagnets whose magnetisation and angular momentum compensation temperatures nearly coincide, the fundamental limitations of ferromagnets can be overcome. We show that the speed limit[21,22] for current-driven domain wall motion in ferromagnets does not exist in ferrimagnets with vanishing angular momentum, and we attain speeds for SOT-driven motion exceeding 1300 m/s. We then show that these same materials can host magnetic skyrmions approaching 10 nm in size at room-temperature and zero applied field, which until now has only been possible at cryogenic temperatures under fields >1 T[8,23].

7.1 Modeling of the sublattice $M_{s,i}(T)$ contributions

To model the dynamics and the velocities of domain walls (DWs) in ferrimagnetic materials, we need to know the spin densities $S(T)$ and S_0. These parameters can be calculated by knowledge of the individual sublattice saturation magnetisations $M_{\mathrm{s},i}(T)$ and the Landé g-factors. The $M_{\mathrm{s},i}(T)$ data can be extracted from the total $M_s(T)$ curve following the approach of Kim *et al.*[16,24], who describe the element-specific magnetisations by a power law with a common critical point at the Curie temperature T_c. In equations,

$$M_{\mathrm{s}}(T) = M_{\mathrm{s,Co}}(T) - M_{\mathrm{s,Gd}}(T) \tag{7.1}$$

with $M_{\mathrm{s,Co}} = a_{\mathrm{Co}}\left(1-\frac{T}{T_{\mathrm{c}}}\right)^{b_{\mathrm{Co}}}$ and $M_{\mathrm{s,Gd}} = a_{\mathrm{Gd}}\left(1-\frac{T}{T_{\mathrm{c}}}\right)^{b_{\mathrm{Gd}}}$. Here, a_i and b_i are the zero temperature magnetisations and the critical exponents of the two elements, respectively. These model parameters can be extracted analytically from the linear slope of the $M_{\mathrm{s}}(T)$ data near $T_{\mathrm{M}} = 240$ K. Specifically,

$$b_{\mathrm{Gd}} = \tau_{\mathrm{M}} \frac{M_{\mathrm{s}}'(T_{\mathrm{M}})T_{\mathrm{c}} + a_{\mathrm{Co}} b_{\mathrm{Co}} (\tau_{\mathrm{M}})^{b_{\mathrm{Co}}-1}}{a_{\mathrm{Co}} (\tau_{\mathrm{M}})^{b_{\mathrm{Co}}}} \tag{7.2}$$

and

$$a_{\mathrm{Gd}} = a_{\mathrm{Co}} (\tau_{\mathrm{M}})^{b_{\mathrm{Co}}-b_{\mathrm{Gd}}}, \tag{S3}$$

where $\tau_{\mathrm{M}} = T_{\mathrm{M}}/T_{\mathrm{c}}$. We now assume $a_{\mathrm{Co}} = 1.4 \times 10^6\ \mathrm{A/m^2}$, i.e., the zero temperature bulk magnetisation of Co, as well as $b_{\mathrm{Co}} = 1/2$ and $T_{\mathrm{c}} = 450$ K. The result is

$$M_{\mathrm{s,Co}} = 1.40\,\frac{\mathrm{MA}}{\mathrm{m}}\left(1 - \frac{T}{450\ \mathrm{K}}\right)^{0.5}, \tag{S4}$$

$$M_{\mathrm{s,Gd}} = 1.71\,\frac{\mathrm{MA}}{\mathrm{m}}\left(1 - \frac{T}{450\ \mathrm{K}}\right)^{0.76}. \tag{7.3}$$

These functions are in excellent agreement with the experimental data, see Figure 7.1, and consistent with similar measurements of GdFeCo[16]. The Gd sublattice $M_{\mathrm{s,Gd}}$ dominates at low temperatures $T < T_{\mathrm{M}}$, while the Co sublattice has a stronger magnetic moment at higher temperatures $T_{\mathrm{M}} < T < T_{\mathrm{c}}$. Note that any errors originating from our estimates of a_{Co}, b_{Co}, and T_{c} only affect the extracted value of g_{Co} and not the qualitative or quantitative shape of the predicted $v(j, T)$ behavior in the main paper.

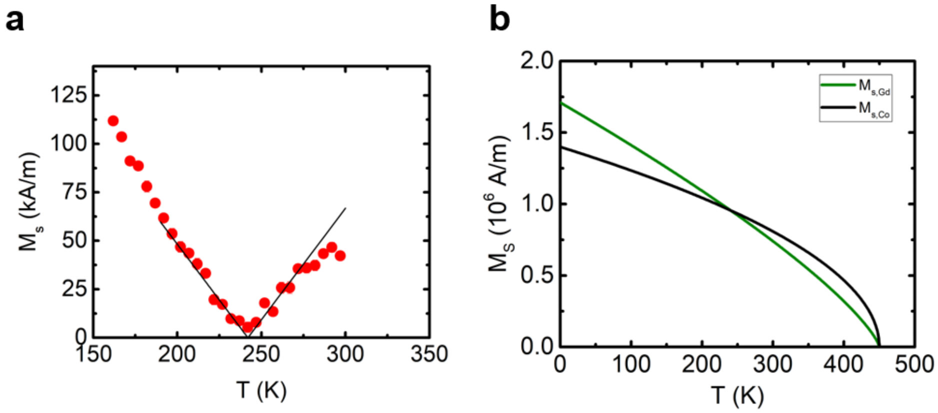

Figure 7.1 | a, Saturation magnetisation $M_{\mathrm{s}}(T)$ data measured on a continuous film reference sample by vibrating sample magnetometry and linear fit near magnetic compensation T_{M} to extract the model parameters. **b,** Extracted sublattice component magnetisations $M_{\mathrm{s,Co}}$ and $M_{\mathrm{s,Gd}}$ as a function of temperature T, showing a crossover at the magnetic compensation temperature $T_{\mathrm{M}} = 240$ K.

7.2 Current pulse profile and velocity calibration

Current-driven dynamics of domain walls requires injection of high bandwidth current pulses in to the magnetic sample. For instance, a domain wall will moving at 1km/s will travel a distance of 1um every nanosecond. Moreover, high voltages are needed to supply enough current into these resistive devices. For this reason, high bandwidth pulses for DW motion experiments were delivered to the sample from a custom built nanosecond pulse generator via a waveguide. A low duty cycle was used to avoid heat build-up and damage.

Pulse Duration

The velocity of a DW is calculated by measuring the distance the DW has moved during a current pulse of known duration. Thus, it is critical to accurately determine the effective width of each pulse. To inject current across the sample, we designed a high voltage pulse generator capable of producing 40 V pulses with a rise and fall time of about 400 ps. The width of the pulse was controllable using precisely timed start and stop signals generated by a Stanford Research DG535 delay generator. The pulse shape was measured with a 20 GHz bandwidth Tektronix 11801 sampling oscilloscope with a SD-26 sampling head. The injected pulses are not perfectly square (see Fig 7.2a), so we define the effective pulse width t_{pulse} to be the area of the pulse divided by the peak pulse height. By this definition, in the case of a linear v(j) curve, the velocity determined as the ratio of total displacement to the effective pulse width is equal to the instantaneous velocity at the peak pulse amplitude. To eliminate effects from the small nonzero offset (Fig 7.2a), we define a threshold current density, j_{th}, above which we measure the area under the curve. DW motion measurements were performed using a narrow, nominally 1ns size pulse rather than a longer pulse with a more square shape (see Fig. 7.2a). This was done for two reasons: 1) to reduce the large effects of heating on the sample (see Supplementary II) and 2) pulses of longer duration caused field-free switching of the sample.

For a single pulse measurement, the velocity depends on the choice of threshold current density, j_{th}. Fortunately, we can completely eliminate this ambiguity by measuring the displacement for a variety of pulses (Fig. 7.2b) for which the pulse width t_{pulse} is determined using the same threshold j_{th}. Figure 7.2b shows the change in lateral position of a DW Δx as a function of t_{pulse}, where the red data points use $j_{\mathrm{th}} = 0.03 \times 10^{12}\,\frac{\mathrm{A}}{\mathrm{m}^2}$ and the orange data points use $j_{\mathrm{th}} = 0.33 \times 10^{12}\,\frac{\mathrm{A}}{\mathrm{m}^2}$. The slope $\mathrm{d}\Delta x/dt_{\mathrm{pulse}}$ is the same for both thresholds (345 m/s). This slope varies by less than 1% over a wide range of j_{th}, thereby providing a robust and meaningful definition of DW velocity. In the main text, we use $j_{\mathrm{th}} = 0.33 \times 10^{12}\,\frac{\mathrm{A}}{\mathrm{m}^2}$, i.e., the value where the $\Delta x/t_{\mathrm{pulse}}$ and $\frac{\mathrm{d}\Delta x}{dt_{\mathrm{pulse}}}$ are the same, and perform all experiments at fixed $t_{\mathrm{pulse}} = 1.1$ ns.

Domain wall velocity measurement

In a typical DW velocity measurement, one or more pulses are applied to drive a domain wall between sets of wide field MOKE image acquisitions. The position of the domain wall is measured from the wide field images (Figure 7.2c). The average velocity v is calculated by $v = \frac{\Delta x}{n\, t_{\mathrm{pulse}}}$ where n is the number of pulses applied. In each measurement, enough pulses are applied to translate the domain wall by a distance of at least 20 µm, unless the DW velocity is so small that doing so would take a prohibitive amount of time. At any point where a velocity is reported, the error bar indicates the standard deviation of at least 5 independent, repeated measurements of the DW motion under those conditions. A typical sequence involves setting the temperature, measuring velocity for a series of current densities, then returning to the first current density and beginning the second repeat measurement.

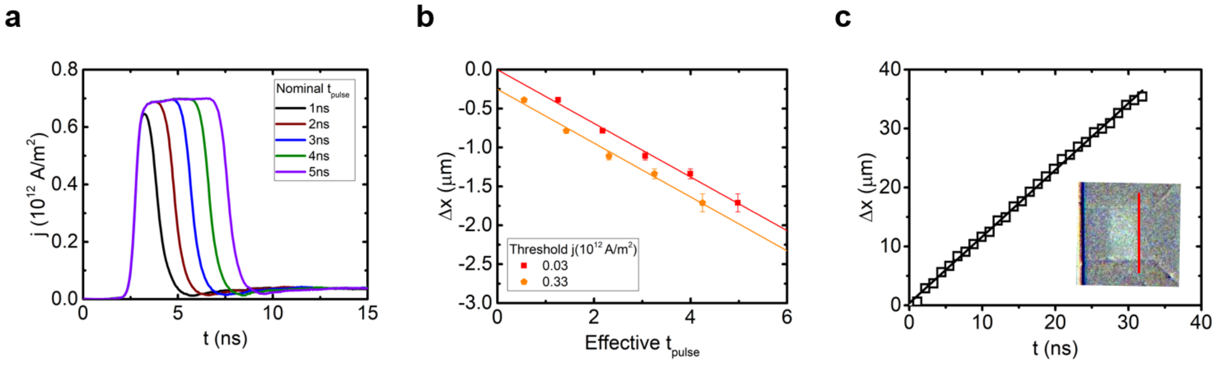

Figure 7.2 | Pulse calibration and velocity measurement. a, Temporal profile of current pulses j with nominal width from 1 to 5 ns after transmission through our sample. **b,** Measured displacement Δx versus t_{pulse} for the five waveforms in (a), where the effective pulse widths t_{pulse} were determined using two different thresholds as indicated in the legend j_{th}. **c,** Displacement of domain wall Δx as a function of cumulative pulse duration t. **inset,** Example Kerr image, in which the red line indicates the position of a DW.

7.3 Modeling of ferrimagnetic soliton dynamics

Magnetisation dynamics in ferromagnets follows the Landau-Lifshitz-Gilbert equation

$$\dot{\mathbf{m}} = -\frac{\gamma\mu_0}{1+\alpha^2}\mathbf{m}\times\mathbf{H} + \frac{\gamma\alpha\mu_0}{1+\alpha^2}\mathbf{H}_\perp \tag{7.4}$$

with γ the gyromagnetic ratio, α the Gilbert damping, and $\mathbf{m}$ the magnetisation $\mathbf{M}$ normalized by its saturation value M_s. $\mathbf{H} = -\frac{\delta E}{\delta \mathbf{M}}$ is the effective magnetic field, including applied and internal contributions, with $\mathbf{H}_\perp = -\mathbf{m}\times(\mathbf{m}\times\mathbf{H})$ the component perpendicular to $\mathbf{m}$. The first term in Eq. (7.4) causes precession around $\mathbf{H}$ while the weaker dissipative term slowly brings $\mathbf{m}$ toward $\mathbf{H}$. This indirect mechanism often limits switching and domain wall speeds in ferromagnets.

In the case of ferrimagnets with strongly exchange-coupled antiparallel sublattices, Eq. (7.4) can be adapted by renormalizing γ and α to[25]

$$\gamma \rightarrow \gamma' = \frac{M_s(T)}{S(T)} \tag{7.5}$$

$$\alpha \rightarrow \alpha' = \frac{S_0}{S(T)} \tag{7.6}$$

with

$$M_\mathrm{s}(T) = \left|M_{\mathrm{s},1}(T) - M_{\mathrm{s},2}(T)\right| \tag{7.7}$$

$$S(T) = \left|\frac{M_{\mathrm{s},1}(T)}{\gamma_1} - \frac{M_{\mathrm{s},2}(T)}{\gamma_2}\right| \tag{7.8}$$

$$S_0 = \alpha_0 \left(\frac{M_{\mathrm{s},1}(T)}{\gamma_1} + \frac{M_{\mathrm{s},2}(T)}{\gamma_2}\right), \tag{7.9}$$

where subscripts denote sublattices, α_0 parametrizes the damping, and $\gamma_i = g_i\mu_\mathrm{B}/\hbar$ is the gyromagnetic ratio (with g the Landé g-factor, μ_B the Bohr magneton, and $\hbar$ the reduced Planck constant). M_s and stray fields vanish at the temperature T_M, which is generally distinct from the angular momentum compensation temperature T_A where the net spin density $S(T) = 0$. Most effective fields scale as $1/M_\mathrm{s}(T)$, suggesting applied torques might become extremely efficient near T_M. However, since $\gamma \propto M_\mathrm{s}$, $\gamma\mathbf{H}$ remains finite and so no anomalies are expected as $M_\mathrm{s} \rightarrow 0$. At T_A, by contrast, both γ and α diverge so that the precessional term in the Landau-Lifshitz-Gilbert equation vanishes, leaving

$$\dot{\mathbf{m}} = \frac{\mu_0 M_\mathrm{s}(T)}{S_0}\mathbf{H}_\perp = \frac{1}{S_0}\mathbf{h}_\perp, \tag{7.10}$$

with $\mathbf{h}_\perp = \mu_0 M_s(T)\mathbf{H}_\perp = \delta E/\delta\mathbf{m}$. This fundamentally changes the dynamics of solitons (quasi-particles) such as DWs and skyrmions. In general, the precession term of the Landau-Lifshitz-Gilbert equation leads to topological gauge terms in the Lagrangian and in the equation of motion of any magnetic soliton[26] and ultimately to typical topological dynamics, such as the Walker breakdown of DWs and the Hall effect[27,28] and gyration[29] of skyrmions. At T_A, all of these effects vanish and magnetic quasi-particles behave like Newtonian particles, i.e., they move immediately and rapidly in the direction of applied force[12,30,31], which is highly desirable for many applications.

7.4 Fast domain wall motion near angular momentum compensation

We examine spin texture statics and dynamics in $Gd_{44}Co_{56}$, an amorphous ferrimagnetic alloy whose antiferromagnetically-coupled sublattices (Fig. 7.3a) possess similar g-factors so that T_{A} is close to T_{M}. Perpendicularly magnetized Ta(1)/Pt(6)/$Gd_{44}Co_{56}$(6)/TaO_x(3) (thicknesses in nm) samples were grown using d.c. magnetron sputtering at nominal room temperature with an Ar sputter gas pressure of 3 mTorr and a background base pressure of $\sim 2 \times 10^{-7}$ Torr. Samples were deposited on thermally oxidized Si wafers. The composition of the alloy was chosen to yield compensation near room temperature We neglect current shunting through the Ta seed layer, as the resistivity of Ta is approximately 10 times higher than in Pt. GdCo was co-deposited using separate Co and Gd targets, and the composition was controlled by varying the Gd sputter gun current. Deposition rates were calibrated using x-ray reflectivity measurements of film thickness. The bottom Pt layer serves as a source of SOT owing to the spin Hall effect in Pt, while simultaneously generating a strong Dzyaloshinskii-Moriya interaction (DMI). The top TaO_x is a protective cap. Figure 7.3b shows the temperature (T) dependence of M_{s} and coercivity H_{c}, obtained by vibrating sample magnetometry and magneto-optical Kerr effect (MOKE) polarimetry, respectively Figure 7.3c,d shows representative out-of-plane MOKE hysteresis loops. $M_{\mathrm{s}}(T)$ vanishes and $H_{\mathrm{c}}(T)$ diverges at $T \approx 240$ K, which identifies this temperature as T_{M}. The MOKE contrast inverts across T_{M} as expected, since it arises primarily from the Co sublattice which is parallel (antiparallel) to the net magnetisation above (below) T_{M}.

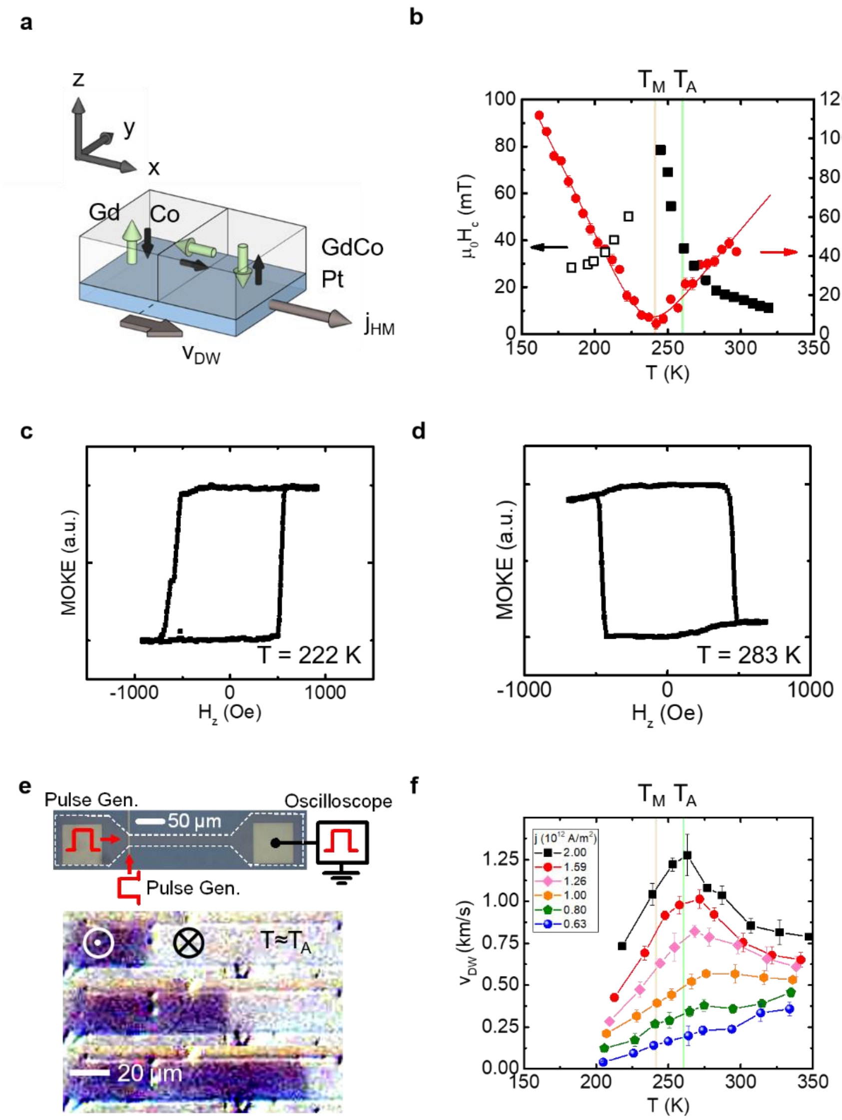

Figure 7.3 | Measurement of T_A and T_M. a, Schematic of Pt/Co44Gd56 layer structure with ferrimagnetic Co44Gd56 exhibiting perpendicular magnetic anisotropy (TaO$_x$ cap not shown). Green arrows (black arrows) indicate the Gd (Co) sublattice moments in a domain wall (DW) structure. **b,** Coercivity $\mu_0 H_c$ and saturation magnetisation M_s as a function of temperature. Open (filled) squares indicate positive (negative) sign of the MOKE signal at positive field saturation. Representative MOKE hysteresis loops are measured at $T = 222\ K$ (**c**) and $T = 283\ K$ (**d**). The orange and green vertical lines indicate magnetic compensation T_M and angular momentum compensation T_A, respectively. **e,** Kerr microscopy images showing current-driven DW motion near T_A, where a train of N current pulses with amplitude $j_{HM} = 1.5 \times 10^{12}\ \mathrm{A/m^2}$ was injected between each image frame. **f,** Domain wall velocity v_{DW} as a function of temperature for various current densities. Error bar represents the standard deviation of 5 to 20 independent measurements of domain wall velocity (Fig. 7.2). Sample temperature was corrected for instantaneous heating during current application (see Fig. 7.10).

Domain wall motion was studied in lithographically patterned tracks using wide-field Kerr microscopy. Figure 7.3e shows a series of Kerr snapshots acquired as nanosecond current pulses were injected to drive a domain wall along the track (Methods). Both up–down and down–up domain walls move along the current flow direction, consistent with SOT-driven left-handed Néel domain walls5,6,22. Figure 7.3f shows domain wall velocity (v_{DW}) versus T for several current densities j_{HM} in the Pt layer. The $v_{DW}(T)$ curves are shifted horizontally to account for Joule heating (Supplementary Figs. 7.10 and 7.11). At a low current, v_{DW} increases monotonically with T, whereas at a larger current vDW exhibits a pronounced peak at T ≈ 260 K, significantly above T_M.

7.5 Measurement of χ via DC domain wall depinning measurements and field assisted creep

The effective field per unit current density, χ ,acting on the DW due to damping-like spin orbit torque, was measured using a custom built, wide-field (MOKE) microscope system with focused laser capabilities, using a spot size of ~ 10 μm. Measurements were performed on a lithographically defined magnetic wire of 200×40 μm^2 in dimension. χ was measured using two techniques, both yielding consistent results.

DC Domain Wall Depinning

In this technique, the propagation field of a pre-nucleated domain wall is recorded as a function of DC current density in the heavy metal underlayer of the magnetic material, and the field-to-current ratio is used as a measure of χ, similarly to the work in Ref [32]. The procedure is as follows. A triangular magnetic field is swept at a fixed rate ($1/60$ s from zero to maximum field) and hysteresis loops are measured using a focused laser spot at a fixed distance $\sim 150\ \mu\text{m}$ away from a DW nucleation line. At the zero-field crossing of the triangle wave (time t_0), a domain wall is nucleated at the left end of the magnetic track using the Oersted field from a current pulse injected through the orthogonal nucleation line, see Fig. 7.4a. When the applied field reaches the DW propagation field, the DW is swept across the laser spot. The field at which the magnetisation switches below the laser spot is the propagation field H_{prop}.

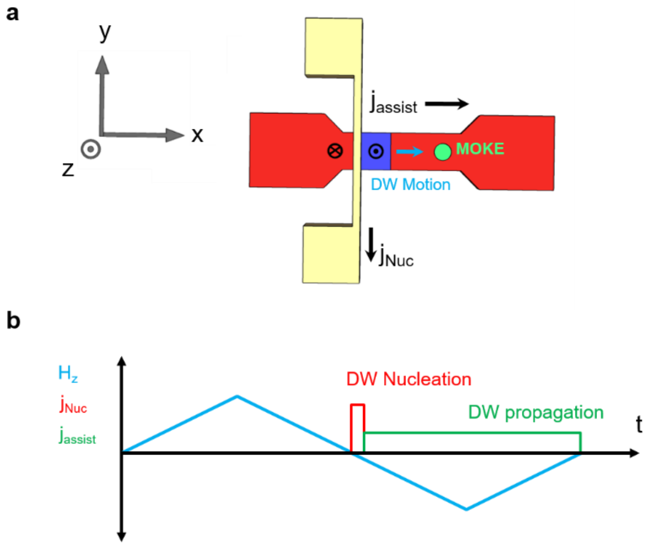

Figure 7.4 | Schematic of DC current DW depinning. a, Schematic diagram of DC current domain wall depinning measurement. **b,** Sequence of applied fields and currents. First, a reset field saturates the magnetisation uniformly down (up-part of the triangular field ramp). At time t_0, the field ramp crosses zero and a nucleation pulse j_{nuc} generates a domain-wall pair near the nucleation line. Lastly, a DC domain wall propagation current j_{assist} is applied while out-of-plane field H_z ramps. The value of H_z when the domain wall passes beneath the MOKE laser spot is recorded as the propagation field H_{prop}.

If we omit the DW nucleation pulse, the switching field under the MOKE laser corresponds to the nucleation field H_{nuc}. By including the DW nucleation pulse, the switching field under the MOKE laser corresponds to the propagation field H_{prop}. For measurements of χ, we include the nucleation pulse on only one of the zero crossings of the triangle wave (see Figs

7.4b). Thus, when plotting the Kerr signal (proportional to M_z) versus the out-of-plane field H_z, the data appear as a hysteresis loop, where the switching field on one side corresponds to the nucleation field H_nuc and that on the other side corresponding to the propagation field H_prop. Whenever the latter is smaller than the former, one can be assured that the switching indeed occurs via propagation of the single nucleated DW at the nucleation line. During the DW propagation along the track, we apply a DC current along the track of varying magnitude (see Fig 7.4b). Fig. 7.5b shows the propagation field as a function of DC current density, which verifies that the current acts as an out-of-plane effective field that can assist or hinder DW propagation. Each point on this curve was extracted averaging the results for ten switching cycles to account for stochasticity in DW propagation. The slope of $H_\mathrm{prop}(j)$, is taken as χ.[32] Measurements were performed at various temperatures and $\chi(T)$ is shown as closed square symbols in Figure 7.5e.

Note that this type of measurement requires $H_\mathrm{prop} < H_\mathrm{nuc}$, where H_nuc is the threshold at which the applied field nucleates DWs in the track. This can be seen in Fig. 7.5a, where H_nuc is the switching field at negative fields and H_prop is the switching field at positive fields. Below T_M, we find that the DW nucleated near the nucleation line by the current pulse remains pinned at out-of-plane fields H_z that are sufficient to nucleate other DWs in the track. This makes the depinning measurement unreliable below T_M, since the DW responsible for magnetisation switching is undefined. Hence, at lower temperatures we use field-assisted creep of current-driven DWs to extract χ, which was shown in Ref [32] to similarly yield χ.

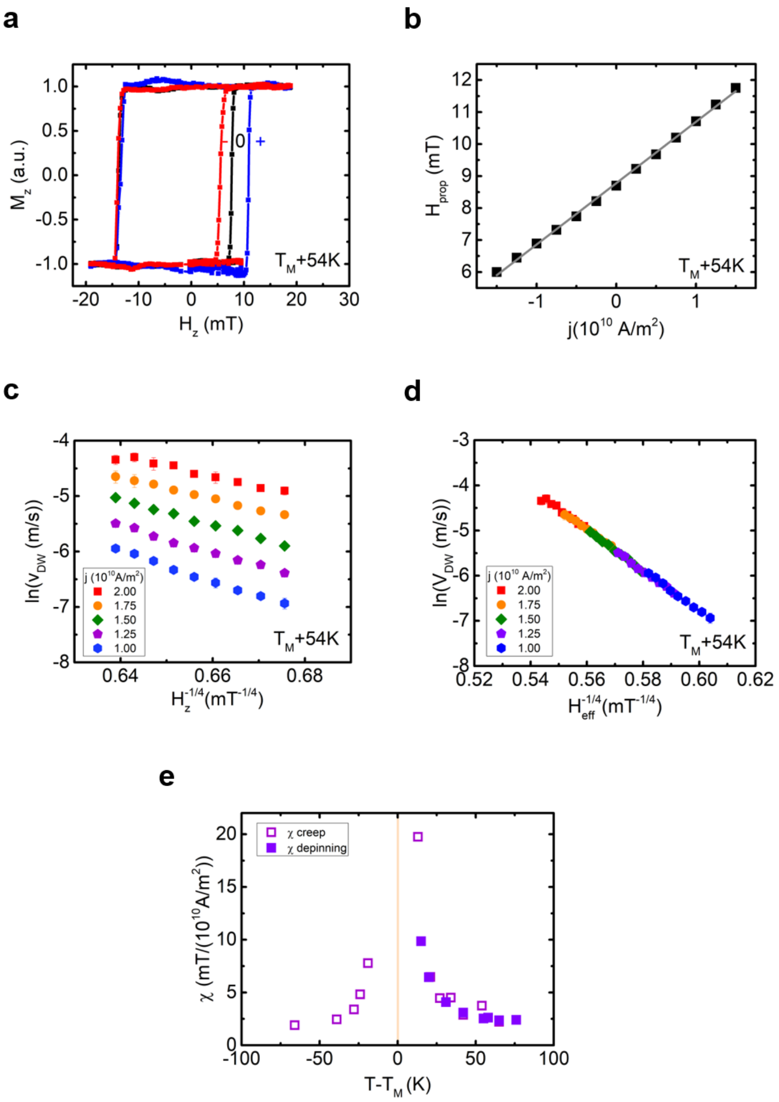

Figure 7.5 | χ measured via DC domain wall depinning and field assist creep. a, Exemplary, normalised domain wall DC depinning hysteresis loops with positive (blue), negative (red), and no (black) current j applied. $M_z$is the z-component of the magnetisation **b,** H_{prop} (positive zero crossing) as a function of DC current j, the slope of which yields χ. **c,** Domain wall velocity as a function of field for various DC creep currents. **d**, Equating j as an effective field $H_{\text{eff}} = H_{\text{z}} + \chi j$, the measurements lie along the same line. **e,** Resulting χ from both domain wal DC depinning (closed squares) and current assisted creep (open squares) across magnetic compensation T_{M}.

Field Assisted Creep

The DW velocity was measured as in the main paper, but using much smaller current densities j. In addition, an out-of-plane field pulse was applied simultaneously with the current. Both current and field were rectangular pulses with 50 ms duration. The DW displacement was measured by wide-field Kerr imaging of the domains before and after the combined current-field pulse. For each temperature, several combinations of current and field were assessed. The equivalence of applied current and applied field is evaluated by calculating χ as the ratio of the change in velocity with current to the change in velocity with field, $\chi = \frac{(dv/dj)}{(dv/dH_{\mathrm{z}})}$, over the discrete series of measurements[33]. The velocity is plotted as a function of H_{z} for a series of different current densities in Figure 7.5c. After transforming j into an effective field $H_{\mathrm{eff}} = H_{\mathrm{z}} + \chi j$, the measurements all lie along the same line (Fig. 7.5d), indicating the equivalence of field and current driven DW motion in the creep regime. The field-assisted creep measurement (open squares) and the DC depinning measurement (filled squares) show precise agreement, see Figure 7.5e.

7.6 Hall effect measurements

Figures 7.6a,b show the generalized harmonic voltage measurement configuration used to independently quantify the damping-like SOT above and below compensation. The harmonic data were measured on a film of Ta(1)/Pt(8)/GdCo(12)/TaO_x(3) film (thicknesses in nm) where T_{M} was 40 K higher than in the sample of the main text.[34] The film was patterned into a Hall cross geometry 5 μm wide × 12 μm long with 3 μm wide side contacts as shown schematically in Figs. S6a,b. An applied a.c. longitudinal current, $5.0 \times 10^{10}\,\frac{\mathrm{A}}{\mathrm{m}^2}$ at 1.7 kHz, senses the out of plane component of the magnetisation via the anomalous Hall effect and simultaneously exerts

SOT on the magnetisation. We apply a magnetic field H_x with a small out-of-plane component ($\theta_H = 80°$ is the angle to the out-of-plane axis) to maintain a single-domain state at all fields. Figs. 7.6c,d show typical first ($V_{\omega 1}$) and second ($V_{\omega 2}$) harmonic voltages for 313 K and 223 K, respectively.

The sign of the AHE signal inverts across magnetic compensation, following the transition metal sublattice as shown elsewhere.[34–36] The net perpendicular magnetic anisotropy is determined from the first harmonic voltage measurement by fitting to the Stoner-Wohlfarth model. Then the damping like SOT is determined by[37,38]

$$H_{\mathrm{SH}} = 2\frac{dV_{2\omega}}{dH_x} / \frac{d^2V_{\omega}}{dH_x{}^2}. \tag{7.11}$$

We correct for the contribution of the Planar Hall Effect (PHE) as described in [37,39,40]. We find that the ratio of the PHE coefficient to that of the AHE is within 0.03 to 0.05 over all measured temperatures.

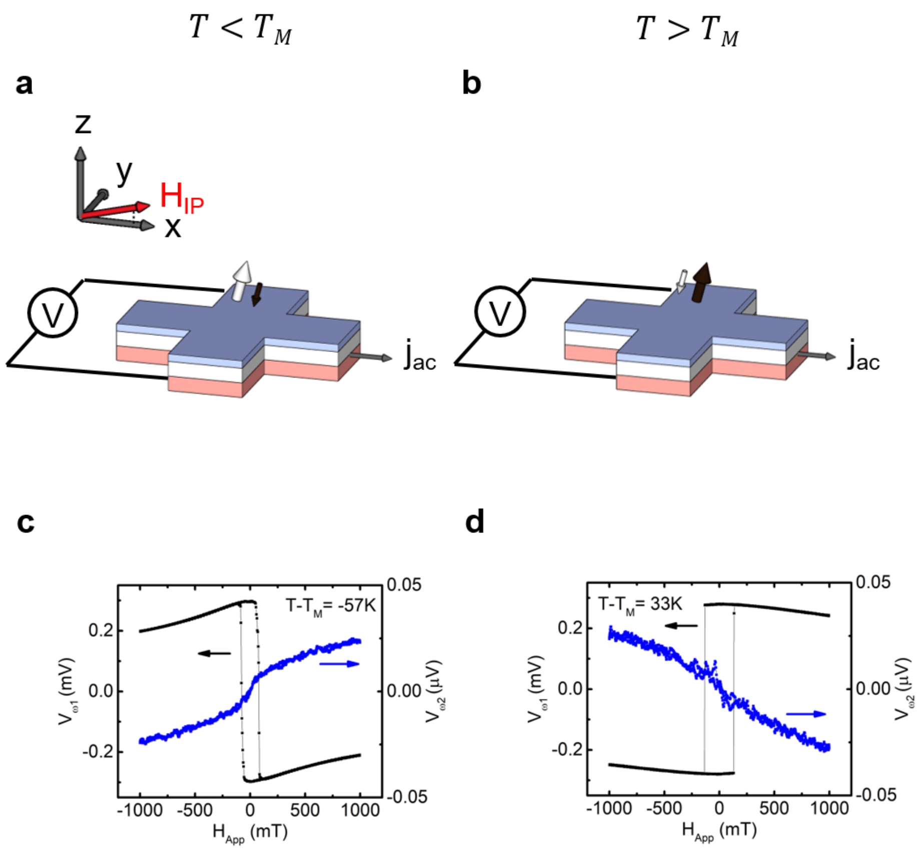

Figure 7.6 | Harmonic anisotropy and SOT measurements. a,b, Schematic of Hall cross for harmonic voltage measurement below (**a**) and above (**b**) magnetic compensation T_{M}. H_x is the applied in-plane field **c,d**, First ($V_{\omega 1}$) and second ($V_{\omega 2}$) harmonic voltage as a function of applied field H_{App}.

Figure 7.7a,b shows the dependence of crystal anisotropy field $H_{\mathrm{K_u}}$ on $T - T_{\mathrm{M}}$ and $\frac{1}{M_{\mathrm{S}}}$, respectively. The crystal anisotropy field is $H_{\mathrm{K_u}} = H_{\mathrm{K}} + M_{\mathrm{s}}$, where H_{K} is the result of the first harmonic voltage measurement under in-plane applied field, and M_{s} equals the demagnetising field in the homogeneously out-of-plane magnetised thin film. From the fit, the internal anisotropy energy is $K_{\mathrm{u}} = 53\ \mathrm{kJ/m^3}$. Because $H_{\mathrm{K_u}}$ exhibits a $\frac{1}{M_{\mathrm{S}}}$ dependence, we can conclude that K_{u} does not significantly depend on temperature, within the experimental measurement range.

Damping-like effective fields $H_{\mathrm{DL}}(T)$ from harmonic measurements are plotted in Figures 7.7c,d as a function of temperature. These fields are directly correlated to the efficiency of driving a DW with SOT via $\chi = \frac{\pi}{2} H_{\mathrm{SH}}/j$.[41,42] For direct comparison with the DW measurements in Fig. 7.5, we therefore plot $\frac{\pi}{2} H_{\mathrm{SH}}$ in Fig. 7.7. Both measures of SOT efficiency scale linearly with $\frac{1}{M_{\mathrm{s}}t}$. The thickness term t is explicitly included because the H_{SH} measurements were carried out on a sample with 12 nm GdCo and the χ measurements used a sample with 6 nm GdCo. H_{SH} exhibits the same $\frac{1}{M_{\mathrm{s}}}$ dependence and sign across compensation, confirming the results measured with DW depinning.

Fits to these two measures of SOT efficiency are expected to yield the same slopes. However, we observe that the slope of the harmonic measurement is approximately half that of the DW depinning measurement (Figures 7.8b,c). This may be explained by differences in layer thicknesses. First, the thickness of the Pt in the harmonic measurement was 8 nm, compared to 6 nm for the depinning measurement. Due to the limited spin diffusion length of Pt of 1.2 nm,[43] thicker Pt films will appear to exhibit reduced spin Hall angle as spin current generated in the distant Pt region is attenuated before it reaches the interface. Further complicating the comparison, the distribution of current density in the heterostructure is not known, and all current is assumed to flow in the Pt layer. Independent of these uncertainties, the harmonic measurements confirm the sign and $\frac{1}{M_{\mathrm{s}}}$ dependence of SOT across compensation.

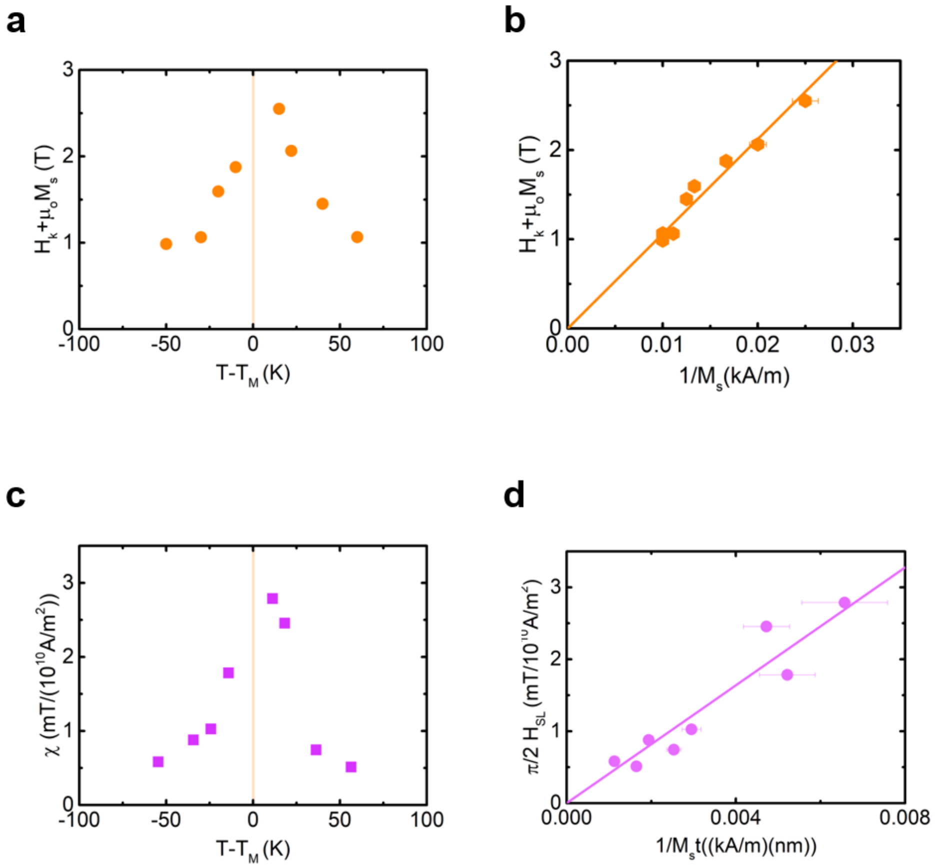

Figure 7.7 | Harmonic anisotropy and SOT measurements. Crystal anisotropy field H_{K_u} (**a,b**) and spin Hall field H_{SH} (**c,d**) as a function of temperature $T - T_{\mathrm{M}}$ and $M_s t$. Divergence at magnetic compensation T_{M} and an inverse magnetisation $\frac{1}{M_{\mathrm{S}}}$ dependence are clearly seen.

7.7 Summary of Current Induced Effective Fields

The SOT and DMI effective fields diverge at T_{M} and not at the velocity peak, implying that their divergence is not responsible for the dramatic velocity enhancement in Fig. 7.3f. This is experimentally verified in figure 7.8a, showing field- and current-driven DW velocity in the creep regime, where identical scaling is observed in both cases. Current hence acts like an easy-axis effective field $H_z^{\mathrm{eff}} = \chi\, j_{\mathrm{HM}}$, as expected for damping-like SOT acting on Néel DWs. In that case[21]

$\chi = \frac{\pi}{2}\frac{\hbar\Theta_{\mathrm{SH}}^{\mathrm{eff}}}{2e\mu_0 M_s t}$, with t the magnetic film thickness, e the electron charge, and $\Theta_{\mathrm{SH}}^{\mathrm{eff}}$ the effective spin Hall angle. Figures 2b,c show that $\chi(T)$ scales as $1/M_{\mathrm{s}}(T)$, as expected from theory and previous studies[44–48], from which we determine $\Theta_{\mathrm{SH}}^{\mathrm{eff}} = 0.155$, which is nearly independent of temperature in this range. Harmonic SOT measurements are consistent with these results (see Figs. 7.6, 7.7).

The DW chirality and DMI effective field H_{DMI} can be obtained from the dependence of v on longitudinal field H_x [6]. SOT-driven DW velocity increases (decreases) when H_x is parallel (antiparallel) to H_{DMI}, which sets the orientation of the Néel DWs. The measured positive (negative) slopes of $v(H_x)$ for down-up (up-down) DWs in Fig. 1d indicate left-handed chirality, both above and below T_{M}. Extrapolation to $v = 0$ yields H_{DMI}, which is related to D through $H_{\mathrm{DMI}} = \frac{D}{\mu_0 M_{\mathrm{s}}\Delta}$ with Δ the DW width[22]. As seen in Figs. 7.8e,f, H_{DMI} diverges as $1/M_{\mathrm{s}}(T)$, and we find $D = 0.12\ \mathrm{mJ/m^2}$. This compares well to DMI reported for Pt/ferromagnet systems[5,6,49,50] and Pt/ferrimagnet systems[51] considering the differences in *t*.

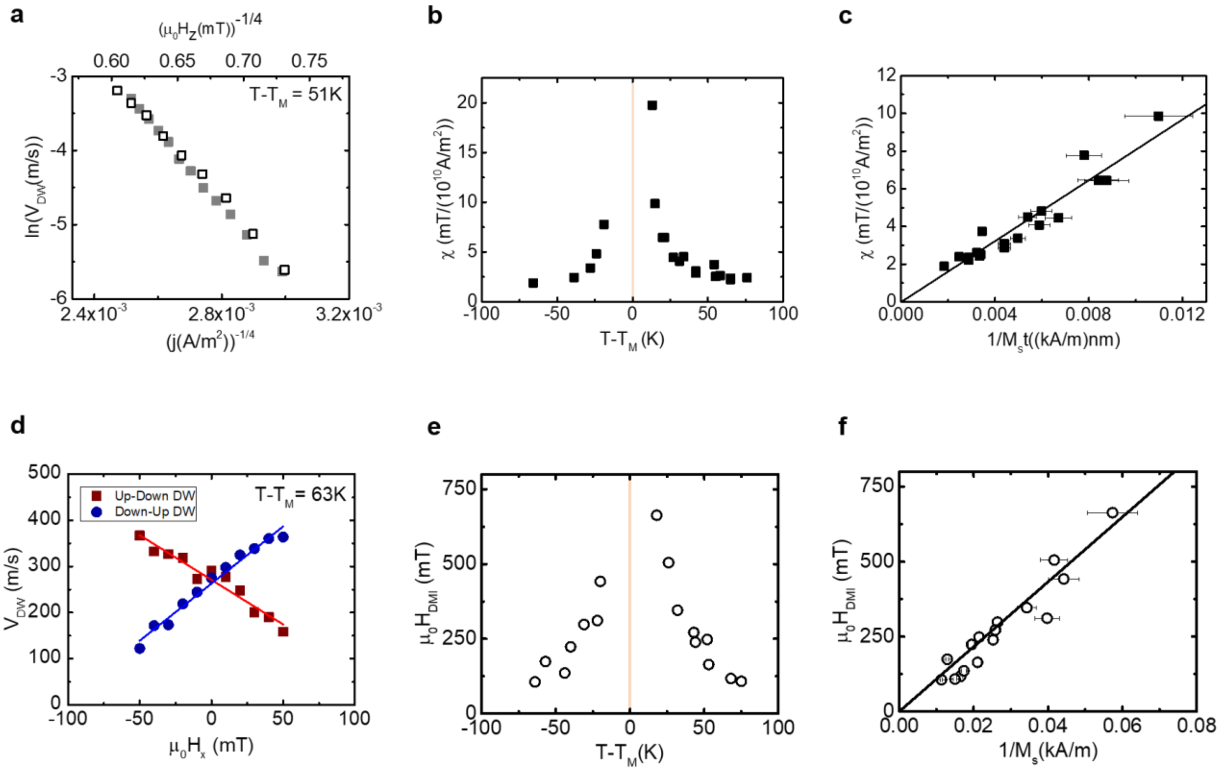

Figure 7.8 | Spin Orbit Torques and Dzyaloshinskii-Moriya Interaction. a, Out of plane field ($\mu_0 H_z$) and in-plane current (j) driven domain wall velocity v_{DW} in the creep regime. **b,** Spin orbit torque effective field per unit current density, χ, as a function of temperature T. Divergence occurs at magnetic compensation T_M (orange vertical line). **c,** χ plotted as a function of inverse saturation magnetisation M_s^{-1}. **d,** Exemplary domain wall velocity as a function of longitudinal applied field $\mu_0 H_x$ at $T - T_\mathrm{M} = 63\ K$. The $\mu_0 H_x$-intercept of the linear fit gives the DMI effective field $\mu_0 H_\mathrm{DMI}$ [6]. **e,** $\mu_0 H_\mathrm{DMI}$ as a function of T. Divergence occurs at T_M (orange vertical line). **f,** $\mu_0 H_\mathrm{DMI}$ effective field as a function of M_s^{-1}. Error bars in **e,f** are propagated from $M_s(T)$ fit (see Fig. S1).

7.8 One Dimensional Model of a Ferrimagnet

The spin Hall effect-driven velocity of chiral DWs in ferromagnets is given in the 1D model by[22]

$$v_\mathrm{FM} = \frac{\gamma}{M_\mathrm{s}} \frac{\pi}{2} \frac{D j_\mathrm{HM}}{\sqrt{j_\mathrm{HM}^2 + \alpha {j_0}^2}}, \tag{7.12}$$

where $j_0 = \frac{2etD}{\hbar\theta_{\mathrm{SH}}\Delta}$. The velocity first increases linearly with current, $v_{\mathrm{FM}} \approx \frac{\gamma}{\alpha M_{\mathrm{s}}}\frac{\pi}{2}D\frac{j_{\mathrm{HM}}}{j_0}$, eventually saturating toward $v_{\mathrm{sat}} = \frac{\gamma}{M_{\mathrm{s}}}\frac{\pi}{2}D$ for $j_{\mathrm{HM}} > \alpha j_0$, which serves to limit DW speed. However, in ferrimagnets, α and γ are replaced by $\alpha'(T)$ and $\gamma'(T)$, yielding

$$v_{\mathrm{FiM}} = \frac{\pi}{2}\frac{Dj_{\mathrm{HM}}}{\sqrt{(S(T)j_{\mathrm{HM}})^2 + (S_0 j_0)^2}}, \tag{7.13}$$

which is independent of M_{s}. The denominator instead depends on the net spin density $S(T)$, which vanishes at T_{A} so that $v(j_{\mathrm{HM}})$ never saturates, allowing very high velocities to be attained.

Equation 9 explains well the $v(T)$ curves in Fig. 7.3e. At small $j_{\mathrm{HM}} \ll j_0$ the velocity is always in the linear regime since $S_0 j_0$ dominates in the denominator. At larger j_{HM}, the velocity is in the saturation regime except near $T \sim T_{\mathrm{A}}$ where $S(T) = 0$. This leads to a velocity maximum at T_{A} but no critical behaviour, consistent with Fig. 1d. We conclude that the velocity peak in Fig. 7.3e corresponds to the angular momentum compensation temperature $T_{\mathrm{A}} \approx 260$ K. Comparing T_{A} and T_{M} yields $g_{\mathrm{Gd}} = 2.0$ and $g_{\mathrm{Co}} = 2.05$, reasonably consistent with values reported for GdCo[52].

Figure 7.9 shows $v(T)$ calculated from Eq. (9) for several j_{HM}, using experimentally-determined parameters and modeling $M_{\mathrm{s,Gd}}(T)$ and $M_{\mathrm{s,Co}}(T)$ by fitting $M_{\mathrm{s}}(T)$ (see Section 7.1). Figure 7.9b shows corresponding calculated $v(j_{\mathrm{HM}})$ curves, which highlight the reason for the enhanced velocities observed near T_{A} in Fig. 7.3e. Far from compensation, $v(j_{\mathrm{HM}})$ increases linearly and then saturates. As T_{A} is approached, velocity saturation occurs at increasingly high j_{HM}, and when $T = T_{\mathrm{A}}$, $v(j)$ is always linear. Figure 7.9c shows experimental $v(j)$ curves at various cryostat temperatures, along with fits using the 1D model in which the Joule heating-induced temperature variation and pinning is included (see sections 7.8, 7.9). The latter finally explains the monotonic increase of $v(T)$ at small j_{HM}. Overall, we find that the simple effective ferromagnet model with scaled α and γ agrees well with our experimental data, implying that it accurately describes the underlying physics.

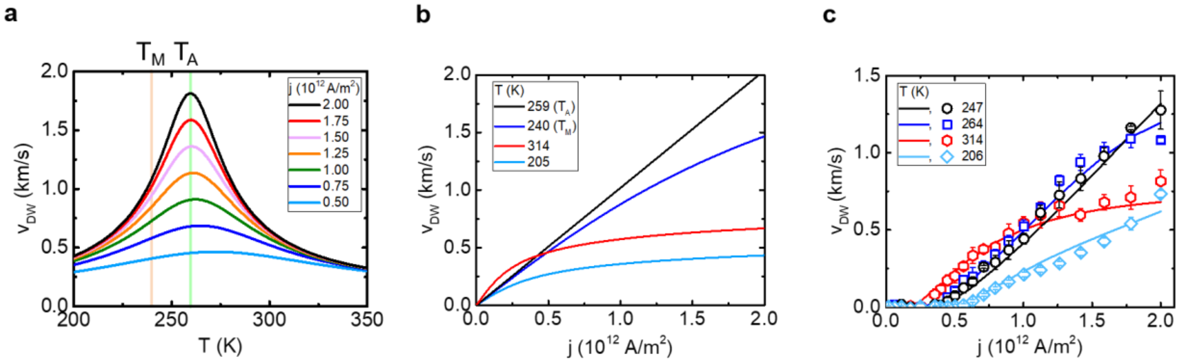

Figure 7.9 | Accurate modeling of temperature- and current-dependence of domain wall velocities. a, Terminal domain wall velocity v_{DW} as a function of temperature T as predicted by Eq. (7.13). The velocity peaks at angular momentum compensation T_A but does not diverge. Peaks are less pronounced at smaller heavy metal current density j_HM. **b,** Same data as in (a) plotted as a function of j instead of T. Near T_A the velocity $v(j)$ is linear for all j. **c,** Experimental $v(j)$ data (open data points) overlaid with a full 1D DW model (lines), including the experimental current pulse shape as well as thermal and pinning effects (see Methods and Fig. S3). Joule heating leads to a saturation of the data even near $T_A = 260$ K because the device temperature changes during the 1 ns pulse. Reduced de-pinning threshold at elevated temperatures is responsible for the sizable monotonic variation of v with T at small j. Error bar represents the standard deviation of 5 to 20 independent measurements of domain wall velocity (see Fig. 7.2)

7.9 Domain wall track heating calibration

The current pulses applied to our samples cause significant Joule heating at high current densities, which is important to account for since the magnetic properties depend sensitively on temperature. To characterise the temperature rise due to Joule heating, we utilise the fact that heating also induces small changes to the sample resistance. Thus, to measure the temperature of the sample, we monitor the current through the device (and hence its resistance) as a function of time. We convert the resistance into a temperature rise using a pre-calibrated measurement of DC sample resistance as a function of environmental temperature.

Experimentally this is done as follows: first, we send 50 ns current pulses of various amplitude through the sample and terminate the pulse into a digital sampling oscilloscope (Fig. 7.10a). A very low amplitude reference pulse with negligible heating serves to calibrate the shape of the pulse. Subsequent high amplitude pulses have the same shape at the input of the device (uniformly scaled). However, since heating increases the device resistance with time, the ratio of transmitted to incident voltage decreases at later times of the pulse, since a larger fraction of the pulse is absorbed in the sample. The (time-dependent) ratio of transmitted voltage at high amplitudes to transmitted voltage of the low amplitude reference pulse is therefore a direct measure of the time-dependent temperature increase $\Delta T(t)$ of the device.

Quantitatively, the resistance of the track can be computed from the circuit diagram in Fig. 7.10a knowing the voltage read at the oscilloscope after the pulse is transmitted across the sample. We then convert device resistance into temperature using an experimental calibration. Using the pre-calibrated measurement of DC sample resistance (Fig. 7.10b), the change in resistance of the track is $\frac{\Delta R}{R} = 7.6 \times 10^{-4}\ \mathrm{K}^{-1}$, nearly constant over the range of temperatures for which DW velocity was measured. Applying this conversion, we plot the temperature of the DW track during a 50 ns pulse of several amplitudes in Figure 7.10c.

The sample temperature exhibits an upward exponential decay, which is well described by the following rate equation:

$$\frac{dT}{dt} = hj^2 - (c_0 + c_1 j^2)\Delta T, \tag{7.14}$$

the solution of which is

$$\Delta T(t) = \Delta T_\infty (1 - \exp(-ct)), \tag{7.15}$$

where $\Delta T_\infty = \frac{hj^2}{c}$ is the equilibrium temperature at the end of very long pulses and $c = c_0 + c_1 j^2$ is the rate at which this equilibrium is approached. We can understand the terms of rate equation as follows: the term hj^2 is the temperature-independent thermal power deposited in the microstrip due to the application of current. The effective heating coefficient h includes the specific heat of the device as well as the resistance of the sample. Note that sample resistance changes are so small that h is temperature-independent in a very good approximation.

The second term $-c\Delta T$ with $c = c_0 + c_1 j^2$ in the rate equation describes the cooling of the sample. Here, $\Delta T = T - T_0$, where T_0 is the substrate temperature. This is an approximation of the heat equation that actually involves spatial gradients of the temperature. In particular, we assume that spatial gradients are proportional to ΔT. The proportionality is quantified by the effective cooling coefficient c. A constant c is not capable of describing our data because the spatial gradients also depend on the rate of temperature change: the faster the track heats up, the larger the thermal gradient is at the interface with the substrate. Fortunately, a slightly more sophisticated approximation can fully represent the experiments: since the heating rate depends on the dissipated electrical power $\propto j^2$, we can express $c = c(j^2)$ as a function of j^2. Experimentally, we see that a linear expansion $c(j^2) \approx c_0 + c_1 j^2$ is sufficient to describe the time-dependent heating, at least for time scales up to 50 ns.

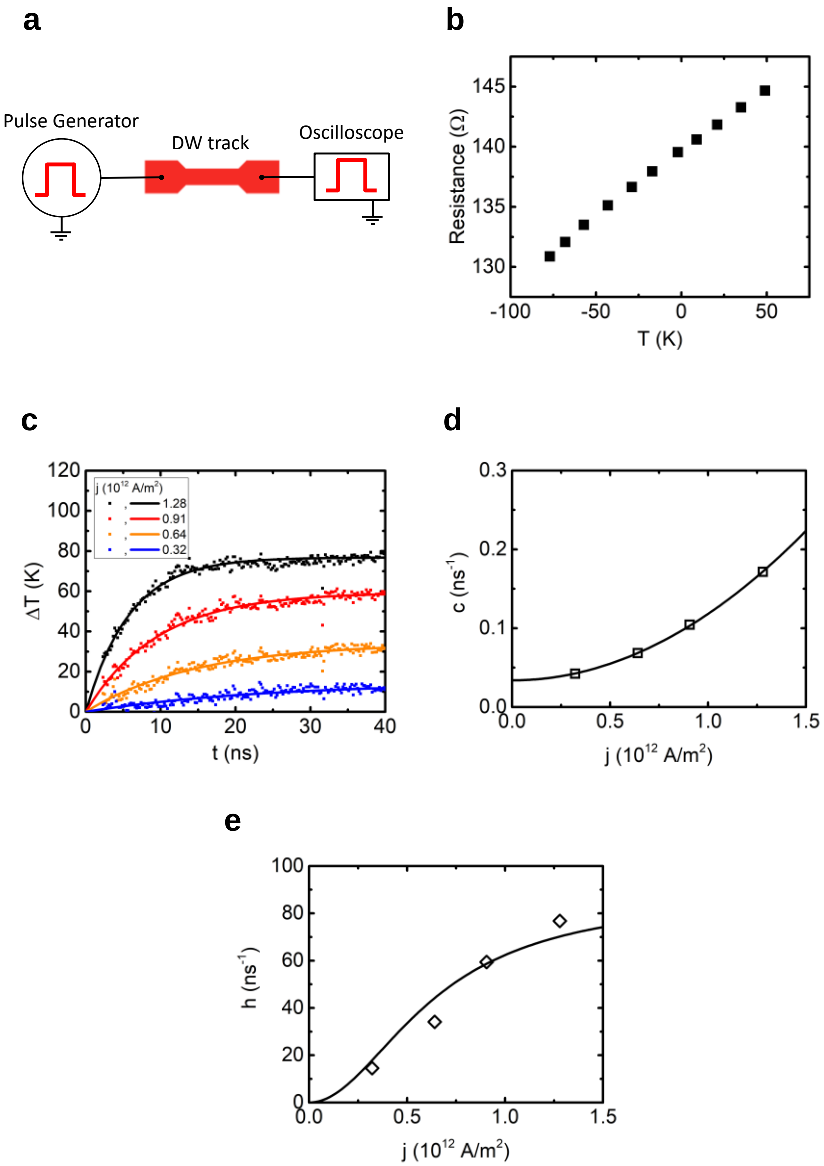

Figure 7.10 | Domain wall track heating calibration. a, Electrical schematic of the time-dependent resistance measurement of the sample. The amplitude of the pulse which passes through the sample is a direct measure of the sample resistance, which in turn is a measure of the sample temperature. **b,** Calibration curve of device resistance as a function of environmental temperature T. **c,** Temperature increase ΔT as a function of time t after the start of a 50 ns pulse. Points show experimental data which we fit with an exponential functions (curves) to determine the heating rate at short times. **d,e,** cooling and heating coefficients as a function of current density j. h, c_0, c_1 are extracted from fits (lines) to the data (points).

To extract the coefficients h, c_0, and c_1, we fit the experimental $\Delta T(t)$ with the exponential function in Eq. (7.15). We then plot ΔT_∞ and $c(j)$ and fit the expected quadratic dependence on j in Figures 7.10d,e. The experimental data are in excellent agreement with our simplified model. We obtain $h = 7.37 \frac{\mathrm{K\,ns^{-1}}}{\mathrm{TA\,m^{-2}}}$, $c_0 = 0.0339\ \mathrm{ns^{-1}}$, and $c_1 = 0.0843\ \frac{\mathrm{ns^{-1}}}{\mathrm{TA\,m^{-2}}}$. That is, a current of $10^{12}\,\frac{\mathrm{A}}{\mathrm{m^2}}$ heats the wire with 7.37 K per nanosecond, while the cooling by the substrate is $\sim$0.12 K per nanosecond per K of temperature difference ΔT. These numbers are in agreement with similar previous studies[53,54].

7.10 Realistic modeling of $v(j, T)$

Figure 7.9c shows DW motion predicted by the ferrimagnetic 1D DW model taking into account the time-dependent current density of the Gaussian pulse as well as heating and cooling according to Eq. (S6) and pinning. Specifically, we use the equations derived by Martinez *et al.*[22] and replace α and γ with the scaled ferrimagnetic parameters, see main text (note that $\gamma_0 = \mu_0\gamma$ in Martinez' model). We furthermore set $H_{x,y,z} = 0$ (no external field is applied), $H_K = 0$ (in-plane stray fields are insignificant due to the low M_s of our material), $H_\mathrm{R} = 0$ (ignoring the field-like SOT term for simplicity), and $\chi = 0$ (we find DW tilting to be insignificant in our material system). Finally, we are just interested in the magnitude of the DW velocity and hence we set without loss of generality $Q = 1$. In total, we use the equations

$$\dot{x} = \frac{\Delta}{1+\alpha(T)^2}\left(\Omega_A + \alpha(T)\Omega_B\right) \tag{7.16}$$

$$\dot{\Phi} = \frac{-\alpha(T)\Omega_A + \Omega_B}{1+\alpha(T)^2} \tag{7.17}$$

with

$$\Omega_A = \gamma(T)\mu_0 H_{\mathrm{DMI}} \sin\Phi \tag*{7.18}$$

$$\Omega_B = \frac{\pi}{2}\gamma(T)\mu_0 H_{\mathrm{SH}} \cos\Phi \tag*{7.19}$$

and $\alpha(T)$, $\gamma(T)$, H_{DMI}, and H_{SH} as defined in the main text. We start with a domain wall at position $x = 0$ with a Néel type domain wall angle $\Phi = 0$. We then simulate a Gaussian current pulse $j(t) = j_0 \exp\left(-\frac{2t^2}{(1\ \mathrm{ns})^2}\right)$, which is in accurate agreement with the recorded transmitted pulse shape of a nominally 1 ns long pulse, see Fig. 7.11a. Both in the discussion of experiments and in the modeled curves, we refer to the peak amplitude j_0 if we talk about “current density of the pulse”, e.g., in plots.

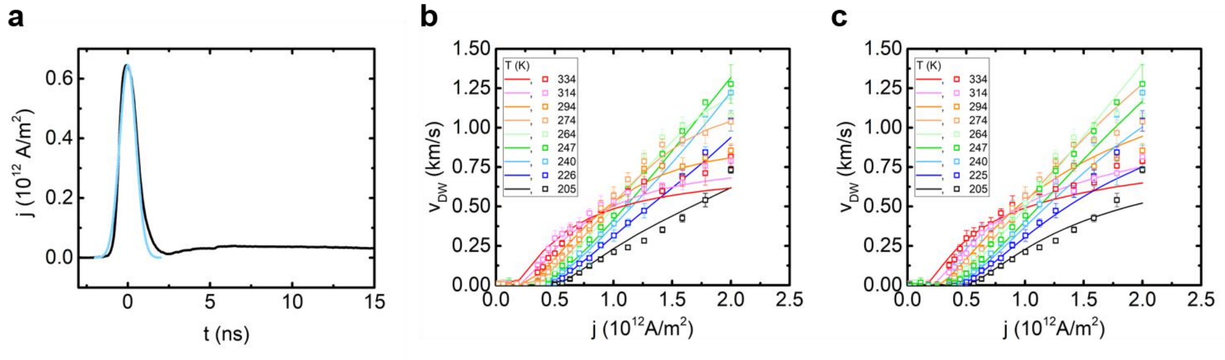

Figure 7.11 | Modeling of v(j,T) a, Transmitted current pulse j through sample (black line) fitted with a Gaussian profile (blue line). The ferrimagnetic 1D domain wall model $v_{DW}(j)$ curves (solid lines) overlaid with experimental data (open squares) are shown with pinning and heating effects included (**b**), and with only pinning and no heating effects included (**c**). Error bars represents the standard deviation of 5 to 20 independent measurements of domain wall velocity (see Fig. 7.2)

We simulate the domain wall motion starting at $t_{\mathrm{s}} = -2$ ns and ending at $t_{\mathrm{e}} = 2$ ns in steps of 50 ps. At every time step, we first calculate the new sample temperature according to the heat rate equation Eq. (7.14) and update $\alpha(T)$, $\gamma(T)$, and $M_s(T)$ accordingly. Then, we calculate the new x and Φ by numerically solving the differential equations (7.16) and (7.17) for the 50 ps time interval using a current density of $\max(0, j(t) - j_{\mathrm{pinning}})$ and using the previous

x and Φ as initial conditions. The current offset j_{pinning} takes into account the fact that DWs in the experiment only move above a critical current density, which depends linearly on temperature: $j_{\mathrm{pinning}}(T) = \left(-2.6 \times 10^{9} \frac{T}{\mathrm{K}} + 1.02 \times 10^{12}\right) \mathrm{A/m^2}$. The differential equation is numerically solved using NDSolve in Wolfram Mathematica. The result of the simulation is the velocity, which is defined by the final position $x(t_{\mathrm{e}})$ divided by the experimentally calibrated effective duration of 1.1 ns of this pulse.

Figs. 7.11b and c show the velocity as a function of substrate temperature T and peak current density j (where those quantities are sometimes referred to as T_0 and j_0, respectively). In Fig. 7.11b, heating and pinning are taken into account as described before, while Fig. 7.11c shows the same simulation without heating. The two models only deviate when j is large and T is close to T_{A}. In particular, the strongest effects are observed when the temperature crosses T_{A} near the peak of the pulse. In all other cases, heating plays a minor role. Overall, the model describes the data extremely well, in particular considering that α_0 and g_{Co} were the only fit parameters.

7.11 Small DMI skyrmions

Owing to their weak stray fields, compensated ferrimagnets can also host much smaller room-temperature skyrmions than ferromagnets[12]. So far, room-temperature skyrmions have all been much larger than the 1-10 nm skyrmions seen in single-layer ferromagnets at cryogenic temperatures[23,55], with sizes ranging from ~30 nm to 2 µm[49,50,56]. The larger sizes relate to the dominant dipolar interactions in the heavy-metal/ferromagnet multilayers commonly used to realise them[12]. This can be understood from the distinct skyrmion energy E versus radius R landscape. Figure 7.12a shows such a typical $E(R)$ curve, calculated for a ferromagnetic multilayer. Similar to circular domains in bubble materials[57], $E(R)$ exhibits a minimum formed by a balance of stray field, dipolar, and domain wall energies, separated from $R = 0$ by a maximum that pushes the equilibrium radius out to larger R. The minimum defines a stray field skyrmion[12], with a characteristic strong field-dependent size (Fig. 7.12a,c), collapse at a finite diameter and finite field, and expansion into stripes at zero field. At room temperature, the collapse diameter of such stray field skyrmions is much larger than 10 nm for realistic material parameters, as described in Ref [12].

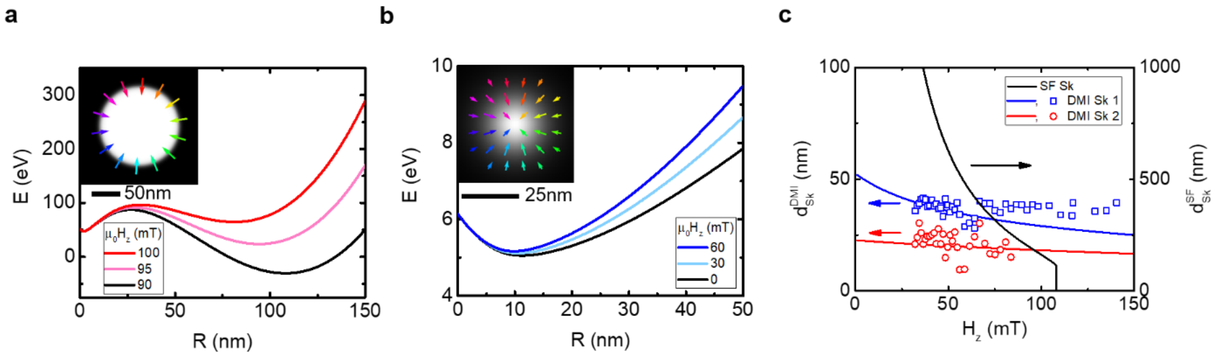

Figure 7.12 | Stray field versus DMI skyrmions. a,b Analytically-calculated energy E versus radius R at several applied fields $\mu_0 H_z$. **a** shows a stray field skyrmion, using parameters typical of heavy-metal/ferromagnet multilayers, and **b** shows a DMI-stabilised skyrmion, using parameters corresponding to Pt/$Gd_{44}Co_{56}$/TaO_x (see Methods). Insets show micromagnetically-simulated spin structures at a field of 100 mT in **a**, and at zero field in **b**; arrows in **b** refer to one of the sublattices. **c,** Calculated skyrmion diameter d_{sk} versus $\mu_0 H_z$ for the stray field skyrmion in **a** (solid black curve) and for the DMI skyrmion in **b** (solid red curve). The solid blue curve was calculated using the material parameters except for the anisotropy, which was $16\ \mathrm{kJ/m^3}$. Open symbols are experimental data for two skyrmions, whose size difference can be accounted for by a difference in local anisotropy.

In films with strong DMI and simple anisotropy-like stray fields interactions, such as atomically-thin ferromagnets in which nanometer-scale skyrmions have previously been observed[8,23], there is a minimum in $E(R)$ with no intermediate maximum, allowing the equilibrium skyrmion size to be much smaller. This minimum defining such DMI skyrmions[12] exists for any applied field but its depth scales with film thickness[12], which is why ultrasmall ferromagnetic skyrmions[8,23] cannot be stable at room temperature since increasing the film thickness leads to destabilising dipolar fields[12]. In addition, surface-volume stray field interactions in thicker ferromagnets can lead to a non-uniform (twisted) skyrmion profile along the out-of-plane direction[58,59] and hence additional destabilising 3D collapse paths[60].

In compensated ferrimagnets with bulk PMA, film thickness can be increased without increasing stray fields, so the depth of the potential well stabilising DMI skyrmions can be increased[12]. Figure 7.12b shows $E(R)$ computed for parameters corresponding to the ferrimagnet studied here (see Methods), along with a micromagnetically-computed spin structure showing a compact Néel skyrmion. We predict a zero-field-minimum at small R with a depth sufficient for room-temperature stability, and a field-insensitive size, characteristic of DMI skyrmions[12], as seen in Fig. 7.12c. We note that away from T_{M}, stray fields can destabilise DMI skyrmions. However, since stay field energies scale with M_s^2, DMI skyrmions are expected to be stable up to $M_{\mathrm{s}}{\sim}150\,\frac{\mathrm{kA}}{\mathrm{m}}$ in our material, which corresponds to a large temperature range of over 100 K around T_{M} (see Fig. 7.3b).

These predictions were confirmed by room-temperature imaging in a similar Pt/$Gd_{44}Co_{56}$/TaO_x film using x-ray holography. Nanotracks were patterned onto SiN membranes to permit current pulse injection for skyrmion nucleation, as has been shown elsewhere[61–63]. Starting from the out-of-plane saturated state, skyrmions were nucleated by injecting 10 ns current pulses in the presence of an out-of-plane bias field (see Fig. 7.14). Skyrmions appear as circular regions of dark contrast (down magnetisation), in the otherwise up-magnetised (light contrast) film. Every image is independently reconstructed by two high resolution reference holes, and skyrmions are only counted if they meet strict criteria, see Section 7.11 Fig. 7.15. Figures 7.13a shows an exemplary magnetic contrast image following current-pulse nucleation where we identify four skyrmions, as indicated by coloured circles. Figures 7.13b shows a subsequent image of the same state with the four skyrmions visible at the same locations, distinguishing them from background intensity fluctuations that vary randomly from image to image. After some time, the skyrmions tend to vanish, as seen in Fig 7.13c, where after 40 min the smallest of the four skyrmions (with a diameter of 16 nm) has is no longer present. The thermal lifetime of the skyrmions is longer for larger skyrmions, which were observed to persist for several hours in this sample at room temperature.

Skyrmions were observed in a variety of locations and in a broad range of applied fields, see Figs. 7.13a-f. The skyrmions remain stable in zero applied field, as shown in Fig. 7.13f. There is almost no correlation between the positions of skyrmions before and after saturation and re-nucleation. To illustrate this, in Figure 7.13d, coloured squares indicate the absence of skyrmions in the locations they appeared in Figure 7.13a,b. Also, all of the skyrmions disappear in a field of 450 mT, clearly distinguishing them from random contrast variations.

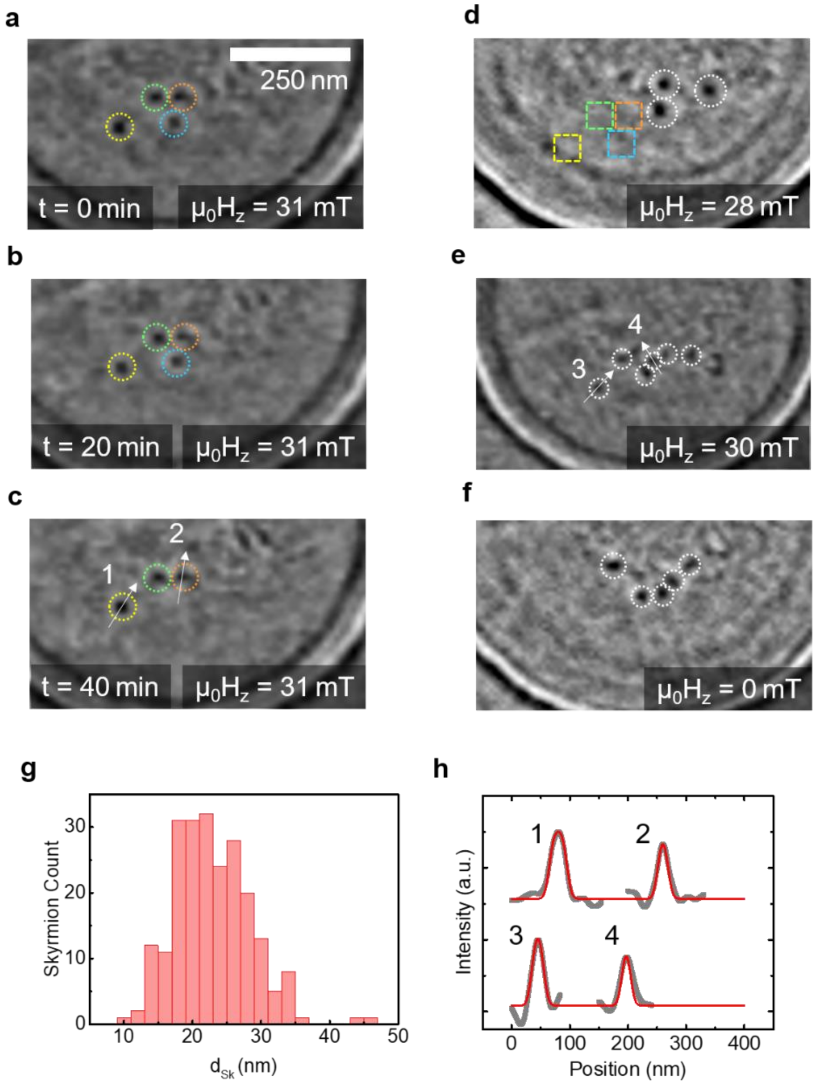

Figure 7.13 | Room-temperature stable ferrimagnetic DMI skyrmions. a-c, Sequence of x-ray holography images of Pt/Co$_{44}$Gd$_{56}$/TaO$_x$ immediately after injecting a nucleation current pulse (**a**), after 20 minutes (**b**) and after 40 minutes (**c**). Skyrmions are outlined by circles for clarity. **d,e**, Skyrmions at different positions obtained after saturating the film and injecting a nucleation current pulse. Coloured squares indicate the absence of skyrmions in locations present in (**a,b**). **j,** Skyrmions under zero out of plane field $\mu_0 H_z$ (nucleated in a bias field which was subsequently reduced to zero). In all images, light (dark) contrast indicates magnetisation out of (in to) the plane. The high-pass filter leads to the ringing in some of the images, as seen in (h). This is not a magnetic feature but simply an artifact from the circular field of view. **k,** Histogram showing the distribution of skyrmion diameters. **l,** Magnetic contrast line scans of the numbered skyrmions in (**c**) and (**e**) (gray points) and fits (red lines, see Fig. 7.14).

The skyrmions show a distribution in size (Fig. 7.13g), with a mean diameter of 23 nm, and minimum observed diameters approaching ~10 nm, which is significantly smaller than has been observed in ferromagnets at room temperature. We attribute the distribution in sizes to dispersion in local magnetic properties. Small variations in anisotropy, for example, lead to significant variation in skyrmion size, as seen in the calculated $R(H_z)$ curves in Fig. 7.12c. The sizes in Fig. 7.13g were conservatively estimated from the largest possible contour of the black region in the images, which accounts for all resolution limiting effects. In reality, skyrmions are hence significantly smaller, since the apparent size includes convolution with the instrument resolution. To estimate the minimum skyrmion size more accurately, we compare line scans of pairs of small and large skyrmions, see Fig.7.13. The peak intensity of the smaller skyrmion is weaker than for the larger skyrmion, which provides a measure of size beyond the resolution limit[49]. Size was estimated by fitting each skyrmion profile to a box function convoluted with a Gaussian of width σ representing the DW width and the imaging resolution, see Fig. 7.15. We identify the skyrmions 1-4 to be 31 ± 6, 17 ± 2, 22 ± 4, and 14 ± 2 nm in diameter, respectively, where the uncertainty comes from noise in the image contrast (see Fig. S10). Finally, as shown in Fig. 7.12c, these skyrmions show a flat $R(H_z)$ dependence and are observed in zero and even negative fields, which is a clear signature of DMI skyrmions. We hence conclude that DMI-stabilised skyrmions are stable at room temperature in this material, which would not be possible in a ferromagnet.

7.12 Holography and Skyrmion Identification

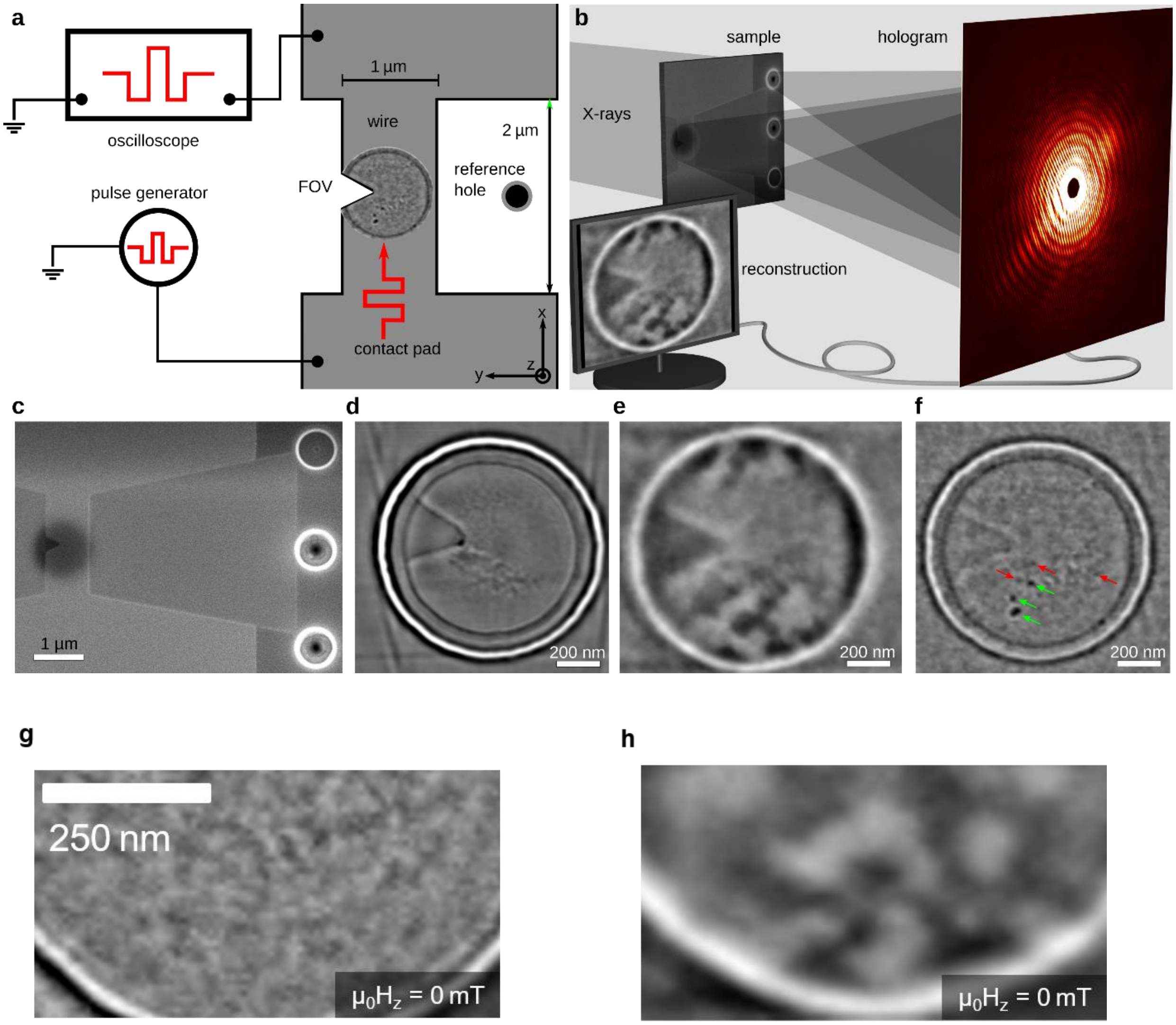

Figure 7.14 | a, Pulse injection setup, showing the microstrip with a notch through which we inject spin orbit torque current pulses. The real-time current density is measured via an oscilloscope. **b,** Schematic of x-ray holographic imaging. The sample is illuminated with coherent circular x-rays at the Co L_3 absorption edge. The scattering pattern of the transmitted light contains the information about the local orientation of the Co magnetisation in the sample. This information is encoded in the amplitude and phase of the wavefield. The phase information is conserved in the detection process by virtue of interference with three reference beams from point-like sources. Each reference interference leads to an independent reconstruction of the magnetic image of the sample, an example of which is shown on the computer screen. **c,** Top-view of the sample geometry in (**b**) acquired using a scanning electron microscope. **d,** Topography of the sample after current-induced annealing, reconstructed from the sum of positive and negative circular light holograms. There is no magnetic information in this image. The large circle is the field of view defined by the holographic mask. The wire shows some signs of damage, in particular in a band-like region near the notch. **e,f,** Magnetic images reconstructed from the difference of positive and negative

x-ray holograms. Note that the topographic features are absent or at least very weak. The three skyrmions in (**f**) are marked with green arrows. Their contrast is clearly above the noise level and the residual topography data. There are several circular features with lower contrast, examples of which are indicated with red arrows. These features are not counted as skyrmions. **g,** Magnetic x-ray holography image of a Pt/$Gd_{44}Co_{56}$/TaO_x nanotrack at zero field after saturation. The image shows a uniform magnetization, which appears neutral gray because the holography images are intrinsically high-pass filtered by the central beamstop that we used to increase the sensitivity to small features such as skyrmions (see Methods) **h,** Labyrinth domains after application of bipolar current pulse train at zero applied field to the state in **(c)**

Figure 7.14 illustrates the data acquisition and analysis process for the skyrmion imaging experiments. The material system is the same as in the domain wall motion part of this study. The only difference is that we now focus on much smaller tracks of 1 µm with and 2 µm length. The center of the wire has a small notch to locally increase the current density, which we found to be helpful for skyrmion nucleation by spin-orbit torques in a previous study[61]. The nanowire and notch are prepared by focused ion beam milling of a wider (10 µm wide) electron beam lithography-patterned track. In the course of experiments, bipolar pulses with amplitude up to $1.7\ \mathrm{TA/m^2}$ and 10 ns width were applied for an extended period of time with cumulative current flow of ~ 40 s in total, after which some topographic inhomogeneities were noted in the vicinity of the notch where the current density was maximum. This suggests some electromigration-induced structural damage, see Fig. 7.14d, and we find no magnetic contrast in this region (see Fig. 7.14e, where labyrinthine domains are visible after current-induced demagnetisation only in the regions away from the notch). We hence focus our analysis on the regions away from the notch where the magnetic properties are minimally affected, as evidenced by clear out-of-plane domains in the demagnetised state, and a lack of magnetic contrast after out-of-plane saturation (see Figs. 7.14g,h), indicating perpendicular anisotropy with full remanence is retained. We note that we cannot, however, rule out annealing-induced changes in magnetic parameters, compared to those extracted from DW motion experiments. Nonetheless, the calculated skyrmion sizes and stabilising energy in Fig. 7.12b agree well with our experiments. We note that we can separate magnetic contrast from topographic features by subtracting holograms recorded with positive helicity from holograms recorded with negative helicity, (see Refs. [64–66] for details of the image reconstruction process) so the contrast features we ascribe to skyrmions are not due to artifacts from the topography. This is also clear from the fact that the skyrmions appear at different positions during each nucleation sequence, as opposed to topographic artifacts, which would be always in the same locations.

Skyrmion appear as dark spots in the magnetic images. In principle, dark spots of various contrast levels and shapes can be found all over the image (Fig. 7.14f), as random noise in the contrast images. To make sure that we only count actual skyrmions for the histogram in Fig. 7.13, we apply several conservative criteria. First, we only count features as skyrmions if their gray level is at least three standard deviations darker than the background mean value (where the standard deviation of background intensity fluctuations is evaluated in an area outside the field of view, which conveniently provides a robust measure of the imaging noise level). Second, our sample has two high resolution reference holes (in addition to one larger reference with low resolution). These references produce two independent image reconstructions and we require that all skyrmions need to be visible in both reconstructions. Third, we confirmed that all identified skyrmions can be annihilated with a magnetic field, unambiguously proving their magnetic nature. And finally, skyrmions need to be sufficiently round, i.e., we do not include stripe-domain-like features in our analysis. In Fig. 7.14f, we point to the three identified skyrmions with green arrows. Red arrows point to other potential skyrmion features which we do not count because their contrast is too weak. Hence, if anything, the histogram in Fig. 7.12g overestimates the average size of skyrmions because we do not count the smallest skyrmions with the weakest contrast.

Figs. 7.14g,h show domain images after saturating the magnetization out-of-plane and subsequently injecting a train of nanosecond current pulses of $1.7 \times 10^{12}\ \mathrm{A/m^2}$ peak amplitude at zero applied field. The image contrast, reflecting the out-of-plane magnetization, is uniform in Fig. 7.14g and shows a labyrinthine domain state in Fig. 7.14h. This suggests that the current pulses effectively demagnetize the system, which we attribute primarily to Joule heating that raises the temperature far above T_{M} so that stray fields can destabilize the magnetization. Significant temperature rise is evidenced by structural degradation outside the region of interest after repeated pulse injection

To analyze the size of the identified skyrmions we again apply a conservative method that yields an upper limit for the skyrmion diameter. Specifically, we search for the largest possible contour that encloses the skyrmion while still describing its apparent size. This procedure is illustrated in Fig. 7.15, showing a magnified skyrmion with the largest possible contour in Fig. 7.15a and the same skyrmion with an attempted slightly brighter (larger) contour in Fig. 7.15b.

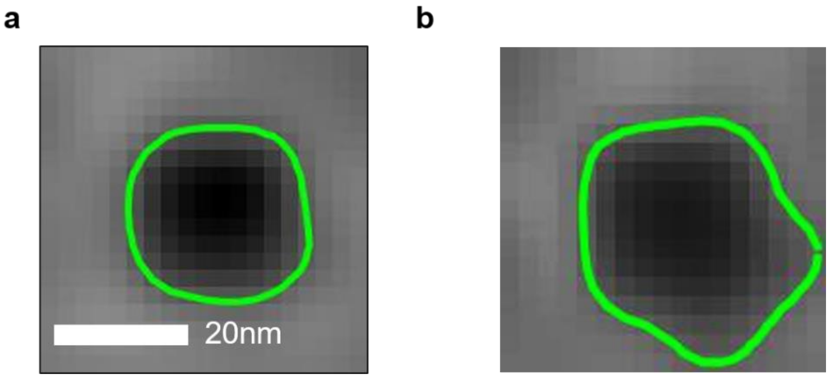

Figure 7.15 | Skyrmion contour size. Skyrmions fit with **a,** largest contour outline describing the skyrmion size and **b,** contour which is too large and does not describe the skyrmion shape.

Clearly, the contour in Fig. 7.15b does not describe the skyrmion. We therefore identify the contour in Fig. 7.15a as the largest possible outline for this particular skyrmion, which intrinsically must be larger than the $m_z = 0$ contour that conventionally describes the skyrmion size. The skyrmion diameter d is then calculated by $d = 2\sqrt{A/\pi}$, where A is the area enclosed by the contour. This quantity d is a very conservative estimate for the skyrmion size since the contour is larger than the $m_z = 0$ outline and because any finite resolution effects of the imaging technique are implicitly included in d. This evaluation of size is used in the histogram Main Text Fig. 7.12g.

Analysis of the line scans in Main Text Fig. 7.12h provides a more accurate assessment of skyrmion diameter for the case when the skyrmion size is close to the resolution limit. By comparing linescans of pairs of skyrmions, the peak intensity can be used to provide a measure of size beyond the resolution limit since skyrmions with size below the instrument resolution exhibit less contrast that those with size greater than the instrument resolution. Size was estimated in this case by fitting each skyrmion profile to a box function convoluted with a Gaussian of width σ representing the DW width and the imaging resolution. The size uncertainties reported are estimated using the following process: The background noise level of the image provides the largest uncertainty. Larger, darker skyrmion peak intensity (relative to background) is used as a reference point for the skyrmions size fits; that is, this contrast level is used as the full-scale contrast between "up" and "down" magnetization states. Since there is noise in the background, there will hence be an uncertainty in the skyrmion size fit. The skyrmions are fitted twice, applying the upper and lower limits of this noise level to the reference peak intensity. The difference in the fitted size is the size of the estimated error bar.

The skyrmionic nature of the identified magnetic features is inferred from their sharp size distribution and from the excellent agreement of their field-dependent size with the theory of DMI skyrmions (Fig. 4m). Their topological nature is further inferred from the measured DMI and other film parameters, which provides a chiral exchange interaction strength sufficient to guarantee a homochiral Néel character as confirmed by micromagnetic simulations (Fig. 4b, inset). In addition, there are only two energy terms that could stabilise features of 10-30 nm in size against thermal annihilation: anisotropy and DMI. Non-topological magnetic grains of similar size are well-known from magnetic hard disks, where they are stabilised by a strong uniaxial anisotropy.[67] Note, however, that such single domain regions of reverse magnetisation only form in a granular medium where the area is decoupled from the rest of the film by non-magnetic grain boundaries. In a continuous exchange-coupled film, such as our samples, a reverse domain needs to be enclosed by a domain wall. The only energy term that can lower the effective domain wall energy sufficiently to stabilise ~10 nm reverse domains is chiral DMI[12]. We therefore can conclude that DMI and exchange are the strongest energies in the observed domains. The domains must be skyrmions because strong DMI leads to homochiral domain walls, i.e., all compact reverse domains in materials with strong DMI are necessarily skyrmions.

7.13 Conclusions

In conclusion, we have demonstrated fast spin-orbit torque driven domain wall motion with velocities exceeding 1 km/s and small DMI skyrmions of sizes approaching 10 nm at room temperature in ferrimagnetic Pt/$Gd_{44}Co_{56}$/TaO_x, which has strong interfacial DMI due to the Pt underlayer. Our experiments confirm that the dynamics of such a ferrimagnet is accurately described by a simple scaled ferromagnet model even close to compensation and at extreme velocities, which makes decades of ferromagnetic research applicable to this class of materials. Ferrimagnets are hence a promising class of materials for spintronic applications based on small, mobile spin textures. Their properties can be controlled by a range of easily accessible knobs, such as interfaces, annealing, and composition. More importantly, they provide a means to realise antiferromagnetic spin systems in which the magnetic state can still be readily detected optically and electrically. Yet, the antiferromagnetic properties of solitonic spin textures, such as skyrmions and DWs, are realised at two distinct temperatures: at magnetic compensation for static properties (such as size) and at angular momentum compensation for the dynamics. Therefore, ferrimagnets such as GdCo with T_M and T_A close together are necessary to simultaneously realise all the benefits of ferrimagnets in potential device applications.

7.14 References

1. Torrejon, J. *et al.* Neuromorphic computing with nanoscale spintronic oscillators. *Nature* **547,** 428–431 (2017).
2. Parkin, S. & Yang, S.-H. Memory on the racetrack. *Nat. Nanotechnol.* **10,** 195–198 (2015).
3. Fert, A., Cros, V. & Sampaio, J. Skyrmions on the track. *Nat. Nanotechnol.* **8,** 152–156 (2013).
4. Olejník, K. *et al.* Terahertz electrical writing speed in an antiferromagnetic memory. *Sci. Adv.* **4,** (2018).
5. Emori, S., Bauer, U., Ahn, S.-M., Martinez, E. & Beach, G. S. D. Current-driven dynamics of chiral ferromagnetic domain walls. *Nat. Mater.* **12,** 611–616 (2013).
6. Ryu, K.-S., Thomas, L., Yang, S.-H. & Parkin, S. Chiral spin torque at magnetic domain walls. *Nat. Nanotechnol.* **8,** 527–533 (2013).
7. Bode, M. *et al.* Chiral magnetic order at surfaces driven by inversion asymmetry. *Nature* **447,** 190–193 (2007).
8. Heinze, S. *et al.* Spontaneous atomic-scale magnetic skyrmion lattice in two dimensions. *Nat. Phys.* **7,** 713–718 (2011).
9. Yang, S.-H., Ryu, K.-S. & Parkin, S. Domain-wall velocities of up to 750 m s−1 driven by exchange-coupling torque in synthetic antiferromagnets. *Nat. Nanotechnol.* **10,** 221–226 (2015).
10. Jungwirth, T., Marti, X., Wadley, P. & Wunderlich, J. Antiferromagnetic spintronics. *Nat. Nanotechnol.* **11,** 231–241 (2016).
11. Baltz, V. *et al.* Antiferromagnetic spintronics. *Rev. Mod. Phys.* **90,** 15005 (2018).
12. Büttner, F., Lemesh, I. & Beach, G. S. D. Theory of isolated magnetic skyrmions: From fundamentals to room temperature applications. *Sci. Rep.* **8,** 4464 (2018).
13. Cheng, R., Xiao, D. & Brataas, A. Terahertz Antiferromagnetic Spin Hall Nano-Oscillator. *Phys. Rev. Lett.* **116,** 207603 (2016).
14. Shiino, T. *et al.* Antiferromagnetic Domain Wall Motion Driven by Spin-Orbit Torques. *Phys. Rev. Lett.* **117,** 87203 (2016).
15. Cheng, R. & Niu, Q. Dynamics of antiferromagnets driven by spin current. *Phys. Rev. B - Condens. Matter Mater. Phys.* **89,** 81105 (2014).
16. Hirata, Y. *et al.* Correlation between Compensation Temperatures of Magnetization and Angular Momentum in GdFeCo Ferrimagnets. *ArXiv* **1710.07779,** (2017).
17. Kim, S. K., Tchernyshyov, O. & Tserkovnyak, Y. Thermophoresis of an antiferromagnetic soliton. *Phys. Rev. B - Condens. Matter Mater. Phys.* **92,** 20402 (2015).
18. Zhang, X., Zhou, Y. & Ezawa, M. Antiferromagnetic Skyrmion: Stability, Creation and Manipulation. *Sci. Rep.* **6,** 24795 (2016).
19. Barker, J. & Tretiakov, O. A. Static and Dynamical Properties of Antiferromagnetic Skyrmions in the Presence of Applied Current and Temperature. *Phys. Rev. Lett.* **116,** 147203 (2016).
20. Kim, K.-J. *et al.* Fast domain wall motion in the vicinity of the angular momentum compensation temperature of ferrimagnets. *Nat. Mater.* **16,** 1187–1192 (2017).
21. Thiaville, A., Rohart, S., Jué, É., Cros, V. & Fert, A. Dynamics of Dzyaloshinskii domain walls in ultrathin magnetic films. *Europhys. Lett.* **100,** 57002 (2012).
22. Martinez, E., Emori, S., Perez, N., Torres, L. & Beach, G. S. D. Current-driven dynamics

of Dzyaloshinskii domain walls in the presence of in-plane fields: Full micromagnetic and one-dimensional analysis. *J. Appl. Phys.* **115,** 213909 (2014).

23. Romming, N. *et al.* Writing and Deleting Single Magnetic Skyrmions. *Science (80-.).* **341,** 636–639 (2013).
24. Kim, K. J. *et al.* Fast domain wall motion in the vicinity of the angular momentum compensation temperature of ferrimagnets. *Nat. Mater.* **16,** 1187–1192 (2017).
25. Wangsness, R. K. Sublattice Effects in Magnetic Resonance. *Phys. Rev.* **91,** 1085–1091 (1953).
26. Tchernyshyov, O. Conserved momenta of a ferromagnetic soliton. *Ann. Phys. (N. Y).* **363,** 98–113 (2015).
27. Litzius, K. *et al.* Skyrmion Hall effect revealed by direct time-resolved X-ray microscopy. *Nat. Phys.* **13,** 170–175 (2017).
28. Jiang, W. *et al.* Direct observation of the skyrmion Hall effect. *Nat. Phys.* **13,** 162–169 (2017).
29. Büttner, F. *et al.* Dynamics and inertia of skyrmionic spin structures. *Nat. Phys.* **11,** 225–228 (2015).
30. Woo, S. *et al.* Current-driven dynamics and inhibition of the skyrmion Hall effect of ferrimagnetic skyrmions in GdFeCo films. *Nat. Commun.* **9,** 959 (2018).
31. Zhang, X., Zhou, Y. & Ezawa, M. Magnetic bilayer-skyrmions without skyrmion Hall effect. *Nat. Commun.* **7,** 10293 (2016).
32. Emori, S., Bono, D. C. & Beach, G. S. D. Interfacial current-induced torques in Pt/Co/GdOx. *Appl. Phys. Lett.* **101,** 42405 (2012).
33. Emori, S., Bauer, U., Ahn, S.-M., Martinez, E. & Beach, G. S. D. Current-driven dynamics of chiral ferromagnetic domain walls. *Nat. Mater.* **12,** 611–6 (2013).
34. Ueda, K., Mann, M., De Brouwer, P. W. P., Bono, D. & Beach, G. S. D. Temperature dependence of spin-orbit torques across the magnetic compensation point in a ferrimagnetic TbCo alloy film. *Phys. Rev. B* **96,** 64410 (2017).
35. Mishra, R. *et al.* Anomalous Current-Induced Spin Torques in Ferrimagnets near Compensation. *Phys. Rev. Lett.* **118,** 167201 (2017).
36. Je, S. G. *et al.* Spin-orbit torque-induced switching in ferrimagnetic alloys: Experiments and modeling. *Appl. Phys. Lett.* **112,** 62401 (2018).
37. Hayashi, M., Kim, J., Yamanouchi, M. & Ohno, H. Quantitative characterization of the spin-orbit torque using harmonic Hall voltage measurements. *Phys. Rev. B* **89,** 4425 (2014).
38. Kim, J. *et al.* Layer thickness dependence of the current-induced effective field vector in Ta|CoFeB|MgO. *Nat. Mater.* **12,** 240–5 (2013).
39. Garello, K. *et al.* Symmetry and magnitude of spin-orbit torques in ferromagnetic heterostructures. *Nat. Nanotechnol.* **8,** 587–593 (2013).
40. Avci, C. O. *et al.* Fieldlike and antidamping spin-orbit torques in as-grown and annealed Ta/CoFeB/MgO layers. *Phys. Rev. B - Condens. Matter Mater. Phys.* **89,** 4419 (2014).
41. Thiaville, A., Rohart, S., Jué, É., Cros, V. & Fert, A. Dynamics of Dzyaloshinskii domain walls in ultrathin magnetic films. *Europhys. Lett.* **100,** 57002 (2012).
42. Emori, S. *et al.* Spin Hall torque magnetometry of Dzyaloshinskii domain walls. *Phys. Rev. B* **90,** 4427 (2014).
43. Zhang, W. *et al.* Determination of the Pt spin diffusion length by spin-pumping and spin Hall effect. *Appl. Phys. Lett.* **103,** 242414 (2013).

44. Ueda, K., Mann, M., Pai, C.-F., Tan, A.-J. & Beach, G. S. D. Spin-orbit torques in Ta/TbxCo100-x ferrimagnetic alloy films with bulk perpendicular magnetic anisotropy. *Appl. Phys. Lett.* **109,** 232403 (2016).
45. Seung Ham, W. *et al.* Temperature dependence of spin-orbit effective fields in Pt/GdFeCo bilayers. *Appl. Phys. Lett.* **110,** 242405 (2017).
46. Roschewsky, N., Lambert, C.-H. H. & Salahuddin, S. Spin-orbit torque switching of ultralarge-thickness ferrimagnetic GdFeCo. *Phys. Rev. B* **96,** 64406 (2017).
47. Mishra, R. *et al.* Anomalous Current-Induced Spin Torques in Ferrimagnets near Compensation. *Phys. Rev. Lett.* **118,** 167201 (2017).
48. Je, S.-G. G. *et al.* Spin-orbit torque-induced switching in ferrimagnetic alloys: Experiments and modeling. *Appl. Phys. Lett.* **112,** 62401 (2018).
49. Moreau-Luchaire, C. *et al.* Additive interfacial chiral interaction in multilayers for stabilization of small individual skyrmions at room temperature. *Nat. Nanotechnol.* **11,** 444–448 (2016).
50. Woo, S. *et al.* Observation of room-temperature magnetic skyrmions and their current-driven dynamics in ultrathin metallic ferromagnets. *Nat. Mater.* **15,** 501–506 (2016).
51. Tono, T. *et al.* Chiral magnetic domain wall in ferrimagnetic GdFeCo wires. *Appl. Phys. Express* **8,** 73001 (2015).
52. Binder, M. *et al.* Magnetization dynamics of the ferrimagnet CoGd near the compensation of magnetization and angular momentum. *Phys. Rev. B* **74,** 134404 (2006).
53. You, C.-Y., Sung, I. M. & Joe, B.-K. Analytic expression for the temperature of the current-heated nanowire for the current-induced domain wall motion. *Appl. Phys. Lett.* **89,** 222513 (2006).
54. Fangohr, H., Chernyshenko, D. S., Franchin, M., Fischbacher, T. & Meier, G. Joule heating in nanowires. *Phys. Rev. B* **84,** 54437 (2011).
55. Romming, N., Kubetzka, A., Hanneken, C., Von Bergmann, K. & Wiesendanger, R. Field-dependent size and shape of single magnetic Skyrmions. *Phys. Rev. Lett.* **114,** 117203 (2015).
56. Jiang, W. *et al.* Blowing magnetic skyrmion bubbles. *Science (80-.).* **349,** 283–6 (2015).
57. Bogdanov, A. N. *Magnetic Domains. The Analysis of Magnetic Microstructures*. *Low Temperature Physics* **25,** (1999).
58. Dovzhenko, Y. *et al.* Magnetostatic twists in room-temperature skyrmions explored by nitrogen-vacancy center spin texture reconstruction. *Nat. Commun.* **9,** 2712 (2018).
59. Legrand, W. *et al.* Hybrid chiral domain walls and skyrmions in magnetic multilayers. *Sci. Adv.* **4,** eaat0415 (2018).
60. Milde, P. *et al.* Unwinding of a Skyrmion Lattice by Magnetic Monopoles. *Science (80-.).* **340,** 1076–1080 (2013).
61. Büttner, F. *et al.* Field-free deterministic ultrafast creation of magnetic skyrmions by spin–orbit torques. *Nat. Nanotechnol.* **12,** 1040–1044 (2017).
62. Hrabec, A. *et al.* Current-induced skyrmion generation and dynamics in symmetric bilayers. *Nat. Commun.* **8,** 15765 (2017).
63. Legrand, W. *et al.* Room-Temperature Current-Induced Generation and Motion of sub-100 nm Skyrmions. *Nano Lett.* **17,** 2703–2712 (2017).
64. Büttner, F. Dynamic Imaging with X-ray Holography. in *Holographic Materials and Optical Systems* (InTech, 2017). doi:10.5772/66689
65. Eisebitt, S. *et al.* Lensless imaging of magnetic nanostructures by X-ray spectro-

holography. *Nature* **432,** 885–888 (2004).

66. Pfau, B. & Eisebitt, S. X-Ray Holography. in *Synchrotron Light Sources and Free-Electron Lasers* 1093–1133 (2016).
67. Weller, D. *et al*. High K/sub u/ materials approach to 100 Gbits/in/sup 2/. *IEEE Trans. Magn.* **36,** 10–15 (2000).

8. INTERFACE-DRIVEN CHIRAL DOMAIN WALLS AND THEIR DYNAMICS IN MAGNETIC INSULATING GARNETS[2]

---

[2] This chapter contains work previously published Can Onur Avci, Ethan Rosenberg, Lucas Caretta, Felix Büttner, Maxwell Mann, Colin Marcus, David Bono, Caroline A. Ross & Geoffrey S. D. Beach, "Interface-driven chiral magnetism and current-driven domain walls in insulating magnetic garnets," *Nat. Nanotechnol.* Advanced online publication (2019)

8.0 Introduction and Motivation

Chiral exchange interactions manifest from broken spatial inversion symmetry. Whereas only a limited number of inversion-asymmetric bulk magnetic materials are known[1–3], engineered interfaces can induce a chiral Dzyaloshinskii-Moriya interaction (DMI) in common centrosymmetric ferromagnets[4–7], in which topological spin textures would otherwise not be found. So far, most research has focused on metallic ferromagnet/heavy-metal bilayers, in which chiral spin textures can be stabilized by interfacial DMI at room temperature[8–10]. Such systems simultaneously benefit from the large spin Hall effect present in DMI-inducing heavy metals like Pt, which provides a source of pure spin current to manipulate chiral spin textures efficiently[8,11].

Due to their chemical and structural complexity, magnetic oxides exhibit a broader range of exotic and useful properties than metals, and oxide-based spintronics may permit functionalities not otherwise readily achieved[12–14]. Insulating magnetic oxides are of particular interest due to their low damping, large magnon diffusion length, and the possibility to generate and transmit pure spin currents with minimal dissipation[15,16]. However, realization of chiral spin textures in magnetic oxides remains a challenge, as few bulk chiral magnetic oxides are known[3]. Interface-induced DMI in centrosymmetric oxides has so far only been studied in conducting oxides at cryogenic temperatures[17–19], using indirect magneto-transport measurements whose interpretation can be ambiguous[20,21].

Here, we use current-driven domain wall (DW) motion in Pt capped magnetic insulating garnets to quantify an interfacial DMI that manifests at the magnetic oxide-substrate oxide interface at room temperature. We examined perpendicularly magnetized oxides containing and lacking a rare-earth transition metal ion and show that the DMI only manifests when a rare-earth element is present. Moreover, we characterize domain wall dynamics as a function of rare-earth iron garnet (ReIG) film thickness. Finally, using both in-plane current and magnetic field we drive domain walls near relativistic limits. Materials examined were perpendicularly-magnetized 2.4-24 nm thick $Tm_3Fe_5O_{12}$ (TmIG), 7 nm $Tb_3Fe_5O_{12}$ (TbIG), and 5 Bi-YIG films grown epitaxially on (111)-oriented $Gd_3Ga_5O_{12}$ substrate, and 6 nm TmIG grown on (111)-oriented substituted-$Gd_3Ga_5O_{12}$ substrate. All samples were covered by a 4 nm-thick Pt layer.

Magnetic oxides were grown on single-side polished substrates by pulsed laser deposition (PLD) using 248 nm KrF excimer laser with 10 Hz repetition rate. The targets were prepared from Fe_2O_3 and Tm_2O_3 or Tb_2O_3 powder by a mixed oxide sintering method. Before and during deposition, the substrate holder was heated to a set point temperature of 900°C, corresponding to a substrate temperature of 650°C, in an oxygen atmosphere of 150 mTorr. The target-sample distance was 8 cm and the cooling rate of the chamber after deposition was 10 °C/min. Metallic overlayers (Pt and Cu/Pt) were deposited by d.c. magnetron sputtering at room temperature with base pressure $< 2 \cdot 10^{-7}$ Torr and the deposition rate of ~2 nm/minute. Film thicknesses were determined using a pre-calibrated deposition rate.

Samples are patterned into lithographically-defined DW racetrack devices. Au Contacts are patterned at each end for current injection into the Pt overlayer. An orthogonal Au strip line is patterned over the racetrack to nucleate DW via an Oersted field. Perpendicular magnetisation was detected using a custom-built scanning magneto-optical Kerr effect (MOKE) system with a focused laser spot of $\sim 8\ \mu m$. Samples structures are defined using contact-mask photolithography followed by Ar^+ ion milling. DW tracks varied in width (10-80 μm) and length (50-200 μm). The contact pads and the DW nucleation line were defined in a second photolithography step followed by Ta(5 nm)/Au(60 nm) sputter deposition and lift-off. Fig. 8.1a-c show MOKE hysteresis loops for 2.4 nm, 6 nm, and 24 nm TmIG samples, confirming their uniaxial perpendicular anisotropy.

Fig. 8.1d-f characterizes switching in the TmIG/Pt bilayers. The current induced spin Hall switching of the TmIG under a d.c. in-plane bias is characterized via MOKE. Low current densities required for switching reflect significant spin transparency between the Pt and TmIG and a large damping-like torque. TmIG thicknesses as high as 24 nm can be switching with low in-plane current and magnetic field.

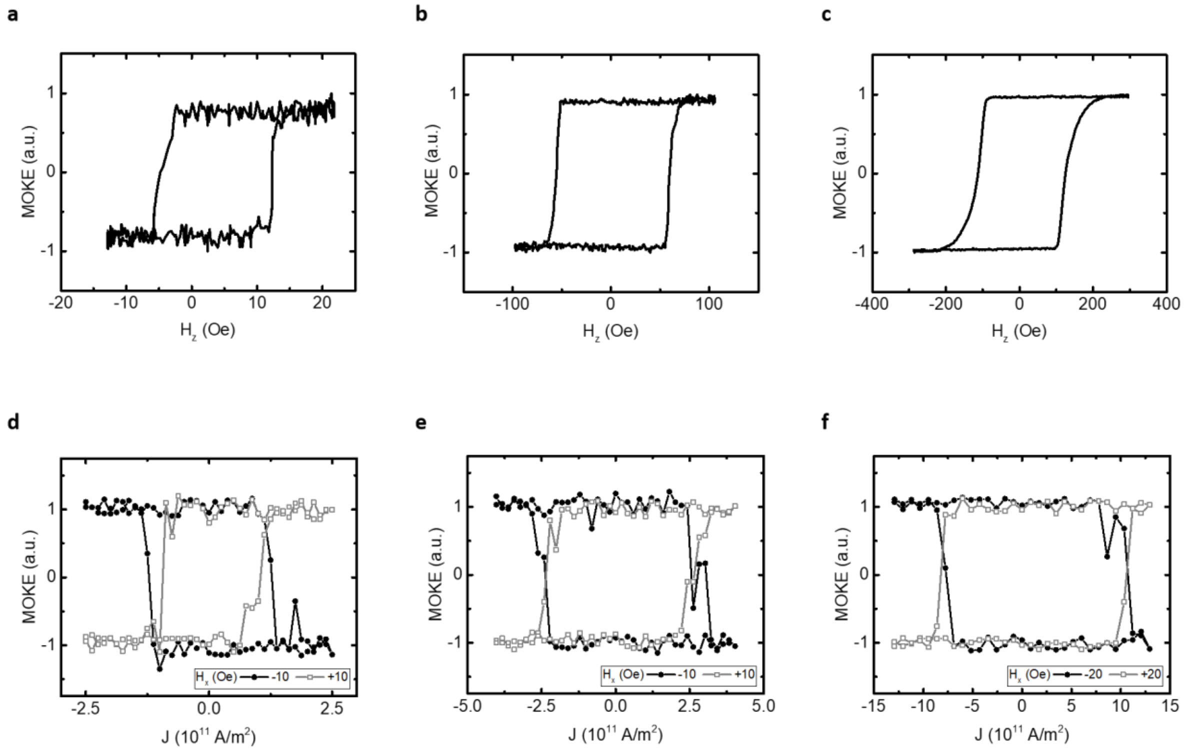

Figure 8.1 | MOKE hysteresis loops and current-induced switching diagrams for a/d) 2.4 nm, b/e) 6 nm, and c/f) 24 nm GGG/TmIG/Pt films.

8.1 Current Assisted Domain Wall Motion

In addition to magnetic switching, the damping-like torque provided from the Pt overlayer can also be used to drive Neel domain walls in the TmIG. The damping-like torque manifests as an easy-axis magnetic field driving the DW. To characterise this effective field, we measure the propagation field H_p of the domain wall under a d.c. bias current in lithographically defined DW racetracks (Fig 8.2a). H_p is extracted from MOKE hysteresis loops, where a DW in nucleated from an overlaid Au stripline on half of the hysteresis loop. The switching field corresponds to the magnetic field required to depinn the DW H_p. A current is applied concurrently with the propagating domain wall and helps or hinders the domain wall propagation (Fig 8.2b). The change in propagation field ΔH_p with current is plotted in fig 8.2c for the 6 nm GGG/TmIG/Pt film. The relative change in propagation field ΔH_p with current density j (slope of Fig. 8.2c) describes the effective easy axis magnetic field per unit current density, also referred to as the spin Hall efficiency χ. The damping-like torque acts as an easy axis magnetic field driving the domain wall

$$H_{eff} = \frac{\pi}{2} H_{DL} \cos(\psi) \qquad 8.1$$

where ψ is the angle between the domain wall magnetisation and the domain wall normal (x-axis). Thus, for a damping-like torque to act on a DW, it must have no-zero Neel character. The non-zero slope in Fig. 8.2c implies that the DWs have Neel character $\psi \neq \frac{\pi}{2}$. Moreover, we find that up-down and down-up DWs have oppositely oriented moments, as H_{eff} is of opposite sign. This suggests that the DWs are homochiral and stabilized by a chiral exchange field, H_{DMI}.

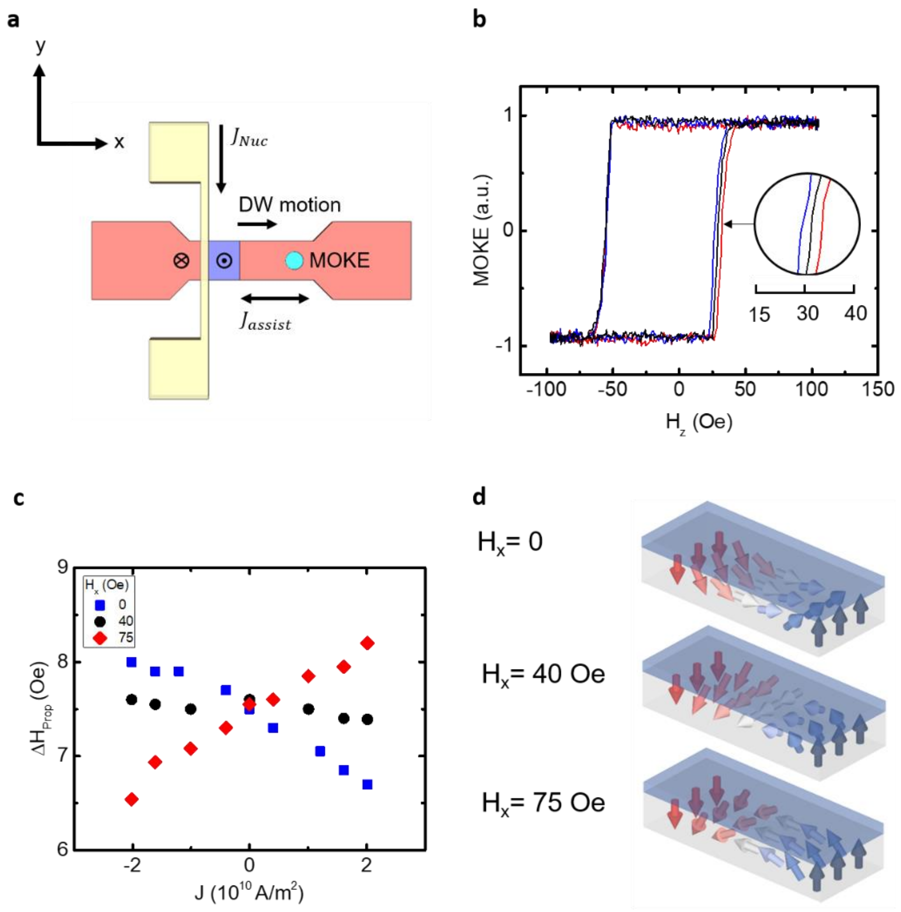

Figure 8.2 | a) Device schematic showing DW racetrack geometry. DWs are nucleated via current flowing through an orthogonal overlaid stripline generating an Oe field. Switching is characterized downstream of the nucleated DW via laser MOKE. b) Exemplary hysteresis loops for TmIG(6 nm)/Pt(4 nm), where the negative switching field is the nucleation field, and the positive switching field is the propagation field. Blue and red overlays show propagation field with an assisting or hindering in-plane current. c) Change in propagation field with applied longitudinal current for three in plane field strengths. d) DW orientation for the three longitudinal fields shown in c).

To confirm this and to quantify the strength of the DMI, we measure the spin Hall efficiency χ as a function of longitudinal in-plane field H_x as previously demonstrated in Emori *et al*[22], and explained in Chapter 6. From Eq. 1, the strength of H_{eff} should vary with ψ. As shown in Fig. 8.2d, applying an in-plane longitudinal magnetic field to the DW can force the DW to rotate from a Neel $\psi = 0$ orientation to a Bloch $\psi = \frac{\pi}{2}$ orientation. Under this condition, H_{eff} is zero, and the spin Hall efficiency is zero. This is illustrated by the $H_x = 75\ Oe$ curve in Fig. 8.2b, whose slope is negligible. Additionally, applying a larger in-plane magnetic field can force the DW to a Neel orientation of the opposite handedness, inverting the spin hall efficiency χ, as seen by the $H_x = 150\ Oe$ curve in Fig. 8.2b. Here, we measure χ as a function of in-plane field for up-down and down-up DWs and plot this in Figure 8.3a. This is effectively a hard-axis hysteresis loop of the moment in the domain wall, where the “switching field” corresponds to the DMI effective field H_{DMI}, and the breadth of one half of the loop corresponds to the DW anisotropy field H_k. Figure 8.3b shows the spin Hall magnetometry data for a series of TmIG, TbIG, and Bi-YIG film of varying thickness and substrate. Notably, we find that both TmIG and TbIG show a significant DMI; however, Bi-YIG does not, regardless of thickness. This suggest that a rare earth element is required for persistence of the DMI in magnetic insulating garnet. We find a similar value for the DMI effective field in TmIG grown on different substrates. The different substrates (GGG and SGGG) have slightly different lattice parameters, which gives rise to a different induced strain in the TmIG film.

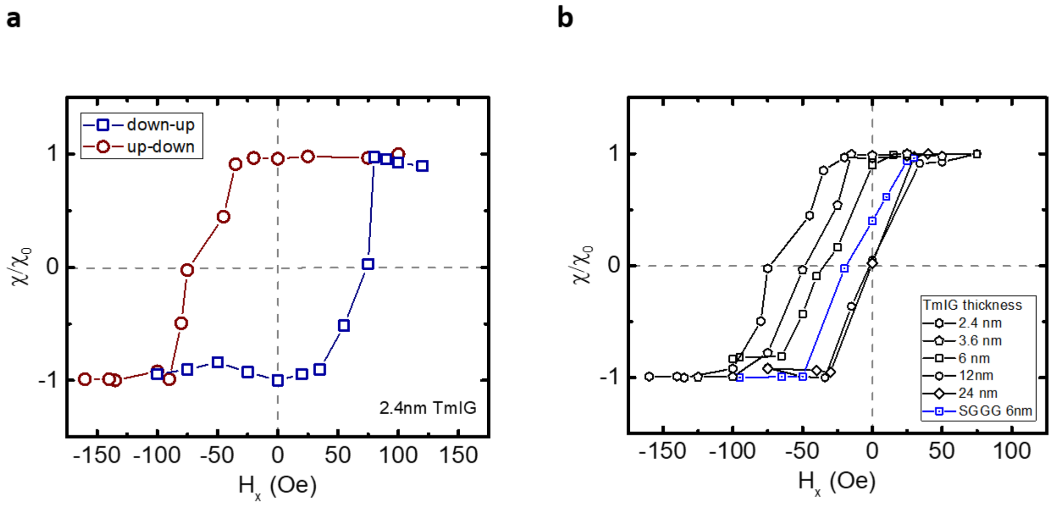

Figure 8.3 | a) Normalized spin Hall efficiency χ as a function of in-plane field for up-down and down-up domain walls in TmIG (2.4 nm)/Pt(4 nm). The “switching field” here corresponds to the DMI effective field. Up-down domain walls for a series of TmIG films are shown in (b).

Pt is known to induce strong DMI at Pt/ferromagnetic-metal interfaces, but the chirality in all previously-studied systems is left-handed when the Pt layer is underneath ferromagnetic metal, i.e., on the substrate side[23]. Surprisingly, the DWs in this system are also left-handed despite the fact that Pt is on top of the magnetic layer, not below. This implies that the DMI may not be from the ReIG/Pt interface. This is evidenced by the in-plane field dependence in Fig. 8.2, and the fact that DWs move in the electron flow direction, opposite to that in metallic systems such as Pt/Co(Fe). To gain more insight into the origin of the chiral effective field, we modify the interface between the garnet and the Pt.

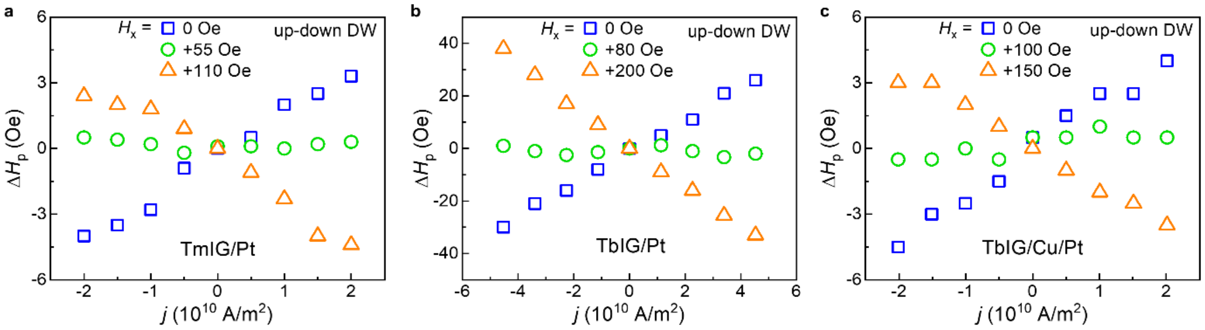

Figure 8.4 | Change in propagation field with current for a) TmIG(5 nm)/Pt (6 nm), b) TbIG(7 nm)/Pt(4 nm), and c) TbIG(7 nm)/Cu(2 nm/Pt(4 nm).

If Pt were responsible for the interfacial DMI, then inserting a Cu spacer should significantly decrease its strength. Comparison between Figs. 8.4a,b show this is not the case. It is known from previous works that adding even a few Å dusting layer between Pt and the ferromagnet is sufficient to entirely quench interfacial DMI[11,24]. The observation that insertion of 2 nm of Cu between Pt and the TmIG produces no measurable change in DMI indicates strongly that DMI is not induced by the Pt. The fact that the 2 nm Cu layer does change dramatically the damping-like torque at this interface in our experiment confirms that it is thick and continuous enough to change the nature of the interface itself. On the other hand, if bulk-like contributions played a role, one may expect a dependence on the heavy rare-earth ion, whose orbital moment is different for Tm and Tb, but this also is not observed. Moreover, cycloidal order (Néel textures) require a form of DMI associated with broken inversion symmetry at a surface, not in the bulk[4]. Since the DMI is insensitive to the top interface and occurs generally in these rare-earth garnets, the substrate oxide/magnetic oxide interface may instead play the dominant role. Rashba splitting is known to manifest at oxide-oxide interfaces[25,26] such as $LaAlO_3$/$SrTiO_3$, which exhibit a variety of emergent two-dimensional magnetic phenomena[13]. Rashba-generated DMI has recently been predicted at oxide-oxide interfaces[27,28], and Rashba-induced DMI can occur even in materials lacking strong spin-orbit coupling[7].

8.2 Thickness Dependence of Micromagnetic Parameters

Figure 8.5 shows the dependence of Magnetisation M, domain wall width Δ, DMI D, and the spin Hall efficiency χ with TmIG thickness t as determined by spin Hall magnetomoetry data and VSM. When plotting the raw magnetisation M as a function of thickness (Fig 8.5a), we find a fitted non-zero x-intercept of $\sim 1.4\ nm$, suggesting that a finite amount of material is not magnetic, ie - indicating a dead layer in the material of size about one unit cell. Δ is calculated from the breadth of the spin Hall magnetometry, the domain wall anisotropy field H_k, data through

$$H_k = \frac{M_s t \ln 2}{\pi \Delta} \qquad 8.2$$

Δ is plotted in Fig 8.5b. Interestingly, Δ decreases with decreasing remarkably TmIG thickness. The domain wall width is given in terms of energies by

$$\Delta = \sqrt{A/K_u} \qquad 8.3$$

where A is the exchange constant and K_u is the uniaxial anisotropy energy. In ReIG films grown by PLD (see Chapter 3), the anisotropy arises from magnetocrystalline, magnetoelastic, and shape anisotropy. The total magnetic anisotropy can be written as[29]:

$$K_u = -\frac{K_1}{12} + \frac{9}{4}\lambda_{111} c_{44}\left(\frac{\pi}{2} - \frac{\beta}{2}\right) + \left(\frac{\mu_0}{2}\right) M_s^2 \tag{8.4}$$

where the first term is the magnetocrystalline anisotropy, the second is the magnetoelastic term, and the third is the shape anisotropy term. K_1 is the first order cubic anisotropy constant, λ_{111} is the magnetostriction coefficient of bulk TmIG, β is the distortion angle of the lattice and c_{44} is the shear modulus for TmIG at room temperature. The dominant term that gives rise to PMA is the magnetoelastic term, which is not expected to change as a function of thickness. In particular, the strain state of the TmIG is expected to remain constant with decreasing thickness. Thus, from Eq. 8.4, we would expected a several order of magnitude decrease in the exchange constant A to be responsible for the dramatic decrease in the domain wall width Δ with decreasing thickness. This is not completely surprising, as intermixing is expected at the substrate oxide – magnetic insulator interface.

Using the spin Hall magnetometry data, we extract the DMI energy D from the DMI effective field using expression 8.5,

$$H_{DMI} = \frac{D}{\mu_0 \Delta M_s} \tag{8.5}$$

From Fig 8.5c,d, we find that both the DMI and the spin Hall efficiency scale inversely with TmIG thickness, further elucidating the interfacial origin of the DMI in ReIG films. Normalized to the film thickness, D is nearly two orders of magnitude lower than in Pt/metallic-ferromagnet systems. However, since the threshold DMI strength (D^{th}) required to stabilize Néel DWs[30] scales as the DW demagnetizing energy, $|D^{th}| = (2t\ln(2)/\pi^2)\mu_0 M_s^2$ (here t is the magnetic layer thickness), the threshold required for Néel DWs in these low-M_s garnets is a factor of ~10^2 smaller than a 1 nm-thick Co film.

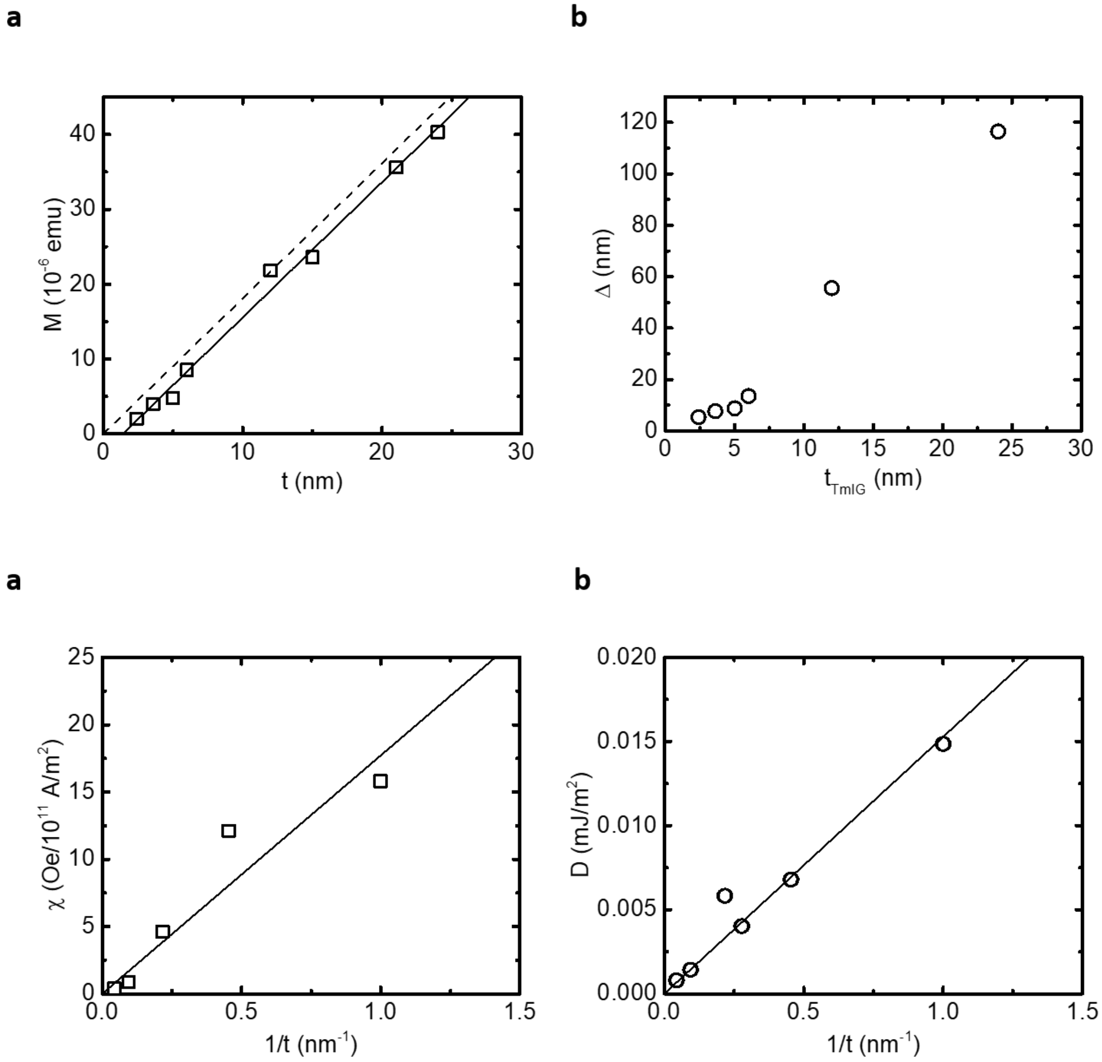

Figure 8.4 | Thickness dependence of a) M, b) Δ, c) χ, and d) D, illustrating the interfacial nature of the SOT and the DMI.

8.3 Anomalous Ultra-fast Current-Driven Domain Wall Dynamics in TmIG

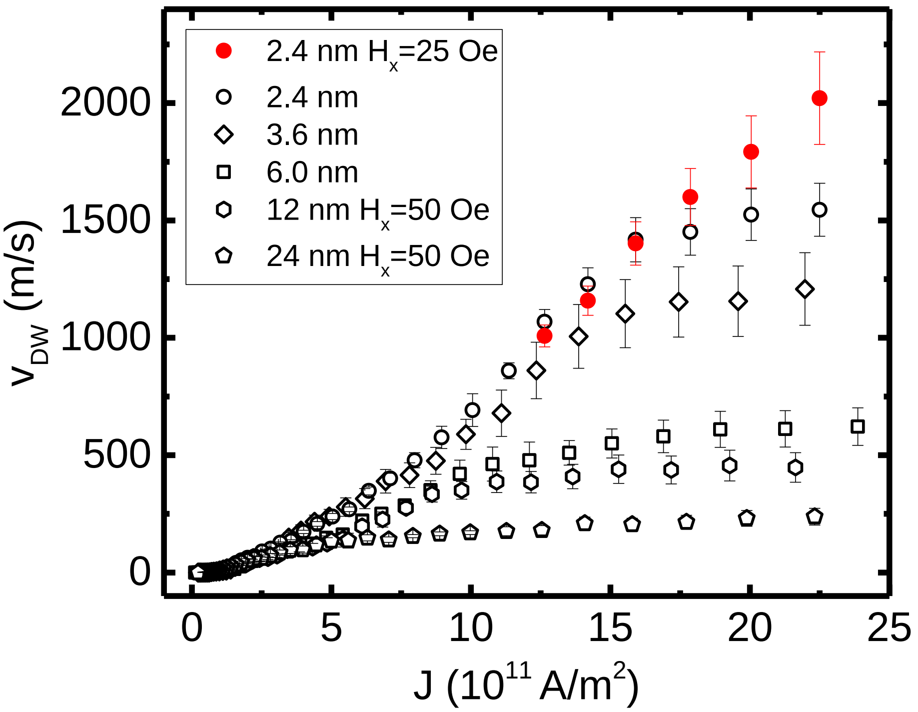

Figure 8.5 | High speed, current-driven domain wall velocity in TmIG/Pt films. 12 and 24 nm TmIG DWs lack Neel character, thus an in-plane field is needed to drive them into motion. 2.4, 3.6, and 6.0 nm TmIG films velocity is limited by DMI strength. Applying an in-plane field to the 2.4 nm sample increase the saturation velocity.

As a significant spin Hall torque and DMI are present in the TmIG films, we characterize the current driven motion of high speed DWs. Figure 8.5 shows the DW velocity v_{DW} as a function of current density J in the Pt overlayer for various thickness of TmIG. Several observations can be made. First, we see a depinning threshold as low as $0.4\ x\ 10^{11}\,\frac{A}{m^2}$, which is which is about an order of magnitude lower than in polycrystalline metallic systems[24,31,32]. Second, while fast domain wall motion has been observed in other multi-sublattice films[33] at magnetic compensation and in synthetic anti-ferromagnets,[32] they occur at significantly higher current density and are particularly temperature sensitive in the case of compensated ferrimagnets. As the angular momentum compensation point is predicated to be much lower than room temperature for TmIG, we expect relatively lower sensitivity to temperature.

Moreover, we find that the velocities in these chiral TmIG films can be even larger than compensated metallic ferrimagnets[33], reaching velocities greater than $1500\,\frac{m}{s}$ with no magnetic field applied. As described in Chapter 7 and ref.[33], in ferrimagnets, the DW velocity can be written

$$v(j) = \frac{\pi}{2}\gamma_{eff}\Delta \frac{\mu_0(H_x + H_{DMI})}{\sqrt{1 + \left(\alpha_{eff}\left(H_{DMI} + \frac{H_x}{H_{SHE}}\right)^2\right)}} \tag{8.6}$$

In the low current density limit, the DW velocity v_{DW} is described by

$$v_{DW}^{low\ j} = \frac{\pi}{2}\frac{\gamma\Delta}{\alpha}\mu_0 H_{SHE} \tag{8.7}$$

And in the high current regime the DW velocity can be described by

$$v_{DW}^{high\ j} = \frac{\pi}{2}\gamma\Delta\mu_0(H_D + H_x) \tag{8.8}$$

While the DMI is necessary to drive DWs with current alone, an in-plane field greater than the DW anisotropy field can be used to force the domain wall into a Neel configuration. Thus, in films with little or no DMI, a small in-plane field can be applied to allow to the spin Hall current to act on the DW. Such is the case for 12 nm and 24 nm TmIG samples shown in Fig. 8.5. A small in-plane field orients the wall into a Neel configuration, and here the velocity plateau is set by the strength of the in-plane field.

The saturation of the curves in Figure 8.5 can be attributed to the DMI in the systems, with thinner films having a larger value of DMI, and hence a larger saturation. Moreover, if the DMI is in fact limiting the DW motion and saturating the DW velocity, applying a longitudinal in-plane field should increase the saturation velocity, as seen in Eq. 8.8. The red data points in Figure 8.5 demonstrates this. At $H_x = 0$, the DW velocity in 2.4 nm TmIG saturates near $1500\,\frac{m}{s}$; however upon the application of $H_x = 25\ Oe$, the domain wall velocity continues to increase, overcoming the DMI limited plateau.

Fig. 8.6 shows that v varies linearly with H_x as expected for chiral Néel DWs driven by damping-like torque. The field at which the extrapolated velocity vanishes is H_DMI, which is in close agreement with our depinning measurements (Fig. 8.3). Hence, the DMI plays a critical role in the current-driven DW dynamics; however, as discussed in Chapter 7, the fast velocities cannot be accounted for the DMI strength alone. This can be seen b examining the effective damping and gyromagnetic ratio, α_{eff} and γ_{eff}, respectively.

From both the high J and low J velocity, and the domain wall width Δ, one can extract the effective damping α_{eff} and gyromagnetic ratio γ_{eff} by taking the slope of the low field velocity with current density and the slope of the high current density velocity with in-plane field H_x ,

$$\frac{dv_{DW}^{low}}{d\mu_0 H_{SHE}} = \frac{\pi}{2}\left(\frac{\gamma_{eff}\Delta}{\alpha_{eff}}\right) \qquad 8.9$$

$$\frac{dv_{DW}^{high}}{d\mu_0 H_x} = \frac{\pi}{2}\gamma_{eff}\Delta \qquad 8.10$$

Taking the ratio of Eqns. 8.9 and 8.10 yields α_{eff} without any assumptions or free parameters. And by using the domain wall width Δ from spin Hall magnetometry measurements, one can also calculate γ_{eff}. A summary of γ_{eff}, α_{eff}, α_0 are shown in Table 8.1.

Table 8.1 | Summary of magnetic parameter of TmIG/Pt

t_{TmIG}	t_{mag}	Δ (nm)	H_{DMI}	α_{eff}	γ_{eff}	α_0
(nm)	(nm)	(nm)	(Oe)	-	-	$\mu = \gamma_0\Delta/\alpha_0$ □
2.4	1.0	5.42	95.0	2.51	208.73	0.0240
3.6	2.2	7.70	72.0	1.79	141.12	0.0253
6.0	4.6	13.56	56.0	0.92	63.04	0.0291
12.0	10.6	55.55	3.0	0.16	12.78	0.0256
24.0	22.6	116.45	1.6	0.05	4.11	0.0255

Here, t_{TmIG} is the thickness of the TmIG layer deposition, while t_{mag} is the t_{TmIG} minus the dead layer thickness determined from VSM measurements. At large thickness of TmIG, both α_{eff} and γ_{eff} are of similar magnitude at one expects for these systems far away from angular momentum compensation. However, it is apparent from Fig. 8.6 that both α_{eff} and $\gamma_{eff} \propto g_{eff}$ diverge as the thickness of TmIG decreases and the net spin density $S = \frac{M_s}{\gamma_{eff}}$ of the magnetic insulator vanishes at small thickness, indicating that the material is approaching angular momentum compensation, or some other phenomenon is leading to anomalously high domain wall velocities in this material system as the magnetic layer thickness decreases.

While the effective damping parameter diverges near T_A, the angular momentum compensation temperature, the dissipation itself does not. S_α is the coefficient of the Rayleigh dissipation function and is well behaved at all thicknesses (Fig 8.6d). This is effectively weights the site-specific damping constants of the garnet.

$$S_\alpha = \sum_i \alpha_i \frac{|M_{s,i}|}{\gamma_i} \tag{8.12}$$

To more naturally characterise the damping constant in ferrimagnets, we can define a mean single-ion damping constant $S_\alpha = \sum_i \alpha_i \frac{|M_{S,i}|}{\gamma_i} \equiv \tilde{\alpha} \sum_i \frac{|M_{S,i}|}{\gamma_i}$, where for TmIG this value is $\tilde{\alpha} \approx 0.0048$. Magnetic damping is typically evaluated by assuming $g = 2$ from ferromagnetic resonance linewidth of domain wall mobility data. In these techniques, the ratio of $\frac{\gamma}{\alpha}$ would not diverge, as both α and γ diverge. Thus, based on the domain wall velocities observed here, the most readily compared value to literature is obtained by extracting the DW mobility and assuming $g = 2$ andusing measured values of domain wall width Δ. This results in a thickness-independent value of $\alpha_0 = 0.026$ for TmIG.

It is unusual that we find that the single-ion damping constant $\tilde{\alpha}$ remains thickness-independent, as spin-pumping from Pt typically causes a significant increase in damping at thin t in metallic systems. Moreover, we conclude that the divergent behavior of g and α_{eff} are directly linked to the anomalously high saturation velocity in TmIG. One possible explanation is if terms are not captured by the effective ferromagnet model. The so-called exchange torque that can arise in multi-sublattice systems with low exchange coupling[32]. This would manifest as a large coefficient in Eq. 8.7 at low thicknesses, and could offer an alternative explanation to the vanishing of angular momentum at thin t, leading to high velocities. In the effective ferromagnet model introduced in Chapter 7, we assumed infinite exchange coupling, meaning that opposing sublattices in the ferrimagnet are always collinear. This was a reasonable assumption in GdCo, as the spin Hall torque is generally known to act of the transition metal, not the rare earth element.

As a result, Gd simply follows the Co moment. In TmIG, transition metal Fe is located on both sublattices, meaning a torque is applied to both sublattices. This could result in a scissoring of the two sublattice magnetisations, resulting in an enhanced DW torque to exchange. Finally, show in in Fig. 8.6d, although the net spin density is decreasing, the intrinsic dissipation $S_\alpha = M_s \frac{\gamma_{eff}}{\alpha_{eff}}$ remains constant.

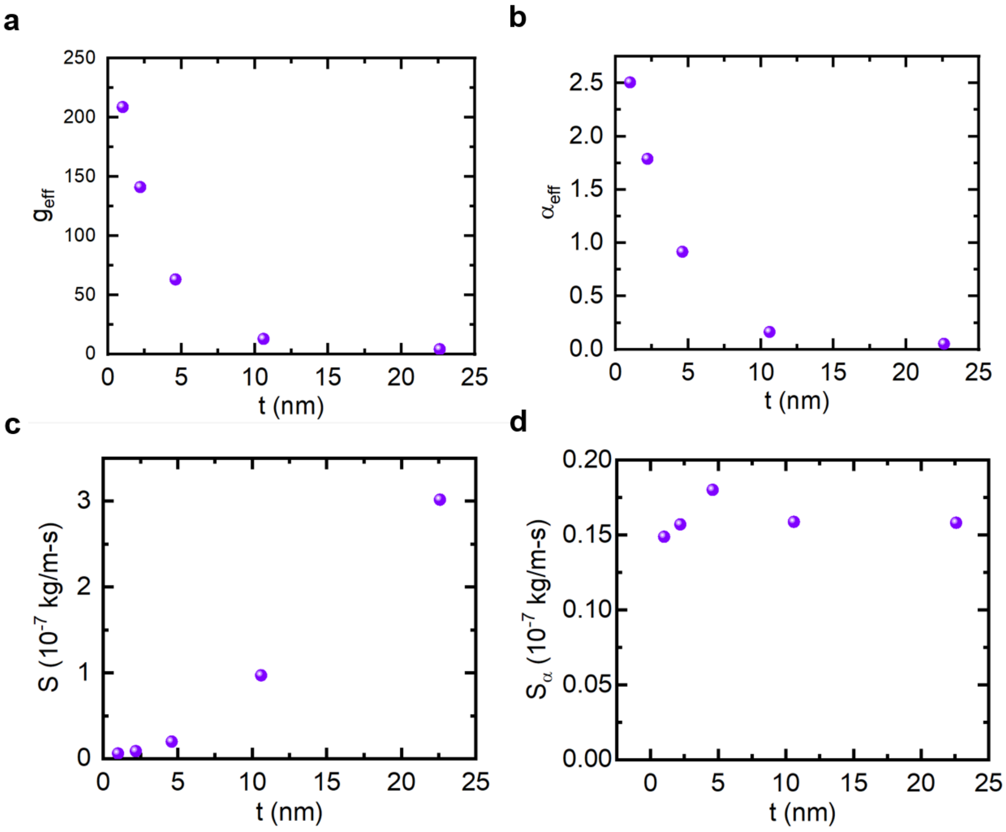

Figure 8.6 | a) g_{eff}, b) α_{eff}, c) S, and d) S_α as a function of TmIG thickness. An anomalous vanishing of the angular momentum S occurs at small thickness t; however the dissipation rate, S_α remains constant.

8.4 Relativistic Domain Wall Motion in Bi-YIG

While we have observed astonishingly fast domain wall velocities in both Pt/GdCo/TaO$_x$ and TmIG/Pt heterostructures, there is a fundamental limit for which a domain wall can travel in a magnetic material. This so called "speed limit" is set by the magnon group velocity[34–40]. Fast dynamics and ease of probing in ferrimagnets allow us an opportunity to reach the magnon group velocity. For ferrimagnets, the max velocity is given by

$$v_{max} = A/dS_{tot} \tag{8.13}$$

where A is the exchange constant, d is the interatomic spacing, and $S_{tot} = \sum_i \frac{|M_{S,i}|}{\gamma_i}$. Similar to objects reaching the speed of light, there is a Lorentz contraction of the domain wall

$$\Delta = \Delta_0\sqrt{1 - \left({}^{v}/_{v_{max}}\right)} \tag{8.14}$$

where Δ is the contracted domain wall width, Δ_0 is the non-contracted domain wall width and the ratio $v/v_{max}$is the ratio of the domain wall velocity to the max velocity. Thus, the typical equations of motion can be simply adapted to account for "relativistic kinetics" by scaling the domain wall width Δ where the domain wall velocity is adapted to

$$v = \frac{\gamma_{eff}\Delta}{\alpha_{eff}}H_{eff} \rightarrow \frac{\gamma_{eff}\Delta_0}{\alpha_{eff}}H_{eff}\sqrt{1 - \left({}^{v}/_{v_{max}}\right)} \tag{8.15}$$

In the case of spin Hall driven domain walls, H_{eff} is the spin Hall effective field H_{SHE}, and hence Eq 8.15 can be readily rearranged to yield a simple analytical expression for the domain wall velocity in the relativistic limit.

$$v = \frac{\tilde{v}}{\sqrt{1 + [\tilde{v}/v_{max}]^2}} \tag{8.16}$$

with

$$\tilde{v} = \frac{\pi}{2}\frac{\gamma_{eff}\Delta_0}{\alpha_{eff}}\frac{\mu_0 H_{SH}}{\sqrt{1 + \left[H_{SH}/\alpha_{eff}H_x\right]^2}} \tag{8.17}$$

One can compute $v(j)$ as usual for a ferrimagnet and insert this into Eq 8.16 to find the limiting behavior. While fast current-driven dynamics can be seen in TmIG, an alternative magnetic insulator Bi-YIG is known to have significantly lower Gilbert damping α_0 than TmIG. Equation 8.7 shows us that the low-drive mobility of a domain wall scales inversely with damping. Consequently, larger domain wall velocities could be obtained in Bi-YIG. As Bi-YIG has no measureable DMI, an in-plane field is needed to orient the domain wall in a Neel configuration, and thus the velocity plateau is limited by the strength of the in-plane field, rather than the DMI. Figure 8.7a plots the velocity of domain walls in Bi-YIG as a function of current density for various in-plane fields. As a comparison, the domain wall velocity of the 2.4 nm TmIG/Pt film is overlaid in grey. Apparent is the larger initial velocity slope of the Bi-YIG sample, indicative of the expected lower damping. With increasing in-plane field, the Bi-YIG velocity plateau increases, reaching remarkable speeds of ~4300 m/s. Using the low and high drive slopes of the velocity, we find that a similar divergence of g_{eff} in BiYIG as TmIG, indicating that this is a general feature of magnetic insulator garnets.

Interestingly, the velocity plateau ceases to increase with increasing in-plane field above $H_x = 140\ Oe$. This domain wall “speed limit” is not defined by the in-plane field, but rather the emission of spin waves from the domain wall. The domain wall has reached the group velocity of magnons in this system, reaching near relativistic speeds.

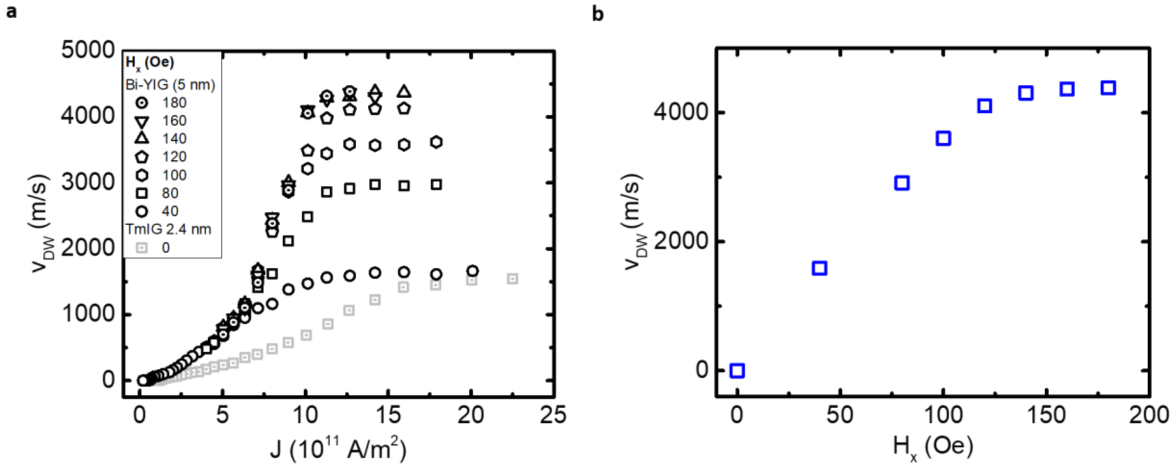

Figure 8.7| a) Domain wall velocity in Bi-YIG as a function current density for various in plane fields and b) as a function of in-plane field at a fixed current density. Velocity plateau in (b) indicates magnon group velocity is reached.

Using Expressions 8.13, we can estimate v_{max} for BiYIG. Using $A = 4.15\times10^{-12}$ J/m, $d = 0.4$ nm, and $S_{tot} = 3.9\times10^{-6}$ kg/m-s, we find $v_{max} = 5200\frac{m}{s}$ in BiYIG (using YIG materials parameters[41]). Using Eq . 14-17 and materials parameters extracted from torque magnetometry, we can calculate the expected spin Hall drive domain wall velocity in BiYIG as a function of current density and in-plane field and plot these in Fig. 8.8. We find that this very closely represents our data, suggesting that we have, for the first time, driven magnetic domain walls to the relativistic magnon group velocity, a fundamental limit for their speed.

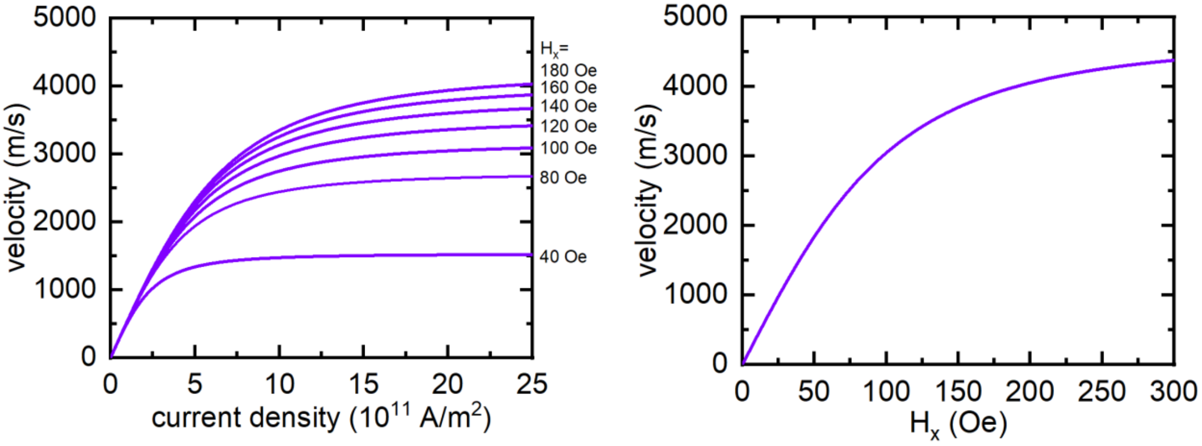

Figure 8.8 | a) Modeled velocity as a function of current density and b) in-plane field.

8.5 Conclusions

In conclusion, we report a significant DMI in centrosymmetric thin-film rare-earth iron garnets that stabilizes Néel DWs with a fixed chirality. We show that spin currents generated by charge current in an adjacent Pt layer can be used to exert substantial damping-like torque on these DWs, leading to efficient current-induced motion at zero applied field. We find small critical currents of a few 10^{10} A/m^2, which we attribute to the high-quality crystalline nature of these materials leading to a low density of defects. Combined with a high current-driven mobility enabled by antiferromagnetic spin dynamics, this allows for fast DW motion at modest current densities, $> 1500\frac{m}{s}$ at $\sim 10^{12}\ A/m^2$. These attributes make rare-earth iron garnets promising for low-power, high-speed DW motions. We find that the interfacial DMI persists whether Pt is in direct contact with the film or not, and occurs generally in a family of RE garnets, and we suggest that it may originate at the substrate oxide-oxide interface by a Rashba-type spin-orbit interaction. Thickness dependent measurements reveal that the origin of the DMI is in fact interfacial. We find that DMI is not present in Bi-YIG, suggesting that the DMI magnetic insulating garnets necessitates a rare earth element.

Although Bi-YIG lacks DMI, we drive domain walls in Bi-YIG with current under an in-plane field. Owing to its low damping, we drive DW as high as 4,300 m/s reaching the magnon group velocity for the first time. This relativistic limit is the fastest a DW can move in a magnetic material. We model this relativistic limit using a simple Lorentz domain wall width contraction model. The possibility to achieve chiral magnetism in magnetic insulators and efficient manipulation of chiral textures by pure spin currents marks an important advance in oxide-based spintronics. From a fundamental perspective, we have reached relativistic DW limits in these systems, marking one of only a few systems discovered where relativistic dynamics can be studied and exploited.

8.6 References

1. Mühlbauer, S. *et al.* Skyrmion lattice in a chiral magnet. *Science (80-.).* **323,** 915–919 (2009).
2. Yu, X. Z. *et al.* Near room-temperature formation of a skyrmion crystal in thin-films of the helimagnet FeGe. *Nat. Mater.* **10,** 106–109 (2011).
3. Seki, S., Yu, X. Z., Ishiwata, S. & Tokura, Y. Observation of Skyrmions in a Multiferroic Material. *Science (80-.).* **336,** 198–201 (2012).
4. Bode, M. *et al.* Chiral magnetic order at surfaces driven by inversion asymmetry. *Nature* **447,** 190–193 (2007).
5. Thiaville, A., Rohart, S., Jue, E., Cros, V. & Fert, A. Dynamics of Dzyaloshinskii domain walls in ultrathin magnetic films. *Eur. Lett.* **100,** 57002 (2012).
6. Fert, A., Cros, V. & Sampaio, J. Skyrmions on the track. *Nat. Nanotechnol.* **8,** 152–156 (2013).
7. Yang, H. *et al.* Significant Dzyaloshinskii-Moriya interaction at graphene-ferromagnet interfaces due to the Rashba effect. *Nat. Mater.* **17,** 605–609 (2018).
8. Woo, S. *et al.* Observation of room-temperature magnetic skyrmions and their current-driven dynamics in ultrathin metallic ferromagnets. *Nat. Mater.* **15,** 501–506 (2016).
9. Boulle, O. *et al.* Room-temperature chiral magnetic skyrmions in ultrathin magnetic nanostructures. *Nat. Nanotech.* **11,** 449–454 (2016).
10. Jiang, W. *et al.* Blowing magnetic skyrmion bubbles. *Science (80-.).* **349,** 283–6 (2015).
11. Ryu, K., Yang, S., Thomas, L. & Parkin, S. S. P. Chiral spin torque arising from proximity-induced magnetization. *Nat. Commun.* **5,** 3910 (2014).
12. Bibes, M. & Barthélémy, A. Oxide spintronics. *IEEE Trans. Electron. Dev.* **54,** 1003–1023 (2007).
13. Bhattacharya, A. & May, S. J. Magnetic Oxide Heterostructures. *Ann. Rev. Mater. Res.* **44,** 65–90 (2014).
14. Chumak, A. V, Vasyuchka, V. I., Serga, A. A. & Hillebrands, B. Magnon spintronics. *Nat. Phys.* **11,** 453 (2015).
15. Kajiwara, Y. *et al.* Transmission of electrical signals by spin-wave interconversion in a magnetic insulator. *Nature* **464,** 262–266 (2010).
16. Cornelissen, L. J., Liu, J., Duine, R. A., Youssef, J. Ben & Van Wees, B. J. Long distance transport of magnon spin information in a magnetic insulator at room temperature. *Nat. Phys.* **11,** 1022–1026 (2015).
17. Matsuno, J. *et al.* Interface-driven topological Hall effect in SrRuO3-SrIrO3 bilayer. *Sci. Adv.* **2,** e1600304 (2016).
18. Ohuchi, Y. *et al.* Electric-field control of anomalous and topological Hall effects in oxide bilayer thin film. *Nat. Commun.* **9,** 213 (2018).
19. Wang, L. *et al.* Ferroelectrically tunable magnetic skyrmions in ultrathin oxide heterostructures. *Nat. Mater.* **17,** 1087–1094 (2018).
20. Kan, D., Moriyama, T., Kobayashi, K. & Shimakawa, Y. Alternative to the topological interpretation of the transverse resistivity anomalies in SrRuO3. *Phys. Rev. B* **98,** 180408(R) (2018).
21. Gerber, A. Interpretation of experimental evidence of the topological Hall effect. *Phys. Rev. B* **98,** 214440 (2018).
22. Emori, S. *et al.* Spin Hall torque magnetometry of Dzyaloshinskii domain walls. *Phys.*

Rev. B **90,** 4427 (2014).
23. Heide, M. & Bihlmayer, G. Dzyaloshinskii-Moriya interaction accounting for the orientation of magnetic domains in ultrathin films: Fe/W(110). *Phys. Rev. B* **78,** 140403 (2008).
24. Ryu, K.-S., Thomas, L., Yang, S.-H. & Parkin, S. Chiral spin torque at magnetic domain walls. *Nat. Nanotechnol.* **8,** 527–533 (2013).
25. Veit, M. J., Arras, R., Ramshaw, B. J., Pentcheva, R. & Suzuki, Y. Nonzero Berry phase in quantum oscillations from giant Rashba-type spin splitting in LaTiO3/SrTiO3heterostructures. *Nat. Commun.* **9,** 1458 (2018).
26. Caviglia, A. D. *et al.* Tunable Rashba Spin-Orbit Interaction at Oxide Interfaces. *Phys. Rev. Lett.* **104,** 126803 (2010).
27. Banerjee, S., Erten, O. & Randeria, M. Ferromagnetic exchange, spin-orbit coupling and spiral magnetism at the LaAlO 3/SrTiO 3 interface. *Nat. Phys.* **9,** 626–630 (2013).
28. Banerjee, S., Rowland, J., Erten, O. & Randeria, M. Enhanced stability of skyrmions in two-dimensional chiral magnets with rashba spin-orbit coupling. *Phys. Rev. X* **4,** 031045 (2014).
29. Quindeau, A. *et al.* Tm3Fe5O12/Pt Heterostructures with Perpendicular Magnetic Anisotropy for Spintronic Applications. *Adv. Electron. Mater.* **3,** 1600376 (2017).
30. Lemesh, I., Büttner, F. & Beach, G. S. D. Accurate model of the stripe domain phase of perpendicularly magnetized multilayers. *Phys. Rev. B* **95,** 174423 (2017).
31. Miron, I. M. *et al.* Fast current-induced domain-wall motion controlled by the Rashba effect. *Nat. Mater.* **10,** 419–423 (2011).
32. Yang, S., Ryu, K. & Parkin, S. Domain-wall velocities of up to 750 m s − 1 driven by exchange-coupling torque in synthetic antiferromagnets. *Nat. Nanotech.* **10,** 221–226 (2015).
33. Caretta, L. *et al.* Fast current-driven domain walls and small skyrmions in a compensated ferrimagnet. *Nat. Nanotechnol.* **13,** 1154–1160 (2018).
34. Yan, M., Andreas, C., Kákay, A., García-Sánchez, F. & Hertel, R. Fast domain wall dynamics in magnetic nanotubes: Suppression of Walker breakdown and Cherenkov-like spin wave emission. *Appl. Phys. Lett.* **99,** 122505 (2011).
35. Kim, S. K., Tserkovnyak, Y. & Tchernyshyov, O. Propulsion of a domain wall in an antiferromagnet by magnons. *Phys. Rev. B* **90,** 104406 (2014).
36. Gomonay, O., Jungwirth, T. & Sinova, J. High Antiferromagnetic Domain Wall Velocity Induced by Néel Spin-Orbit Torques. *Phys. Rev. Lett.* **117,** 017202 (2016).
37. Shiino, T. *et al.* Antiferromagnetic Domain Wall Motion Driven by Spin-Orbit Torques. (2016). doi:10.1103/PhysRevLett.117.087203
38. Shiino, T. *et al.* Antiferromagnetic Domain Wall Motion Driven by Spin-Orbit Torques. *Phys. Rev. Lett.* **117,** 087203 (2016).
39. Zhang, Y., Yuan, H. Y., Wang, X. S. & Wang, X. R. Breaking the current density threshold in spin-orbit-torque magnetic random access memory. *Phys. Rev. B* **97,** 144416 (2018).
40. Yang, H., Yuan, H. Y., Yan, M. & Yan, P. Atomic antiferromagnetic domain wall propagation beyond the relativistic limit. (2018).
41. Malozemoff, A. P. & Slonczewski, J. C. *Magnetic domain walls in bubble materials*.

9. ALL OPTICAL MOTION OF CHIRAL DOMAIN WALLS AND SKYRMION BUBBLES

9.0 Introduction and Motivation

The manipulation of magnetism with femtosecond laser excitations began with the observation of ultrafast demagnetization in ferromagnets[1,2] and was soon followed by the discovery of all optical switching (AOS) in GdFeCo ferrimagnets[3–7]. Today, the mechanism of AOS is well understood, enabling a low-power, sub-picosecond manipulation of magnetism for spintronics[4,8,9]. Deterministic, single shot AOS has been limited to rare-earth transition metal ferrimagnets, whereas in transitional metal ferromagnets, helicity dependent, multi-shot switching occurs through a thermal demagnetization and re-magnetisation process resulting from helicity-dependent propagation of domain walls (DWs)[10–12]. This gave rise to the study of helicity-dependent optical DW motion in transition-metal ferromagnets and ferromagnetic semiconductors. Simultaneously, it was discovered that the anisotropic exchange interaction, also known as the Dzyaloshinskii-Moriya Interaction (DMI), can be present in non-centrosymmetric materials systems, giving rise to new chiral forms of spin textures, such as skyrmions and homochiral Neel DWs[13–18]. It is the DMI that is responsible for enabling current-driven dynamics of spin textures in non-symmetric systems driven by the spin-Hall effect. Moreover, the same DMI that give rise to AOS in ferrimagnetic systems also give rise to ultra-small and ultrafast current-driven spin textures[19], making ferrimagnets the one of the most promising technologies for beyond-CMOS data storage and computing.

However, the role of the DMI and chirality in all optical domain wall motion (AO-DWM) has been nearly neglected, as nearly AO-DWM studies are performed on symmetric stacks lacking the inversion asymmetry needed for DMI. Here, we systematically study the role of DMI in AO-DWM of ferrimagnetic GdCo. We achieve deterministic, single shot thermally-driven motion of chiral Neel DWs in Co-rich Pt/GdCo/Ta trilayers exhibiting significant DMI. We find that that the DW motion does not depend on light helicity, but rather on the orientation of the DW (Neel versus Bloch), revealing the role of the DMI in AO-DWM for the first time. Micromagnetic simulations, in combination with atomistic simulations, support this observation, indicating that coherent AO-DWM in GdCo necessitates Neel DWs, as Bloch DWs propagate incoherently due to (something about Bloch points and Walker breakdown). Atomistic simulations also reveal that the DW motion occurs at fast velocities of at least 1000 m/s. Finally, we demonstrate that this same principle can be applied to drive to skyrmion bubbles at ultrafast speeds all-optically for the first time.

9.0 All Optical Domain Wall Motion in High DMI, Co-Rich Pt/$Gd_{14}Co_{86}$/Ta/Pt

We examined AO-DWM in Pt(6 nm)/Gd_xCo_{1-x}(6 nm)/Ta(y)/Pt(4-6 nm) films (see Fig. 9.1a), where the heavy metal Pt underlayer serves as the source of interfacial DMI in the ferrimagnet, and the thickness of Ta in the Ta(y)/Pt(4-6 nm) overlayer was varied to control the strength of the DMI in the film. The Gd_xCo_{1-x} was sputter deposited onto Si/SiO_2 wafers with a varied composition to tune the compensation temperature of the film to above and below room temperature. First, we examine an asymmetrically stacked, Co-Rich system, where $x = 14$ and $y = 0\,nm$. Figure 1b shows deterministic all-optical toggle switching in this film using linearly polarized 1 ps infrared laser pulses, as measured using differential MOKE microscopy. The laser is incident normal to the sample surface. The robustness of AOS in the system demonstrates the quality of the film. A fluence-pulse duration phase map of AOS using 1 ps linearly light pulses is shown in Fig. 9.1c, where blue shaded regions correspond to conditions that allow for toggle switching, whereas blue regions correspond to regions that do not. Consistent with other studies, we find that the critical fluence (F_c) required for AOS increases with increasing pulse duration, and above a critical pulse duration, thermal demagnetisation of the film occurs (open squares).

To study AO-DWM, first a reverse domain is nucleated in a saturated film using AOS with a 1 ps light pulse at a fluence $F > F_c$. Subsequently, the fluence F is lowered to $0.95F_c$, where no AOS occurs. Then, the laser is rastered across the sample in 200 nm incremental steps, where at each step a single light pulse is incident on the sample. The 200 nm increment allows for significant overlap of the sub critical fluence pulse with the already nucleated domain. This results in propagation of the DW along the direction of the laser rastering. As the fluence of light used was below F_c, any changes in magnetisation can only be attributed to DW motion and not AOS. Figure 9.1d-e shows snapshots of the AO-DWM in the Pt/$Gd_{14}Co_{86}$/Ta/Pt heterostructure measured quasi-statically by MOKE microscopy. Here, AO-DWM occurs using right handed (Fig. 9.1d), left handed (Fig 9.1e), and linearly polarized (Fig. 9.1f) 1 ps light. The red circle indicates the approximate positon and size of the laser spot when the pulse is applied. The laser spot has a Gaussian profile with a FWHM of approximately $20\ \mu m$. As seen in Fig. 9.1d-e, the light cannot only be used to enlarge a domain, but also shrink a domain via DW motion by rastering the laser spot in the reverse direction, making the AO-DWM a completely reversible process. No magnetic field is applied during the DW propagation. Unlike AO-DWM in ferromagnetic systems, the helicity-independence of this process suggests that the DW motion is purely due to a thermally activated process, rather than a two-step demagnetisation and helicity-dependent propagation of DWs.

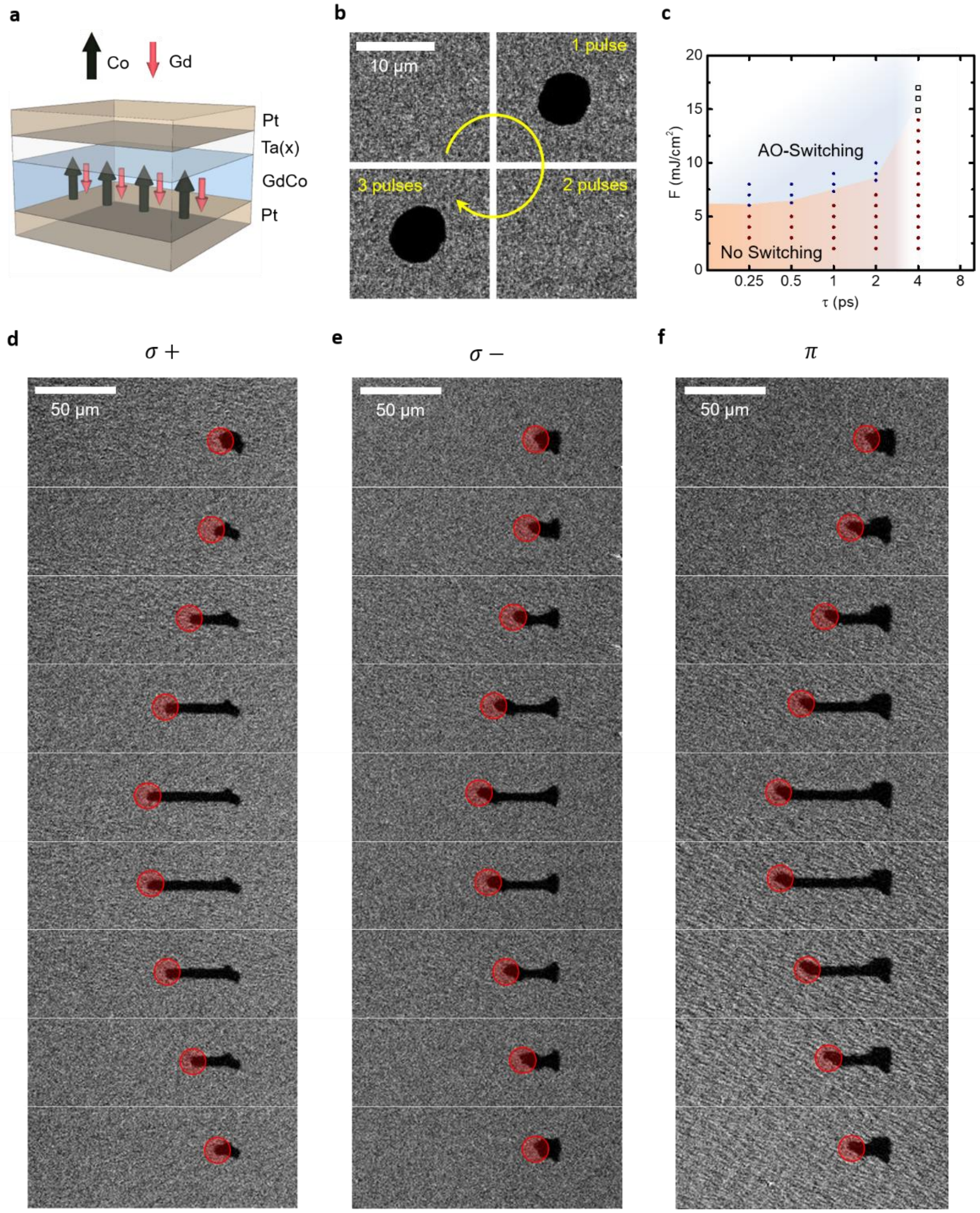

Figure 9.1 | a) Schematic of structure of perpendicularly magnetised Pt(6 nm)/Gd$_x$Co$_{1-x}$(6 nm)/Ta(y)/Pt(4-6 nm). Ta(4 nm) adhesion layer not shown. Black (red) arrows indicate the Co (Gd) sublattice moments. MOKE microscopy image of optical switching (b) and fluence (F)-pulse length (τ) optical switching phase diagram (c) in Pt/Gd$_{14}$Co$_{86}$/Ta(3 nm)/Pt. Blue points indicate toggle optical switching, red points indicate no switching, and open squares indicate thermal demagnetisation. Frames of all optical domain wall motion for d) right- and e) left- circularly polarized light, and f) linearly polarized light. Several hundred laser raster steps pulses are applied between each frame. Red circles indicate the approximate size and location of laser pulses.

9.1 All Optical Domain Wall Motion in Gd-Rich Pt/$Gd_{30}Co_{70}$/Ta/Pt

While AO-DWM is present in the asymmetric, Co-Rich Pt/$Gd_{14}Co_{86}$/Ta/Pt heterostructures, this is not the case for Gd-Rich samples. Figure 9.2a,b show layer schematics for Pt(6 nm)/Gd_xCo_{1-x}(6 nm)/Ta(3 nm)/Pt(4 nm) samples, where $x = 14$ in the Co-rich sample (Fig. 9.2a) or $x = 30$ in the Gd-rich sample (Fig. 9.2b). As shown in Fig. 9.2, while the net magnetisation of the two systems points in the same direction, the dominant elemental magnetic moment is a function of the composition. This results in the two sample having significantly different magnetic compensation temperatures T_M defined where the net magnetisation of the sample is zero. This is illustrated in Fig. 9.2c,d, where the net magnetisation of the ferrimagnetic systems is measured as a function of temperature using vibrating sample magnetometry. While T_M of the Co-Rich sample lies well below room temperature, T_M of the Gd-rich sample lies well above room temperature. Moreoever, at room temperature, the MOKE contrast inverts for Co- and Gd-rich samples as expected, because it arises primarily from the Co sublattice, which is parallel (antiparallel) to the net magnetization in Co- (Gd-)rich sample at room temperature (Fig. 9.2c,d insets). Like the Gd-Rich sample, we find deterministic, all-optical toggle switching using linearly polarized 1 ps laser pulses. This is seen in the MOKE microscopy images in Fig. 9.2e.

Interestingly, we find that thermally driven AO-DWM does not occur in the Gd-Rich Pt/$Gd_{30}Co_{70}$/Ta/Pt heterostructure (Fig 9.2f). In ferrimagnetic systems, effective fields, such as the coercivity H_c and anisotropy field H_k, are expected to diverge at T_M, where the net magnetisation of the film is completely compensated. This is exactly what we find in the Co-rich heterostructure (Fig 9.2c), as H_c, as measure by laser MOKE, begins to diverge as the sample magnetisation M_s decreases at temperatures below room temperature. However, in the case of Gd-rich heterostructure, the coercivity does not diverge at magnetic compensation, but rather stays mostly constant, even though the Kerr angle inverts across T_M as expected, indicated by the open symbols in Fig. 9.2d. As the Curie temperature of Gd is below room temperature, we attribute this peculiar trend to a lowering of anisotropy with temperature in Gd dominant systems. We speculate that this

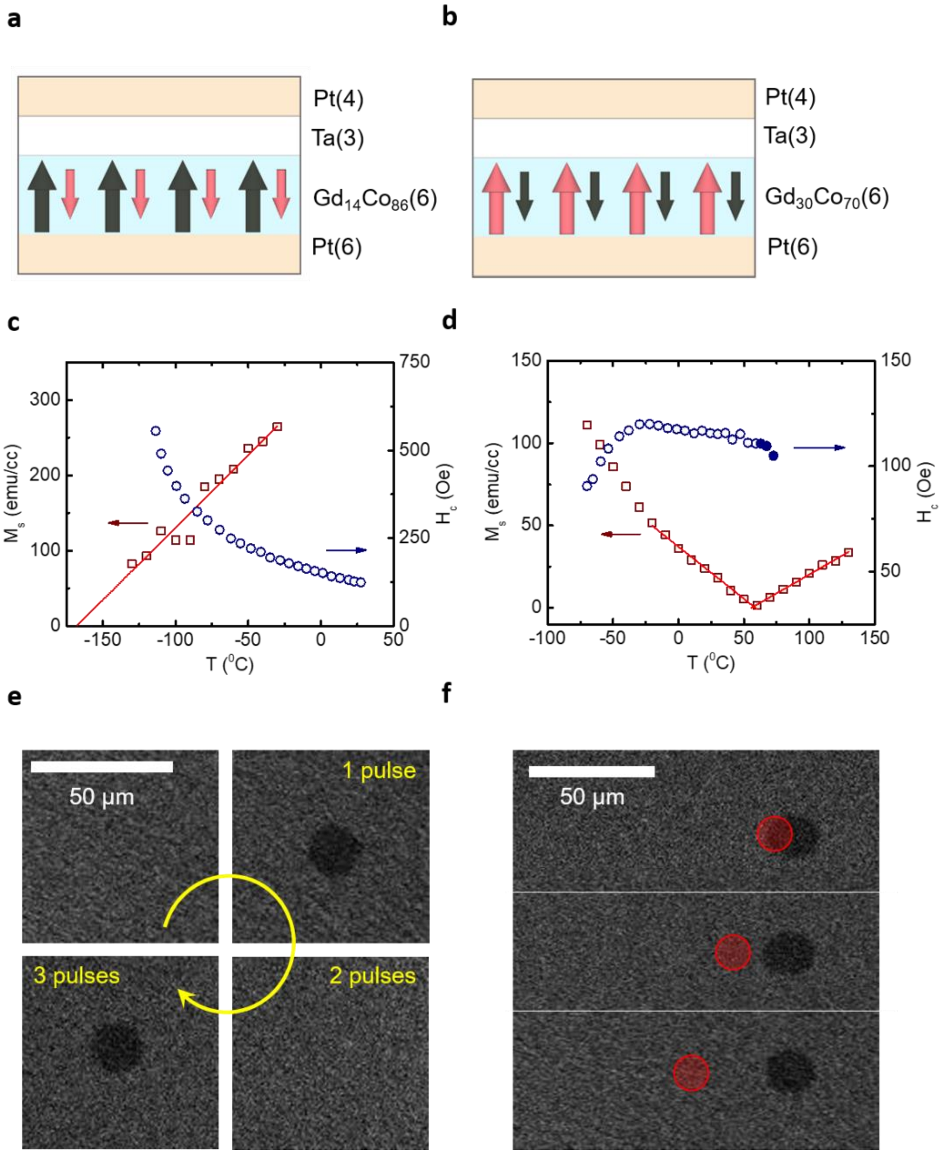

Figure 9.2 | Schematic of asymmetric a) Co-rich Pt(6 nm)/Gd$_{14}$Co$_{86}$(6 nm)/Ta(3 nm)/Pt(4 nm) and b) Gd-rich Pt(6 nm)/Gd$_{30}$Co$_{70}$(6 nm)/Ta(3 nm)/Pt(4 nm) films. M_s (squares) and H_c (circles) as a function of temperature in c) Co-rich and d) Gd-rich films. Filled circles in (d) indicate inversion of the Kerr angle. e) MOKE microscopy image showing toggle switching in Gd-rich film. f) MOKE microscopy showing absence of AO-DWM in Gd-rich film. The red circle indicates the approximate size and location of the rastering laser pulse.

loss of anisotropy is also what is responsible for the non-observation of AO-DWM in this material.

9.2 Incoherent DW motion in low DMI, Co-Rich Pt/$Gd_{14}Co_{86}$/Pt

To understand to role of the DMI in AO-DWM in $Gd_{14}Co_{86}$, we compare optical DW motion in asymmetrically stacked Pt/$Gd_{14}Co_{86}$/Ta/Pt to symmetrically stacked Pt/$Gd_{14}Co_{86}$/Pt heterostructures. Both ferrimagnetic samples have nominally the same Co-rich composition and only differ in stack sequence, as shown in Fig 9.3a. The structurally symmetric sample (Fig 9.3b) is expected to have near no interfacial DMI, as the DMI from symmetric Pt underlayers and overlayers cancels. Conversely, the asymmetric stack (Fig. 9.3a) is anticipated to have strong interfacial DMI, as the Pt underlayer provides a much larger contribution to the DMI than the Ta overlayer. This is confirmed via Brillion light scattering (BLS), shown in Fig. 9.3c,d for the asymmetric and symmetric samples, respectively. The spectra illustrates the non-reciprocal propagation of spin waves resulting from the DMI at a fixed wave vector, k. This is seen as a shift in frequency Δf between modes of opposite wave vector sign ($\pm k$), shown as the Stokes and Anti-stokes peaks. The strength of the DMI is linearly related to this frequency shift through

$$\Delta f = \frac{2\gamma D}{\pi M_s} k \tag{9.1}$$

where γ is the gyromagnetic ratio and D is the strength of the DMI. Using $\gamma = xxx$, the computed values of D are xxx and xxx for the asymmetric and symmetric stacks, respectively. Thus, DWs driven by AO-DWM in asymmetric Pt/$Gd_{14}Co_{86}$/Ta/Pt (Fig 9.1) were of chiral Neel type, while DWs in symmetric Pt/$Gd_{14}Co_{86}$/Pt are Bloch.

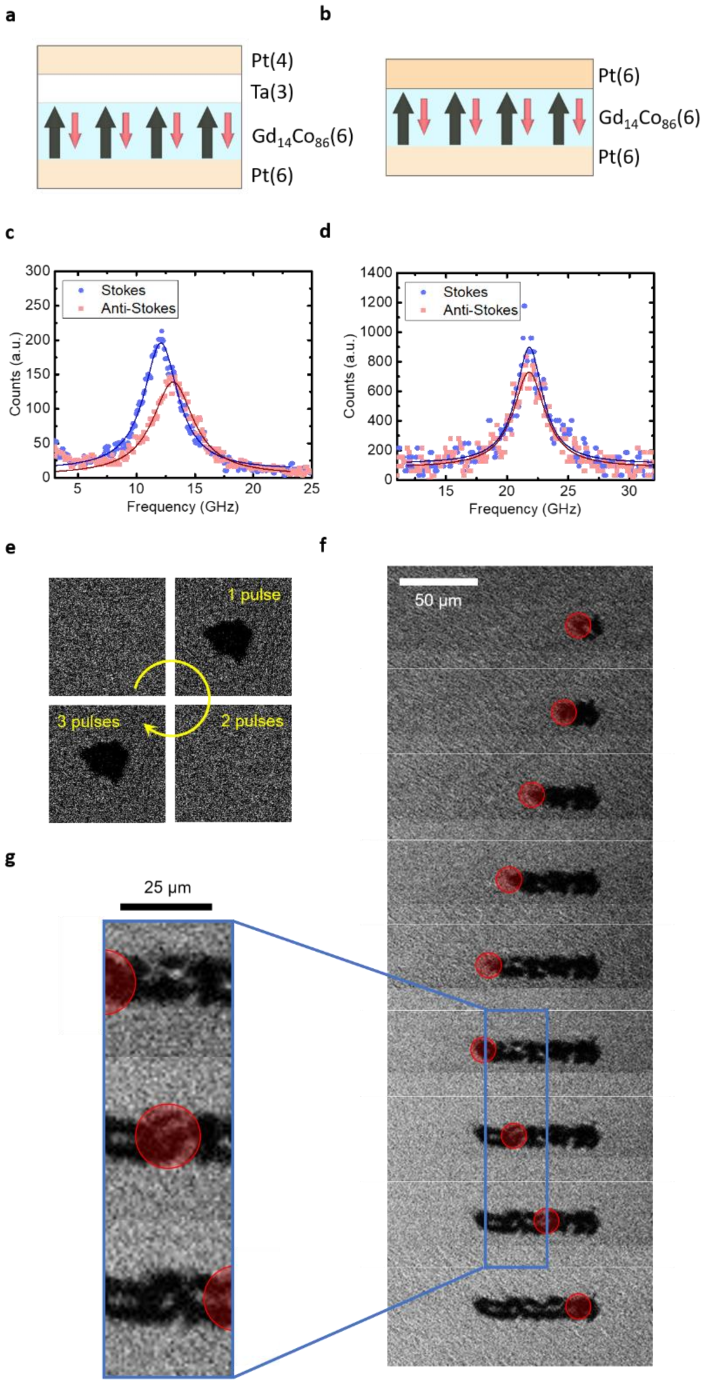

Figure 9.3 | Schematic of asymmetric a) asymmetric Pt(6 nm)/$Gd_{14}Co_{86}$(6 nm)/Ta(3 nm)/Pt(4 nm) and b) symmetric Pt(6 nm)/$Gd_{14}Co_{86}$(6 nm)/Pt(6 nm) films. Corresponding BLS spectra for c) high and d) low DMI films. e) MOKE microscopy image showing toggle switching in low DMI film. f) MOKE microscopy showing incoherent DW motion in low DMI film. The red circle indicates the approximate size and location of the rastering laser pulse. g) zoom in showing the magnetic texture

While the symmetric Pt/$Gd_{14}Co_{86}$/Pt also shows similar deterministic all-optical toggle switching to asymmetric Pt/$Gd_{14}Co_{86}$/Ta/Pt (Fig 9.3e), the light-induced DWM of Bloch DWs in this system is qualitatively different. Fig. 9.3f depicts the optical motion of DWs in the near-zero

DMI system. Rather than coherent AO-DWM seen in the system with significant DMI, the near-

zero DMI system depicts incoherent DW motion, resulting in a demagnetized magnetisation state. Moreover, up reversing the direction of the rastering laser, the incoherent DW propagation changes magnetisation state of the system, as shown by the amplified images in Fig 9.3g. Incoherent DW motion of Bloch domain walls is consistent across the several symmetric Pt/$Gd_{14}Co_{86}$ /Pt samples and over a broad laser fluence, ranging from $0.9F_c < F < 0.99F_c$, where at fluences $F < 0.9F_C$ no DW motion occurs, and $F > F_c$ AOS occurs. These results indicate that coherent AO-DWM in ferrimagnetic films requires significant DMI to be present.

--- section explaining the reasoning behind Bloch domain walls, Walker breakdown, etc---

--- section of atomistic modeling and simulations---

9.3 All Optical, High Speed Motion of Skyrmions

The same principle used to drive DWs optically in section 9.2 can be used to drive chiral skyrmion bubbles at fast speeds in a nominally identical Pt/$Gd_{14}Co_{86}$/Ta/Pt asymmetric stack with high DMI. Here, a reverse bubble is nucleated in the uniformly magnetised ferrimagnetic heterostructure using a laser fluence $F > F_c$. We have shown previously that subsequent laser pulses offset by 200 nm can cause AO-DWM using a fluence $F \sim 0.95F_c$. However, by using a slightly lower fluence $0.85F_c < F < 0.95F_c$, a pair of DWs, rather than a single DW, are driven into motion, resulting in a small chiral bubble or skyrmion bubble to “pinch” off from the reverse nucleated domain. Subsequent pulses drive the skyrmion bubble into motion, analogous to AO-DWM. Figure 9.4a-c show snapshots of the all-optical skyrmion motion (AO-SM) in the Pt/$Gd_{14}Co_{86}$/Ta/Pt heterostructure measured quasi-statically by MOKE microscopy. The red circle indicated the approximate size and position of the laser during a pulse. Similarly to AO-DWM, AO-SM occurs using right handed (Fig. 9.4a), left handed (Fig 9.4b), and linearly polarized (Fig. 9.4b) 1 ps light. This suggests that the mechanism of skyrmion motion is similar to that of DW motion.

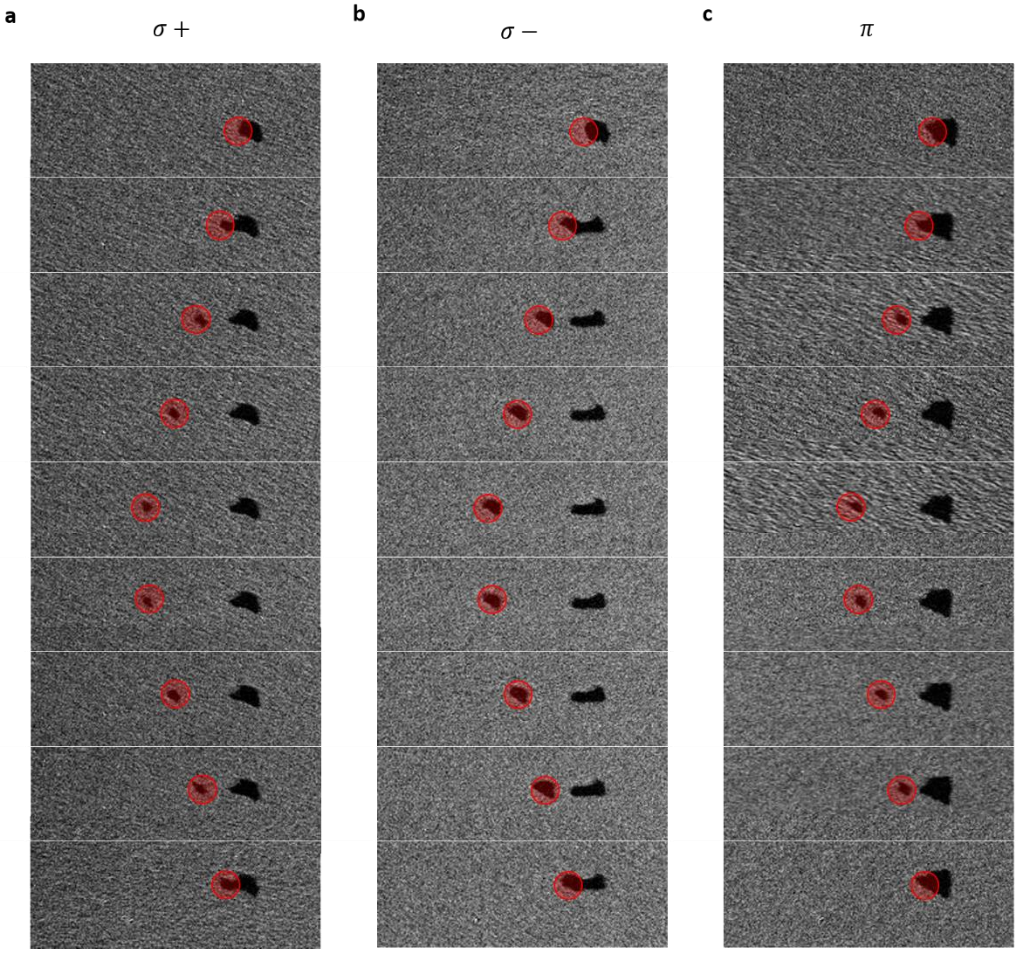

Figure 9.4 | Frames of all optical skyrmion bubble motion for a) right- and b) left- circularly polarized light, and c) linearly polarized light. Several hundred laser raster steps pulses are applied between each frame. Red circles indicate the approximate size and location of laser pulses.

9.4 Conclusions

In summary, we have studied for the influence of the DMI and magnetic compensation on single shot, all optical DW motion in ferrimagnetic GdCo. We have shown that in chiral systems with strong enough interfacial DMI to stabilize chiral Neel domain walls, a sub-critical switching laser fluence can be used to propagate DWs. We use this concept to both expand and contract domains at high speeds. Moreover, we find that in symmetric samples with low DMI, incoherent

DW motion occurs, resulting in the demagnetisation of the film. We demonstrate, for the first time, all optical motion of skyrmions and show motion at very high speeds, bridging the communities of femtosecond magneto-optics and chiral magnetism. The properties of ferrimagnets can be controlled by a range of easily tunable engineering parameters, such as interfaces, annealing and composition. Combined with their potential for ultrafast dynamics, small statics, and optical manipulation, they represent a promising class of materials for the future of spintronics.

9.5 References

1. Beaurepaire, E., Merle, J.-C., Daunois, A. & Bigot, J.-Y. Ultrafast Spin Dynamics in Ferromagnetic Nickel. *Phys. Rev. Lett.* **76,** 4250–4253 (1996).
2. Koopmans, B. *et al.* Explaining the paradoxical diversity of ultrafast laser-induced demagnetization. *Nat. Mater.* **9,** 259–265 (2010).
3. Stanciu, C. D. *et al.* All-Optical Magnetic Recording with Circularly Polarized Light. *Phys. Rev. Lett.* **99,** 047601 (2007).
4. Radu, I. *et al.* Transient ferromagnetic-like state mediating ultrafast reversal of antiferromagnetically coupled spins. *Nature* **472,** 205–208 (2011).
5. Ostler, T. A. *et al.* Ultrafast heating as a sufficient stimulus for magnetization reversal in a ferrimagnet. *Nat. Commun.* **3,** 666 (2012).
6. Lambert, C.-H. *et al.* All-optical control of ferromagnetic thin films and nanostructures. *Science* **345,** 1337–40 (2014).
7. Stupakiewicz, A., Szerenos, K., Afanasiev, D., Kirilyuk, A. & Kimel, A. V. Ultrafast nonthermal photo-magnetic recording in a transparent medium. *Nature* **542,** 71–74 (2017).
8. Lalieu, M. L. M., Lavrijsen, R. & Koopmans, B. Integrating all-optical switching with spintronics. *Nat. Commun.* **10,** 110 (2019).
9. Vahaplar, K. *et al.* Ultrafast Path for Optical Magnetization Reversal via a Strongly Nonequilibrium State. *Phys. Rev. Lett.* **103,** 117201 (2009).
10. Medapalli, R. *et al.* Multiscale dynamics of helicity-dependent all-optical magnetization reversal in ferromagnetic Co/Pt multilayers. *Phys. Rev. B* **96,** 224421 (2017).
11. El Hadri, M. S. *et al.* Two types of all-optical magnetization switching mechanisms using femtosecond laser pulses. *Phys. Rev. B* **94,** 064412 (2016).
12. John, R. *et al.* Magnetisation switching of FePt nanoparticle recording medium by femtosecond laser pulses. *Sci. Rep.* **7,** 4114 (2017).
13. Ryu, K.-S., Thomas, L., Yang, S.-H. & Parkin, S. Chiral spin torque at magnetic domain walls. *Nat. Nanotechnol.* **8,** 527–533 (2013).
14. Emori, S., Bauer, U., Ahn, S.-M., Martinez, E. & Beach, G. S. D. Current-driven dynamics of chiral ferromagnetic domain walls. *Nat. Mater.* **12,** 611–616 (2013).
15. Uchida, M., Onose, Y., Matsui, Y. & Tokura, Y. Real-space observation of helical spin order. *Science* **311,** 359–61 (2006).
16. Bode, M. *et al.* Chiral magnetic order at surfaces driven by inversion asymmetry. *Nature* **447,** 190–193 (2007).
17. Rößler, U. K., Bogdanov, A. N. & Pfleiderer, C. Spontaneous skyrmion ground states in magnetic metals. *Nature* **442,** 797–801 (2006).
18. Romming, N. *et al.* Writing and Deleting Single Magnetic Skyrmions. *Science (80-.).* **341,** 636–639 (2013).
19. Caretta, L. *et al.* Fast current-driven domain walls and small skyrmions in a compensated ferrimagnet. *Nat. Nanotechnol.* **13,** 1154–1160 (2018).

10. CONCLUSIONS AND OUTLOOK

As device density and speeds are nearing fundamental limitations, the hunt for beyond CMOS technology has been attracting research from a number of fields. Some of these include carbon-based technologies, superconducting technologies, and topological material technology. A promising form that offers easy integration into existing systems is spintronics. Over the past decade, academic and industrial research has demonstrated new ways of efficiency manipulating magnetisation and detecting spin. The field of spintronics arguably began with the discovery of giant magnetoresistance (GMR) and tunnel magnetoresistance (TMR), whose scientific and technological interests led to one of the fastest awarded Nobel Prizes in history. GMR and TMR quickly began implemented in hard disk drives as magnetic sensing read heads, impacting information storage density and speed immediately. Not soon after, it was theorized that the GMR or TMR read heads themselves could be used as small information storage bits if the magnetisation of the free layer could be manipulated or switched. These devices are known as magnetic tunnel junctions (MTJ), which, in array can, form magnetic random access memory (MRAM).

Historically speaking, the only way to manipulate a magnetic material is by using another magnet’s stray field. This provides a method, although inefficient to manipulate the magnetisation of a free layer of an MTJ. However, a number of breakthroughs have allowed the manipulations and switching of magnetisation of an MTJ free layer by using currents and voltages which provide a spin torque to the magnetic layer. This spin torque effectively acts like a magnetic field, and are hence, often termed “effective fields.” Among the most prominent are spin-transfer torque and spin orbit torques (SOT). These torques are detailed in Chapter 4. It was shown that a SOT, manifesting in asymmetric magnetic heterostructures adjacent to a heavy metal, can be used to drive domain walls at very fast velocities in ferromagnets. Magnetic domain walls and chiral skyrmions have been conceptualized as potential information bits. This promising approach encodes bits of information using these spin textures that can be translated by currents across racetrack-like wire devices. This racetrack-like wire would comprise the free-layer of an MTJ. However, ferromagnets have fundamental limitations that inhibit further progress: large stray fields limit bit sizes and precessional dynamics limit operating speeds.

In this thesis, we have provided a means to overcome these fundamental limitations by using a different, broader class of magnetic materials: ferrimagnets. Ferrimagnets are a multi-sublattice magnetic system, where each sublattice is of opposite magnetic orientation. We have demonstrated fast SOT-driven domain wall motion with velocities that exceed 1 km s^{-1} at angular momentum compensation and small Dzyaloshinskii-Moriya (DMI) skyrmions of sizes that approach 10 nm near magnetic compensation at room temperature in ferrimagnetic Pt/$Gd_{44}Co_{56}$/TaO_x, which has a strong interfacial DMI due to the Pt underlayer. Our experiments confirm that the dynamics of such a ferrimagnet is accurately described by a simple scaled ferromagnet model, even close to compensation and at extreme velocities. In this simple model, we assume the ferrimagnetic has infinite exchange coupling, meaning that the Gd and Co are always collinear, which makes decades of ferromagnetic research applicable to this class of materials.

The broad class of ferrimagnets also encompasses magnetic garnet insulators. Recently, magnetic insulator films have been grown with perpendicular magnetisation, making them ripe for domain wall motion experiments. Moreover, Magnetic oxides exhibit rich fundamental and technologically desirable properties for spin-based memory, logic, and signal transmission. Particularly, their low damping can allow for very large domain wall mobility, and their insulating properties allow for pure spin transfer and no current shunting. We show that the interfacial DMI can manifest at the substrate oxide – magnetic insulator interface, a key ingredient for realizing fast, SOT driven motion of domain walls. centrosymmetric thin-film rare-earth iron garnets that stabilizes Néel DWs with a fixed chirality. We show that spin torques generated by charge current in an adjacent Pt layer can be used to exert substantial damping-like torque on these DWs, leading to efficient current-induced motion at zero applied field. Combined with a high current-driven mobility enabled by antiferromagnetic spin dynamics, this allows for fast DW motion at modest current densities. We drive domain walls in rare-earth iron garnet ferrimagnetic insulators at velocities exceeding 1500 m/s at current densities near 10^{12} A/m^2. By applying an in-plane field to further stabilize the Neel domain wall, we have shown that domain walls can propagate even faster speeds, overcoming the velocity limit set by the plateau, reaching velocities over 2000 m/s. Furthermore, we find that the interfacial DMI only manifests in magnetic insulators if a rare-earth element is present. This suggests that 4f electrons are necessary to manifest DMI in these material systems.

Although the DMI is not present in Bi-YIG, its low ultra-low damping make it a desirable material for domain wall motion. By applying an in-plane field, we stabilize Neel domain walls, which allow for SOT driven motion. We show that domain wall velocities in BiYIG can reach speeds as high at 4000 m/s and are limited to the strength of the in-plane field applied. However, beyond 140 Oe in-plane, we find that the domain wall velocity is no longer limited by the in-plane field applied, but the by the magnon group velocity in Bi-YIG. We show that this fast domain wall velocity reaches relativistic speeds, hitting a fundamental speed limit of domain walls.

Ferrimagnets are therefore promising for spintronic applications based on small, very mobile spin textures. Their properties can be controlled by a range of easily tunable engineering parameters, such as interfaces, annealing and composition. More importantly, they provide a means to realize antiferromagnetic spin systems in which the magnetic state can still be readily detected optically and electrically.

Chiral Spin Textures and Dynamics in Multi-Sublattice Magnetic Materials

by

Lucas Marcelo Caretta